Measurement of Centrality Dependence of Elliptic Flow for Identified Hadrons in Au + Au Collisions at $\sqrt{s_{\mathrm{NN}}} = 200$ GeV

Hiroshi MASUI

September 2007

Measurement of Centrality Dependence of Elliptic Flow for Identified Hadrons in Au + Au Collisions at $\sqrt{s_{\mathrm{NN}}} = 200$ GeV

Hiroshi MASUI
(Doctoral Program in Physics)

Submitted to the Graduate School of
Pure and Applied Sciences
in Partial Fulfillment of the Requirements
for the Degree of Doctor of Philosophy in
Science

at the
University of Tsukuba

Abstract

Quark-gluon plasma (QGP) is a new state of matter comprised of the deconfined quarks and gluons. It is expected to exist in the early Universe, a few μsec after the Big Bang or in a core of neutron star. Ultra-relativistic heavy ion collision is a unique tool to reach such a very hot and/or dense state on the earth.

Elliptic flow is one of the most promising probe to explore the early stage of heavy ion collisions. It is defined by the second harmonics of the azimuthal anisotropy (v_2) with respect to the reaction plane. Once the local thermal equilibrium is attained, elliptic flow is determined through (1) the initial geometry overlap, and (2) the initial density profile. Therefore, elliptic flow could be sensitive to the possible local thermal equilibrium in the produced matter.

The elliptic flow of identified hadrons has been measured for a broad range of centrality selection and up to transverse momentum $p_{\mathrm{T}} = 4$ GeV/c in the PHENIX experiment at the Relativistic Heavy Ion Collider (RHIC) in Au + Au collisions. The statistics is increased by a factor 20 compared to previous measurements, and it enable us to study detailed centrality dependence of v_2 for identified hadrons. Particle identification has been performed with Time-Of-Flight Counter and Electro-Magnetic Calorimeter by measuring mass square calculated from flight time, flight path length, and momentum ($\pi^{\pm}$, $K^{\pm}$, $p/\bar{p}$, $d/\bar{d}$) and invariant mass reconstruction from the decay product ($\phi \to K^+K^-$). The magnitude of v_2 has been measured with the event plane method. Event plane is determined by the Beam-Beam Counter (BBC) located at forward and backward rapidities, and the elliptic flow of produced hadrons are obtained at the Central arm spectrometer at mid rapidity with respect to the event plane. The large rapidity interval, $|\Delta\eta| \sim 3$, between the Central arm and the BBC has an advantage to reduce the possible non-flow effects, which are correlations among particles and are not oriented from the reaction plane and becomes dilute the true signal of elliptic flow.

Distinct features of the results are follows;

- The transverse momentum dependence of v_2 shows the mass ordering at low p_{T}, i.e. smaller v_2 for heavier hadrons at a given p_{T} ($v_2(\pi) > v_2(K) > v_2(p) \geq v_2(\phi) > v_2(d)$).

- At higher p_{T}, however, v_2 for mesons saturate earlier than that for baryons while the v_2 for baryons are still increasing with p_{T} ($v_2(\pi) \approx v_2(K) \approx v_2(\phi) < v_2(p) \approx v_2(d)$).

- v_2 increase with centrality. The centrality dependence of v_2 is qualitatively consistent with that of initial geometry overlap (eccentricity) estimated by Glauber Monte Carlo simulation.

In order to study the relation between the inital spatial anisotropy (eccentricity, $\langle\varepsilon\rangle$) and final elliptic flow, the eccentricity scaling of v_2 has been studied for a wide range of centrality. We have observed that the participant eccentricity, which is defined by the principal axes of participating nucleons, is the relevant geometric quantity to explain the scaling of $v_2/\langle\varepsilon\rangle$ across Au + Au and Cu + Cu collisions. This result suggest that $v_2/\langle\varepsilon\rangle$ is determined by the number density of nucleons even if the system size is different.

We have developed an extended Blast-wave model, in which collective flow is defined by the gradient of density profile, in order to study the sensitivity of the initial density profile to v_2. Freeze-out temperature (T) and the radial flow velocity (β_T) have been extracted for both transverse momentum spectra and v_2, independently. We have observed that extracted T from v_2 are about $100 - 200$ MeV larger than that from spectra and the results obtained from N_{coll} density profile have always smaller χ^2/NDF for both spectra and v_2. This result may suggest that the v_2 is developed by the number of collisions among the constituents since the number of collisions are closely related to the degree of thermalization. The average radial flow velocity is almost same for spectra and v_2. In order to see the sensitivity of the eccentricity in the measured v_2, we have performed the Blast-wave fitting with the simple 1D in-plane expansion of the system. By expanding the initial density profile, we have observed that T from v_2 fit decreases with the eccentricity, while those from spectra fit and the radial flow velocity are almost unchanged. T from v_2 fit is as large as the chemical freeze-out temperature if we assume that the kinetic freeze-out takes place at the $\langle\varepsilon\rangle$ obtained by the azimuthal HBT analysis. Larger T from v_2 fit than that from spectra fit at the kinetic freeze-out may suggest that the freeze-out of v_2 could be earlier than that of spectra. These results are consistent with the picture of the collective in-plane expansion, where the initial eccentricity is quenched and the magnitude of v_2 is developed through the time evolution.

The quark number scaling of v_2 has been further examined. We have observed that quark number scaling of v_2 works for $p_\mathrm{T}/n_q > 1$ GeV/c, where n_q denote the number of constituent quarks in each hadron ($n_q = 2$ for mesons, 3 for baryons and 6 for deuterons). However, clear mass dependence has been observed for $p_\mathrm{T}/n_q < 1$ GeV/c. By assuming that v_2 is driven by the transverse kinetic energy ($KE_\mathrm{T} = m_\mathrm{T} - m_0$) instead of p_T, we have observed that the quark number scaling with KE_T holds for π, K and p in all centrality classes and for almost all KE_T range, except for low KE_T, $KE_\mathrm{T}/n_q < 0.3$ GeV. Since the pressure gradient is directly linked to the transverse kinetic energy, this results could suggest that the collective pressure gradient is the driving force of elliptic flow. We have also observed that the quark number scaling with KE_T works for ϕ and d in minimum bias and in other centrality bins. Since ϕ mesons do not suffer from the hadronic interactions, the observation of the quark number scaling of v_2 for ϕ mesons could indicate the partonic collectivity in the pre-hadronic phase of heavy ion collisions.

Contents

List of Figures

Acknowledgements

I would like to start thanking my adviser, Yasuo Miake, for his continuous encouragement, his great help of my reserch, and for making sure my presentations going well. He has treated me like a researcher not a student throughout these years. His careful reading of my thesis, comments and suggestions led much improvement of the results in the thesis.

I also would like to thank ShinIchi Esumi. This thesis would never been happend without him. He often give some new ideas about not only the physics topics, but also the method on flow analysis and always kindly answer my questions on all topics.

Many thanks to the staffs and colleagues in University of Tsukuba. In particular, Tatsuya Chujo, Motoi Inaba, and Shingo Sakai, Masahiro Konno, Maya Shimomura, Masaya Oka, Kentaro Miki, Takanori Sato, Yoshimasa Ikeda, Rei Tanabe, Kengo Watanabe, Dousatsu Sakata, Masato Sano, Naoki Shiohara, Natsumi Seya, Chang Peng, Hiroki Yokoyama, Midori Kajigaya, Kankuro Sato, Eitarou Sato and many other colleagues for their advice, suggestions and fluitfull discussions.

I was spent about a half of these years at Brookhaven National Laboratory. I am very grateful to the PHENIX-J group, lead by Hideki Hamagaki, for their hospitality and financial support. I want to thank Kyoichiro Ozawa during my stay at BNL. He is always a good mentor and adviser. I also would like to thank other colleagues in Tokyo University and Hiroshima University for their friendship, encouragement and valuable discussions.

Many thanks to the PHENIX Collaboration, for running the experiment and for providing the huge data sets. Especially, I would like to thank Roy A. Lacey and Arkadij Taranenko for very useful discussions about the elliptic flow results.

Finally, I want to thank my parents. I could never finished my thesis without their great help and understanding. They keep encouraging me and believing that I could do the best.

Chapter 1

Introduction

The ultimate goal of the experiments with relativistic heavy ion collisions is to study the properties of the quark-gluon plasma (QGP), which is a new state of matter at very high density and/or very high temperatures. It is expected that a new state of matter may be created under such extreme conditions, where quarks and gluons are no longer confined inside hadrons and can move freely. The relativistic heavy ion collision offer a unique opportunity to achieve those conditions on the earth. In this chapter, we introduce the quantum chromodynamics (QCD) which is the essential theory to describe the relativistic heavy ion collisions, and introduce the major feature of the the experimental observables at the Relativistic Heavy Ion Collider (RHIC).

1.1 Quantum Chromodynamics (QCD)

Quantum Chromodynamics (QCD) is the theory to describe the strong forces between quarks, where they are the fundamental building blocks of the matter and carry the color charge analogous to the electric charge in quantum electrodynamics (QED). In QCD, gluons are the force medians and they carry the strong force, as photons carry the electromagnetic force in QED. While photons carry no electric charge, gluons also carry color charge and they can interact among themselves.

The classical Lagrangian density for QCD is

$$\mathcal{L}_{cl} = \sum_{f}^{N_f} \bar{q}_f \left(i\gamma^\mu D_\mu - m_f \right) q_f - \frac{1}{4} F^a_{\mu\nu} F^{\mu\nu}_a \tag{1.1}$$

where q_f is the quark field of flavor f and mass m_f (f runs from 1 to 3). The covariant derivative, D_μ is

$$D_\mu = \partial_\mu + ig\frac{\lambda_a}{2} A^a_\mu \tag{1.2}$$

where λ_a is the eight Gell-Mann matrices. $F^a_{\mu\nu}$ is the gluon field strength tensor defined as

$$F^a_{\mu\nu} = \partial_\mu A^a_\nu - \partial_\nu A^a_\mu + g f_{abc} A^b_\mu A^c_\nu \tag{1.3}$$

where A^a_μ is the gluon field (a runs from 1 to 8), and f_{abc} is the structure constants of the SU(3) group. g is defined as $g \equiv \sqrt{4\pi\alpha_s}$, and α_s is the coupling constant of the strong force, which represent the strength of the interactions between quark-gluon, and gluon-gluon interactions.

At short distances, the running coupling constant for the strong force becomes small by the anti-screening feature of the color charge because the gluons are not neutral in color. This property is known as **asymptotic freedom**. Asymptotic freedom means that the typical length scale decreases (or the momentum scale increases) the coupling constants decreases. Because of the smaller coupling constants at smaller distance, pertubative QCD (pQCD) calculation can only be performed for interactions with large momentum transfers (Q). As one can see in Fig. 1.1, the measurements of running coupling constants are in very good agreement with the calculations by pQCD. Although pQCD works very well involving larger momentum transfers, it cannot be used to calculate for the processes with larger distances (or smaller momentum transfers).

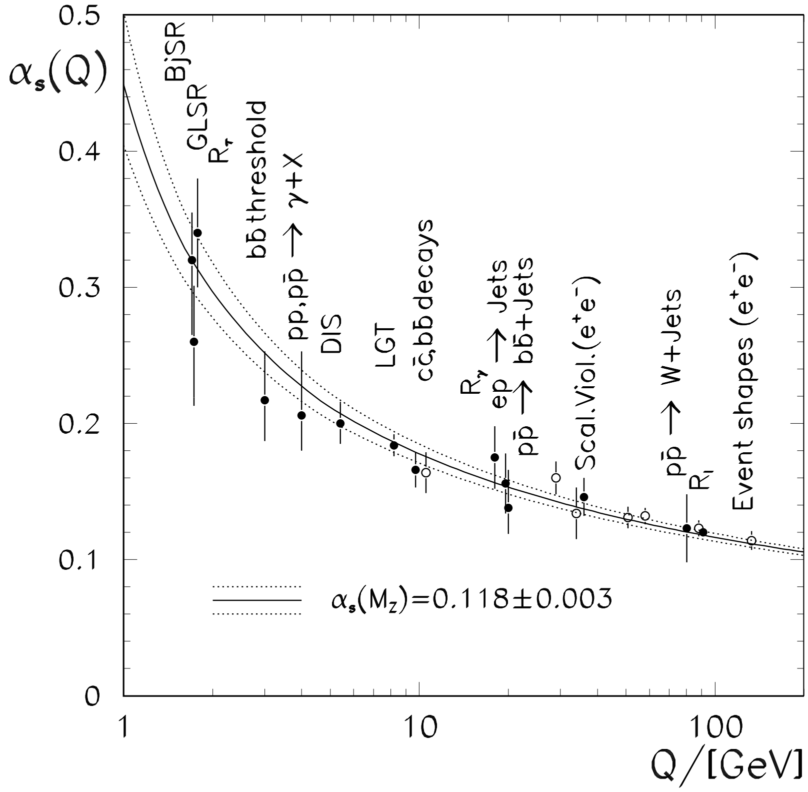

Figure 1.1: The running strong coupling constants as a function of momentum transfers Q by various types of measurements in different experiments, compared to the QCD predictions [1].

A typical form of phenomelogical QCD $q\bar{q}$ pair potential is

$$V_{q\bar{q}} = -\frac{a(r)}{r} + Kr \tag{1.4}$$

where r is the distance between q and $\bar{q}$, and K is the string tension between quark pair. The first term is the color Coulomb potential, and the second term is the linear confining potential which is the unique properties of QCD: the potential increase linearly with the increase of distance.

In the strong coupling regime, the energy to separete two quarks increases linearly with increasing the distance between them. A new $q\bar{q}$ pair is produced when the energy contained between the two quarks becomes more than the twice of the rest momentum of a quark. Therefore, no deconfined quarks have ever been observed. It is known as **confinement** of quarks.

In order to study the strong coupling regime where the perturbative QCD calculations is not valid, Lattice QCD calculations is considered as a strong tool to perform with numerical path integrals of the QCD Lagrangian on a four-dimensional Euclidean lattice with box size L and lattice spacing a. A modern thermodynamical lattice QCD at finite temperature and density suggests that quarks and gluons are deconfined if sufficiently high temperature and/or density are reached.

Fig. 1.2 shows the energy density divided by T^4 as a function of temperature scaled by the critical temperature T_c calculated by Lattice QCD [2]. Current calculations shows that ϵ/T^4 increases rapidly around a critical temperature $T_c \simeq 155 - 175$ MeV. And its values of critical temperatures corresponds to an critical energy density $\epsilon_c \simeq 0.5 - 1$ GeV/fm^3 [2]. Because ϵ/T^4 corresponds to the number of degrees of freedom, this rapid increase of ϵ/T^4 indicate a transition to a new state of matter, namely **quark-gluon plasma (QGP)**.

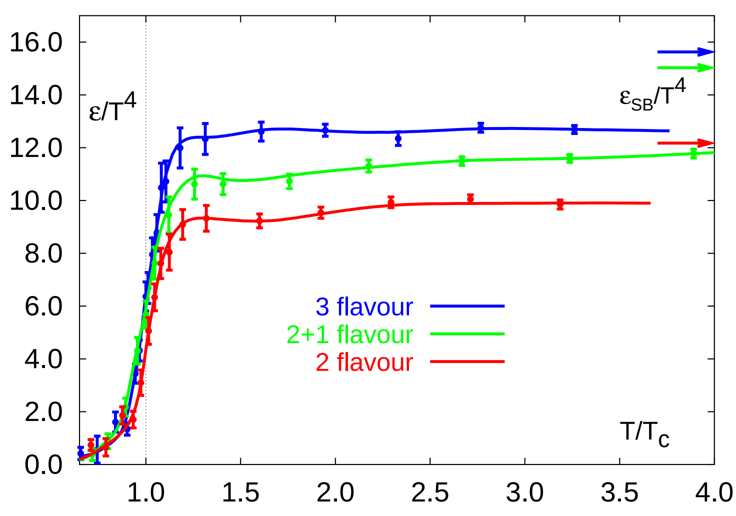

Figure 1.2: The energy density divided by T^4 (ϵ/T^4) as a function of temperature scaled by the critical temperature T_c calculated in Lattice QCD simulation [2]. The arrows on the right side indicate the values of ϵ/T^4 for the Stefan-Boltzmann limit.

1.2 Relativistic Heavy Ion Collisions

Table 1.1: Summary of current and proposed heavy ion programs with facilities, the typical ion beams, and the center of mass energy per nucleon pair

Machine	Location	Ion beam	$\sqrt{s}$ (GeV)	Start of experimental program
AGS	BNL	^{16}O, ^{28}Si	5.4	Oct, 1986
		^{197}Au	4.8	Apr, 1992
SPS	CERN	^{16}O, ^{32}S	19.4	Sep, 1986
		^{208}Pb	17.4	Nov, 1994
RHIC	BNL	^{197}Au	130	2000
		^{197}Au	200	2001
		d + ^{197}Au	200	2003
		^{197}Au	62.4	2004
		^{197}Cu	200	2005
		^{197}Au	200	2007
LHC	CERN	^{208}Pb	5600	2007 (projected)

As seen in Chapter 1.1, QCD predicts a very hot and dense matter consists of deconfined quarks and gluons, quark-gluon plasma (QGP). Relativistic heavy ion collisions is considered to be a unique tool to create such a state of matter under extremely high temperature and/or density on the earth. QGP phase is also expected to exist in the early Universe (after a few micro sec after the Big-Bang), and in the interior of neutron stars. Therefore the observation and study the matter under such extreme conditions has an impact not only on the nuclear physics, but also on the astrophyics and the high-energy physics.

Since 1980's various experiments have taken place both at the Brookhaven National Laboratory (BNL) and European Organization for Nuclear Research (CERN). Table 1.1 summarize the current and proposed heavy ion programs at BNL and CERN. While both AGS and SPS were provided beams with fixed target experiments, RHIC and LHC are the colliders, where two heavy ions accelerate up to nearly the speed of light and collide each other.

The relativistic heavy ion collisions are dynamic processes with typical time scales of an order 10 fm/c. Even if the QGP is created in collisions, the system expands and cools rapidly back to a hadron gas through a QCD phase transition. In order to probe the formation of the QGP, the signals which is sensitive to the QCD phase transitions should be observed as many as possible.

1.2.1 Collision Geometry

In relativistic heavy ion collisions, the geometry of the collisions can be defined by the participant spectator model. Fig. 1.3 shows a schematic view of heavy ion collision between symmetric Lorentz contracted projectile and target nuclei in the center of mass frame. The **impact parameter b** is the distance between the center of nuclei and characterize the **centrality** of collision. The nucleons taking part in the primary collisions

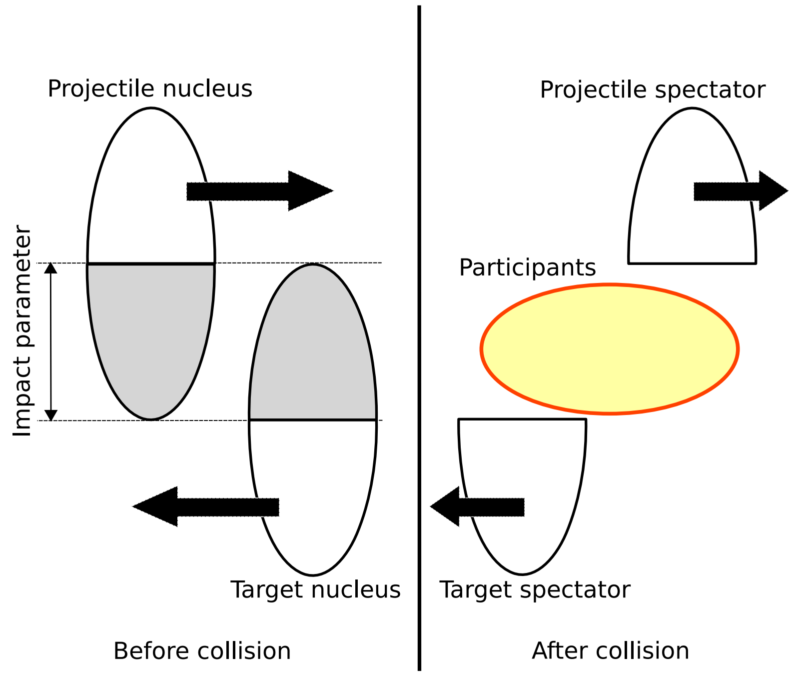

Figure 1.3: A schematic view of the geometry for a heavy ion collision.

are called as **participants** and the rest that are not participated in the collisions are called as **spectators**.

In most heavy ion experiments, the impact parameter is estimated by measuring the size of the participants and/or the spectators. The participants and the spectators are well separated experimentally because the spectator keeps it longitudinal velocity and mostly emitted in the forward (backward) rapidity, while the secondary particles from participants are peaked around mid-rapidity.

Once the impact parameter of the collision is determined, the Glauber Model [3] provides the number of participant nucleons (N_{part}), number of nucleon-nucleon collisions (N_{coll}), and the spatial eccentricity (ε) for a given impact parameter. These quantities can be calculated analytically or numerically under the following assumptions;

- Collisions of two nuclei are expressed in terms of the individual interactions of the constituent nucleons.

- At high energies, nucleons travels on straight line trajectories and are essentially undeflected.

- Inelastic nucleon-nucleon cross-section is independent of the number of collisions for a nucleon underwent before.

Analytical expressions of these quantities can be found in Appendix A.

What is the relation between these quantities and the experimental observables ? In proton-nucleus collisions, the total multiplicity scales with the number of participants

N_{part} (in other words, "wounded nucleons") [4]. In nucleus-nucleus collisions, it is also found that the total multiplicity is proportional to be N_{part} [5]. N_{part} is scaled with the volume of the interaction region, therefore the total multiplicity is given by

$$\frac{dN}{dy} \propto N_{part} \propto A. \tag{1.5}$$

For processes involving large momentum transfer (hard scattering processes), all nucleon-nucleon collisions are assumed to be independent because of their small cross-sections. Therefore, the cross-sections for hard-scattering processes should scale with the number of binary nucleon-nucleon collisions.

Perfect fluid hydrodynamics suggest that initial anisotropy in the coordinate space are directly converted into the momentum anisotropy in the final momentum space. Since hydrodynamic model always assumes the local thermal equilibrium, the relation between initial spatial eccentricity and the final momentum anisotropy could provide the signal of possible thermalization in the early stage of heavy ion collisions.

1.2.2 Time Evolution

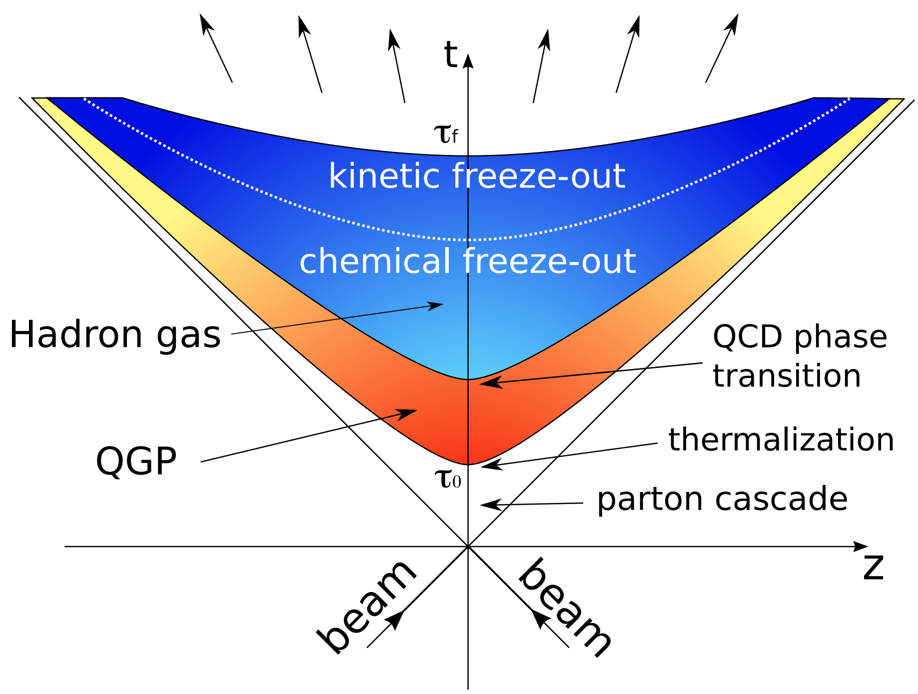

Figure 1.4: A sketch of the space-time picture of a relativistic heavy-ion collision.

Fig. 1.4 shows a simplified space-time evolution of a heavy ion collision which consists of 4 stages; (i) a parton cascade stage, (ii) a QGP phase, (iii) an interacting hadron gas phase and (iv) a free hadron stage.

Parton cascade stage: $0 < \tau < \tau_0$

Several models are proposed to describe the dynamics of initial parton-parton scattering in heavy ion collisions: the color-string models [6], color glass condensate [7], and perturbative QCD models [8]. The parton production mechanism in parton cascade stage, however, is not well understood, and it is being actively studied both from theoretical and experimental point of view.

QGP phase and QCD phase transition: $\tau_0 < \tau < \tau_f$

The frequent scatterings of the partons leads to the local thermal equilibrim at τ_0. Once the local thermal equilibrium is attained, the relativistic hydrodynamics can be used to describe the evolution of the system. The basic equations of relativistic hydrodynamics are the conservation of the energy-momentum tensor and the baryon number

$$\partial_\mu T^{\mu\nu} = 0 \tag{1.6}$$
$$\partial_\mu j_B^\mu = 0 \tag{1.7}$$

where $T^{\mu\nu}$ is the energy momentum tensor, and j_B^μ is the baryon number current. In the perfect fluid approximation, they are given by

$$T^{\mu\nu} = (\epsilon + P)u^\mu u^\nu - g^{\mu\nu}P \tag{1.8}$$
$$j_B^\mu = n_B u^\mu \tag{1.9}$$
$$u^\mu = \gamma(1, v_x, v_y, v_z) \tag{1.10}$$

where ϵ is the local energy density, P is the local pressure, n_B is the baryon number density, and u^μ is the fluid four-velocity. There are 6 unknown variables: ϵ, P, n_B, and v_x, v_y, v_z, and the conservation laws in Eq. (1.6) and (1.7) contains 5 independent equations. The equation of state (EOS) relating ϵ and P provides an additional equation to solve the space time evolution of six thermodynamical variables.

Once an equation of state is choosen, one can solve the set of equations until the system undergoes a freeze-out at $\tau = \tau_f$ with the full numerical integration using the full 3D hydrodynamics, or with assuming some symmetry and simplify the equations in just one or two dimensions.

Freeze-out and free hadrons stage: $\tau_f < \tau$

The plasma expansion lead the drop of temperature, eventually hadronization takes place and relative number of species of the emitted particles is fixed at **chemical freeze-out** temperature. The particles are rescattering each other until the hadronic interactions no longer occured. **Kinetic freeze-out** happens if the kinetic equilibrium is no longer maintained, and no further hadronic intearctions occur until the free streaming particles are detected.

Only the hadrons from the free hadrons stage can be detected in the heavy ion experiments. It is very challenging to probe the early stage of the heavy ion collisions with hadrons measured in the final stage.

1.3 Major Features of Experimental Observables at RHIC

In this section, we present the selected experimental observables obtained at RHIC and discuss the relation to the collision dynamics and the bulk properties of QGP.

1.3.1 Achieved Energy Density

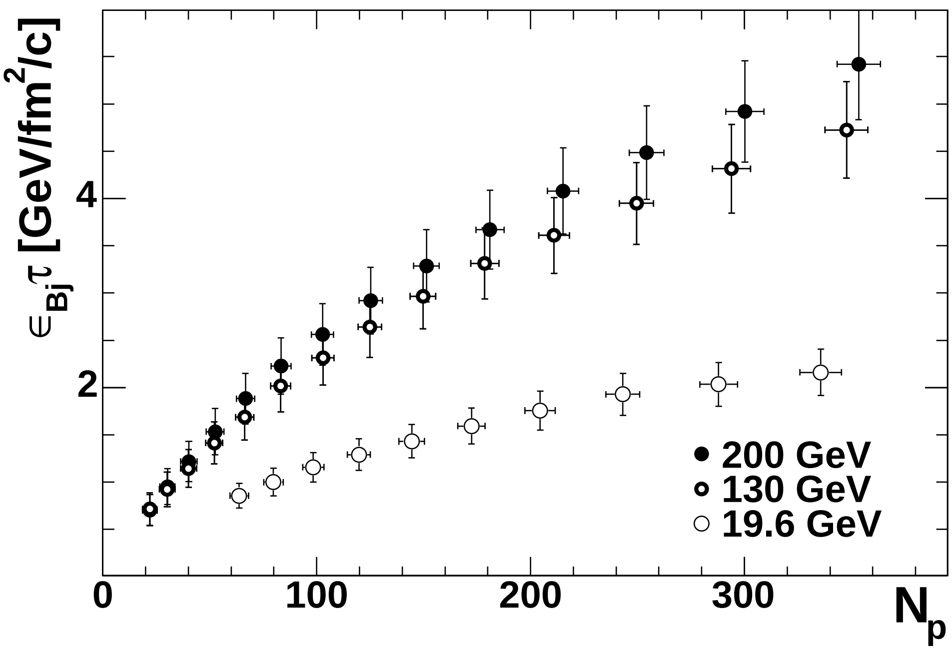

Figure 1.5: $\epsilon_{Bj} \cdot \tau$ as a function of number of participants (N_p) in different $\sqrt{s_{NN}}$ [9].

The average transverse energy of particles (dE_T/dy) can be used to estimate the energy density achieved in the heavy ion collisions with the Bjorken formula [9]

$$\epsilon_{Bj} = \frac{1}{\pi R^2 \tau} \frac{dE_T}{dy} \tag{1.11}$$

where τ is the formation time and R is the radius of nucleus. Eq. (1.11) is derived from perfect fluid hydrodynamics with free streaming particles at τ, which is defined as the proper time when the system reaches local thermal equilibrium.

Fig. 1.5 shows the Bjorken energy density for three different center-of-mass energies calculated from the measured dE_T/dy. For the 5 % most central collisions, $\epsilon_{Bj} \cdot \tau$ was 2.2 ± 0.2, 4.7 ± 0.5, and 5.4 ± 0.6 GeV fm^{-2}c^{-1} for $\sqrt{s_{NN}}$ = 19.6, 130 and 200 GeV, respectively. An estimate with $\tau = 0.6$ (1.0) fm gives $\epsilon_{Bj} = 9$ (5.4) GeV/fm^3 for $\sqrt{s_{NN}}$ = 200 GeV, which is larger than the critical energy density $\epsilon_c \sim 1$ GeV/fm^3 prediced from Lattice QCD calculations. Thus, the energy density of the matter created at top RHIC energy is well above the threshold for QGP formation.

1.3.2 Radial Flow

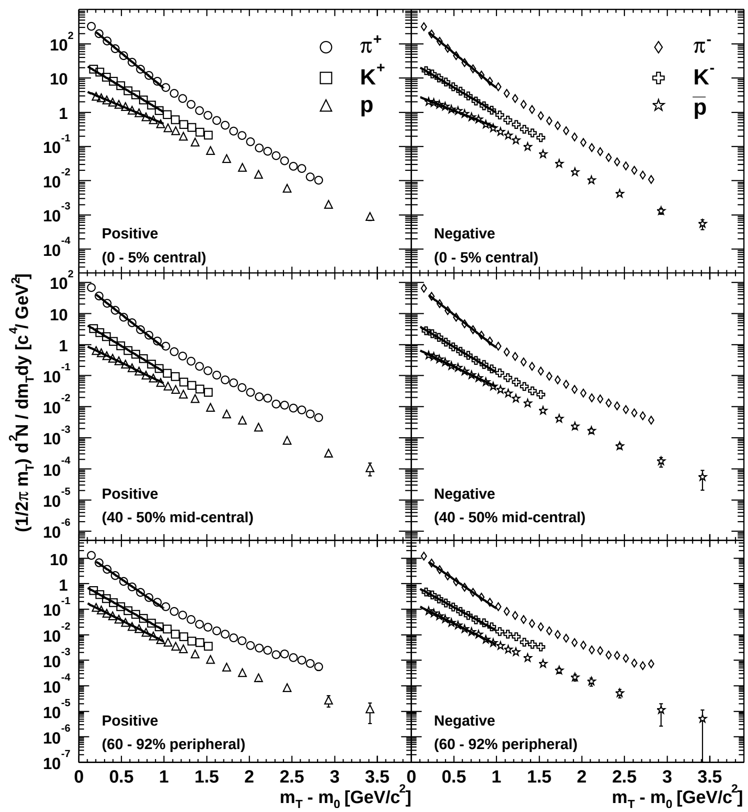

Figure 1.6: Centrality dependence of transverse mass m_{T} distributions for $\pi^{\pm}$, $K^{\pm}$ and $p(\bar{p})$ in Au + Au collisions at $\sqrt{s_{\mathrm{NN}}} = 200$ GeV. The lines on each spectra represent the fitting results with m_{T} exponential function [10].

The produced hadrons carry informations about the collision dynamics and the history for entire space-time evolution of the system, so that the measurements of the transverse momentum distributions of identified hadrons could be an essential tool to study the collision dynamics.

Fig. 1.6 shows the transverse mass spectra for identified particles in different centrality selections. The transverse mass spectra can be described by an exponential shape

$$E\frac{d^3\sigma}{dp^3} \propto \exp\left(-\frac{m_T}{T}\right) \tag{1.12}$$

where $m_{\mathrm{T}}= \sqrt{m_0^2 + p_T^2}$ denotes the transverse mass of hadrons, m_0 is the hadron mass, p_{T} is the transverse momentum, and T is the inverse slope parameter. The inverse slope parameter is often interpreted as the temperature of the system. In the high energy

$p+p/p+A$ collisions, the inverse slope parameters are common ($T \approx 150$ MeV) for various particle species [11]. This phoenomenon is known as "m_{T} *scaling*" and suggest that the spectra of hadrons with different masses would have similar slopes.

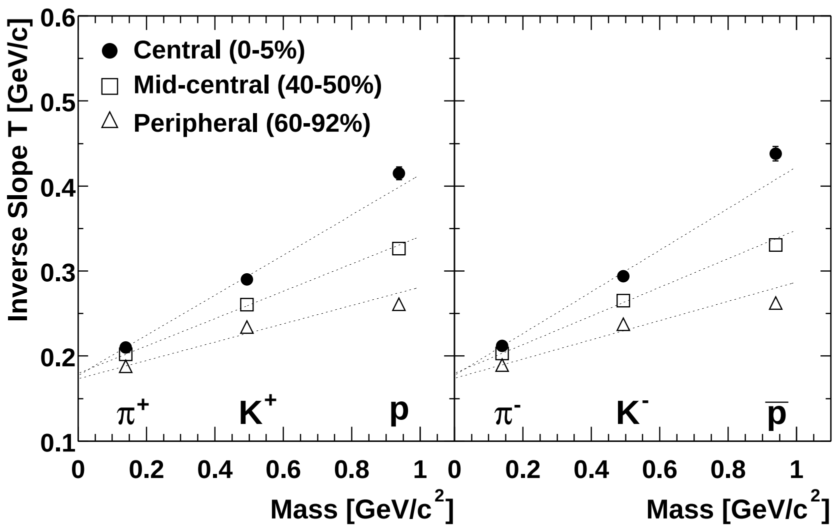

Figure 1.7: Centrality and mass dependence of inverse slope parameter T in Au + Au collisions at $\sqrt{s_{\mathrm{NN}}} = 200$ GeV. The dotted lines represent a linear fit of the data for each centrality bin with Eq. (1.14) [10].

Fig. 1.7 summarize the centrality and particle type dependence of the inverse slope parameters in Au + Au collisions. The inverse slope parameters increase with increasing particles mass in all centrality bins. For central collisions, the slope is more rapidly increasing for heavier particles. These mass dependence of slope parameters are not observed in $p+p/p+A$ collisions. Such mass dependences are considered as the evidence of common outward radial flow created by the strong interaction among the produced particles, and well describe the phenomelogical hydrodynamical model (**blast-wave model**) [12]. The collective radial flow are incorporated into the trasverse mass spectra as

$$\frac{dN}{m_T dm_T} = A m_T \int_0^\infty r dr I_0 \left(\frac{p_T \sinh \rho}{T_f} \right) K_1 \left(\frac{m_T \cosh \rho}{T_f} \right) \tag{1.13}$$

where I_0 and K_1 represent the modified Bessel functions of first and second kind respectively, $\rho = \tanh^{-1} \beta(r)$ denotes the transverse rapidity, $\beta(r)$ is the radial flow velocity, and T_f is the kinetic freeze-out temperature. In the limit of $m \gg T_f$, $m \gg p_{\mathrm{T}}$, and $T_f \gg m\beta^2$ the inverse slope parameter becomes

$$T_{eff} \simeq T_f + \frac{1}{2} m_0 \langle \beta \rangle^2 . \tag{1.14}$$

Eq. (1.14) shows the heavier the particles, the more they gain momentum or energy from the radial flow velocity, and thus the effective temperature becomes larger.

1.3.3 Azimuthal Anisotropy

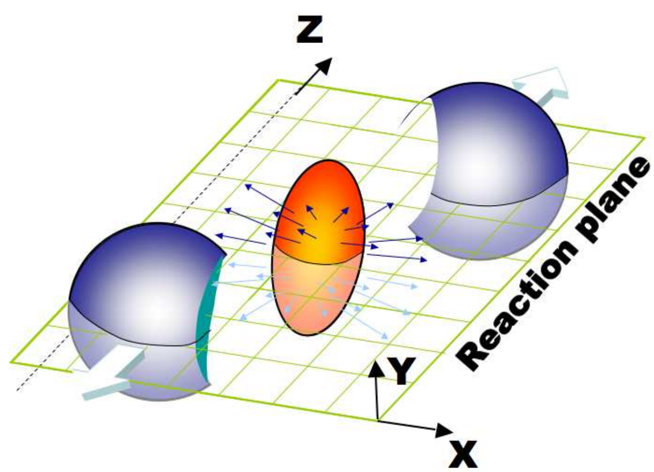

Figure 1.8: A sketch of the non-central nucleus-nucleus collision.

Azimuthal anisotropic emission of particles in momentum-space is expected to be sensitive to the early stage of collisions. In non-central collisions, the initial overlap of two nuclei in the transverse plane becomes almond shape as depicted in Fig. 1.8. The **reaction plane** is defined as the plane where the directions of beam and the vector connecting the center of both nuclei (impact parameter). The azimuthal anisotropy of emitted particles is quantitatively evaluated by using Fourier expansion series as

$$E\frac{d^3N}{dp^3} = \frac{1}{2\pi}\frac{dN}{p_T dp_T dy}\left(1 + 2v_1\cos\left(\phi_{lab} - \Psi\right) + 2v_2\cos\left(2[\phi_{lab} - \Psi]\right) + ...\right) \tag{1.15}$$

where ϕ_{lab} is the azimuthal angle of emitted particles in the fixed labratory frame, Ψ denotes the azimuthal angle of the reaction plane, and v_n is the magnitude of each harmonics [13]. In this thesis, we only focus on **elliptic flow (v_2)**, which is the 2^{nd} harmonics of Fourier expansion in Eq. (1.15).

There are several reasons why elliptic flow is thought to be sensitive to the early stage of heavy ion collisions.

1. Thermalization

The magnitude of elliptic flow is strongly influenced by the relation between the mean free path λ and the typical length scale of the system R. If thermalization is achieved, that is $\lambda \ll R$, the magnitude of elliptic flow is proportional to the initial eccentricity ($v_2 \propto \varepsilon$). Since the ratio of λ/R is characterized as the degrees of thermalization (Knudsen number), the ratio v_2/ε could be an indicator of possible thermalization in the early stage of heavy ion collisions.

2. Sensitive to the equation of state

In the hydrodynamical picture, the pressure gradient is the driving force of the elliptic flow. In non-central collisions, the pressure gradients between the produced matter and the external vacuum is steeper in the direction of reaction plane (in-plane) than in the direction of perpendicular to the reaction plane (out-of-plane). The larger in-plane pressure gradient convert the initial spatial eccentricity into the in-plane elliptic flow in the final momentum space. The pressure gradient is closely related to the EOS so that the emission pattern of elliptic flow could be sensitive to the existence of the QGP phase in the early stage.

The magnitude of elliptic flow could also be sensitive to the phase transition. If the phase transition is of the first order, the pressure stays constants during the phase transition. This results in vanishing the speed of sound $c_s = \sqrt{\partial P/\partial \epsilon}$ (softening the EOS). Hence, the magnitude of elliptic flow significantly reduces if the softening of EOS happens.

3. Self-quenching signal with time

The observed elliptic flow is sensitive to the time scale of equilibrirum. The system expands radially before the hydrodynamical evolution, thus the initial spatial anisotropy is reduced by the time when equilibrium is achieved. The observed v_2 could be diluted if equilibration does not occur early times of collisions. In the late evolution stage, the stronger in-plane pressure gradient could also lead the system expanding more rapidly in that direction, therefore reducing the initial spatial anisotropy.

Fig. 1.9 shows the PHENIX results of v_2 for identified hadrons as a function of p_T in minimum bias events. The data shows that for $p_\mathrm{T} < 2$ GeV/c, the particles with lighter mass have a larger v_2 for a given p_T, which is in good agreement with the hydrodynamical model calculation. Since the hydrodynamical model assumes the very rapid thermal equilibrium ($\tau \simeq 0.6$ fm/c), the results of v_2 suggest that the local thermal equilibrium could be attained at very early time in the heavy ion collisions. A striking feature is that the observed v_2 for $p_\mathrm{T} > 2$ GeV/c of p and $\bar{p}$ are larger than that of π and K. This trend is in sharp contrast to the its p_T dependence of hydrodynamical model calculation, which would predict to keep the same mass ordering for entire p_T range. Such a behavior of v_2 is predicted by the quark coalescence/recombination mechanism [15].

Assuming the quarks and antiquarks distributions are the same, the invariant spectrum of mesons and baryons are proportional to the product of the invariant spectra of constituents in the coalescence model [16]. The hadron spectra at mid-rapidity are

$$\frac{dN_M}{d^2p_T}(p_T) = C_M(p_T)\left(\frac{dN_q}{d^2p_T}(p_T/2)\right)^2 \tag{1.16}$$

$$\frac{dN_B}{d^2p_T}(p_T) = C_B(p_T)\left(\frac{dN_q}{d^2p_T}(p_T/3)\right)^3 \tag{1.17}$$

where N_M, N_B, N_q denote the yield of mesons, baryons and quarks, C_M and C_B are the probabilities for $q\bar{q} \rightarrow$ meson and $qqq \rightarrow$ baryon coalescence [15]. If partons have only

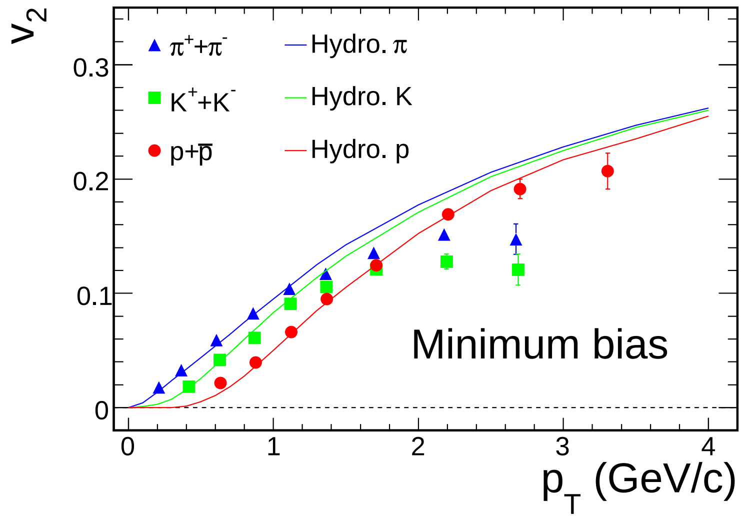

Figure 1.9: v_2 as a function of p_{T} for identified π, K and p in minimum bias events in Au + Au collisions at $\sqrt{s_{\mathrm{NN}}} = 200$ GeV. The lines represent the result of a hydrodynamical calculations including a first-order phase transition with freeze-out temperature of 120 MeV [14].

elliptic flow, i.e.,

$$\frac{dN_q}{p_T dp_T d\phi_q} = \frac{1}{2\pi}\frac{dN_q}{p_T dp_T}\left(1 + 2v_{2,q}\cos\left(2\phi_q\right)\right) \tag{1.18}$$

where ϕ_q is the azimuthal angle of partons relative to the direction of reaction plane. v_2 is defined as

$$v_2 = \frac{\int_0^{2\pi} d\phi \;\cos\left(2\phi\right) dN/p_T dp_T d\phi}{\int_0^{2\pi} d\phi \; dN/p_T dp_T d\phi} \tag{1.19}$$

then from Eq. (1.16), one immediately obtains the elliptic flow of meson and baryons with the assumption of $v_2^q \ll 1$

$$v_2^M(p_T) \;\approx\; 2v_{2,q}\left(\frac{p_T}{2}\right) \tag{1.20}$$

$$v_2^B(p_T) \;\approx\; 3v_{2,q}\left(\frac{p_T}{3}\right) \tag{1.21}$$

where p_{T} is the transverse momentum of hadrons.

Fig. 1.10 demonstrates the quark number scaling of v_2 as a function of p_{T}/n_q in minimum bias events from PHENIX and STAR experiments, where n_q denotes the number of constituent quarks in each hadron [17]. The scaled v_2 values above 0.6 GeV/c lie on a universal curve for all particle species, except for π. The deviation for π may be caused by the resonance decay contributions [18, 19], or it may be difficult to describe the pion production by a constituent quark model because the assumed constituent quark masses are significantly larger than current quark masses [15, 20].

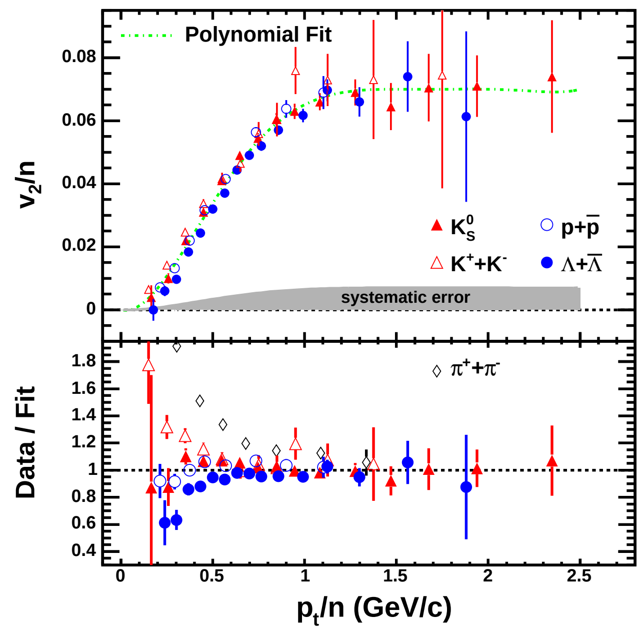

Figure 1.10: v_2 for Identified hadrons as a function of p_{T} in minimum bias collisions. Both horizontal and vertical axis are divied by the number of constituent quarks for each hadron ($n_q = 2$ for mesons, $n_q = 3$ for baryons) [17].

This results support the picture of hadron production via the coalescence of constituent quarks with collective anisotropic flow and suggest that the elliptic flow has been established in the partonic phase in the heavy ion collisions. One could see that the quark number scaling of v_2 breaks for $p_{\mathrm{T}} < 0.6$ GeV/c. There is another scaling variable, $KE_{\mathrm{T}} = m_{\mathrm{T}} - m_0$ (GeV), which can describe the scaling of v_2 in entire p_{T} range up to $p_{\mathrm{T}} = 4$ - 5 GeV/c. The validity of quark number scaling of v_2 with KE_{T} will be discussed in the thesis.

1.3.4 Blast-wave model

As we already discussed in Section 1.2.2 and 1.3.3, the space-time evolution of the QGP phase can be described by relativistic hydrodynamics. And the calculation of hydrodynamical model is consistent with the results of v_2 for $p_{\mathrm{T}} < 2$ GeV/c. Since the hydrodynamical model assumes local thermal equilibrium, the agreement of v_2 with hydrodynamical model prediction indicates that the local thermal equilibrium is attained very rapidly ($\tau \sim 1$ fm/c).

In order to describe the evolution of heavy ion collisions, full 3-D hydrodynamical simulation should be perfomed with Eq. (1.6) - (1.10). Instead of employing full 3-D hydrodynamical simulation, one could solve the set of equations analytically with some assumptions. Blast-wave model is one of the hydro-inspired model which help us to verify the configuration just after the thermal kinetic freeze-out.

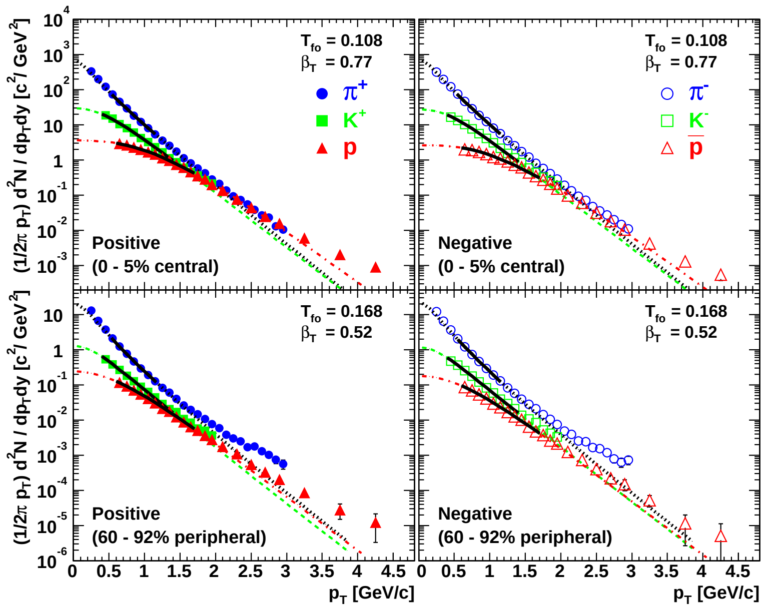

Figure 1.11: Transverse momentum spectra for positive (left) and negative (right) π, K, p in $0-5$ % centrality (top) and $60-92$ % centrality (bottom). Solid lines represent the fitting results by Blast-wave model.

Fig. 1.11 shows transverse momentum spectra for π, K and p in most central ($0-5$ %) and peripheral ($60-92$ %) events [21]. The calculation by Blast-wave model is in good agreement with the data as shown by the solid lines in the figure. The parameters are extracted by fitting single transverse momentum spectra for π, K and p simultaneously with the Blast-wave model. It is found that the freeze-out temperature (average radial flow velocity) increase (decrease) from central to peripheral collisions. This anti-correlation of T and $\langle\beta_T\rangle$ is consistent with the collective expansion picture.

Several blast-wave framework also trys to fit the v_2 with additional parameters: ε, β_2, where ε is the spatial eccentricity at the freeze-out, and β_2 is the 2^{nd} harmonic coefficient of radial flow velocity or radial transverse rapidity [22]. Since these models consider the bulk properties where the kinetic freeze-out takes place, the parameters are extracted by fitting single particle spectra and v_2 simultaneously.

However, v_2 is thougt to be more sensitive to the early stage of heavy ion collisions compared to the single particle spectra, one can expect that v_2 has different sensitivities on the parameters from transverse momentum spectra. Thus, one could extract bulk properties, such as temperature and radial flow velocity, in the early stage of collisions by comparing with measured v_2 and blast-wave model.

1.4 Thesis Motivation

In this chapter, we reviewed several observables which is thought to be the signatures of the QGP. The estimated Bjorken energy density is larger than 5 GeV/fm^3, which is well above the critical energy density predicted by the Lattice QCD calculations. The results of single particle transverse momentum spectra are consistent with the description by the model with collective transverse expansion.

The results of v_2 for identified hadrons at $p_{\mathrm{T}} < 2$ GeV/c are in good agreement with the calculation of ideal hydrodynamical model with very rapid thermalization, $\tau_0 \sim 1$ fm/c. It indicate that the thermal equilibrium have been attained for early stage of heavy ion collisions at RHIC. For $p_{\mathrm{T}} > 2$ GeV/c, however, the deviation from hydrodynamic model is observed and that trend of v_2 can be well described with the quark coalescence mechanism. This results indicate that the elliptic flow was developed in the partonic phase of heavy ion collisions.

In this thesis, we present the measurements of centrality dependence of identified hadron elliptic flow in $\sqrt{s_{\mathrm{NN}}} = 200$ GeV Au + Au collisions at RHIC-PHENIX experiment. Our main goals are as follows;

1. Study the relation between initial geometry overlap (eccentricity) and final momentum elliptic flow.
2. Study the sensitivity of initial density profile to the elliptic flow by Blast-wave model, and extract freeze-out temperature (T) and radial flow velocity (β_T).
3. Test the validity of the quark number scaling of v_2 for several different centrality with π, K, p, d and ϕ

As we already shown in 1.3.3, elliptic flow is expected to be proportional to the eccentricity if the local thermal equilibrium is achieved. Therefore, it is important to measure the centrality dependence of elliptic flow in order to understand how the initial eccentricity is converted into the final elliptic flow. We examine the eccentricity scaling of v_2 in Au + Au and Cu + Cu collisions with several different definitions of eccentricity, and also study the sensitivity of scaled v_2 with different density profile, namely number of participant and number of collision density.

The blast-wave model successfully describes the transverse momentum spectra in heavy ion collisions. Several blast-wave models also describe the elliptic flow by simultaneous fitting with both spectra and v_2. However, magnitude of v_2 saturate earlier than p_{T} spectra so that v_2 may have different sensitivity to the early stage of heavy ion collisions. The sensitivity of v_2 to the density profile are studied and extract bulk thermodynamic properties, such as freeze-out temperature and radial flow velocity, by the extended blast-wave model. It takes into account the density and velocity profiles estimated by Glauber model, while the usual blast-wave model assume that density is constant inside the overlap zone and velocity profile is proportional to the transverse radius $r = \sqrt{x^2 + y^2}$.

Quark number scaling of v_2 suggest that the existence of universal curve for hadrons with ligth quarks for $p_{\mathrm{T}}/n_q > 0.6$ GeV/c, and that the coalescence of constituent quarks could be dominant particie production at that p_T range. Quark number scaling of v_2 has been studied in minimum bias events. However, the magnitude of v_2 strongly depends on the collision centrality. Therefore, it is crucial to test the validity of quark number scaling for each centrality, from central to peripheral collisions. We study the validity of the quark number scaling of v_2 for identified hadrons in the measured centrality range.

More concrete evidence of quark coalescence would be provided by the measurment of v_2 for ϕ meson. Because the lifetime of ϕ meson in vacuum is larger ($\approx$ 45 fm/c) compared to the typical length scales of the medium ($\sim$ 10 fm), and the cross-section for scattering of strange hadrons by non-strange hadrons are small ($\sim$ 9 mb) [23]. Thus, if elliptic flow was developed in a phase involving hadrons interacting with their hadronic cross sections, one would expect that v_2 of the ϕ could be significantly smaller than that of other hadrons. On the other hand, if the elliptic flow was established in the pre-hadronic phase, the ϕ meson provide an important test for the quark number scaling as we already discussed in the last section. Since its mass is similar to that of the proton, its v_2 should be additive with the v_2 of the two constituent quarks.

Chapter 2

Experimental Apparatus

2.1 Relativistic Heavy Ion Collider (RHIC)

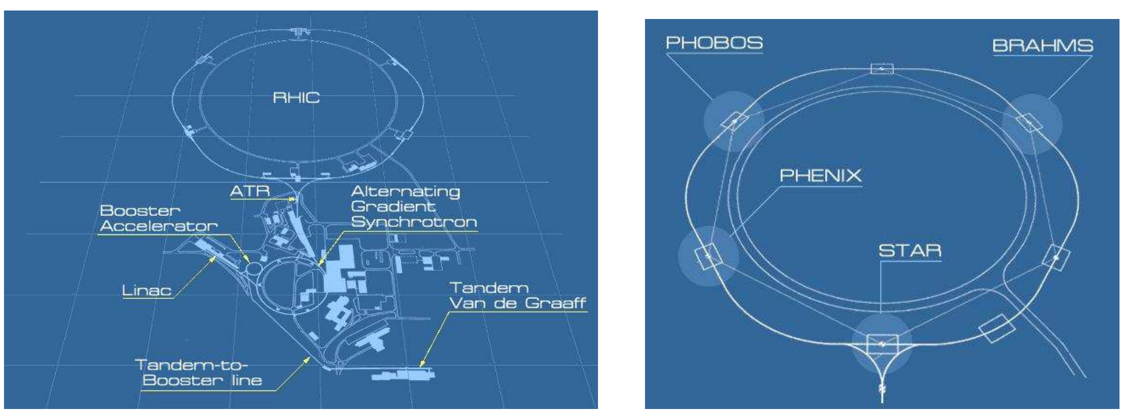

(a) (b)

Figure 2.1: (a) A schematic of the RHIC complex. (b) The layout of the detectors around the RHIC tunnel.

The Relativistic Heavy Ion Collider (RHIC) [24, 25] is located at Brookhaven National Laboratory (BNL) and is the highest energy collider in the world. RHIC is capable of colliding a wide variety of particle species from A = 1 (protons) to A $\sim$ 200 (gold), at present. One obtains energies up to 100 GeV per nucleon for Au + Au collisions and up to 250 GeV for protons. The designed luminosity [1] is 2×10^{26} cm^{-2} s^{-1} for Au ions and 1.4×10^{31} cm^{-2} s^{-1} for protons. A schematic of the RHIC complex is shown in Fig. 2.1.

The RHIC consists of two quasi-circular concentric accelerator/storage rings on a common horizontal plane, one ("Blue Ring") for clockwise and the other ("Yellow Ring") for counter-clockwise beams. The circumference of RHIC ring is 3.8-km. An existing

[1] the number of interactions per unit time per unit cross-section

chain of hadron accelerators, i.e., the Tandem Van de Graff, the Booster, and the Alternating Gradient Synchrotron (AGS) are used as the heavy ion injector to the collider rings.

2.2 PHENIX Detector Overview

The Pioneering High Energy Nuclear Interaction eXperiment (PHENIX) is one of the large experiments at RHIC. The PHENIX detector comprises four instrumented spectrometers or arms and three global detectors [26]. The detector consists of a number of subsystems. The rapidity and ϕ coverages and other features of these subsystems used in this thesis is given in Table 2.1.

Table 2.1: Summary of PHENIX detector subsystems used in this thesis

Element	$\Delta\eta$	$\Delta\phi$	Purpose and special features
Magnet			
Central (CM)	± 0.35	360^o	Up to 1.15 T m
Global detectors			
Beam-beam (BBC)	$\pm$(3.0 to 3.9)	360^o	Start timing, fast vertex
ZDC	± 2 mrad	360^o	Minimum bias trigger
Tracking			
Drift Chamber (DC)	± 0.35	$90^o \times 2$	Good momentum and mass resolution $\Delta m/m = 1.0$ % at $m = 1$ GeV
Pad Chambers (PC)	± 0.35	$90^o \times 2$	Pattern recognition, tracking for nonbend direction
Particle identification			
Time-of-Flight (TOF)	± 0.35	45^o	Good hadron identification, $\sigma < 100$ ps
PbSc EMCal	± 0.35	$90^o + 45^o$	For both calorimeters, photon and electron detection and energy measurement

Table 2.2 provide the *recorded* integrated luminosity at PHENIX and the statistics on the total number of events achieved by PHENIX in Runs 1 through 5.

Table 2.2: Summary of PHENIX data sets acquired in RHIC Runs 1 through 5.

Run	Year	Species	$\sqrt{s_{NN}}$ (GeV)	$\int Ldt$	N_{tot}
01	2000	Au + Au	130	1 μb^{-1}	10 M
02	2001/2002	Au + Au	200	24 μb^{-1}	170 M
		$p+p$	200	6.35 pb^{-1}	3.7 G
03	2002/2003	d + Au	200	2.74 nb^{-1}	5.5 G
		$p+p$	200	0.15 pb^{-1}	3.7 G
04	2003/2004	Au + Au	200	241 μb^{-1}	1.5 G
		Au + Au	62.4	9 μb^{-1}	58 M
05	2004/2005	Cu + Cu	200	3 nb^{-1}	8.6 G
		Cu + Cu	62.4	0.19 nb^{-1}	0.4 G
		Cu + Cu	22.5	2.7 μb^{-1}	9 M
		$p+p$	200	3.8 pb^{-1}	85 B

2.3 PHENIX Central Magnet (CM)

The PHENIX magnet system [27] is composed of three spectrometer magnets with warm iron yokes and water-cooled copper coils. The Central Magnet (CM) is energized by two pairs of concentric coils, which are "Outer" and "Inner" coils, and provides a field around the interaction vertex that is parallel to the beam. A schematic drawings of magnet system is shown in Fig. 2.2.

The data in this thesis only consisted of the "Inner + Outer" configuration. Since the field is a very good approximation phi-symmetric and axial so that most of the bending of charged particle's trajectory occurs in phi, and not in theta. The parameters for the central magnet are shown in Table 2.3.

2.4 The Global Detectors

The global properties of the heavy ion collisions, including the collision vertex along the beam direction, the trigger and timing information, the collision centrality, the multiplicity, and the event plane are characterized by a set of global detectors around the beam line. In this thesis, the Zero Degree Calorimeters (ZDC), and the Beam Beam Counters (BBC) are used.

2.4.1 Zero Degree Calorimeter (ZDC)

Fig. 2.3 A) shows an overhead drawing of the PHENIX interaction region. A pair of ZDC (Zero Degree Calorimeter) [28] are located on either side of the interaction region, 18 m away, and behind the DX magnet in order to provide universal characterization of

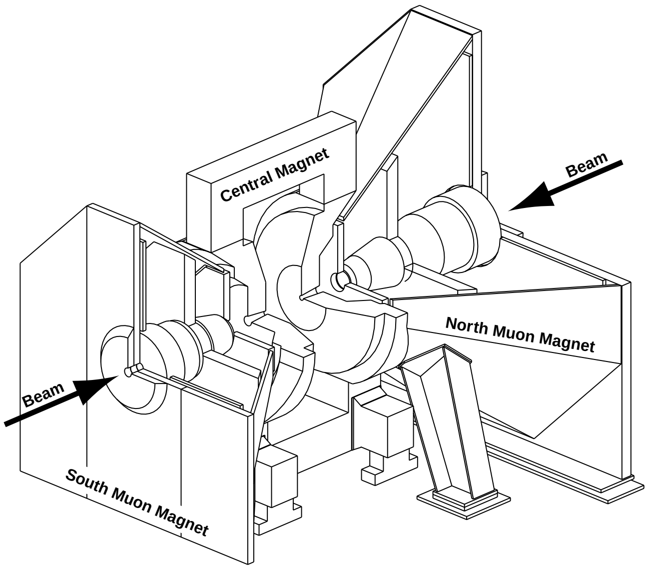

Figure 2.2: Line drawings of the PHENIX magnets, shown in perspective and cut away to show the interior structures. Arrows indicate the beam line of the colliding beams in RHIC.

Table 2.3: Parameters for the PHENIX Central Magnet

Parameter	CM	CM
CM Coils	Inner and Outer	Outer Only
Field configuration	Axial	Axial
Field integral (T-m)	0.43 to 1.15 (Θ=90^o)	0.78 (Θ=90^o)
Wt. (metric tons)	421	421
Pseudorapidity coverage	-0.35 $< \eta <$ 0.35	-0.35 $< \eta <$ 0.35
Polar angle coverage	$70^o < \Theta < 110^o$	$70^o < \Theta < 110^o$
Amp-turns	541,000	248,000
Power (kW)	928	600
Average coil temp. (^{o}C)	23.8(I)/32.1(O)	32.1

heavy ion collisions. Because of the DX magnet, any charged particles are swept away before hitting the ZDC. Fig. 2.3 B) shows the locations of neutrons, gold, and protons after going through the DX magnet.

The ZDC is a small hadron calorimeter, consisting of layers of tungsten plates and scintillator slabs as shown in Fig. 2.4 and detects neutron multiplicities from the heavy ion collisions, giving one of the collision centrality measures. The ZDC pair at each crossing point is also used as a luminosity monitor in steering the beams to collide.

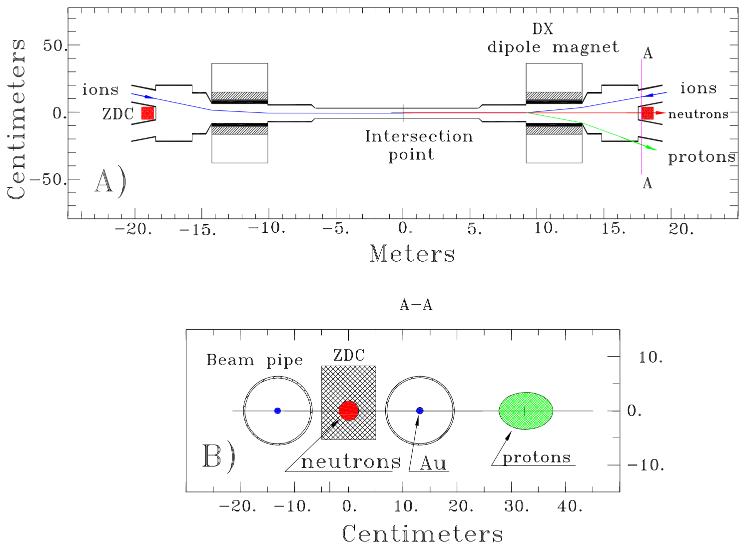

Figure 2.3: A) An overhead view of the interaction region showing the location of the ZDCs as either end, just after the DX magnets and in the crotch where the two rings merge. B) A frontal view of the ZDC and beam-pipe with the locations of neutrons, gold and proton after they are swept by the DX magnet.

2.4.2 Beam-Beam Counter (BBC)

The main role of the BBC (Beam-Beam Counter) [29] is

- to provide the start time for the TOF measurements
- to produce the signal for the PHENIX LVL1 trigger
- to measure the collision vertex point along the beam axis

The BBC consists of two identical sets of counters installed on both sides of the collision point along the beam axis. The BBC is placed 144 cm from the collision point and surround the beam pipe, which covered a pseudorapidity range from 3.0 to 3.9 over the full azimuth. Fig. 2.5 shows the photographs of BBC. Each element of BBC is one-inch diameter mesh-dynode photomultiplier tubes (Hamamatsu R6178) equipped

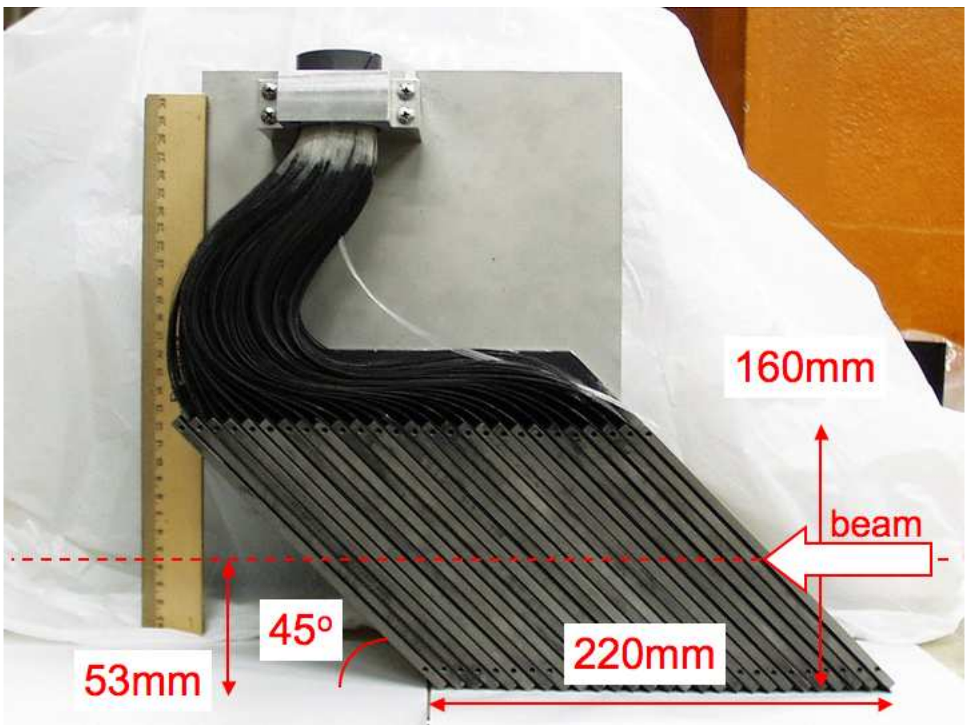

Figure 2.4: A photo of 1 module of the ZDC. The top shows the PMMA fibers which are sandwiched between tungsten plates. These fibers generate and guide cerenkov light to the Hamamatsu R329-2 PMT. The red arrow on the left shows the impact position of the beam.

with 3 cm quartz on the head of the PMT as Cherenkov radiator as shown in Fig. 2.5 (a). Each BBC is composed of 64 PMT elements (Fig. 2.5 (b)) and is installed on the mounting structure surrounding the beam pipe as shown in Fig. 2.5 (c).

The BBC was made to satisfy the following requirements;

1. The BBC must have a capability to function over a large dynamic range from 1 to 30 MIP's in order to cover from p+p to central Au + Au collisions.

2. The BBC is required to be radiation hard because the location of BBC, which is around the beam pipe near the collision point, is very high-level radiation area.

3. The BBC needs to work in a high magnetic field environment ($\sim$ 3 kG) since the BBC is installed just behind the central magnet.

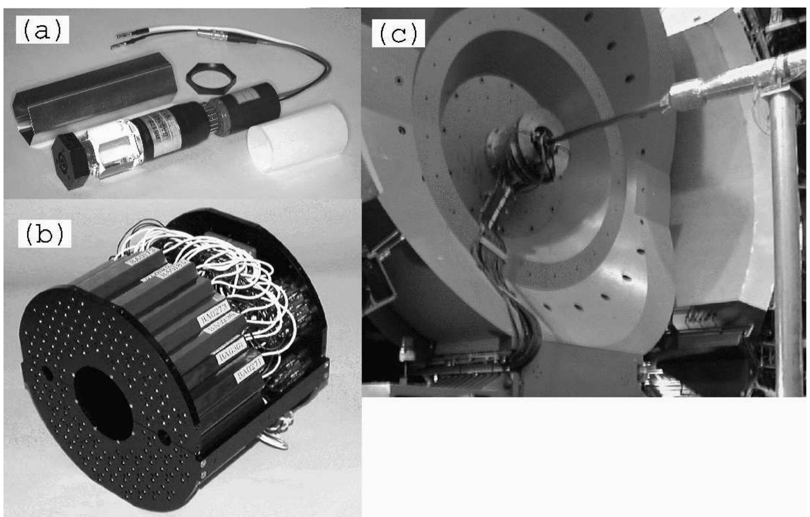

Figure 2.5: (a) Signle Beam-Beam Counter consisting of one-inch mesh dynode photomultiplier tubes mounted on a 3 cm quartz radiator. (b) A BBC array comprising 64 elements. (c) The BBC is shown mounted on the PHENIX detector. The beam pipe can be seen in the middle of the picture. The BBC installed on the mounting structure just behind the central spectrometer magnet.

For both ZDC and BBC, the start time and z-vertex position are determined by using the measured time difference between the south and north detectors and known distance between the two detectors. The start time (T_0) and the z-vertex position (z_{vtx}) are calculated as

$$T_0 = (T_1 + T_2)/2 \tag{2.1}$$

$$z_{vtx} = c \cdot (T_1 - T_2)/2 \tag{2.2}$$

where T_1 and T_2 are the average timing of particles in each counter and c is the speed of light. Typically, the ZDC z-vertex is measured with a resolution of 2.5 cm with an intrinsic timing resolution of 150 ps, and the resolution of BBC z-vertex is 0.6 cm with timing resolution of 40 ps [30].

2.5 The Central Arm Spectrometers

The PHENIX central arm spectrometers consists of two arms, which is east arm (right) and west arm (left). Each arm covers 90^o in azimuth and $|\eta| < 0.35$ [2]. As shown in the Fig. 2.6, each spectrometers consists of layers of tracking and particle identification subsystems.

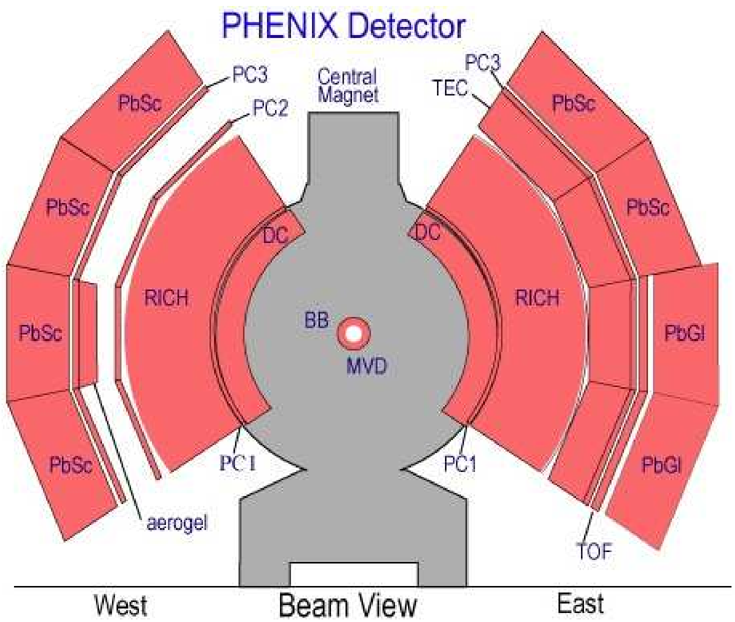

Figure 2.6: The layout of PHENIX central arm spectrometers viewed along the beam axis in Run4 configuration.

The PHENIX central arm spectrometers have three main tracking device, which is Drift Chamber (DC), Pad Chambers (PC), and Time Expansion Chamber (TEC), to measure the momentum of charged particles, reconstruct invariant masses of particle pairs and contributes to particle identification. The three tracking subdetectors are optimized for different purposes.

1. The Drift Chamber (DC) provide high resolution p_{T} measurements and position information used to match tracks for outer subsystems.

2. Three Pad Chambers (PC) designated PC1, PC2, and PC3 provide three dimentional position measurements along the straight line trajectories for charged hadrons outside the magnetic field. PC1 also determine the three-dimensional momentum vector by providing polar angle θ for charged tracks at the exit of the DC.

3. The Time Expansion Chamber (TEC) provides additional tracking and particle identification.

[2] Pseudorapidity, $\eta = -\ln(\tan(\theta/2))$. θ is polar angle.

Particle identification is provided by Ring Imaging CHerenkov counter (RICH), Time Expansion Chamber (TEC), Time-Of-Flight (TOF), Lead Scintillator Electromagnetic Calorimeter (PbSc), and Lead Glass Electromagnetic Calorimeter (PbGl). RICH provide excellent separation of electrons from hadrons over a wide range of momenta in $0.2 < p < 5.0$ GeV/c or greater. TEC is an additional tracking device which helps with moemntum resolution at high p_{T}, and provides electron identification below 2.5 GeV/c through a measurement of dE/dx. The main role of TOF is to provide good hadron separation out to 2.4 (4.0) GeV/c for π/K (K/p) with about 100 ps timing resolution. The EMCal system (PbSc and PbGl) provide a measurement of energy and spatial position of photons and electrons.

In the following sections, we introduce the PHENIX central arm spectrometers focusing on the subsystems which are used in this analysis: DC, PC, PbSc, and TOF. More details about the PHENIX detector can be found in [31, 32, 33].

2.5.1 The Drift Chamber (DC)

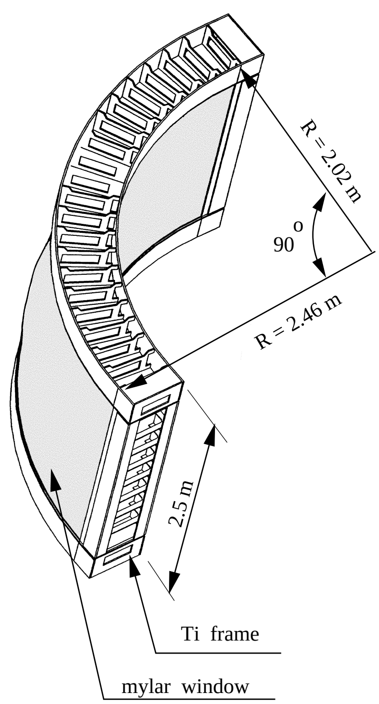

Figure 2.7: Drawing of the Drift Chamber Frame.

The Drift Chamber (DC) [34] is located in the east and west arm at a radial distance of $2.02 < R < 2.46$ m, respectively. One of them is the mirror copy of each other, and each DC covers 90^o in azimuth and 1.8 m along the z direction which corresponds to $|\eta| < 0.35$. The schematic drawing of DC frame is shown in Fig. 2.7.

DC is intended to measure momentum of charged particles with high resolution, $\Delta p_{\mathrm{T}}/p_{\mathrm{T}} \approx 0.5\%$. In order to achieve high momentum resolution, the DC has to satisfy the following requirements:

- Single wire resolution better than 150 μm in the r-ϕ.
- Single wire efficiency better than 99 %.
- Single wire two track separation better than 1.5 mm.
- Spatial resolution in the z direction better than 2 mm.

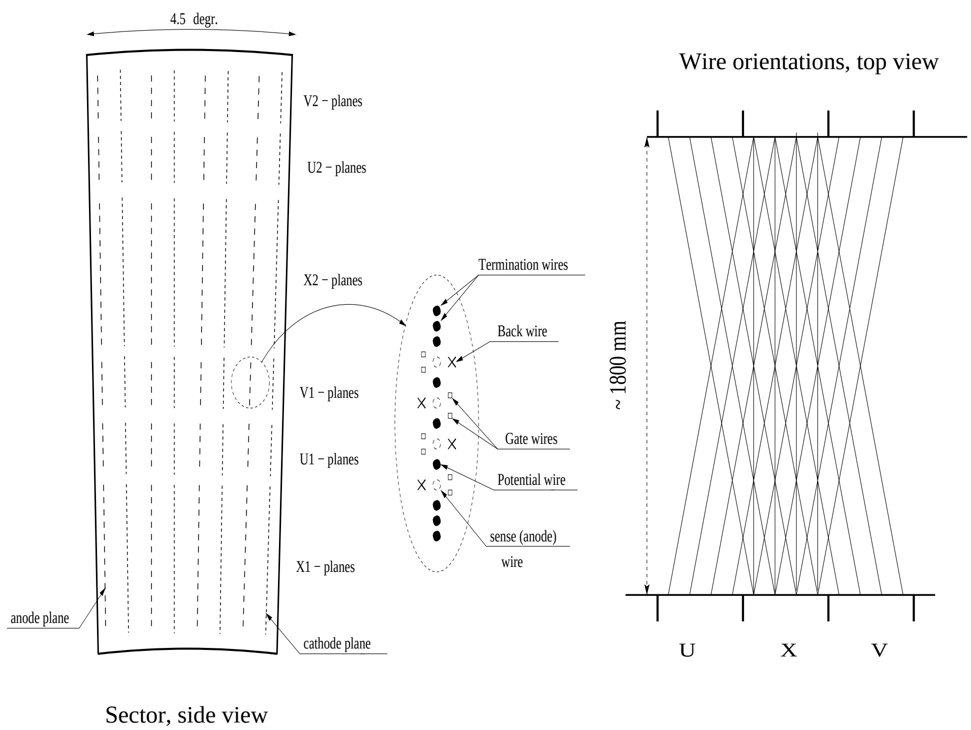

Figure 2.8: The layout of wire position within one sector and inside the anode plane (left). A schematic diagram, top view, of the stereo wire orientation (right).

DC frame can be divided in 20 identical sectors each covering 4.5^o in ϕ. Every sector is filled with six modules of different types: X1, U1, V1, X2, U2, and V2 as shown in Fig. 2.8.

Each module contains 4 sense (anode) planes and 4 cathode planes forming cells with a 2 to 2.5 cm drift space in the ϕ direction. The X1 and X2 wire cells are running in parallel to the beam to perform precise track measurements in r-ϕ. The U and V layers begin in one sector on one side of the frame and end in neighboring sectors on the opposite side. Angle between U, V stereo wires and X wires is about $\pm$ 6^o and measure z coordinate of the track. Each of the X and U, V stereo cells contain 12 and 4 anode (sense) wires, respectively so that there are 40 drift cells in the DC located at different radii. The sense wires (anode) are also electrically isolated in the middle by a low mass kapton strip. The number of readout channels is, therefore, doubled, about $3200 \times 2 = 6400$ channels, for each arm. It is necessary to reduce the track density on a signle wire and perform reliable pattern recognition for the largest track multiplicities at RHIC.

2.5.2 The Pad Chamber (PC)

The Pad Chambers (PC) [35] are multi-wire proportional chambers. The three layers of Pad Chambers are located at the radial distance of 2.5 m (PC1), 4.2 m (PC2), and 4.9 m (PC3) from the interaction region as shown in Fig. 2.6. The PC system determines space points along the straight line particle trajectories since the PCs are located well outside the magnetic field ($R > 2.4$ m). The PCs are the only non-projective detectors in the central arm tracking system, and thus are critical elements of the pattern recognition. PC1 is also essntial for determining the 3-dimentional momentum vector by providing the z coordinate at the exit of the DC.

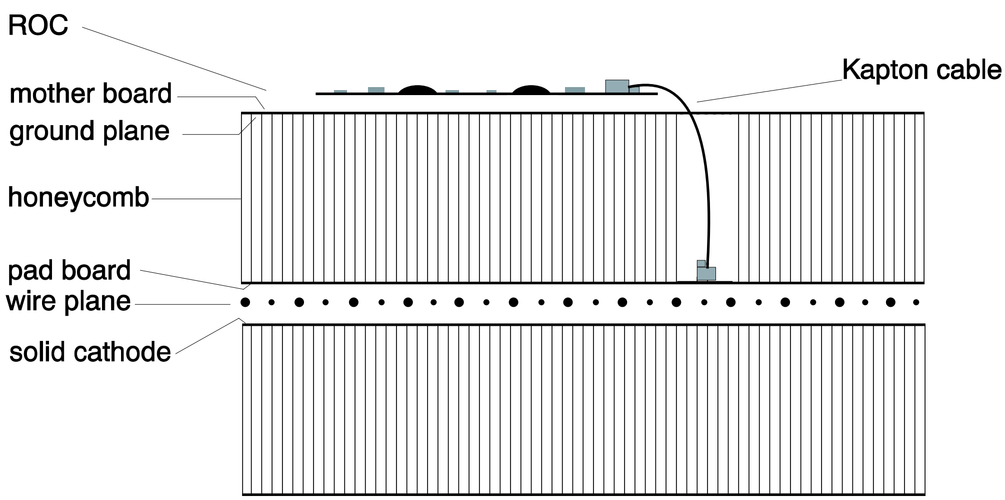

Figure 2.9: Vertical cut through a pad chamber.

Each detector contains a single plane of wires inside a gas volume bounded by two cathode planes as shown in Fig. 2.9. One cathode is finely segmented into an array of pixels. The charge induced on a number of pixels when a charged particle starts an avalanche on an anode wire, is read out through specially designed readout electronics.

The design of pixels is driven by the need for good position resolution in the z-coordinate and a low occupancy even in the high track multiplicities. The design goal for the position resolution was 4 mm so that an anode wire spacing of about 8 mm was motivated. Finally, for a geometrical reasons, a spacing of 8.4 mm was chosen. A cell area of 8.4×8.4 mm^2 was adopted since a square cell geometry was desired.

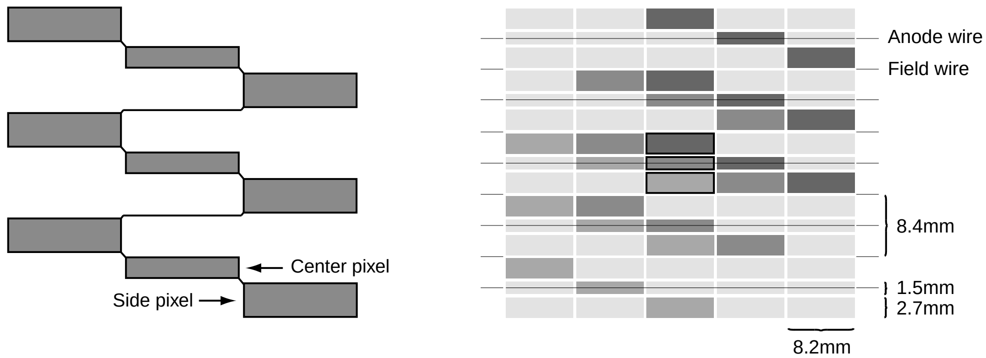

Figure 2.10: The pad an pixel geometry (left). A cell defined by three pixels is at the center of the right picture.

A special pad design was invented, where each cell contains three pixels and an avalanche must be sensed by all three pixels to form a valid hit in the cell in order to reduce the amount of electric and other noise. This arrangement is, however, costly in terms of electronic channels. Thus, the interleaved pixels were ganged together as shown in the Fig. 2.10. Nine pixels are connected to a group and to a common readout channel, such that the three pixels in a cell are always connected to different but neighbouring channels and each cell is defined by its unique channel triplet. This solution saves a factor of nine in readout channels compared to readout of every pixel and a factor of three compared to a readout pad geometry where a cell is the actual electrode connected to an electronics channel.

The performance of PCs are summrized in the Table 2.4 [36].

Table 2.4: Summary of Pad Chamber performance

Chamber	Wire distance (mm)	z resolution (mm)	perp. resolution (mm)	radiation thickness
PC1	8.4	1.7	2.5	1.2 %
PC2	13.6	3.1	3.9	2.4 %
PC3	16.0	3.6	4.6	2.4 %

2.5.3 Lead Scintillator Electromagnetic Calorimeter (PbSc)

The primary role of the Electromagnetic Calorimeter (EMCal) [37] in PHENIX is to provide a measurement of the energies and spatial positions of photons and electrons. The EMCal system consists of 2 differently designed subsystems. The first is a shshlik type sampling calorimeter consisting of 15552 lead and scintillator (PbSc) towers. The other is a homogeneous detector consists of 9216 elements of lead-glass (PbGl). They both have good timing and energy resolutions, although the PbSc has better timing and the PbGl has better spatial and energy resolution. In addition, the PbSc has 0.85 nuclear interaction length in depth so that it has some sensitivity for hadron measurements even though the PbSc was designed as an electromagnetic calorimeter. Having two detectors with different systematics increases the confidence level of the physics results. We will discuss design and operational parameters of the PbSc calorimeter which used in this analysis. More details of PbGl can be found in [37].

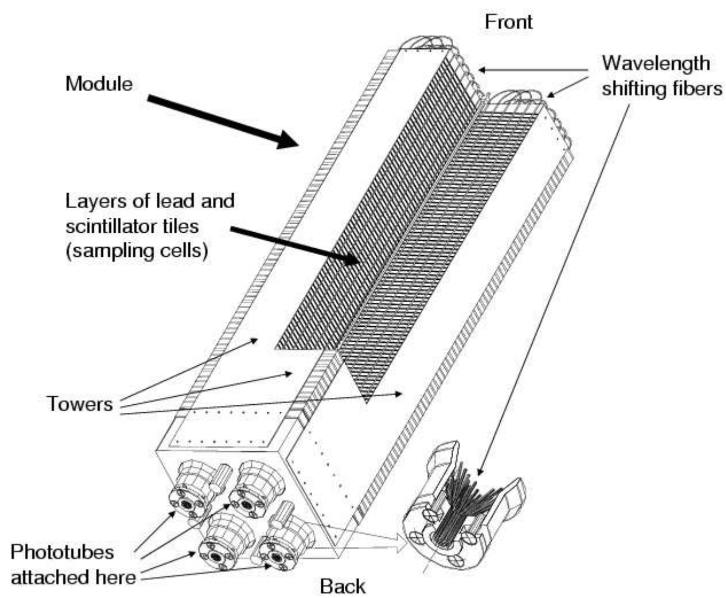

Figure 2.11: Interior view of PbSc calorimeter module showing a stack of scintillator and lead plates, wavelength fiber readout and leaky fiber inserted in the central hole.

The PbSc towers contains 66 sampling cells consisting of alternating tiles of Pb and scintillator. These cells are optically connected by 36 longitudinally penetrating wavelength shifting fibers for light collection. Fig. 2.11 shows a "module" which is mecanically grouped 4 towers together into a signle structural entity. 36 of these modules are hold together to form a "supermodule". 18 supermodule make a "sector". All major PbSc design parameters are listed in Table 2.5.

The nominal energy resolution of PbSc is

$$\sigma(E)/E = 8.1\%/\sqrt{E} \oplus 2.1\% \tag{2.3}$$

The resolution was determined by electron test beams at BNL and CERN under ideal conditions as shown in Fig. 2.12.

Fig. 2.13 shows the timing resolution of PbSc. the PbSc timing resolution is nearly constant at $\sigma \sim 120$ ps for electrons and protons, and $\sigma \sim 270$ ps for pions for energy deposits in the PbSc larger than 0.5 GeV. For the real datas in Run-4 period, the timing resolution is achieved about 400 ps for pions, which provides the particle separation up to $p_{\mathrm{T}} \sim 1$ GeV/c for π/K, and up to $p_{\mathrm{T}} \sim 2$ GeV/c for K/p.

Table 2.5: Individual Pb-Scintillator Calorimeter Tower Parameters

Parameter	Value
Lateral Segmentation	$5.535 \times 5.535\ cm^2$
Active Sampling Cells	66
Scintillator	Polystyrene (1.5% PT / 0.01% POPOP), 0.4 cm
Absorber	Pb, 0.15 cm
Cell Thickness	0.56 cm (0.277 $X_\circ$)
Active Depth	37.5 cm
Radiation Length	18
Nuclear Interaction Length	0.85
WLS Fiber	BCF-99-29a, 0.1 cm
WLS Fibers per Tower	36
PMT Type	FEU115M, MELS, Russia, 3.0 cm
Photocathode	Sb-K-Na-Cs
Luminous Sensitivity	$\geq$ 80 μa/lm
Rise Time (20%–80%)	$\leq$ 5 ns

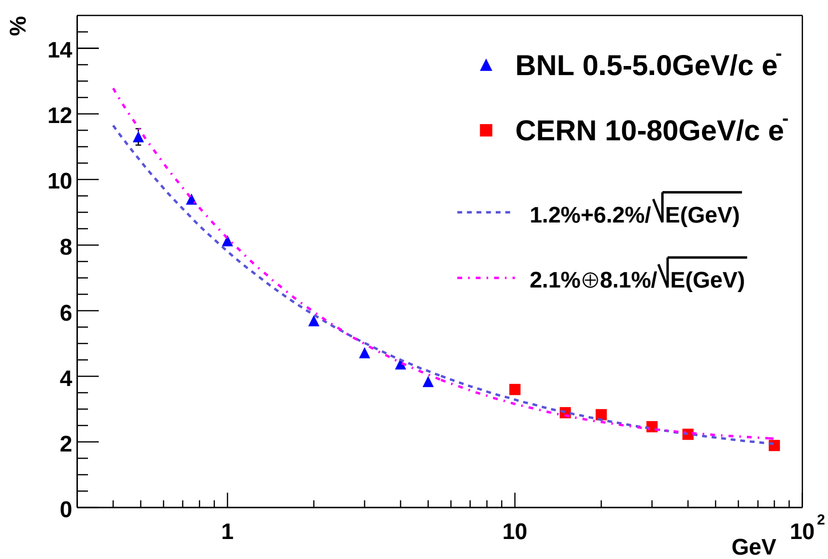

Figure 2.12: PbSc energy resolution obtained by beam tests at CERN and BNL. The dashed line shows a fit to the linear formula $\sigma(E)/E = 1.2\% + 6.2\%/\sqrt{E}$. The dashed-dotted line shows the fit to the quadoratic formula $\sigma(E)/E = 2.1\% \oplus 8.1\%/\sqrt{E}$.

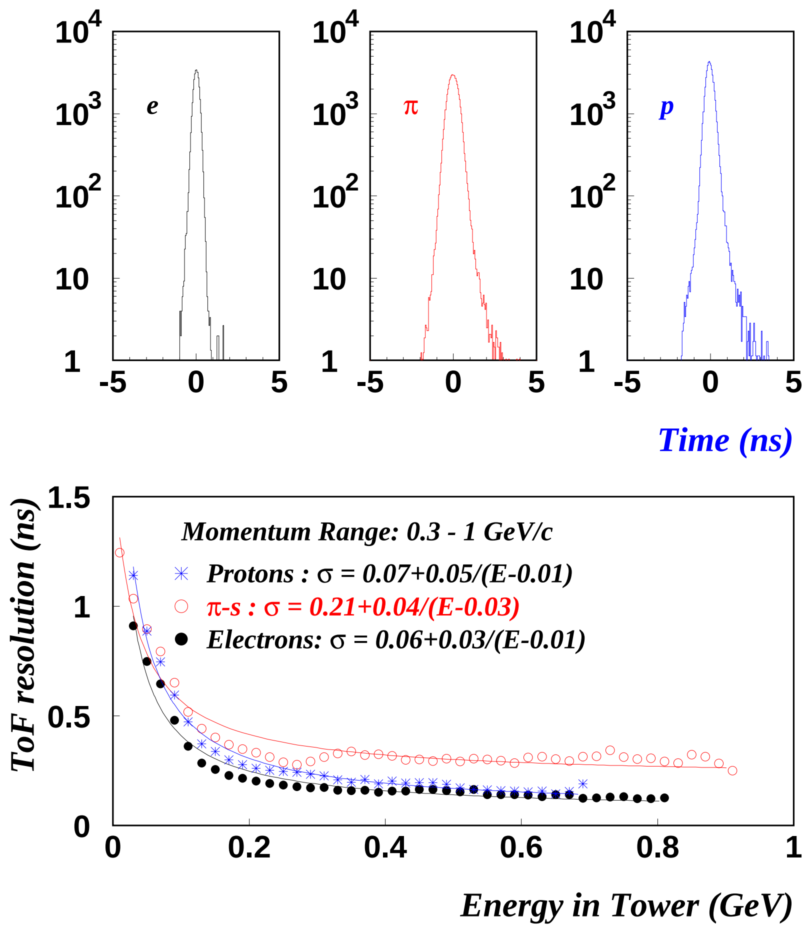

Figure 2.13: PbSc timing resolution for different particles. Top figure shows lineshape for 1 GeV/$c$electrons, pions, and protons. Bottome shows timing resolution in the momentum range $0.3 < p < 1.0$ GeV/c.

2.5.4 The Time-of-Flight Counter (TOF)

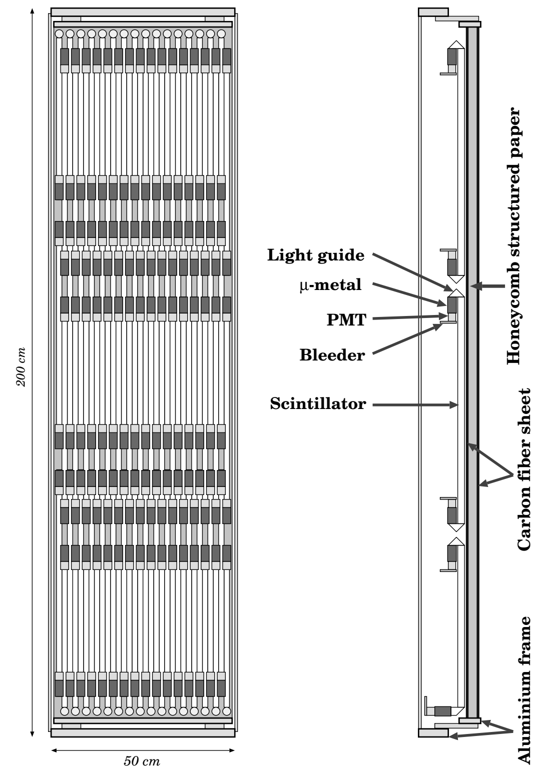

Figure 2.14: Schematic diagram of the components of a single TOF panel, which consists of 96 plastic scintillator with PMT, light guides, and supports at both ends.

The Time-Of-Flight (TOF) system [33] provides a primary device for charged hadron identification in PHENIX and is designed to achieve a very clear particle separation out to high momentum, i.e. π/K separation up to 2.4 GeV/c and K/p separation up to 4.0 GeV/c with 100 ps timing resolution.

The TOF is located at a radial distance of 5.1 m from the collision vertex in the east arm. It convers $70^o \leq \theta \leq 110^o$, which corresponds to $|\eta| < 0.35$, and 30^o in azimuth. The TOF slat is a plastic scintillator (Bicron BC404) with PMT (Hamamatsu R3478S) at both ends. Two different lengths of scintillator (637.7 and 439.9 mm) are used in order to avoid geometrical conflicts between the PMT's of neighboring slats. 96 of these slats are grouped to a TOF wall called as "panel" as shown in Fig. 2.14. 10 panels make a TOF system, thus total 960 slats and 1920 channels of PMT's are installed. The segmentation of TOF system is determined to minimize the probability of double hit. Assuming the rapidity density of the charged particle to be $dN_{ch}/dy = 1500$, the charged particle multiplicity on the TOF is expected to be 9. In order to keep the occupancy below 10 %, the segmentation should be about 1000 and the required area of each segment at a radial distance of 5.1 m from the interaction points is 100 cm^2.

Particle identification for charged particles is performed by combining the information of the BBC, DC, PC, and TOF. Fig. 2.15 shows scatter plot of invserse momentum times charge with respect to the flight time of charged particles in minimum bias Au + Au collisions. This figure clearly demonstrates the particle identification capability of the TOF detector. During Run-4 period, the actual timing resolution of TOF system is about 125 ps, which is enable us to separate π/K up to 2 GeV/c, and K/p up to 3.2 GeV/c.

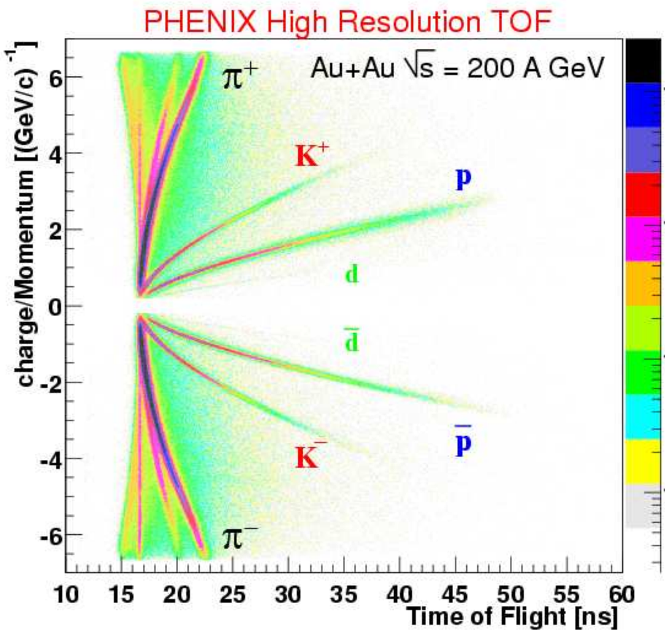

Figure 2.15: Flight time of charged hadrons as a function of inverse momentum in minimum bias Au + Au collisions at $\sqrt{s_{\rm NN}} = 200$ GeV.

Chapter 3

Data Reduction

In this chapter, we present the minimum bias trigger and centrality determination (Section 3.1), event plane determination with BBC (Section 3.2), track reconstruction and momentum determination by the DC (Section 3.3), particle identification by the TOF (Section 3.4), how to extract the v_2 for identified hadrons (Section 3.6), and systematic uncertainties on v_2 (Section 3.7).

3.1 Event selection

3.1.1 Minimum Bias Trigger

Minimum bias trigger is defined by selecting following events on the BBC and the ZDC:

1. BBC
    - At least two PMTs are fired in each BBC and the collision vertex z_{vertex} satisfy $|z_{vertex}| < 38\ cm$ by the online BBC Level-1 trigger.
    - $|z_{vertex}| < 30\ cm$ is required by offline analysis.
2. ZDC
    - At least one forward neutron is detected in each of the two ZDC.

The trigger efficiency for minimum bias Au + Au collisions is studied for both of the BBC and the ZDC [38, 39]. The extracted trigger efficiencies are given by

$$\epsilon_{BBC} = 92.3\% \pm 0.4\%(stat.) \pm 1.6\%(sys.) \quad (3.1)$$

$$\epsilon_{ZDC|BBC} = 99^{+1.0}_{-1.5}\% \quad (3.2)$$

$$\epsilon_{minbias} = \epsilon_{BBC} \times \epsilon_{ZDC|BBC} = 91.4^{+2.5}_{-3.0}\% \quad (3.3)$$

where ϵ_{BBC} is the BBC trigger efficiency estimated by HIJING event generator [40]. $\epsilon_{ZDC|BBC}$ is the ZDC trigger efficiency for BBC Level-1 triggers, and $\epsilon_{minbias}$ is the minimum bias trigger efficiency with the coincidence of BBC and ZDC. Therefore, PHENIX minimum bias trigger selection can cover 91.4% of the Au + Au inelastic cross sections.

3.1.2 Centrality Determination

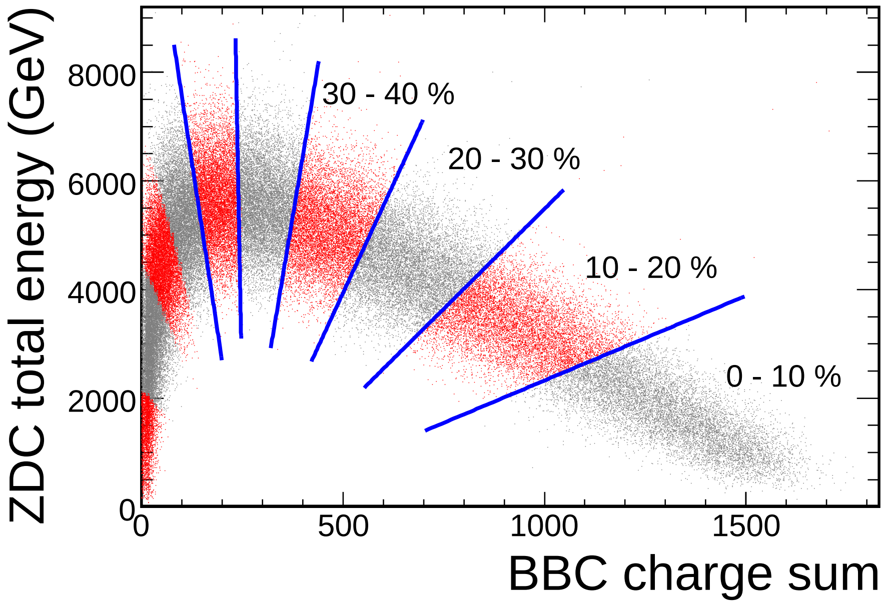

Figure 3.1: Centrality determination using the ZDC total energy and the BBC charge sum. See text for details how to determine the centrality in ZDC-BBC space.

In order to study the collision geometry dependenence of the measured anisotropic flow we should know the relationship between the impact parameter and centrality since we cannot measure impact parameter directly. In PHENIX experiments, the centrality is determined by the measured correlation between the charge deposited in the BBC and the energy deposited in the ZDC.

In Fig. 3.1 the centrality angle ϕ_{cent} is determined in the ZDC energy - BBC charge space, where ϕ_{cent} is the angular position of the event defined as

$$\phi_{cent} = \tan^{-1}\left(\frac{(Q^{BBC} - Q_0^{BBC})/Q_{max}^{BBC}}{E^{ZDC}/E_{max}^{ZDC}}\right) \tag{3.4}$$

where Q^{BBC} and E^{ZDC} are measured charge sum in the BBC and measured total energy in the ZDC, respectively, Q_{max}^{BBC} is the maximum charge sum measured in the BBC and is equal to 1700, $Q_0^{BBC} = 0.15 \cdot Q_{max}^{BBC}$ is the position along the BBC axis from which the angle ϕ_{cent} is determined, and E_{maz}^{ZDC} is the maximum energy deposited in the ZDC and is 8500 GeV. This event with ϕ_{cent} is groupud into the centrality class defined by lower and upper bounds, ϕ_{min} and ϕ_{max} if $\phi_{min} < \phi_{cent} < \phi_{max}$. Since the performance of the BBC and ZDC is changed during the period of Run4, we apply the time dependent correction for both BBC charge and ZDC energy [41].

After centrality is determined we estimate number of participating nucleons (N_{part}) and number of binary collisions (N_{coll}) by using Glauber model based on Monte Carlo simulations. Further details of Glauber model can be found in Appendix A.

3.2 Event Plane

In this section, we introduce the Fourier expansion of azimuthal particle distribution and its properties with respect to the reaction plane. And we also introduce **event plane** which is the estimate of the true reaction plane determined by using the signal of flow itself.

3.2.1 Fourier Expansion of Azimuthal Distribution

Since the azimuthal distribution of emitted particles $dN/d\phi$ is the periodic function with 2π fundamental period, it is natural to expand azimuthal distribution into Fourier series with 2π period.

$$\begin{aligned}\frac{dN}{d\phi} &= \frac{x_0}{2\pi} + \frac{1}{\pi}\sum_{n=1}^{\infty}\left(x_n \cos(n\phi) + y_n \sin(n\phi)\right) \\ &= \frac{x_0}{2\pi}\left(1 + 2\sum_{n=1}^{\infty}\left(\frac{x_n}{x_0}\cos(n\phi) + \frac{y_n}{x_0}\sin(n\phi)\right)\right) \qquad (3.5)\end{aligned}$$

The Fourier coefficients x_n and y_n can be obtained by integrating $dN/d\phi$ with weights proportional to $\cos(n\phi)$ and $\sin(n\phi)$. Here, we introduce the following notation,

$$\langle O \rangle = \frac{\int d\phi \; O \times dN/d\phi}{\int d\phi \; dN/d\phi} \qquad (3.6)$$

where O denotes some observables. Since there is only a finite number of particles in each event, the integral become simply sums over particles found in the event

$$x_n = \int_0^{2\pi} d\phi \, \frac{dN}{d\phi}\cos(n\phi) = \sum_{i=0}^{M} w_i \cos(n\phi_i) \equiv Q_x \qquad (3.7)$$

$$y_n = \int_0^{2\pi} d\phi \, \frac{dN}{d\phi}\sin(n\phi) = \sum_{i=0}^{M} w_i \sin(n\phi_i) \equiv Q_y \qquad (3.8)$$

where i runs over all particles (M) used to determine the event plane, ϕ_i is the azimuthal angle of the emitted i-th particle and w_i is the weight (p_{T}, multiplicity etc) to minimize the dispersion of event plane (i.e. maximize event plane resolution). We define the following two-dimentional vector $\mathbf{Q} = (Q_x, Q_y)$ called as a **flow vector**.

If we assume ϕ in Eq. (3.5) is defined relative to the reaction plane, then $dN/d\phi$ becomes an even function and we can omit y_n terms since the integration would be zero in Eq. (3.8),

$$\frac{dN}{d\phi} = \frac{x_0}{2\pi}\left(1 + 2\sum_{n=1}^{\infty}\frac{x_n}{x_0}\cos(n\phi)\right) = \frac{x_0}{2\pi}\left(1 + 2\sum_{n=1}^{\infty} v_n \cos(n[\phi_{lab} - \Psi])\right) \qquad (3.9)$$

where ϕ_{lab} is the azimuthal angle of fixed orientation in the experiment, Ψ is the azimuthal angle of true reaction plane and $v_n = x_n/x_0$ is the magnitude of anisotropy. We introduce the following two variables,

$$v_n^{obs} = \frac{\sqrt{x_n^2 + y_n^2}}{x_0}, \qquad x_0 = M \langle w \rangle \tag{3.10}$$

$$\Psi_n = \frac{1}{n}\tan^{-1}\left(\frac{y_n}{x_n}\right), \quad 0 \le \Psi_n \le \frac{2\pi}{n} \tag{3.11}$$

From Eq. (3.10) and (3.11), measured azimuthal distribution $r^m(\phi)$ can be given by

$$\begin{aligned} r^m(\phi_{lab}) &= \frac{x_0}{2\pi}\left(1 + 2\sum_{n=1}^{\infty}\left(\frac{x_n}{x_0}\cos(n\phi_{lab}) + \frac{y_n}{x_0}\sin(n\phi_{lab})\right)\right) \\ &= \frac{x_0}{2\pi}\left(1 + 2\sum_{n=1}^{\infty}\left(v_n^{obs}\cos(n\Psi_n)\cos(n\phi_{lab}) + v_n^{obs}\sin(n\Psi_n)\sin(n\phi_{lab})\right)\right) \\ &= \frac{x_0}{2\pi}\left(1 + 2\sum_{n=1}^{\infty} v_n^{obs}\cos(n[\phi_{lab} - \Psi_n])\right) \end{aligned} \tag{3.12}$$

Comparing to Eq. (3.9), and (3.12) one can see that Ψ_n gives event plane, which is the estimate of an azimuthal angle of true reaction plane. It is reconstructed from the reaction products event-by-event basis. The reconstructed plane (event plane) differs in general from the true reaction plane by an error $\Delta\Psi$. Thus, the measured azimuthal angle of event plane Ψ_n is related to the true azimuthal angle of reaction plane Ψ by $\Psi_n = \Psi + \Delta\Psi$. Averaging over many events, one obtains the following relation between the measured and true Fourier coefficients [42]:

$$\begin{aligned} v_n^{obs} &= \langle \cos(n[\phi_{lab} - \Psi_n]) \rangle \\ &= \langle \cos(n[\phi_{lab} - \Psi] - n[\Psi_n - \Psi]) \rangle \\ &= \langle \cos(n[\phi_{lab} - \Psi]) \cdot \cos(n\Delta\Psi) \rangle + \langle \sin(n[\phi_{lab} - \Psi]) \cdot \sin(n\Delta\Psi) \rangle \\ &= \langle \cos(n[\phi_{lab} - \Psi]) \rangle \langle \cos(n\Delta\Psi) \rangle \\ &= v_n \langle \cos(n\Delta\Psi) \rangle \end{aligned} \tag{3.13}$$

from line 3 to 4 we assume that $\phi_{lab} - \Psi$ and $\Delta\Psi$ are statistically independent. And we use the reflection symmetry of $\phi_{lab} - \Psi$ and $\Delta\Psi$, i.e. average sine term vanish under that condition. This assumption is valid for the system with large multiplicity. In section 3.2.4, we derive the analytical formula of event plane resolution, $\langle \cos(n\Delta\Psi) \rangle$, when the multiplicity is large ($M \gg 1$) in a selected window.

3.2.2 Event Plane Determination

Since an azimuthal angle of true reaction plane is unknown, we have to determine estimated reaction plane (**event plane**) experimentally. In this analysis, the BBC is used to determine an event plane for each event. The BBC have several advantages to determine the event plane:

- The BBC has full azimuthal coverage while central arm has only half of full azimuth.
- The BBC is located from 144 cm from the collision points and this corresponds to a pseudo-rapidity $|\eta| = 3.0 - 3.9$. This rapidity gap helps to reduce non-flow contributions, which is the correlations *not* originated from the reaction plane, such as di-jet correlations, resonance decays, and Bose-Einstein correlations.
- The BBC has a very good stability during the entire RUN period.

Event plane is calculated at both south BBC (BBCS) and north BBC (BBCN) by the Eq. (3.14) - (3.16)

$$2\Psi^{obs} = \tan^{-1}\left(\frac{Q_y}{Q_x}\right) \tag{3.14}$$

$$Q_x = \sum_{i=0}^{64} w_i \cos(2\phi_i) \tag{3.15}$$

$$Q_y = \sum_{i=0}^{64} w_i \sin(2\phi_i) \tag{3.16}$$

where Ψ^{obs} is measured azimuthal angle of event plane, Q_x and Q_y is the projection of event plane to x and y axes respectively, ϕ_i is the azimuthal angle of each PMT, and w_i is the weight. We choose charge value on each PMT as a weight. Fig. 3.2 shows the typical response in one event for both south and north BBC. The solid red lines represent the azimuthal angle of measured (uncorrected) event plane. Normally, measured event plane is not always flat because of imperfect detector acceptance, dead channels in BBC's, beam condition and so on. In order to correct those effects, we have 2 calibration steps for event plane. Details of these calibration will be discussed in the next section.

3.2.3 Event Plane Calibration

As we already mentioned in previous section, measured event plane distribution is not always flat because of several effects. In this section, we introduce the detail of calibration for event plane.

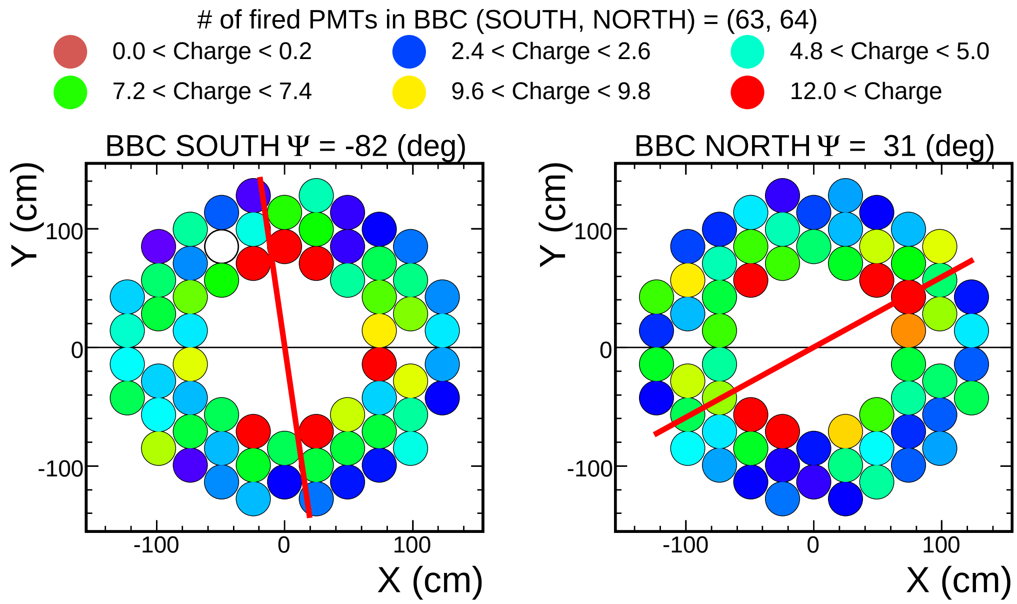

Figure 3.2: Event display how to determine the azimuthal angle of event plane in south BBC (left) and north BBC (right). Solid red lines show the azimuthal angle of measured event plane in this particular event.

Re-centering Calibration

"Re-centering calibration" is defined as

$$2\Psi^{cor} = \tan^{-1}\left(\frac{Q_y^{cor}}{Q_x^{cor}}\right) \tag{3.17}$$

$$Q_x^{cor} = \frac{Q_x - \langle Q_x \rangle}{\sigma_x} \tag{3.18}$$

$$Q_y^{cor} = \frac{Q_y - \langle Q_y \rangle}{\sigma_y} \tag{3.19}$$

where $\langle Q_{x,y} \rangle$ are the mean of Q_x and Q_y distributions, and $\sigma_{x,y}$ are the width of Q_x and Q_y. As we can see in the Fig. 3.3 the width of flow vector become wider in more peripheral bins, while mean is unchanged for all centrality bins. The mean and width of flow vectors are extracted by fitting Q_x and Q_y distributions with gaussian, and parameterized as a function of centrality.

Fig. 3.4 shows the mean and width of flow vectors as a function of centrality. Since detector response of BBC's have very good stability, mean and width does not change during the entire period of run.

Flattening Calibration

Fig. 3.5 show the event plane distribution determined in BBC SOUTH + NORTH. One can see that the event plane with re-centering calibration (blue histogram) is almost

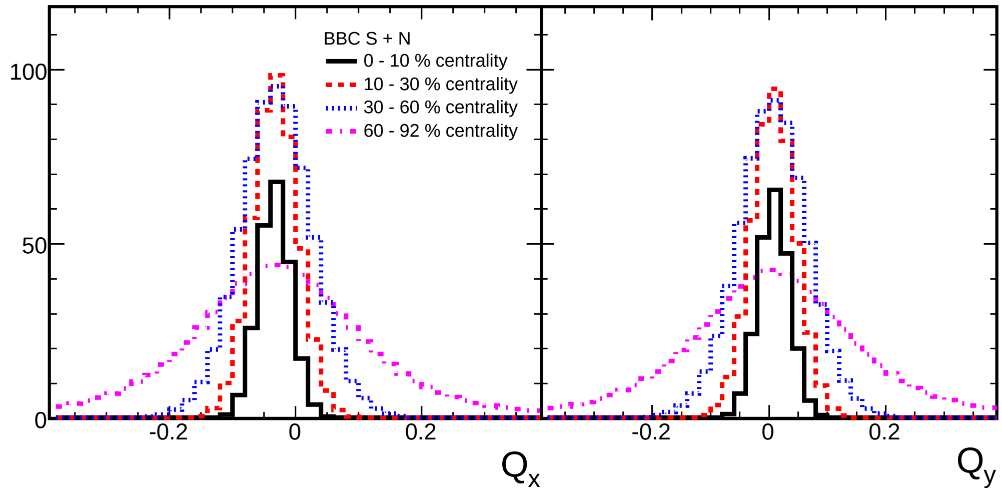

Figure 3.3: Q_x (left) and Q_y (right) distributions for several centrality bins in BBC SOUTH + NORTH. Centrality bins are $0-10\%$ (solid black), $10-30\%$ (dashed red), $30-60\%$ (dotted blue), and $60-92\%$ (dashed-dotted magenda).

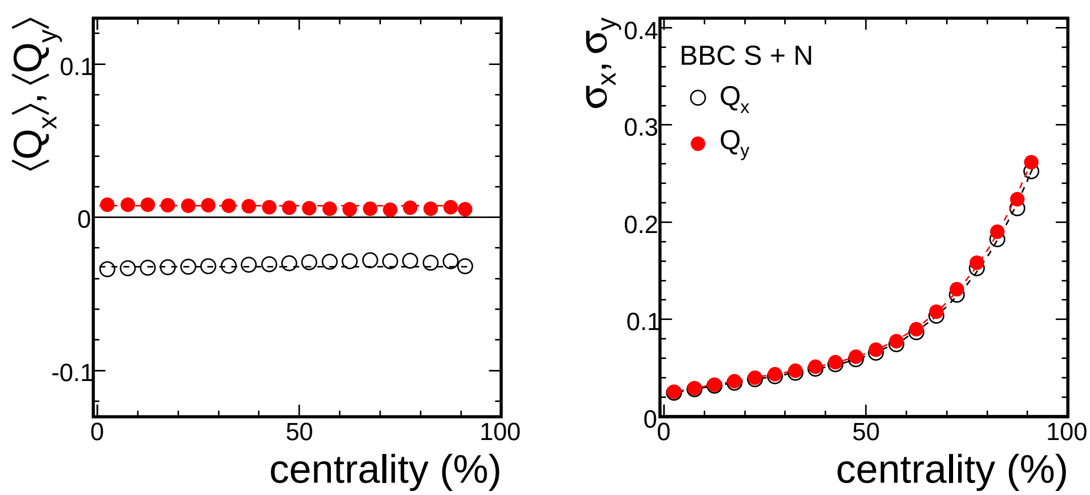

Figure 3.4: Mean (left) and width (right) of flow vectors as a function of centrality. Open black (solid red) symbols show the mean and width of Q_x (Q_y).

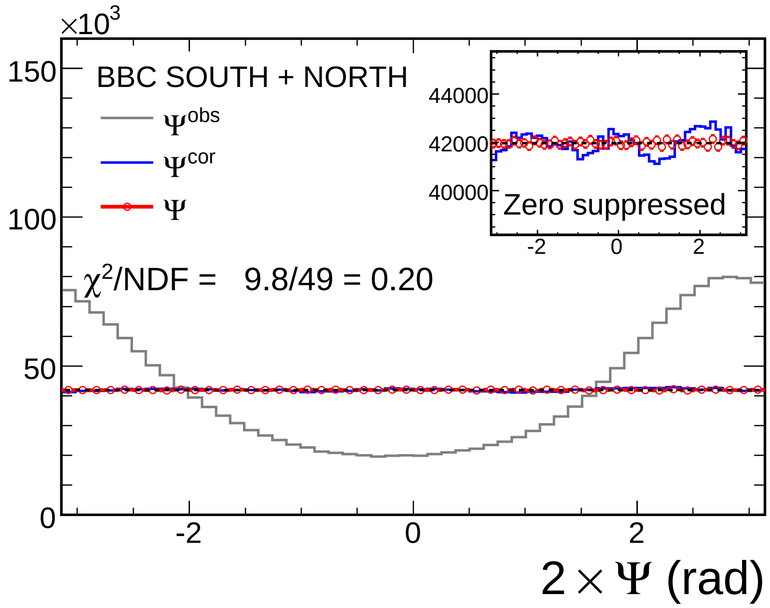

Figure 3.5: Event plane distribution for BBC SOUTH + NORTH, without correction (black), with re-centering calibration (blue), and with re-centering + flattening calibration (red). Top right figure is expanded the same event plane distribution to see the flatteness of event plane.

flat but there is still small non-flat components as shown in top right part in the figure. In order to remove the remaining non-flatness of event plane, we perform "Flattening calibration" which is defined by

$$n\Delta\Psi \equiv \sum_{k=1}^{k_{max}} [A_k \cos(kn\Psi^{cor}) + B_k \sin(kn\Psi^{cor})] \tag{3.20}$$

$$n\Psi \equiv n\Psi^{cor} + n\Delta\Psi \tag{3.21}$$

The coefficients A_k and B_k can be obtained by requiring that k-th Fourier moment of the Ψ distribution is vanished, i.e., requiring isotropic distribution for Ψ. Assuming that the correction $\Delta\Psi$ is small,

$$\begin{aligned}
\langle\cos(kn\Psi)\rangle &= \langle\cos(kn\Psi^{cor} + kn\Delta\Psi\rangle \\
&= \langle\cos(kn\Psi^{cor})\cdot\cos(kn\Delta\Psi)\rangle - \langle\sin(kn\Psi^{cor})\cdot\sin(kn\Delta\Psi)\rangle \\
&\simeq \langle\cos(kn\Psi^{cor})\rangle - \langle\sin(kn\Psi^{cor})\cdot(kn\Delta\Psi)\rangle \\
&= \langle\cos(kn\Psi^{cor})\rangle - kB_k\left\langle\sin^2(kn\Psi^{cor})\right\rangle \\
&= \langle\cos(kn\Psi^{cor})\rangle - \frac{kB_k}{2} \qquad \left(\because \left\langle\sin^2(kn\Psi^{cor})\right\rangle = \frac{1}{2}\right) \\
&= 0 \\
\therefore B_k &= \frac{2}{k}\langle\cos(kn\Psi^{cor})\rangle
\end{aligned} \tag{3.22}$$

Similarly,

$$\begin{aligned}
\langle \sin(kn\Psi) \rangle &= \langle \sin(kn\Psi^{cor} + kn\Delta\Psi \rangle \\
&= \langle \sin(kn\Psi^{cor}) \cdot \cos(kn\Delta\Psi) \rangle + \langle \cos(kn\Psi^{cor}) \cdot \sin(kn\Delta\Psi) \rangle \\
&\simeq \langle \sin(kn\Psi^{cor}) \rangle + \langle \cos(kn\Psi^{cor}) \cdot (kn\Delta\Psi) \rangle \\
&= \langle \sin(kn\Psi^{cor}) \rangle + kA_k \left\langle \cos^2(kn\Psi^{cor}) \right\rangle \\
&= \langle \sin(kn\Psi^{cor}) \rangle + \frac{kA_k}{2} \qquad \left(\because \left\langle \cos^2(kn\Psi^{cor}) \right\rangle = \frac{1}{2} \right) \\
&= 0 \\
\therefore A_k &= -\frac{2}{k} \langle \sin(kn\Psi^{cor}) \rangle \qquad (3.23)
\end{aligned}$$

$$\begin{aligned}
\Psi &= \Psi^{cor} + \Delta\Psi \qquad (3.24) \\
\Delta\Psi &= \sum_k \left(A_k \cos(2k\Psi^{cor}) + B_k \sin(2k\Psi^{cor}) \right) \qquad (3.25) \\
A_k &= -\frac{2}{k} \langle \sin(2k\Psi^{cor}) \rangle \qquad (3.26) \\
B_k &= \frac{2}{k} \langle \cos(2k\Psi^{cor}) \rangle \qquad (3.27)
\end{aligned}$$

where Ψ^{cor} is corrected event plane in Eq. (3.17), and $\Delta\Psi$ is the correction factor from flattening calibration, k is degree of Fourier expansion, and brackets denote the average over all particles in all events. One can see that the event plane distribution with the flattening calibration (red histgoram in Fig. 3.5) becomes flat. We perform flattening calibration run by run basis since the condition of BBC and beam could be changed for different runs.

3.2.4 Event Plane Resolution

In the real experiment, only finite number of particles are emitted and detected in each collision. This introduces some fluctuations in observing the anisotropy on an event-by-event basis. Even if the distribution is azimuthally istoropic, statistical fluctuations can lead to non-zero coefficients v_n.

We first show the following three assumptions in order to simplfy the problem.

1. All particles in the same event and in the same rapidity window can be treated as being independent.
2. The total number of particles in the selected window is relatively large ($M \gg 1$)
3. The magnitude of flow is not fluctuate in the same impact parameter or centrality

Under these assumptions, the event plane resolution can be expressed as [13]

$$\langle \cos(k\theta_n) \rangle = \frac{\sqrt{\pi}}{2} \bar{\chi}_n e^{-\bar{\chi}_n^2/2} \left[I_{(k-1)/2}\left(\frac{\bar{\chi}_n^2}{2}\right) + I_{(k+1)/2}\left(\frac{\bar{\chi}_n^2}{2}\right) \right] \qquad (3.28)$$

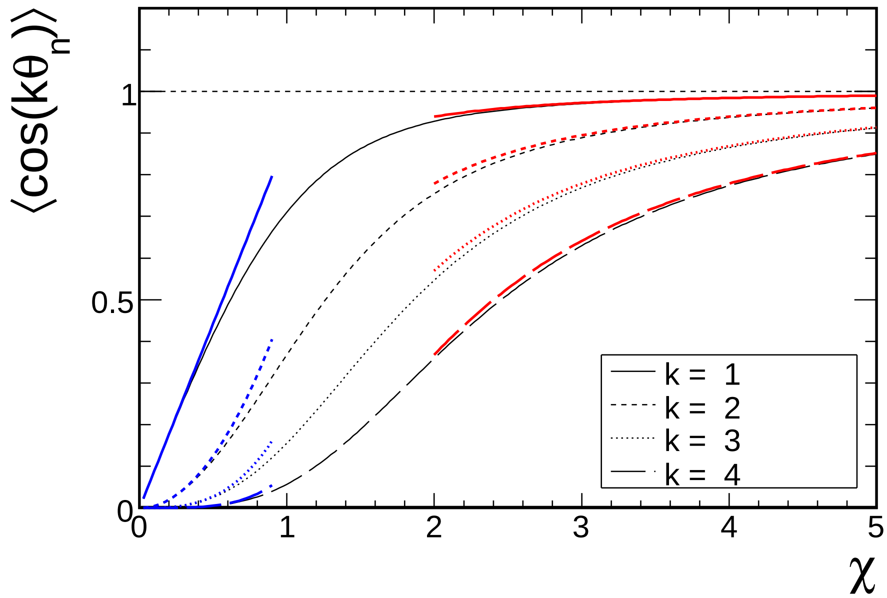

Figure 3.6: Event plane resolution as a function of χ for different index k, $k = 1, 2, 3, 4$. Asymptotic results are also plotted by blue lines ($\chi \ll 1$) from Eq. (B.10), and red lines ($\chi \gg 1$) from Eq. (B.11).

Fig. 3.6 shows the event plane resolution as a function of χ for different k. Blue and red lines in the figure are asymptotic results of the event plane resolution as we derive in Eq. (B.10) and (B.11), respectively.

Since we have two independent event plane from SOUTH and NORTH BBC, we can estimate the event plane resolution by measuring the relative azimuthal angle $\Delta\Psi_n^{BBC} \equiv n(\Psi_n^{BBCS} - \Psi_n^{BBCN})$. Because acceptance of each BBC is same, the multiplicity for each BBC is equal to be half of total multiplicity in both BBC's, $N^{BBCS} = N^{BBCN} = N/2$, the corresponding statistical fluctuation σ_n and $\bar{\chi}_n$ should be:

$$\sigma_n^{BBCS} = \sigma_n^{BBCN} = \frac{1}{\sqrt{N^{BBCS,N}}} \frac{\langle w^2 \rangle}{\langle w \rangle^2} = \frac{\sqrt{2}}{\sqrt{N}} \frac{\langle w^2 \rangle}{\langle w \rangle^2} = \sqrt{2}\sigma_n^{BBC} \tag{3.29}$$

$$\chi_n^{BBCS} = \chi_n^{BBCN} = \frac{v_n}{\sigma_n^{BBCS,N}} = \frac{v_n}{\sqrt{2}\sigma_n^{BBC}} = \frac{\chi_n^{BBC}}{\sqrt{2}} \tag{3.30}$$

One can obtain χ_n by measuring $\left\langle \cos\left(k\Delta\Psi_n^{BBC}\right)\right\rangle = \left\langle \cos\left(kn[\Psi_n^{BBCS} - \Psi_n^{BBCN}]\right)\right\rangle$:

$$\begin{aligned} & \left\langle \cos\left(k\Delta\Psi_n^{BBC}\right)\right\rangle = \left\langle \cos\left(kn[\Psi_n^{BBCS} - \Psi_n^{BBCN}]\right)\right\rangle \\ = & \left\langle \cos\left(kn[\Psi_n^{BBCS} - \Psi]\right)\right\rangle \left\langle \cos\left(kn[\Psi_n^{BBCN} - \Psi]\right)\right\rangle \\ = & \frac{\pi}{8}\bar{\chi}_n^2 e^{-\bar{\chi}_n^2/2} \left[I_{(k-1)/2}\left(\frac{\bar{\chi}_n^2}{4}\right) + I_{(k+1)/2}\left(\frac{\bar{\chi}_n^2}{4}\right)\right]^2 \end{aligned} \tag{3.31}$$

Fig. 3.7 shows the event plane resolution as a function of centrality. As one can see

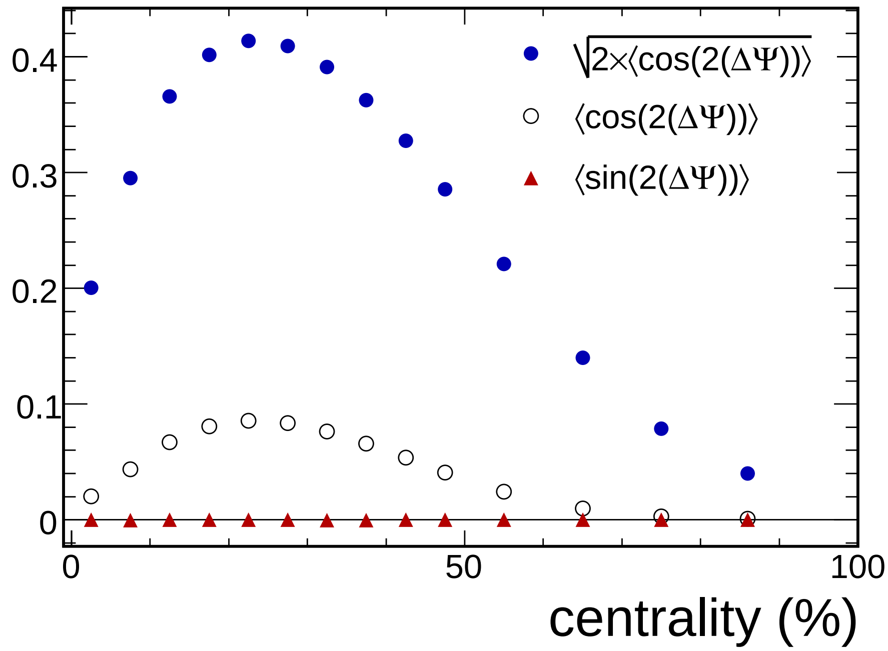

Figure 3.7: Event plane resolution as a function of centrality measured by the correlation between SOUTH and NORTH BBC event plane.

$\left\langle \sin\left(2\Delta\Psi^{BBC}\right)\right\rangle = 0$ for entire centrality bins as we expected from the reflection symmetry of $\Delta\Psi$. Since the maximum value of $\left\langle \cos\left(2\Delta\Psi^{BBC}\right)\right\rangle$ (open black) is less than 0.1, the approximation of small anisotropy limit ($\chi \ll 1$) works very well (see the lines for $k = 1$ in Fig. 3.6). Thus, if $\chi \ll 1$ the event plane resolution is reduced to

$$\begin{aligned}
\left\langle \cos\left(k\Delta\Psi_n^{BBC}\right)\right\rangle &\approx \frac{\pi}{8}\bar{\chi}_n^2 e^{-\bar{\chi}_n^2/2}\frac{1}{\Gamma\left(\frac{k+1}{2}\right)^2}\left(\frac{\bar{\chi}_n^2}{8}\right)^{k-1}\left[1+\frac{2}{k+3}\left(\frac{\bar{\chi}_n^2}{8}\right)\right]^2 \\
&\approx \frac{\pi}{8^k\Gamma\left(\frac{k+1}{2}\right)^2}\bar{\chi}_n^{2k} \\
&= \frac{1}{2^k}\left\langle \cos\left(k\theta_n\right)\right\rangle^2 \\
\therefore \quad \left\langle \cos\left(\theta_n\right)\right\rangle &\approx \sqrt{2\left\langle \cos\left(\Delta\Psi_n^{BBC}\right)\right\rangle} \quad (k=1)
\end{aligned} \tag{3.32}$$

3.2.5 Event Plane QA

After we perform full calibrations, the stability of event plane is checked for each run. Since the direction of event plane should be random, average cosine and sine of event plane azimuthal angle ($\langle\cos(n\Psi)\rangle$, $\langle\sin(n\Psi)\rangle$) should be zero. Examples of event plane QA are shown in Fig. 3.8. As one can see $\langle\cos(2\Psi)\rangle$ and $\langle\sin(2\Psi)\rangle$ are zero for entire event for a given run if the event plane calibration is perfect (right figure). However, if

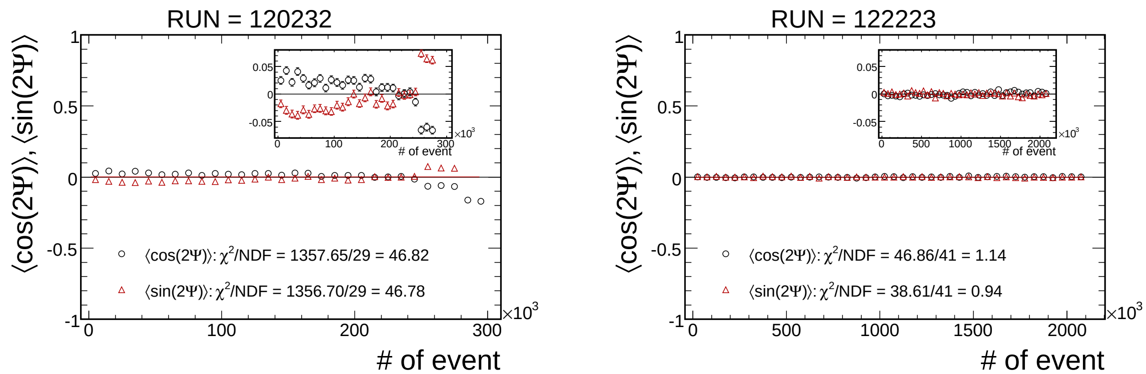

(a) RUN 120232 (b) RUN 122223

Figure 3.8: Average cosine and sine of 2^{nd} harmonic BBC event plane as a function of number of event for RUN 120232 (left, bad run) and for RUN 122223 (right, good run)

you look at the left figure there is still time dependent non-flatness for some runs after the full event plane calibration. These bad runs are less than 1 % fraction of total data so it seems to not affect our final results, but we exclude these runs from analysis.

3.3 Global Track Selection

3.3.1 Track Reconstruction

A typical track in the DC main bend plane ($r - \phi$) is illustrated in Fig. 3.9. The coordinates in the DC are ϕ and α, where ϕ is the azimuthal angle at the intersection of the track with a "reference radius" at the mid-radius of the DC, and α is the inclination of the track at that point. In principle, ϕ and α are equivalent to a slope and intercept; the main difference is that ϕ and α are limited to a given range of possible value while slope and intercept are not. Right hand side in Fig. 3.9 shows the track in the $r - z$ plane, perpendicular to the bend plane. Because of the magnetic field is along the beam (z-) direction, tracks usually have a very small bend in this plane. The coordinates used in this projection are zed, the z coordinate of the intersection point, and β, the inclination of the track at the reference radius.

In order to find a track, hits produced in the detector by the same charged particle have to be found and combined. The tracking is done separately in the $r - \phi$ and the $r - z$ plane. The track reconstruction in $r - \phi$ is realized using a combinatorial hough transform technique [32], where any pair of hits can be mapped to a point in the space defined by azimuthal angle ϕ and track bending angle α.

In this analysis, we require the following conditions for the tracks: (1) Found the hits for X1 and X2 wire in DC, (2) Found the unique hit in UV wire in PC1, (3) Found the (unique) hit in PC1. These requirements corresponds that the DC track quality bit is equal to be 31 or 63.

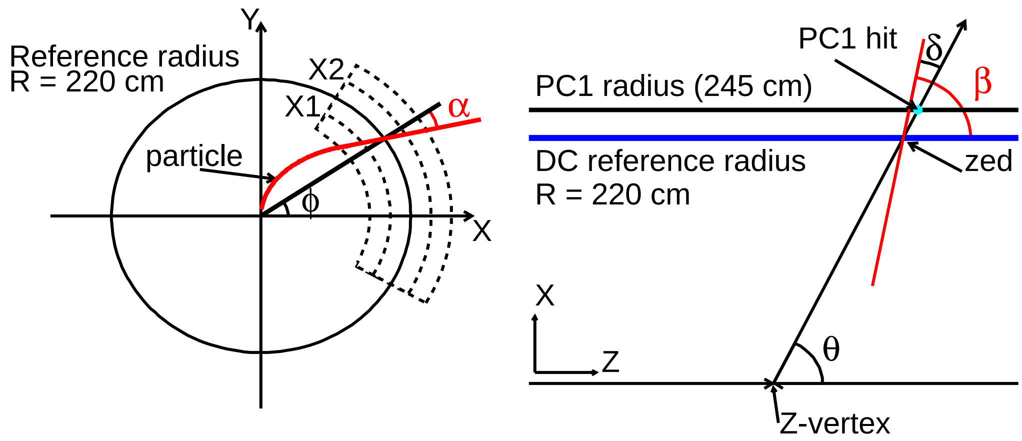

Figure 3.9: (Left) A schematic view of a track in the DC $r-\phi$ plane. ϕ and α are the feature space variables in the combinatorial hough transform technique. (Right) A schematic cutaway view of a track in the DC $r-z$ plane. The associated PC1 hit is indicated by the circle marker. Because the track bending angle δ is small, the track can approximated by the straight line linking the PC1 hit and collision vertex measured by the BBC.

3.3.2 Momentum Determination

The α measured in the DC is closely related to the field integral along the track trajectory. For tracks emitted perpendicular to the beam axis, this relation can be approximated as

$$\alpha \simeq \frac{K}{p_{\mathrm{T}}} \tag{3.33}$$

where $K = 101$ mrad GeV$/c$ is the effective field integral [43]. From Eq. (3.33), one can derive the following form between the momentum resolution and the angular resolution

$$\begin{aligned} \frac{\delta p}{p} &= \frac{\delta\alpha}{\alpha} \\ &= \frac{1}{K}\sqrt{\left(\frac{\sigma_{ms}}{\beta}\right)^2 + (\sigma_\alpha p)^2} \end{aligned} \tag{3.34}$$

where $\delta\alpha$ is the measured angular spread, σ_{ms} and σ_α is the contribution from multiple scattering and from angular resolution of the DC, respectively.

3.3.3 Matching Tracks to Outer Detectors

Tracks are reconstructed by DC-PC1 and projected to the outer tracking detectors by the track model. These detectors are two dimensional walls extending in $r-\phi$ and z directions. Each of them provides a 3-dimensional hit at the detector wall. A wide window around the track intersection point with the detector plane is searched for a list of candidate hits. The one with closest distance to the intersection point is identified as the hit associated with the track.

For primary tracks, the distance in both the $r-\phi$ and the z direction between track projection point and the associated hit position is approximately Gaussian with a width as

$$\sigma_{match} = \sqrt{\sigma^2_{detector} + \left(\frac{\sigma_{ms}}{p\beta}\right)^2} \tag{3.35}$$

where $\sigma_{detector}$ is the finite detector resolution, which include the DC pointing resolution and the detector spatial resolution, and σ_{ms} is the multiple scattering contribution. The mean of the residual distribution ($mean_{match}$) is typically small compared to σ_{match} after detector alignment. A non-zero value of $mean_{match}$ usually results from imperfect detector alignment or the magnetic field map used by the track model. These imperfections can lead to a momentum and charge sing dependence of $mean_{match}$.

The matching distribution needs to be parameterized separately in all tracking detectors for both positive and negative charged particles in $r-\phi$ and z directions, and for collision centrality. The mean and width of matching distribution are extracted by a Gaussian fit, and parameterized as a function of p_{T}. Fig. 3.10 shows $mean_{r-\phi}$, $mean_z$, $\sigma_{r-\phi}$, σ_z as a function of p_{T} and their parameterization for TOF.

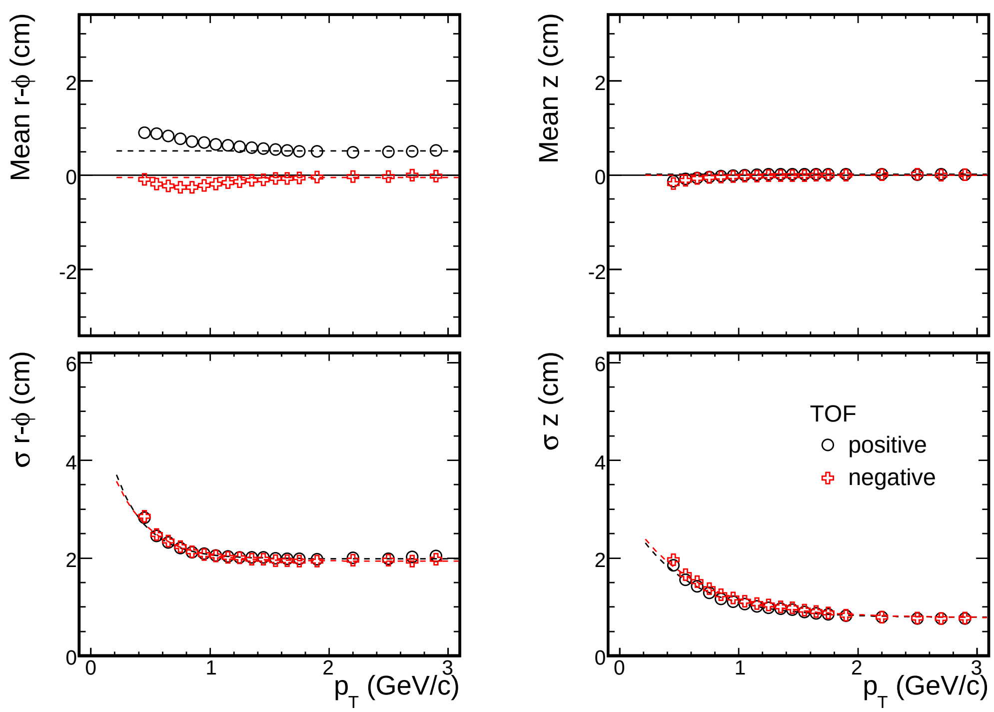

Figure 3.10: TOF matching variables for $r-\phi$ and z as a function of p_{T} and charge. Top figure show $mean_{r-\phi}$ and $mean_z$, and bottom show $\sigma_{r-\phi}$ and σ_z.

3.4 Particle Identification

In the section 3.4.1 we describe particle identification for π, K, p and d with Time-Of-Flight detector by using mass square distributions, and describe ϕ meson identification with invariant mass technique in the section 3.4.3

3.4.1 Mass square distribution

Mass square is given by

$$m^2 = p^2\left(\frac{1}{\beta^2} - 1\right) = p^2\left(\left(\frac{c \cdot t}{L}\right)^2 - 1\right) \tag{3.36}$$

where p is the particle momentum (GeV/c), and velocity β is expressed with the measured time of flight (t), the measured flight path length (L), and the speed of light ($c =$ 29.98 cm/ns),

The width of the mass squared peak depends on both the momentum and time-of-flight resolutions. An analytic form for the width of mass square as a function of momentum resolution δ_p and timing resolution σ_T is determined as follows;

$$\begin{aligned}
\sigma_{m^2}^2 &= \left(\frac{\partial m^2}{\partial p}\right)^2 \delta_p^2 + \left(\frac{\partial m^2}{\partial t}\right)^2 \sigma_t^2 \\
&= \left(2p\left(\frac{1}{\beta^2} - 1\right)\right)^2 \delta_p^2 + \left(2t\left(\frac{pc}{L}\right)^2\right)^2 \sigma_t^2 \\
&= \left(2\frac{m^2}{p}\right)^2 \delta_p^2 + \left(2\frac{cp}{L}\sqrt{m^2+p^2}\right)^2 \sigma_t^2 \\
&= \left(\frac{\delta_p}{p}\right)^2 (4m^4) + \left(\frac{\sigma_t c}{L}\right)^2 \left[4p^2(m^2+p^2)\right].
\end{aligned} \tag{3.37}$$

Using Eq. (3.34) the mass square width can be written as

$$\begin{aligned}
\sigma_{m^2}^2 &= \frac{1}{K^2}\left[\left(\frac{\sigma_{ms}}{\beta}\right)^2 + (\sigma_\alpha p)^2\right](4m^4) + \left(\frac{\sigma_t c}{L}\right)^2 \left[4p^2(m^2+p^2)\right] \\
&= \frac{\sigma_\alpha^2}{K^2}(4m^4p^2) + \frac{\sigma_{ms}^2}{K^2}\left[4m^4\left(1+\frac{m^2}{p^2}\right)\right] + \left(\frac{\sigma_t c}{L}\right)^2 \left[4p^2(m^2+p^2)\right]
\end{aligned} \tag{3.38}$$

A typical mass square distribution is shown in Fig. 3.11. The centroid and with of the mass square for each particle species are extracted by a Gaussian fit. The width is parameterized as a function of p_{T} by Eq. (3.38) with σ_α, σ_{ms} and σ_t as free parameters. The fitting are done for 3 separated Run categories, where

1. ++ field configuration : RUN 105218 - 111593

2. ++ field configuration : RUN 111603 - 115780

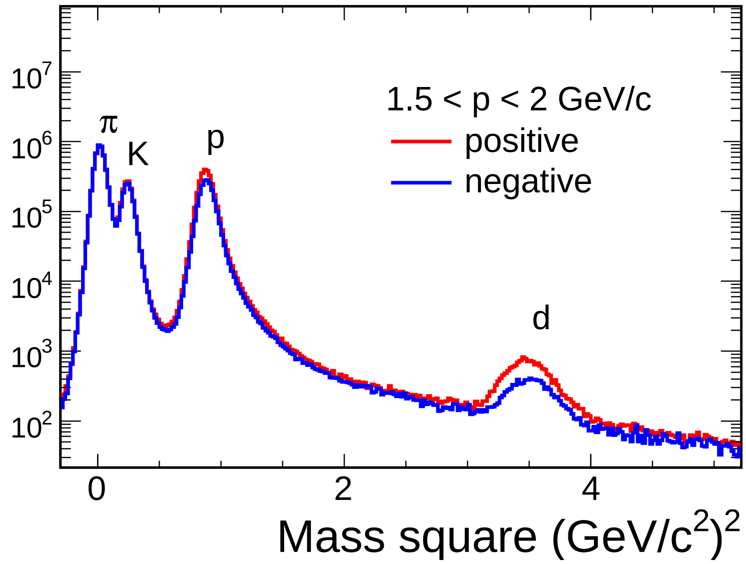

Figure 3.11: Mass square distribution for momentum of 1.5 - 2 GeV/c in TOF.

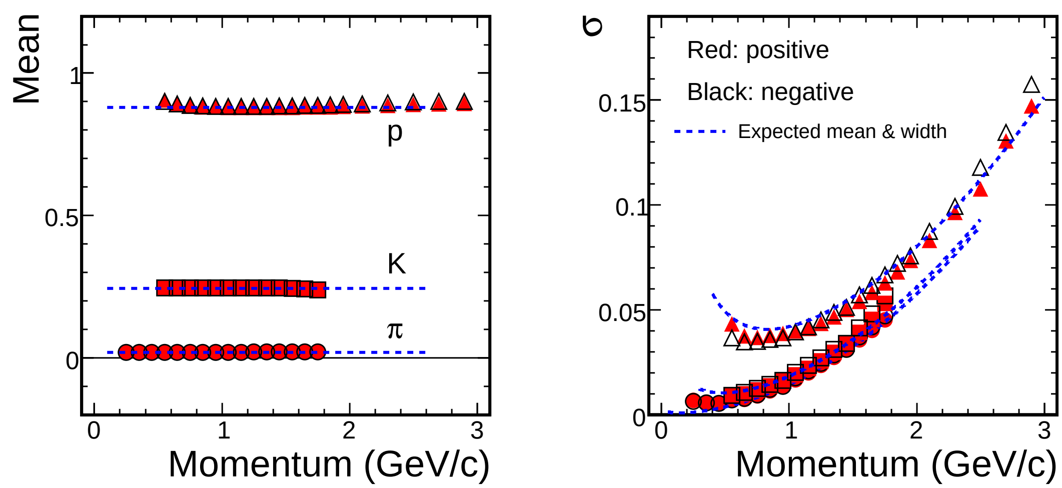

Figure 3.12: Momentum dependence of the centroid (left) and the width (right) of mass square distributions for π, K and p.

3. $--$ field configuration : RUN 116061 - 122223

The momentum dependence of the centroid and width are shown in Fig. 3.12. Dashed blue lines corresponds expected values of the centroid from Particle Data Book value and the width from Eq. (3.38) with one of the parameterization as shown below.

The resulting parameters are extracted for each RUN category [44].

Table 3.1: Fitting results of mass square width for 3 different RUN categories

RUN categories	σ_α (mrad)	σ_{ms} (mrad)	σ_t (ps)
++ field (1)	1.213	1.276	120
++ field (2)	1.192	1.269	120
$--$ field (3)	1.313	1.242	120

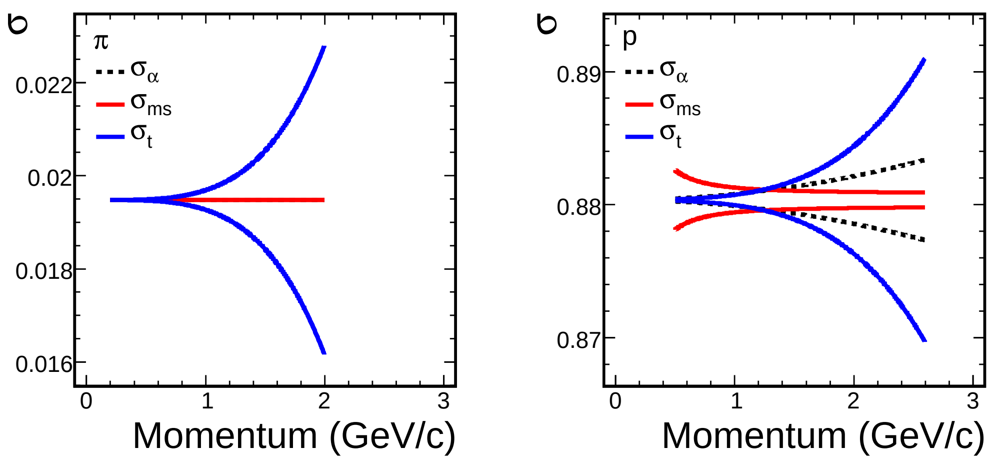

Figure 3.13: The contribution of the 1 σ mass square width for π (left) and p (right). Each contribution is shown by different colors around the expected mass square value. The parameterization of each width is taken from the category (1).

Fig. 3.13 shows the contributions to the mass square width for π and p. Since the π mass is small, the width of mass square is dominated by σ_t in the measured momentum range. For protons, the three terms have different contributions at different momenta. The multiple scattering term dominates at low momentum, i.e. $p < 1$ GeV/c. The momentum resolution term σ_α and σ_t are dominate for intermediate momentum region ($p = 1$ - 1.5 GeV/c), and σ_t starts to become dominant contribution at the high momentum ($p > 1.5$ GeV/c).

3.4.2 Momentum Calibration

Usually, the magnetic field map used by the track model does not reflect the real magnetic field properly. It leads to a systematic momentum shift which is reflected by a shift of the centroid of mass square distribution. This shift Δ_{m^2} can be calculated from the momentum shift Δ_p as

$$\begin{aligned} m_{exp}^2 &= p_{exp}^2 \left(\frac{1}{\beta^2} - 1\right) \\ &= (p + \Delta_p)^2 \left(\frac{1}{\beta^2} - 1\right) \\ &\simeq p\left(\frac{1}{\beta^2} - 1\right) + 2p\Delta_p \left(\frac{1}{\beta^2} - 1\right) \\ &= m^2 + 2\frac{\Delta_p}{p}m^2 \\ \therefore \Delta_{m^2} &= m_{exp}^2 - m^2 = 2m^2 \cdot \left(\frac{\Delta_p}{p}\right) \end{aligned} \tag{3.39}$$

where p_{exp} and m_{exp}^2 is the expected momentum and mass square value, and these are connected to measured momentum and mass square value with Δ_p and Δ_{m^2} as $p_{exp} = p + \Delta_p$ and $\Delta_{m^2} = m^2 + \Delta_{m^2}$. Since momentum shift Δ_p is typically small, a few %, we omit Δ_p^2 term from 2nd to 3rd line in Eq. (3.39). Because Δ_{m^2} is proportional to the particle m^2, a heavy particles such as the protons are more senstive to the momentum scale Δ_p.

A shift of the beam position from the nominal origion of PHENIX detector will produce an systematic offset in mean α value, which can be parameterized as a function of DC azimuthal angle ϕ as:

$$\Delta\alpha = \frac{\Delta x \cdot \sin\phi}{R_{DC}} + \frac{\Delta y \cdot \cos\phi}{R_{DC}} \tag{3.40}$$

where $R_{DC} = 220$ cm is the reference radius of the DC, Δx and Δy are the beam offset. This small change in the beam position can introduce a systematic shift in track α angle, thus affects the measured momentum as follows;

$$\frac{\Delta p}{p} = \frac{\Delta\alpha}{\alpha} = -p\frac{\Delta\alpha}{K} \tag{3.41}$$

Since this change affects the momentum of positive and negative particles in opposite direction, we can determine Δx and Δy from the systematic shift of the measured mass square.

In order to perform a quantitative analysis for momentum scale and beam position offset, we define the modified mass square mean variables of protons and anti-protons as

$$M^+ = \frac{m_p^2 + m_{\bar{p}}^2}{2} - m_{p(PDG)}^2 \tag{3.42}$$

$$M^- = \frac{m_p^2 - m_{\bar{p}}^2}{2} \tag{3.43}$$

where m_p^2 and $m_{\bar{p}}^2$ is the measured mean value of mass square for proton and anti-proton, and $m_{p(PDG)}^2 = (0.9383)^2$ is the mass square of the proton PDG value. From Eq. (3.39) and (3.43) momentum scale can be rewritten by using M^+ as

$$\frac{\Delta_p}{p} = \frac{\Delta_{m^2}}{2m^2} = \frac{M^+}{2m^2} \tag{3.44}$$

Beam position offset can be directly estimated from the intersection point where M^- is equal to be 0. Since Δx is not sensitive to the shift of mass square, we always set to $\Delta x = 0$ in this analysis. Fig. 3.14 show the extracted M^+ and M^- for $1 < p < 1.5$ GeV/c. Momentum range of $1 - 1.5$ GeV/c is choosen to make M^+ and M^- stable where α resolution is dominant. One can see that M^+ is constant over all Δy and M^- depends on Δy linearly. From these results, we conclude that

- Momentum scale factor of 2.2 % is obtained, thus we have to scale down the momentum by 1.022
- Δy is about -0.01 and -0.07 for ++ and $--$ field configuration, respectively.

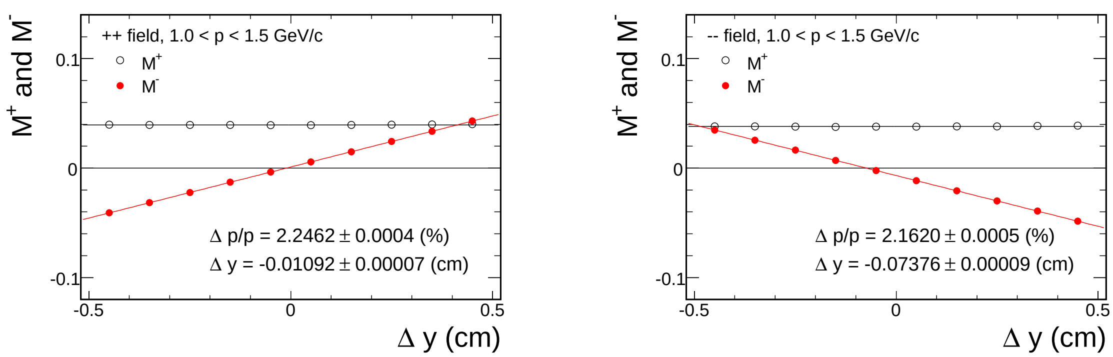

(a) (b)

Figure 3.14: Modified mass square, M^+ and M^-, as a function of Δy in $p = 1 - 1.5$ GeV/c for (a) ++ field configuration and (b) $--$ field configuration. Momentum scale and Δy is determined for each magnetic configuration.

3.4.3 Invariant mass distribution of ϕ

Since a ϕ meson decays with $\tau \sim 1/\Gamma = 1/4.26$ (MeV^{-1}) ~ 46 (fm/c), we cannot directly measure ϕ mesons. Thus, we identify ϕ mesons via $K^+ + K^-$ decay channel by using invariant mass technique. Charged kaons are identified with Time-Of-Flight detector and EM Calorimeter. We use relatively looser track and PID cuts (3 σ) for ϕ analysis compared to π, K and p due to the low statistics of ϕ mesons. Details of track and PID cuts by TOF and EMC for ϕ mesons can be found in Section 3.5.

Invariant mass m_{inv} is obtained by

$$\begin{aligned} m_{inv} &= p_1 \cdot p_2 = E_1 E_2 - \mathbf{p_1} \cdot \mathbf{p_2} && (3.45) \\ E &= \sqrt{m_K^2 + p^2}, \qquad \mathbf{p} = \sqrt{p_x^2 + p_y^2 + p_z^2} && (3.46) \\ \phi_{pair} &= \tan^{-1}\left(\frac{p_{y,1} + p_{y,2}}{p_{x,1} + p_{x,2}}\right) && (3.47) \end{aligned}$$

where E is the total energy, p is the momentum, $m_K = 0.4937$ GeV/c^2 is the mass of kaons, and ϕ_{pair} is the azimuthal angle of p_{T} for ϕ meson.

Fig. 3.15 show the invariant mass distributions in minimum bias event. Since we calculate all possible combinations of K^+ and K^- for a given event, there are always combinatorial background which do not originate from ϕ mesons. The combinatorial background contributions are subtracted with event mixing technique, where K^+ is taken from event i, and K^- from event j ($i \neq j$). Combinatorial background distributions are normalized for m_{inv} = 1.2 - 1.3 GeV/c^2 well separated from the ϕ meson peak.

Fig. 3.16 show the invariant mass distributions after subtracted combinatorial background from foreground. Signal distributions are fitted by the Breit-Wigner + constant functions;

$$\frac{dN}{dm_{inv}} = \frac{1}{2\pi} \frac{p_0 \cdot \Gamma^2}{(m_{inv} - m_0)^2 + \Gamma^2/4} + p_1 \tag{3.48}$$

where p_0, m_0, Γ and p_1 are the free parameters. Extracted m_0 is consistent with the expected value, $m_\phi = 1.019$ within the error bars. Γ values are about 6 MeV, which is larger than expected width $\Gamma_\phi \sim 4$ MeV, due to the effect of mass resolution. We extract the ϕ meson yield by integrating within ± 12 MeV around ϕ meson peak as indicated dashed red lines in the figure.

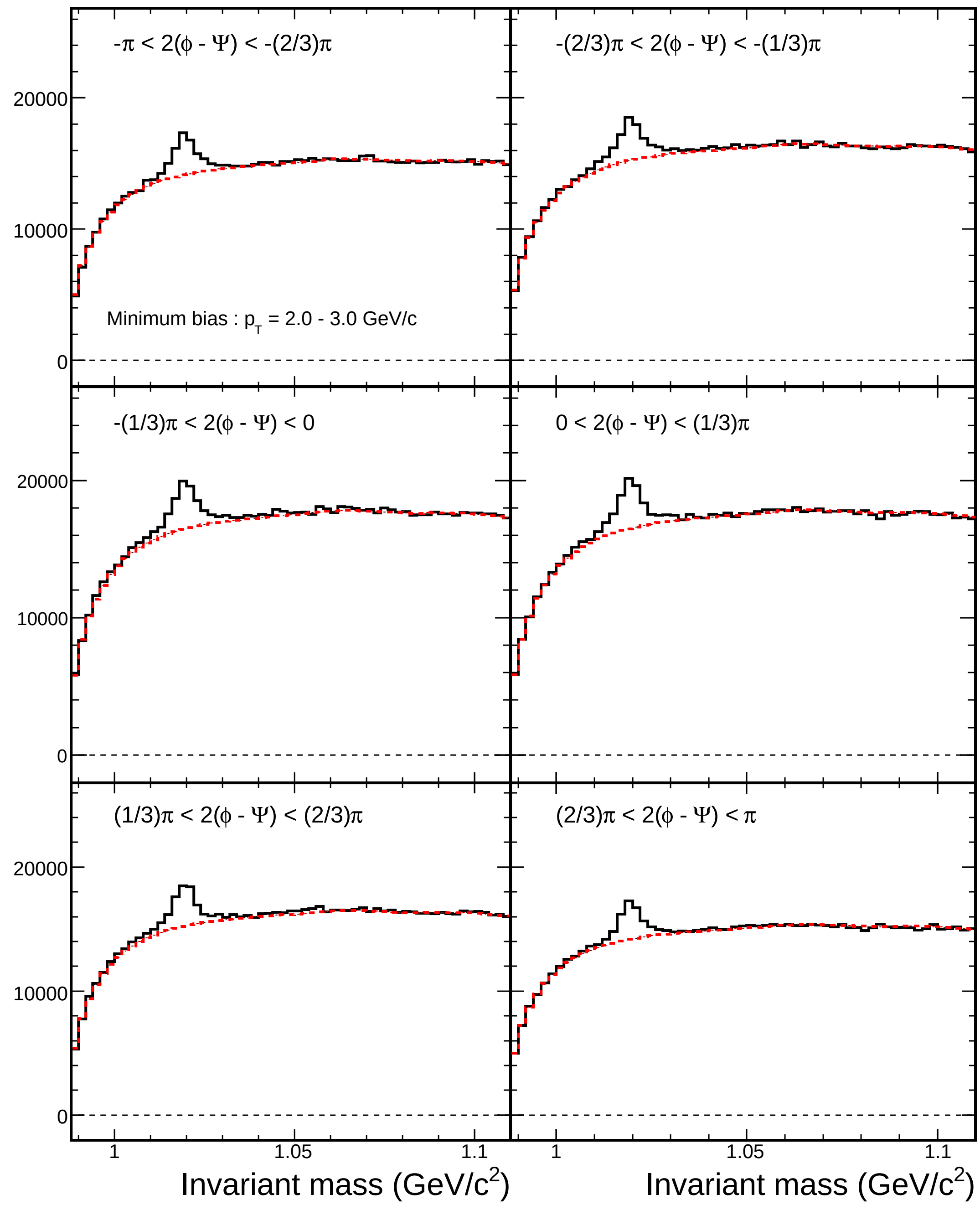

Figure 3.15: Invariant mass distributions via $\phi \rightarrow K^+ + K^-$ for p_{T} = 2 - 3 GeV/c in minimum bias events. Event plane bins are divided into $-\pi < 2(\phi - \Psi) < -2\pi/3$, $-2\pi/3 < 2(\phi - \Psi) < -\pi/3$, $-\pi/3 < 2(\phi - \Psi) < 0$, $0 < 2(\phi - \Psi) < \pi/3$, $\pi/3 < 2(\phi - \Psi) < 2\pi/3$, and $-2\pi/3 < 2(\phi - \Psi) < \pi$ from top to bottom figures. Solid black and dashed red lines show the foreground and combinatorial background invariant mass distributions, respectively.

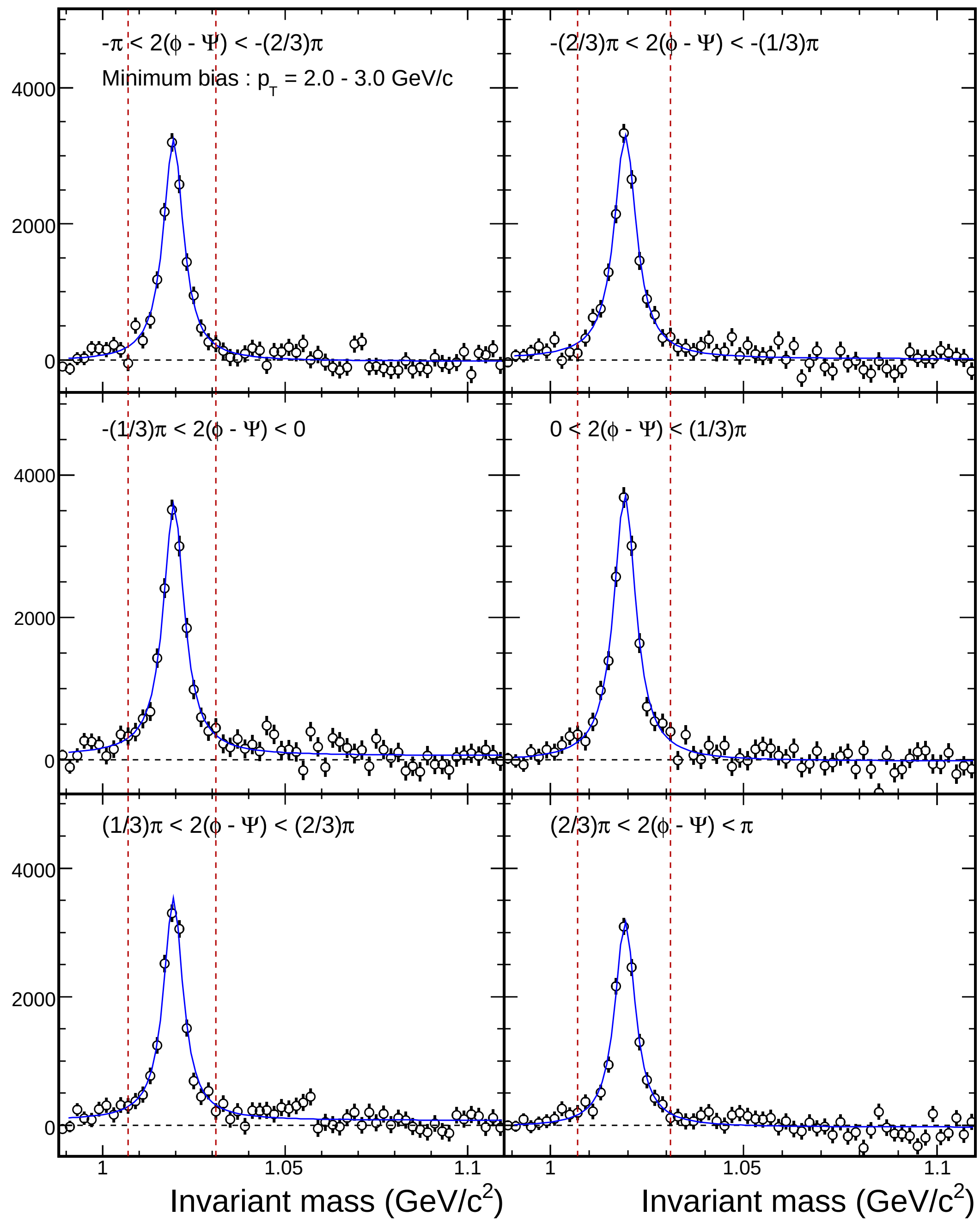

Figure 3.16: Signal invariant mass distributions via $\phi \rightarrow K^{+} + K^{-}$ after subtracted combinatorial background for p_{T} = 2 - 3 GeV/c in minimum bias events. Solid blud lines show the fitting results by Breit-Wigner + constant background functions.

3.5 Cut Conditions

Table 3.2 summarize the cut criteria used in the analysis.

Table 3.2: Summary of cut criteria in this analysis

Cut	Value
Global Event Selection	
Trigger	Minimum bias
Z-vertex	BBC $\lvert z_{vertex}\rvert < 30$ cm
Track Selection (Common)	
DC Track quality	31 or 63
DC *zed*	± 75 cm (see Fig. 3.17)
p_{T} cut off	$p_{\mathrm{T}} > 0.2$ GeV/c
Track Selection (TOF: π, K, p and d)	
TOF energy loss	$E^{tof} > 0.0002 + 0.0014 \times \beta^{-2}$ (see Fig. 3.18)
TOF matching cut	2σ in $r - \phi$ and z directions
PID cut (π, K and p)	2σ cut and veto cut in mass square vs momentum (see Fig. 3.19)
PID cut (d)	2σ cut, where $\sigma(M^2) = 6.38 - 0.449p + 0.11p^2$ and p is the momentum (GeV/c).
p_{T} cut off	π: 0.2 - 4 GeV/c, K: 0.3 - 3 GeV/c, p: 0.5 - 4 GeV/c d: 1 - 4 GeV/c
Track Selection (ϕ)	
TOF	
matching cut	3σ in $r - \phi$ and z directions
PID cut	3σ cut (K) and 2σ veto cut (π, p)
p_{T} cut off	$p_{\mathrm{T}} = 0.3$ - 4 GeV/c
PbSc	
energy cut	ecent > 0.1
PC3 + PbSc matching cut	3σ in $r - \phi$ and z directions
PID cut	3σ cut (K) and 2σ veto cut (π, p) (see Fig. 3.20)
p_{T} cut off	$p_{\mathrm{T}} = 0.3$ - 2 GeV/c

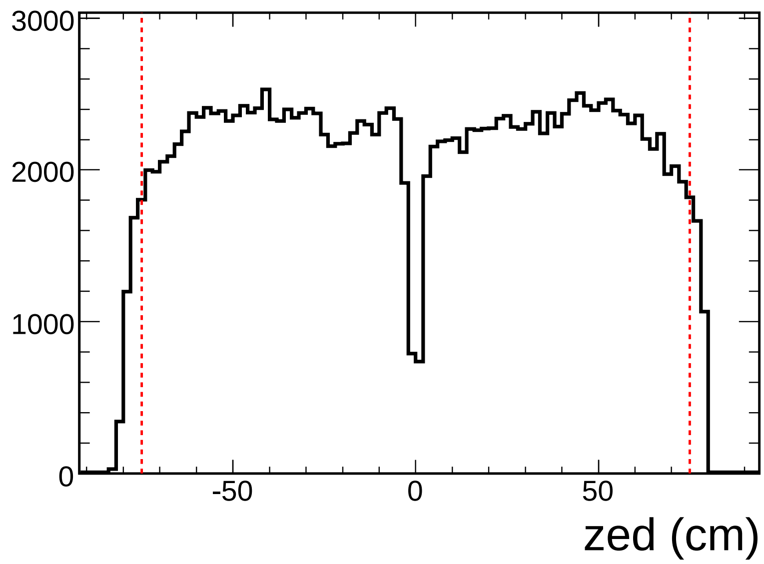

Figure 3.17: *zed* distribution, the z coordinate of the intersection point at DC. Dashed red lines show the z position where $zed = \pm 75$ cm.

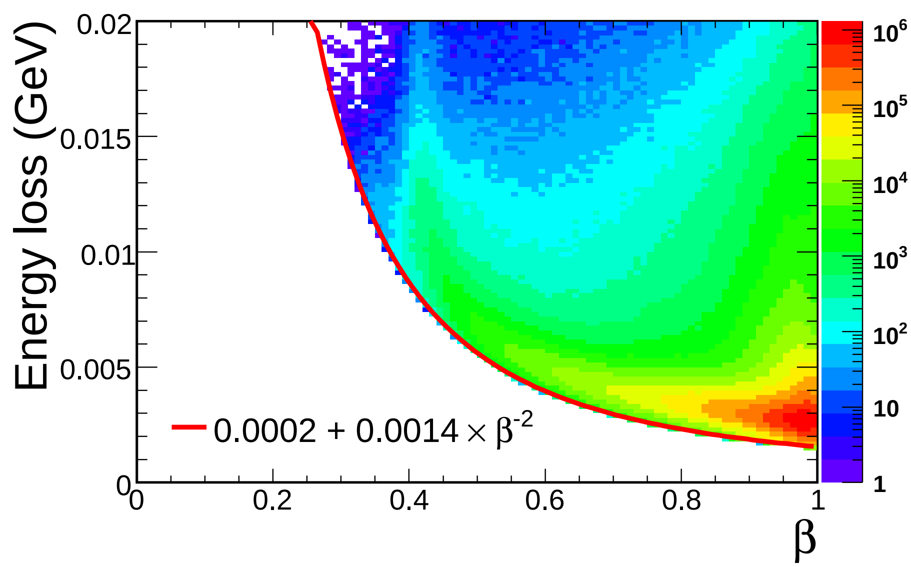

Figure 3.18: Energy loss in TOF scintillators as a function of β. Solid red line shows the energy loss cut, $0.0002 + 0.0014 \times \beta^{-2}$, to remove the background contributions with low energy loss.

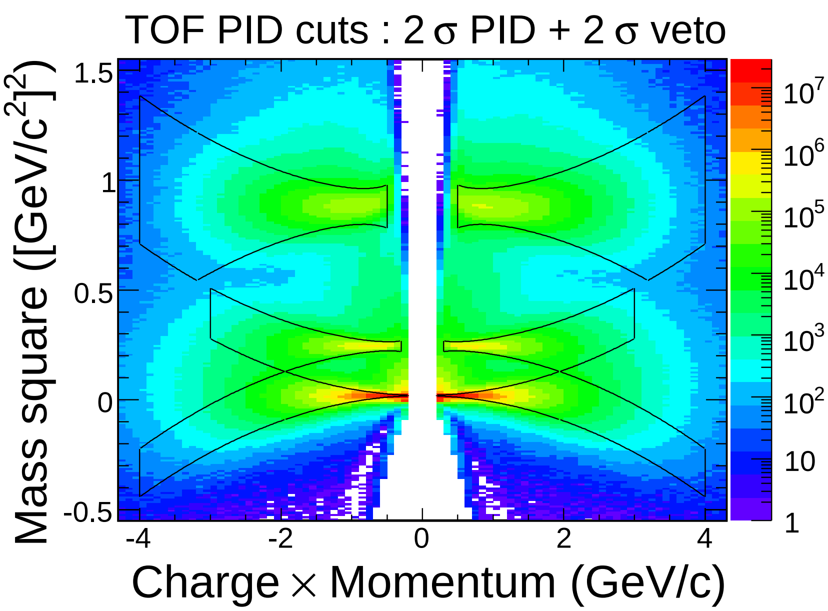

Figure 3.19: Mass square vs charge · momentum. Solid black lines represent the PID cuts for π, K and p (2 σ PID + 2 σ veto cuts).

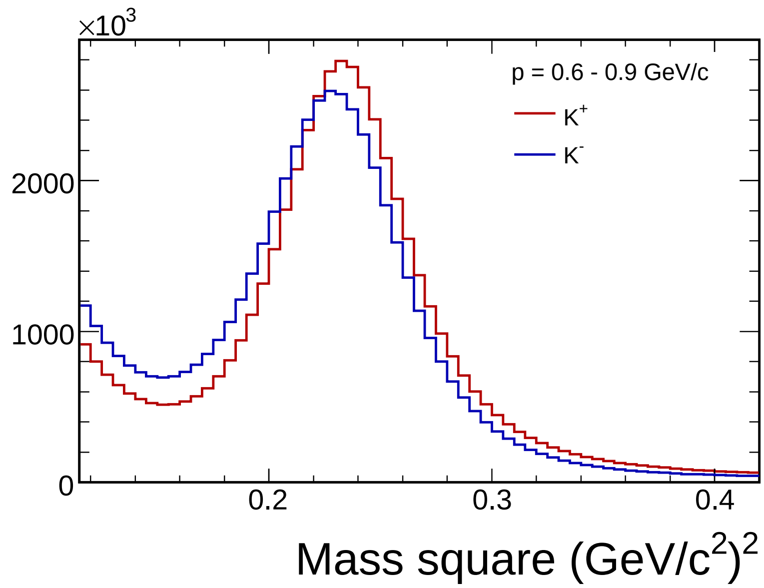

Figure 3.20: Mass square distribution for K^+ (red) and K^- (blue) measured in EMC for $p = 0.6 - 0.9$ GeV/c.

3.6 Extraction of Elliptic flow, v_2

The magnitude of v_2's are obtained with event plane method as introduced in Section 3.2. The azimuthal distributions are measured in central arm ($|\eta| < 0.35$) relative to the event plane measured at BBC ($|\eta| = 3.0 - 3.9$). The finite multiplicity fluctuation lead the dispersion of the event plane, so that the observed v_2's are always smaller than the true v_2 values. We, thererore, need to correct the measured v_2 values with event plane resolution;

$$v_2 = \frac{v_2^{obs}}{\sigma_{EP}} \simeq \frac{\left\langle \cos\left(2[\phi - \Psi_2^{BBC}]\right)\right\rangle}{\sqrt{2\left\langle \cos\left(2[\Psi_2^{BBCS} - \Psi_2^{BBCN}]\right)\right\rangle}} \tag{3.49}$$

where v_2 denote the true v_2 value, v_2^{obs} is the observed v_2, and σ_{EP} is the event plane resolution measured by the correlation between SOUTH and NORTH BBC. As we already discussed in Section 3.2.4, the event plane resolution of BBC can be well approximated by $\sqrt{2\left\langle \cos\left(2\Delta\Psi\right)\right\rangle}$.

In this section, we present the method to extract v_2 for π, K and p (Section 3.6.1), deuterons (Section 3.6.2) and ϕ meson (Section 3.6.3).

3.6.1 Extraction for $v_2(\pi)$, $v_2(K)$ and $v_2(p)$

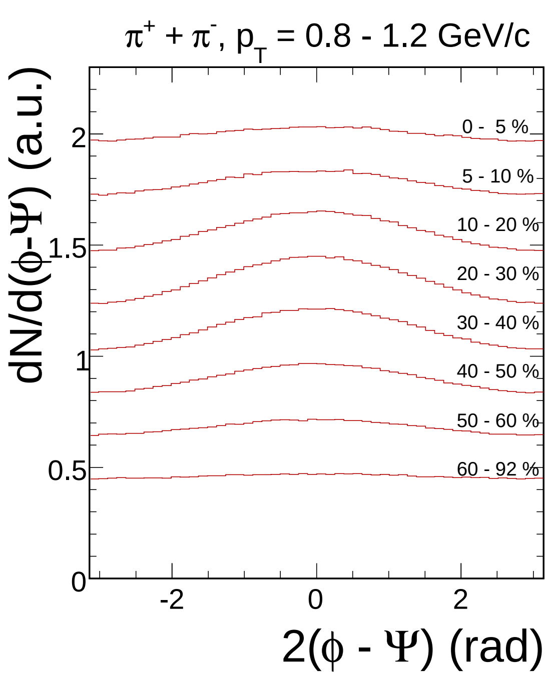

Figure 3.21: Centrality dependence of $dN/d(\phi - \Psi)$ distributions for $\pi^+ + \pi^-$ in p_T = 0.8 - 1.2 GeV/c. Vertical axis is scaled to see the difference of each centrality bin.

Fig. 3.21 shows the centrality dependence of $dN/d(\phi - \Psi)$ distributions for $\pi^+ + \pi^-$ at p_T = 0.8 - 1.2 GeV/c. The measured v_2's are extracted by fitting $dN/d(\phi - \Psi)$

distributions with Fourier expansion of azimuthal distributions;

$$\frac{dN}{d(\phi - \Psi)} = N(1 + 2v_2^{obs} \cos(2(\phi - \Psi_2^{BBC}))) \tag{3.50}$$

where N and v_2^{obs} are free parameters. For $p_T > 2$ GeV/c, π and K start to overlap each other we should consider the contaminations for each particle species. And we also need to take into account the background contribution for $p_T > 3$ GeV/c, arising from the DC tracking. These results and the estimated systematic error will be discussed in the Section 3.7.

3.6.2 Extraction for $v_2(d)$

The following two methods are used to extract deuteron v_2;

- **Subtraction method**
- **Mass square fit method**

The signal extraction in mass square distribution, centrality and p_T dependence of S/B ratio for deuteron are shown below, then we discuss how to extract v_2 from these methods.

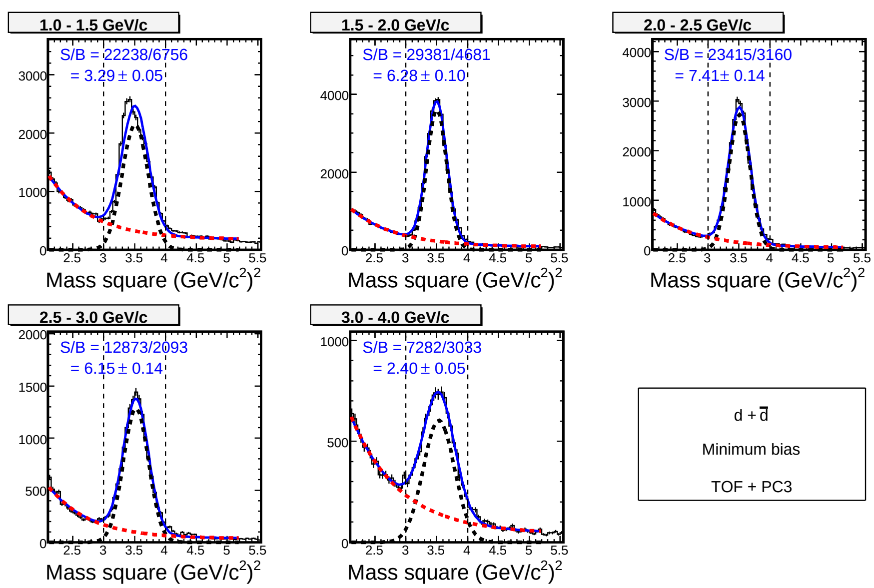

Figure 3.22: Deuteron mass square distribution in minimum bias events. From top to bottom, p_T range is $1.0 - 1.5$ GeV/c, $1.5 - 2.0$ GeV/c, $2.0 - 2.5$ GeV/c, $2.5 - 3.0$ GeV/c, and $3.0 - 4.0$ GeV/c. Solid blue line represent the Gaussian + Exponential function for fitting deuteron peak and background. Dashed red line is the contribution from background, and dashed black line is signal distribution after subtract background contribution.

Fig. 3.22 show mass square distribution of deuteron in minimum bias events with 2 σ TOF + PC3 matching cuts. Signal is extracted by fitting the distribution with gaussian + exponential, then we integrate the yield in $3 < M^2 < 4$ $(\mathrm{GeV}/c^2)^2$.

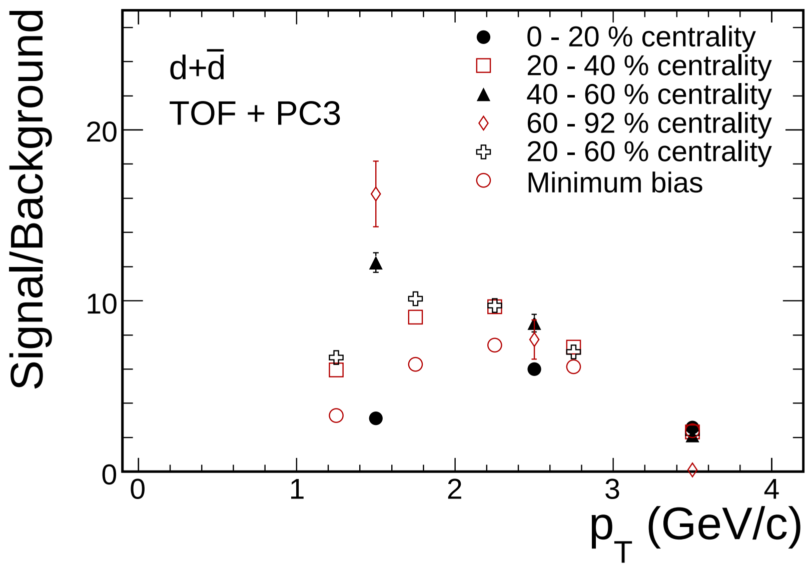

Figure 3.23: Signal to background ratio of deuterons as a function of p_{T} in each centrality.

Signal to background ratio is obtained in each centrality and p_{T} bin, and is shown in Fig. 3.23. The yield of deuterons and S/B ratio are summarized in table 3.3 and used later for calculating signal v_2.

Table 3.3: Summary of centrality dependence of S/B for $d+\bar{d}$

p_{T}	Signal	Background	S/B
centrality 0 - 20 %			
$1 < p_{\mathrm{T}} < 2$ GeV/c	27804 ± 166	8916 ± 94	3.12 ± 0.04
$2 < p_{\mathrm{T}} < 3$ GeV/c	22206 ± 149	3706 ± 60	5.99 ± 0.11
$3 < p_{\mathrm{T}} < 4$ GeV/c	4869 ± 69	1883 ± 43	2.59 ± 0.07
centrality 20 - 40 %			
$1 < p_{\mathrm{T}} < 2$ GeV/c	16131 ± 127	2257 ± 47	7.14 ± 0.16
$2 < p_{\mathrm{T}} < 3$ GeV/c	10723 ± 103	1292 ± 35	8.30 ± 0.24
$3 < p_{\mathrm{T}} < 4$ GeV/c	1957 ± 44	840 ± 28	2.33 ± 0.10
centrality 40 - 60 %			
$1 < p_{\mathrm{T}} < 2$ GeV/c	6203 ± 78	506 ± 22	12.24 ± 0.57
$2 < p_{\mathrm{T}} < 3$ GeV/c	2800 ± 52	322 ± 17	8.69 ± 0.51
$3 < p_{\mathrm{T}} < 4$ GeV/c	432 ± 20	203 ± 14	2.12 ± 0.18
centrality 60 - 92 %			
$1 < p_{\mathrm{T}} < 2$ GeV/c	1237 ± 35	76 ± 8	16.25 ± 1.92
$2 < p_{\mathrm{T}} < 3$ GeV/c	398 ± 19	51 ± 7	7.73 ± 1.15
$3 < p_{\mathrm{T}} < 4$ GeV/c		-	
centrality 20 - 60 %			
$1 < p_{\mathrm{T}} < 2$ GeV/c	22324 ± 149	2787 ± 52	8.01 ± 0.16
$2 < p_{\mathrm{T}} < 3$ GeV/c	13522 ± 116	1628 ± 40	8.31 ± 0.22
$3 < p_{\mathrm{T}} < 4$ GeV/c	2389 ± 48	1062 ± 32	2.25 ± 0.08
Minimum bias			
$1 < p_{\mathrm{T}} < 2$ GeV/c	51462 ± 226	11739 ± 108	4.38 ± 0.04
$2 < p_{\mathrm{T}} < 3$ GeV/c	36149 ± 190	5389 ± 73	6.71 ± 0.10
$3 < p_{\mathrm{T}} < 4$ GeV/c	7282 ± 85	3033 ± 55	2.40 ± 0.05

Subtraction Method

In subtraction method, deuteron v_2 is extracted by the following equations;

$$v_2^{measured} = \frac{Sv_2^d + Bv_2^B}{S+B} = Rv_2^d + (1-R)v_2^B, \qquad R = \frac{S}{S+B} \tag{3.51}$$

$$v_2^d = \left(1 + \frac{B}{S}\right) v_2^{measured} - \frac{B}{S} v_2^B \tag{3.52}$$

where $S(B)$ is the number of deuterons (background) in $M^2 = 3-4$ (GeV/c^2)^2, $v_2^{measured}$ is measured v_2, v_2^B is background v_2 estimated in $1.5-3$ (GeV/c^2)^2 and $4-6$ (GeV/c^2)^2 mass square windows as shown by the shaded yellow area in Fig. 3.24, and v_2^d is deuteron v_2. Measured v_2 is calculated by $\langle \cos 2(\phi_{lab} - \Psi) \rangle$, where ϕ_{lab} is the azimuthal angle of deuterons, Ψ is combined BBC event plane, and bracket denote average over all events and tracks.

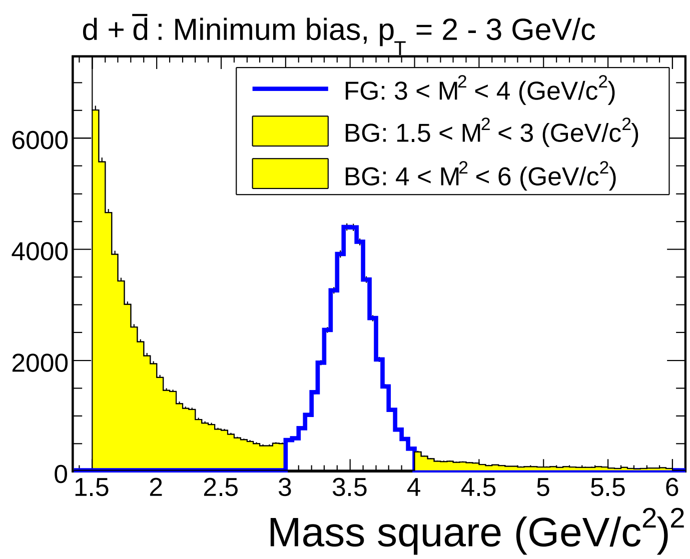

Figure 3.24: Measured deuteron v_2 is calculated in $M^2 = 3-4$ (GeV/c^2)^2 (solid blue line), and background v_2 are estimated in $M^2 = 1.5-3$ (GeV/c^2)^2, and $4-6$ (GeV/c^2)^2 (yellow histograms).

Fig. 3.25 show the centrality dependence of $v_2(d)$. For comparison, $v_2(\pi)$, $v_2(K)$, and $v_2(p)$ are plotted together with $v_2(d)$. In $40-60$ % centrality bin, we cannot estimate the background v_2 values for $M^2 = 4-6$ (GeV/c^2)^2 due to the limited statistics.

Fig. 3.26 shows the deuteron v_2 after subtracting background contributions. Solid black circles and red triangles are extracted by using background v_2 estimated in $M^2 = 1.5-3$ (GeV/c^2)^2 and $4-6$ (GeV/c^2)^2, respectively.

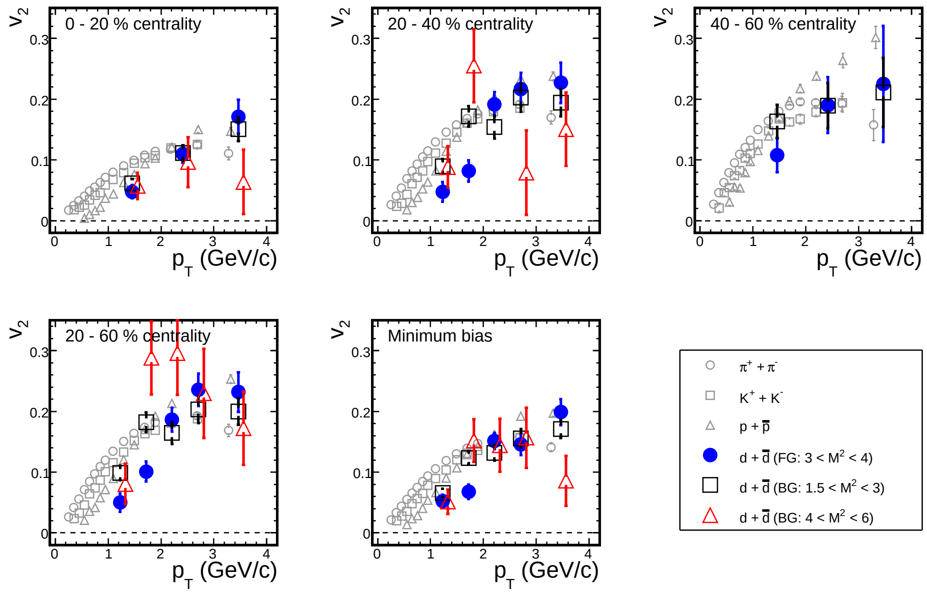

Figure 3.25: Comparison of $v_2(p_T)$ for deuterons by sutraction method in different centrality classes. Solid blue circles represent the measured v_2, open black squares and red triangles are background v_2 estimated in $M^2 = 1.5 - 3$ $(\mathrm{GeV}/c^2)^2$ and $4 - 6$ $(\mathrm{GeV}/c^2)^2$, respectively.

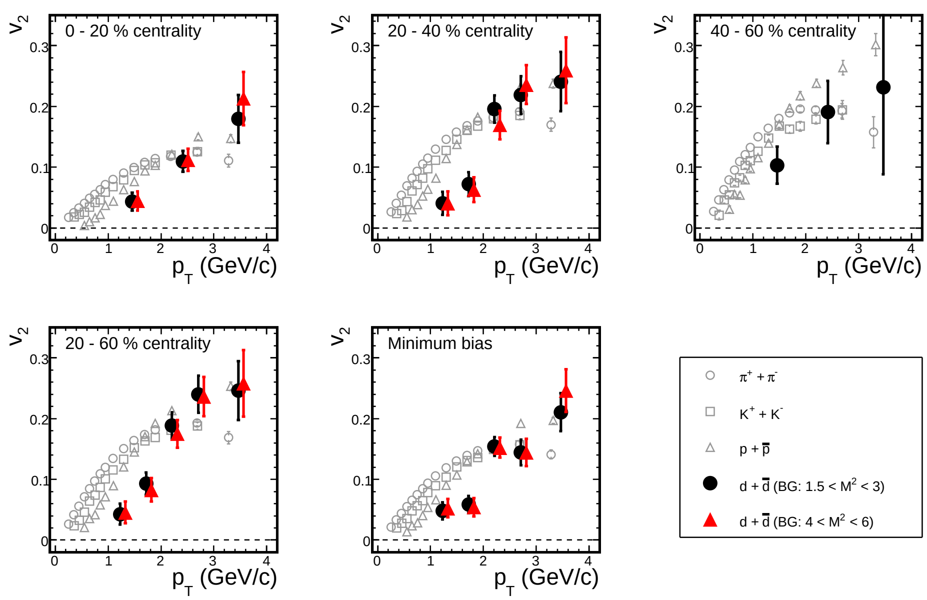

Figure 3.26: Comparison of $v_2^d(p_T)$ by subtraction method in different centrality classes. Solid black circles and red triangles represent the $v_2(d)$ after subtracting the background v_2 which is estimated in $M^2 = 1.5 - 3$ and $4 - 6$ $(\mathrm{GeV}/c^2)^2$, respectively.

Mass Square Fit Method

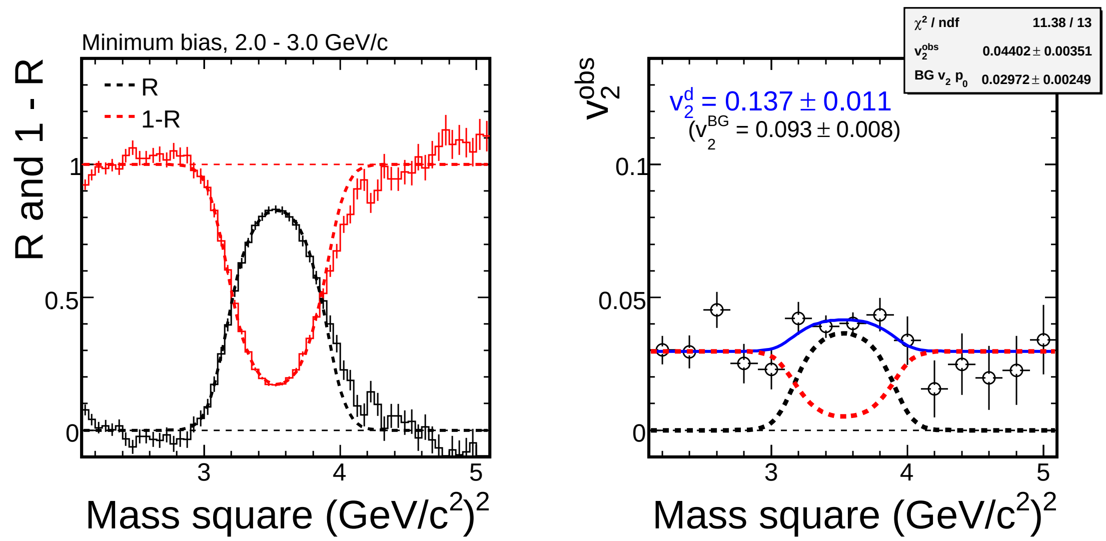

Figure 3.27: (Left) R (black) and $1-R$ (red) as a function of mass square in $2 < p_{\mathrm{T}} < 3$ GeV/c in minimum bias event. (Right) $v_2^{obs} = \left\langle \cos\left(2[\phi_{lab} - \Psi_2^{BBC}]\right)\right\rangle$ as a function of mass square. Blue line shows the fitting result, and black and red dashed line show signal $(S/(S+B) \times v_2^d)$ and background $(B/(S+B) \times v_2^B)$ contribution.

$v_2(d)$ are also measured by simultaneous fitting with both deuteron yield and v_2 as a function of mass square (**Mass square fit method**). In Fig. 3.27, signal (R) and background ratio ($1-R$) are plotted as a function of mass square (left). Right figure shows measured uncorrected v_2 as a function of mass square. We perform fitting by using Eq. (3.51) with fixed deuteron and background yield, which are determined in Fig. 3.27. In this plot, background v_2 (v_2^B) is assumed to be constant over all mass square. We have performed fitting by assuming linear function for background v_2 but the results are unchanged.

Fig. 3.28 shows comparison of deuteron v_2 between subtration method and mass square fit method in different centrality selection. One can see the results of v_2 from two different method is consistent within statistical error bars.

Fig. 3.29 shows comparison of deuteron v_2 from mass square fit method between "TOF + PC3 matching cuts" and "TOF matching cuts only" in different centrality selection. The results are consistent with each other, except for lowerst p_{T} bin.

We choose the results from mass square fit method as final deuteron v_2 since this method takes into account mass square dependent S/B. The systematic error on $v_2(d)$ are estimated from the comparison between different cuts and methods. The evaluated errors are summarized in Section 3.7.3.

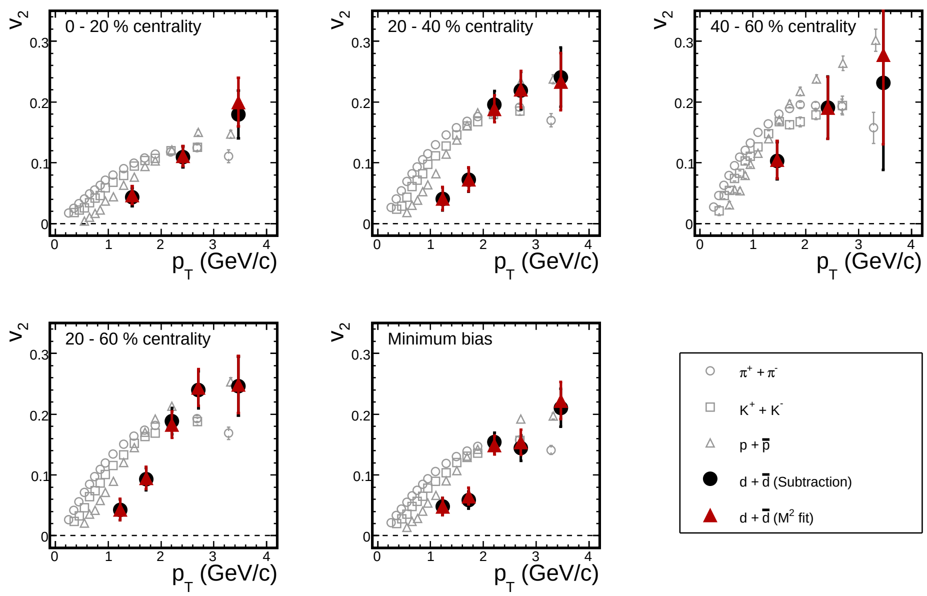

Figure 3.28: Comparison of $v_2^d(p_\mathrm{T})$ between subtraction (black circles) and mass square fit method (red triangles).

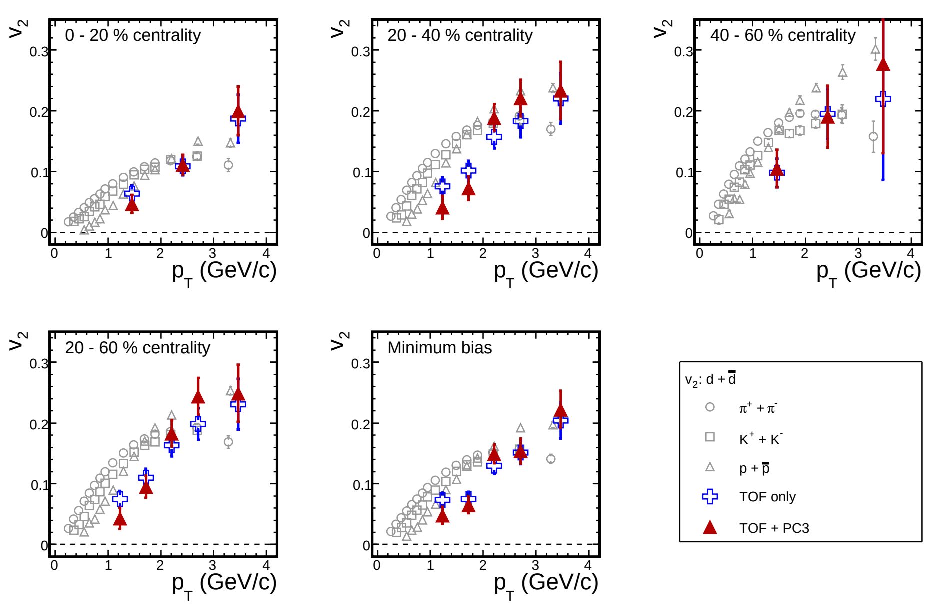

Figure 3.29: Comparison of $v_2^d(p_\mathrm{T})$ between mass square fit method with TOF + PC3 matcing cuts (red triangles) and with TOF matching only (blue crosses).

3.6.3 Extraction for $v_2(\phi)$

Two different techniques are used to extract ϕ meson v_2, which is **Subtraction method**, and **Invariant mass fit method**. We introduce details of these method in following sections, and present the results from both methods.

Event mixing and pair cuts

Event mixing technique is used in order to evaluate the yield of ϕ meson. The following list is the standard event categories to make mixed events with similar global characteristics as real events;

- 20 bins for centrality (5 % step)
- 12 bins for z-vertex (5 cm step)
- 20 bins for event plane ($\pi/20$ step)

Event mixing are not performed across the different runs. Pair cuts are applied to remove ghost tracks in Drift Chamber. Intruder cuts are also used for TOF and PbSc to remove track merging effects. Here is the list of pair cuts.

- $|\Delta zed_{DCH}| > 5.0$ cm, $|\Delta\phi_{DCH}| > 0.03$ rad
- $|\Delta R_{PC1}| > 7$ cm

Pair flow coefficients, $v_n^{\rm pair}$

Recently, N. Borghini *et. al* introduce model independent observables that describe the dependence in azimuth of two particle correlations [45]. According to [45] the probability distribution of a sample of pairs of particles in some range of $p_{\rm T_1}$, $p_{\rm T_2}$, y_1, y_2, $\Delta\phi_{pair} \equiv \phi_2 - \phi_1$ can be written

$$p(\phi_{\rm pair} - \Psi) = \frac{1}{2\pi}\sum_{n=-\infty}^{+\infty} v_n^{\rm pair} e^{in(\phi_{\rm pair}-\Psi)} \tag{3.53}$$

where Ψ is the true (unknown) azimuth of reaction plane in the lab frame, $\phi_{\rm pair}$ is the azimuthal angle of the total transverse momentum $p_{\rm T_1} + p_{\rm T_2}$, and $v_n^{\rm pair}$ is "pair-flow" coefficients defined as $v_n^{\rm pair} = \left\langle e^{-in(\phi_{\rm pair}-\Psi)}\right\rangle$, with the normalization $v_0^{\rm pair} = 1$. Eq. (3.53) can be replaced as

$$p(\phi_{\rm pair} - \Psi) = \frac{1}{2\pi}\left(\sum_{n=-\infty}^{+\infty} [v_{c,n}^{\rm pair}\cos\left(n[\phi_{\rm pair} - \Psi]\right) + v_{s,n}^{\rm pair}\sin\left(n[\phi_{\rm pair} - \Psi]\right)]\right) \tag{3.54}$$

where the real coefficients $v_{c,n}^{\rm pair} = \langle\cos\left(n[\phi_{\rm pair} - \Psi]\right)\rangle$ and $v_{s,n}^{\rm pair} = \langle\sin\left(n[\phi_{\rm pair} - \Psi]\right)\rangle$ are related to the complex $v_n^{\rm pair}$ by the relation $v_n^{\rm pair} = v_{c,n}^{\rm pair} - iv_{s,n}^{\rm pair}$. In the particular case of ϕ meson, symmetry with respect to reaction plane for ϕ_{pair} implies $v_{s,n}^{pair} = 0$, except for experimental baises and fluctuations.

Subtraction Method

In $\phi \rightarrow K^{+} + K^{-}$ analysis, (K^{+}, K^{-}) pairs are sorted into bins of invariant mass m_{inv}, and pair azimuth ϕ_{pair} with respect to the event plane Ψ. Then, $v_2(\phi)$ can be extracted from the following steps;

1. **Count total number of ϕ yield**
   Counts number of ϕ yield in each invariant mass bin ($N_{\phi}(m_{inv})$) after separates it into an uncorrelated part ($N_b(m_{inv})$) centered around the expected mass;

$$N_{\text{pair}}(m_{inv}) = N_{\phi}(m_{inv}) + N_b(m_{inv}) \tag{3.55}$$

   where $N_{\text{pair}}(m_{inv})$ is the number of pairs in each invariant mass bin. Background part is estimated by the event mixing technique. Yield is given by the integral of the correlated part $N_{\phi}(m_{inv})$ over m_{inv}.

2. **Repeat step 1 for each $\phi_{\text{pair}} - \Psi$ bin**

3. **Analyze pair flow coefficients**
   Pair flow coefficients $v_{c,n}^{\phi}$ can be extracted by fitting the azimuthal distribution of ϕ by the Eq. (3.50)

Invariant mass distributions are shown in Fig. 3.15 and 3.16 (see Section 3.4.3). Extracted yield of ϕ meson are plotted for each $\phi_{pair} - \Psi$ bins, then we fit the distribution by the Fourier expansion of azimuthal distributions in Eq. (3.50). The extracted $\Delta\phi_{pair}$ distribution is plotted in Fig. 3.30 Dashed black lines are fitting results by Eq. (3.50).

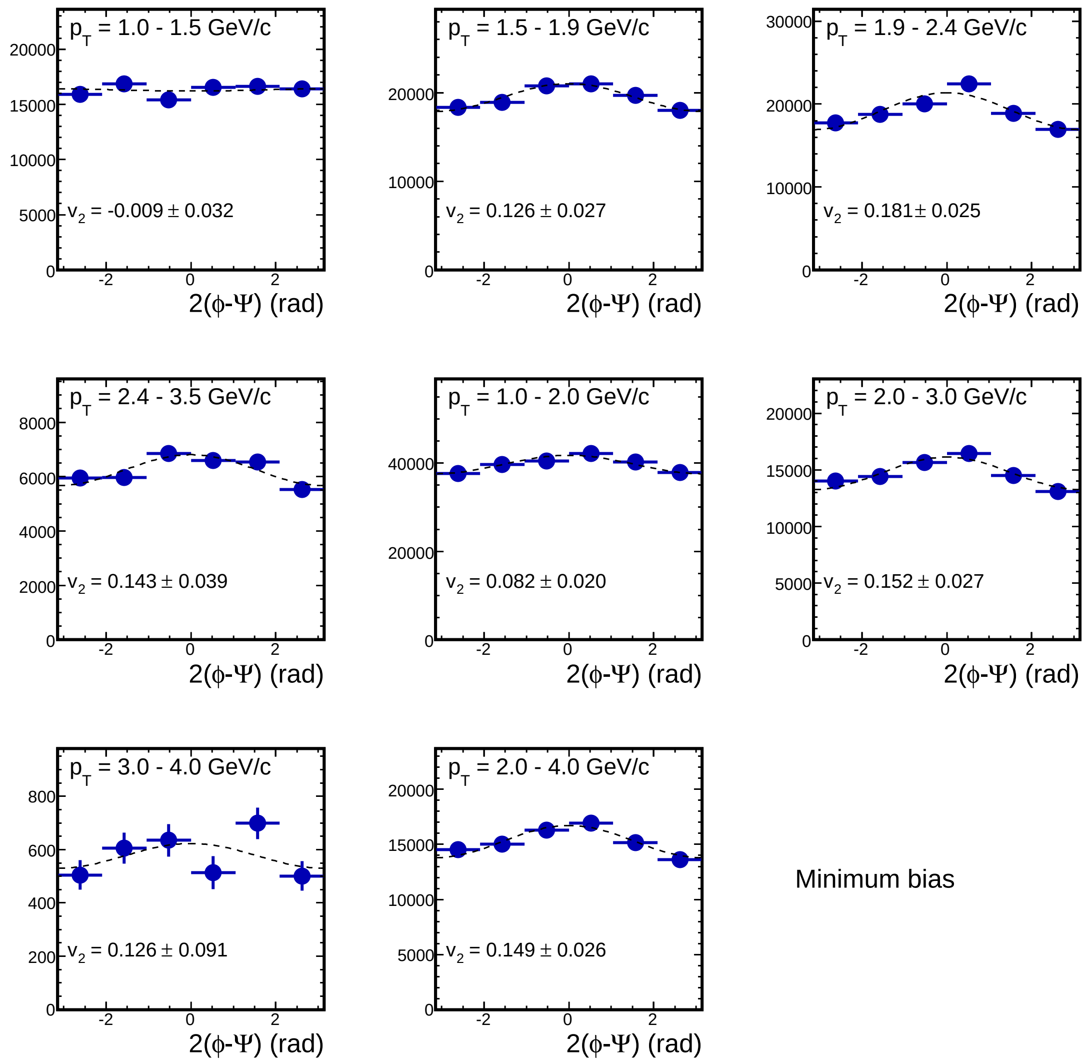

Figure 3.30: Extracted $\Delta\phi_{pair}$ distribution of ϕ mesons for different p_{T} selection minimum bias event. These are fitted by the Eq. (3.50), which is shown by the dashed black lines in the figure.

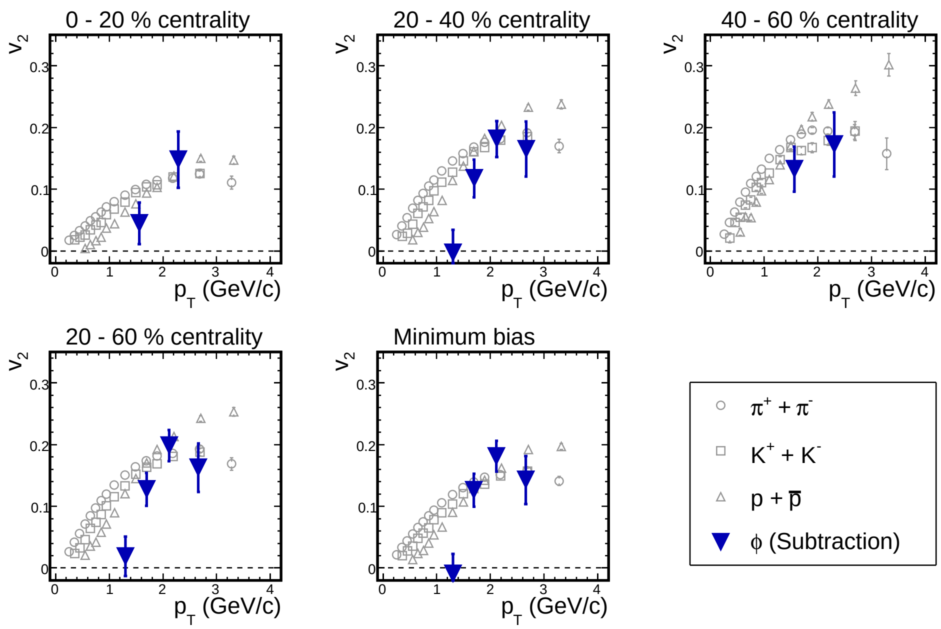

Figure 3.31: Extracted $v_2(\phi)$ as a function of p_{T} in different centrality classes by subtraction method.

Invariant Mass Fit Method

In subtraction method, the decomposition between the background and the peak is performed independently for several bins (typically, $10-20$) in $\phi_{\mathrm{pair}} - \Psi_{BBC}$. But in invariant mass fit method, the decomposition is only performed twice. First step is exactly same as step 1 in subtraction method except for not need to separate $\phi_{\mathrm{pair}} - \Psi_{BBC}$ bins. Next step is analyzing pair flow coefficients from the Eq. (3.56);

$$\begin{aligned} N_{\mathrm{pair}}(m_{inv})v_{c,n}(m_{inv}) &= N_b(m_{inv})v_{c,n}^{(b)}(m_{inv}) + N_\phi(m_{inv})v_{c,n}^{\phi} \\ N_{\mathrm{pair}}(m_{inv})v_{s,n}(m_{inv}) &= N_b(m_{inv})v_{s,n}^{(b)}(m_{inv}) + N_\phi(m_{inv})v_{s,n}^{\phi} \end{aligned} \tag{3.56}$$

As we mentioned in 3.6.3, $v_{s,n}^{pair} = 0$ if there are no experimental biases and flucutuations. If the background consists of uncorrelated particles, one also has $v_{s,n}^{(b)} = 0$. These can be used for checking the validity of the procedure.

Fig. 3.32 show invariant mass distribution, ratio of signal (S) and background yield (B) to total yield ($S + B$), and measured v_2. $v_{s,2} = \left\langle \sin\left(2[\phi_{pair} - \Psi_2^{BBC}]\right)\right\rangle$ (pink traiangles) is also plotted in bottom figure. One can see that $v_{s,2}$ is zero for the mass window we are interested in. We perform the fitting by using Eq. (3.56), which is shown by black line in the figure. Background v_2 is assumed to be second polynominal function, i.e. $v_2^b = p_0 + p_1 m_{inv} + p_2 m_{inv}^2$. The shape of $S/(S+B)$ and $B/(S+B)$ are fixed, thus, number of free parameters for the fitting is 4, one is for measured v_2, and others (p_0, p_1, p_2) are for background v_2.

The results are shown in Fig. 3.33 after repeated the fitting for each (p_{T}, centrality) bins. Results from subtraction method are also plotted for comparison, and both results

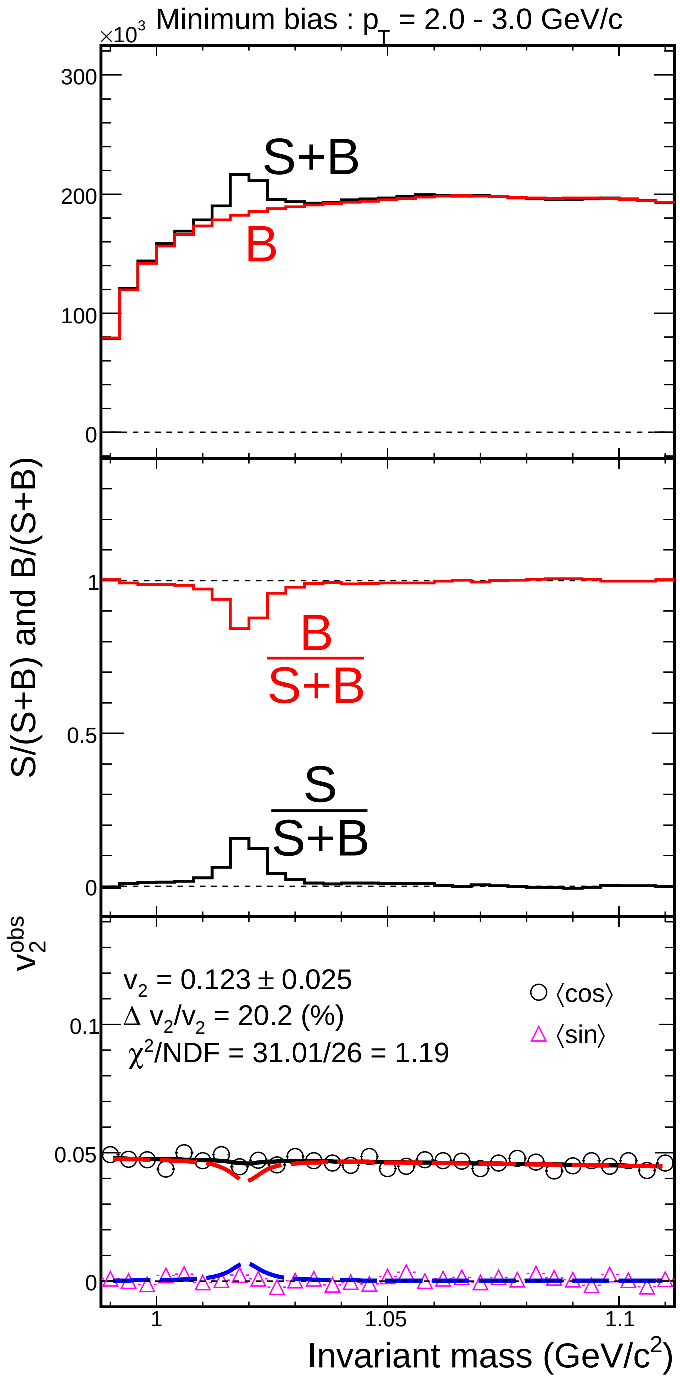

Figure 3.32: Top: Invariant mass distribution for $p_{\mathrm{T}} = 2 - 3$ GeV/c in minimum bias event. Middle: The ratio $S/(S + B)$ (black) and $B/(S + B)$ (red) vs invariant mass. Bottom: measured v_2 $(= \langle \cos(2[\phi_{pair} - \Psi_2^{BBC}]) \rangle)$ vs invariant mass. Black line shows the fitting result by Eq. (3.56). Red and blue line show the signal and background contributions from the fitting result.

are in good agreement within the statistical error bars.

For the stability check of invariant mass fit method, we perform fitting the following conditions;

- Fit background v_2 by linear function (default is quadratic function)
- Fit v_2 in $m_{inv} = 0.99 - 1.2$ GeV/c^2 (default is $m_{inv} = 0.99 - 1.1$ GeV/c^2)
- Fit v_2 by using histogram of $S/(S+B)$ and $B/(S+B)$ (default is Breit-Wigner + constant function)

The results are shown in Fig. 3.34. Largest difference of default invariant mass fit method is coming from subtraction method. The deviation from default fitting method is included in the final systematic error (see Section 3.7).

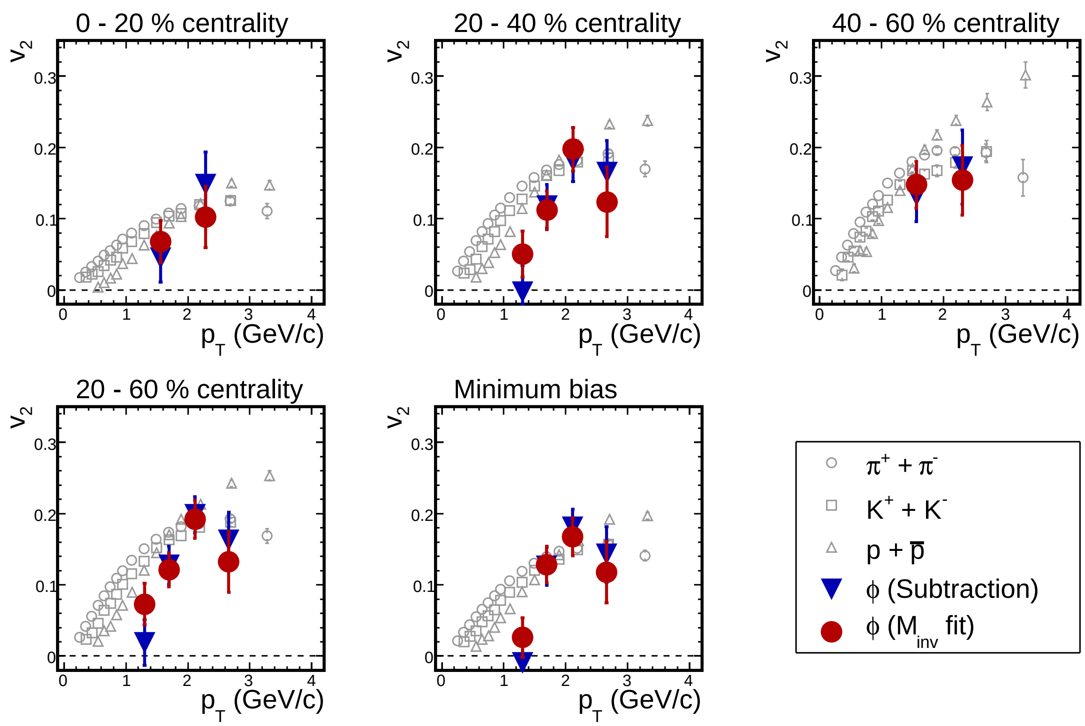

Figure 3.33: Centrality dependence of ϕ meson $v_2(p_T)$ by invariant mass fit method.

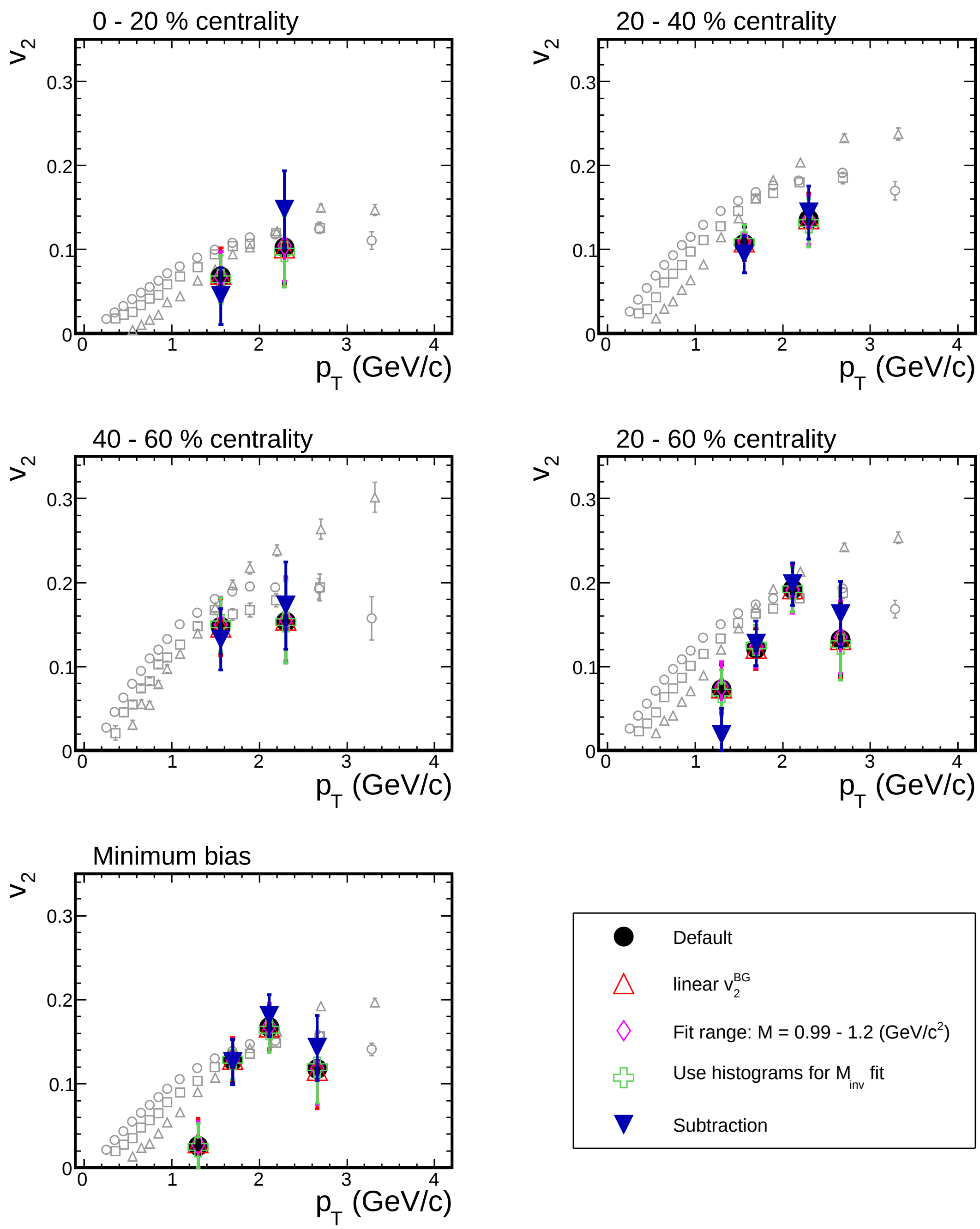

Figure 3.34: Comparison of $v_2(p_T)$ extracted by invariant mass fit method and subtraction method. Solid black circles are default invariant mass fit method, open red triangles are fit method with linear background v_2, open pink rhombus are fit method with $m_{inv} = 0.99 - 1.2$ GeV/c, open green crosses are fit method with histograms of S/B ratio, and solid blue triangles are subtraction method.

3.7 Systematic Uncertainties

3.7.1 Systematic error of BBC event plane

Table 3.4: Summary of systematic error of BBC event plane

Centrality	σ_{EP}	$\sigma_{Flat.procedure}$	$\sigma_{Flat.coefficient}$	σ_{Run}	Total
$0-5$ %	10 %	17 %		1.9 %	20.4 %
$5-10$ %	2.1 %	11 %		1.9 %	12.4 %
$10-15$ %	3.3 %	4 %		0.8 %	7.2 %
$15-20$ %	3.5 %	2 %		0.8 %	6.5 %
$20-30$ %	3.2 %	1 %	5 %	0.5 %	6.0 %
$30-40$ %	2.5 %	1 %		0.6 %	5.7 %
$40-50$ %	1.2 %	1 %		1.3 %	5.4 %
$50-60$ %	1 %	2 %		2.1 %	5.9 %
$60-92$ %	2 %	13 %		7.6 %	16.0 %
$0-10$ %	3.9 %	17 %		1.9 %	18.2 %
$10-20$ %	3.2 %	4 %		1.9 %	7.4 %
$0-20$ %	2.1 %	4 %		1.0 %	6.8 %
$20-40$ %	3.0 %	1 %	5 %	0.3 %	5.9 %
$40-60$ %	1 %	2 %		1.3 %	5.6 %
$20-60$ %	2.9 %	2 %		0.5 %	6.1 %
$0-50$ %	2.2 %	2 %		0.5 %	5.8 %
Minimum bias	2.3 %	3 %		0.8 %	6.3 %

Systematic error of BBC event plane are summarized in Table 3.4. We evaluate the systematic error from (1) comparison of v_2 with respect to the different BBC event plane, such as BBC SOUTH, NORTH, and combined SOUTH + NORTH plane (σ_{EP}), (2) comparison of v_2 for different flattening procedure ($\sigma_{Flat.procedure}$), (3) comparison of v_2 for different number of flattening coefficients ($\sigma_{Flat.coefficient}$), and (4) comparison of v_2 for several Run group (σ_{Run}).

Fig. 3.35 show the $\langle v_2 \rangle$ as a function of centrality for different choice of BBC event plane. We estimate the systematic error from the difference between SOUTH, NORTH and combined plane for each centrality bin.

Fig. 3.36 shows the $\langle v_2 \rangle$ as a function of centrality for different flattening procedure in Run2 [46]. In Run2, we have performed the BBC event plane calibration by (1) Ring by ring gain correction, (2) Re-centering of flow vector by using measured average cosine and sine, and (3) Higher order fourier flattening. This procedure is denoted as **standard** in Fig. 3.36. In **modified** flattening procedure, instead of performing step 2 we remove the special 4 PMT's from each BBC in order to make event plane resolution uniform in azimuthal direction. More details can be found in [46], section 1.

The error $\sigma_{Flat.coefficient}$ comes from the fact that current calibration constants for event plane are not good enough to make event plane flat. This is because the calibration

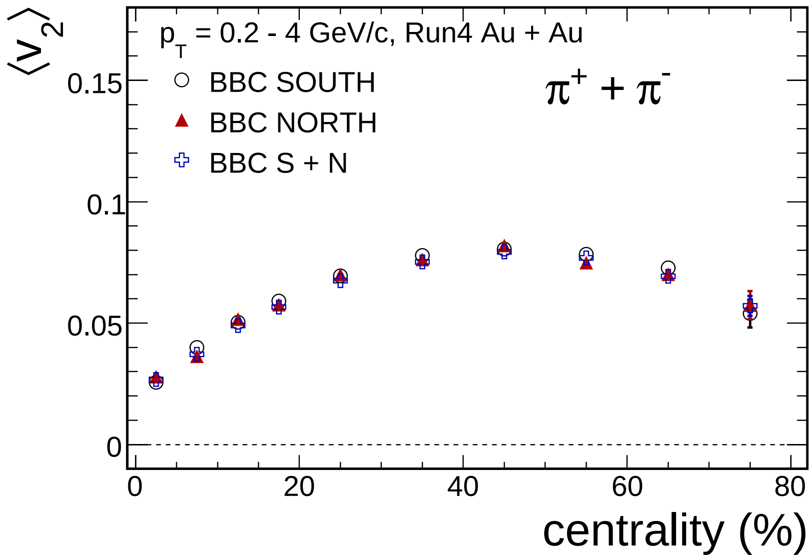

Figure 3.35: Average v_2 as a function of centrality for $\pi^+ + \pi^-$. Integration is performed in $0.2 < p_{\mathrm{T}} < 4$ GeV/c. Open circles show v_2 with BBC SOUTH event plane, solid triangles are NORTH plane, and open crosses are combined SOUTH and NORTH event plane.

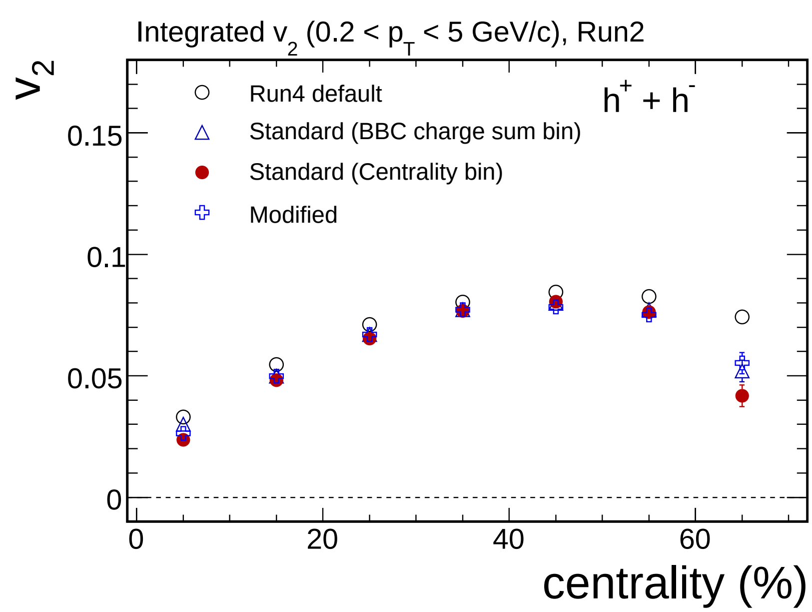

Figure 3.36: Average v_2 as a function of centrality for non-identified hadrons. Integration is performed in $0.2 < p_{\mathrm{T}} < 5$ GeV/c. See text and [46] for the details of flattening procedure.

was done for relatively smaller data sets ($\sim$ 300 k events for each run). We compare the result between current calibration constants in data base and improved flattening calibration by David Winter, which is done by using entire data sets. We find that 5 % difference of v_2 for non-identified charged hadrons almost independent on centrality.

Fig. 3.37 shows the comparison of v_2 for different run group with improved flattening corrections as we mention in previous paragraph. We divide Run-4 data sets into 8 group to see any difference between them. Each group has approximately 100 M event except for group 7 ($\sim$ 50 M event). Run range is listed below for each group;

- Group 0 : $109189 < \mathrm{RUN} < 112124$
- Group 1 : $112128 < \mathrm{RUN} < 114927$
- Group 2 : $114929 < \mathrm{RUN} < 116425$
- Group 3 : $116427 < \mathrm{RUN} < 117297$
- Group 4 : $117303 < \mathrm{RUN} < 118024$
- Group 5 : $118028 < \mathrm{RUN} < 119440$
- Group 6 : $119448 < \mathrm{RUN} < 120416$
- Group 7 : $120419 < \mathrm{RUN} < 122223$

The systematic error is about $1-2$ % for $0-60$ %, and 8 % for $60-92$ % centrality bin.

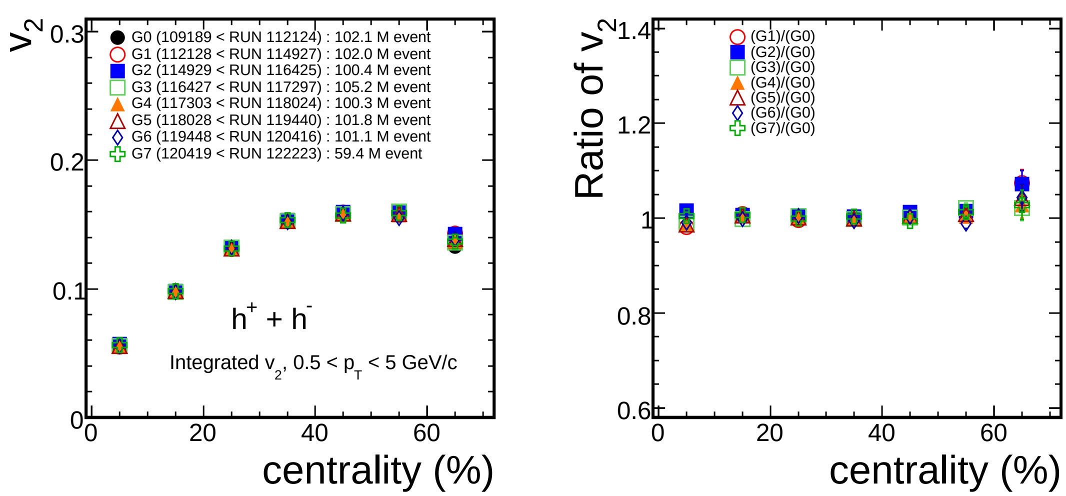

Figure 3.37: (Left) Average v_2 for charged hadrons as a function of centrality. Integrated p_{T} range is $0.5-5$ GeV/c. We divide entire data sets to 7 run groups, G0$-$G7 in order to see the stability of v_2. (Right) The ratio of $\langle v_2 \rangle$ as a function of centrality for several run groups.

3.7.2 Systematic error on $v_2(\pi)$, $v_2(K)$, and $v_2(p)$

The source of systematic error on v_2 for π, K, and p are evaluated from: (1) Cut criteria, (2) Feed down effect on proton v_2 (upper systematic error, see the section below) (3) Background (upper systematic error), and (4) Mis-identification of particles.

Systematic error of cut criteria

We have studied v_2 by changing several cuts, such as matching cut, PID cut, and energy loss cut, in reasonable range to see the effect of each cut. We finally found that the difference of v_2 from each cut is about 1 %, thus total systematic errors from the cut criteria is $\sqrt{0.01^2 \times 3} \sim 1.7$ %.

Systematic error of feed down effect on proton v_2

We have done very detailed study of feed down effect on proton v_2. The effect of feed down from Λ decay has been studied by assuming that the observed proton v_2 is composed of v_2 for direct protons with that for protons from Λ feed down. We further assume that the v_2 for direct proton is equal to that for protons. The v_2 for protons from Λ feed down has been estimated by decay kinematics with measured Λ transverse momentum spectra and v_2. Since the decay protons has smaller p_{T} compared to the original Λ and the magnitude of v_2 is approximately proportioanl to ${p_{\mathrm{T}}}^2$ for baryons, v_2 for decay protons is always larger than that of measured protons. Thus, we only add the upper systematic error from Λ feed down. We found that the effect of feed down on proton v_2 is about 11 % independent on p_{T}, up to 1.5 GeV/c. For $p_{\mathrm{T}} > 1.5$ GeV/c, the contribution of v_2 from Λ feed down is negligible.

Systematic error of background contribution

From the analysis for charged hadron transverse momentum spectra [48], background contribution was found to be dominant in high p_{T} ($p_{\mathrm{T}} \geq 4-5$ GeV/c). Below $p_{\mathrm{T}} = 3$ GeV/c, the background contribution is very small (~ 1 %) in charged hadron v_2 analysis. However, for $4 < p_{\mathrm{T}} < 5$ GeV/c ($p_{\mathrm{T}} > 5$ GeV/c), we found that 8 % (17 %) correction is needed from background contributions [47]. We study background contribution for π, K, p separately since the background contribution and those v_2 might be different for different particle species. The procedure how to extract the signal v_2 is similar to that in [47], i.e.

1. Fitting ΔR distribution by Gaussian + 2^{nd} polynominal, and then fix the shape of signal and background ($\Delta R \equiv \sqrt{(\Delta\phi)^2 + (\Delta z)^2}$).

2. Fit v_2 vs ΔR by Eq. (3.57), and extract v_2^S

$$v_2^{measured} = \frac{N_S v_2^S + N_B v_2^B}{N_S + N_B} \tag{3.57}$$

$$v_2^S = \frac{N_S + N_B}{N_S} v_2^{measured} - \frac{N_B}{N_S} v_2^B \tag{3.58}$$

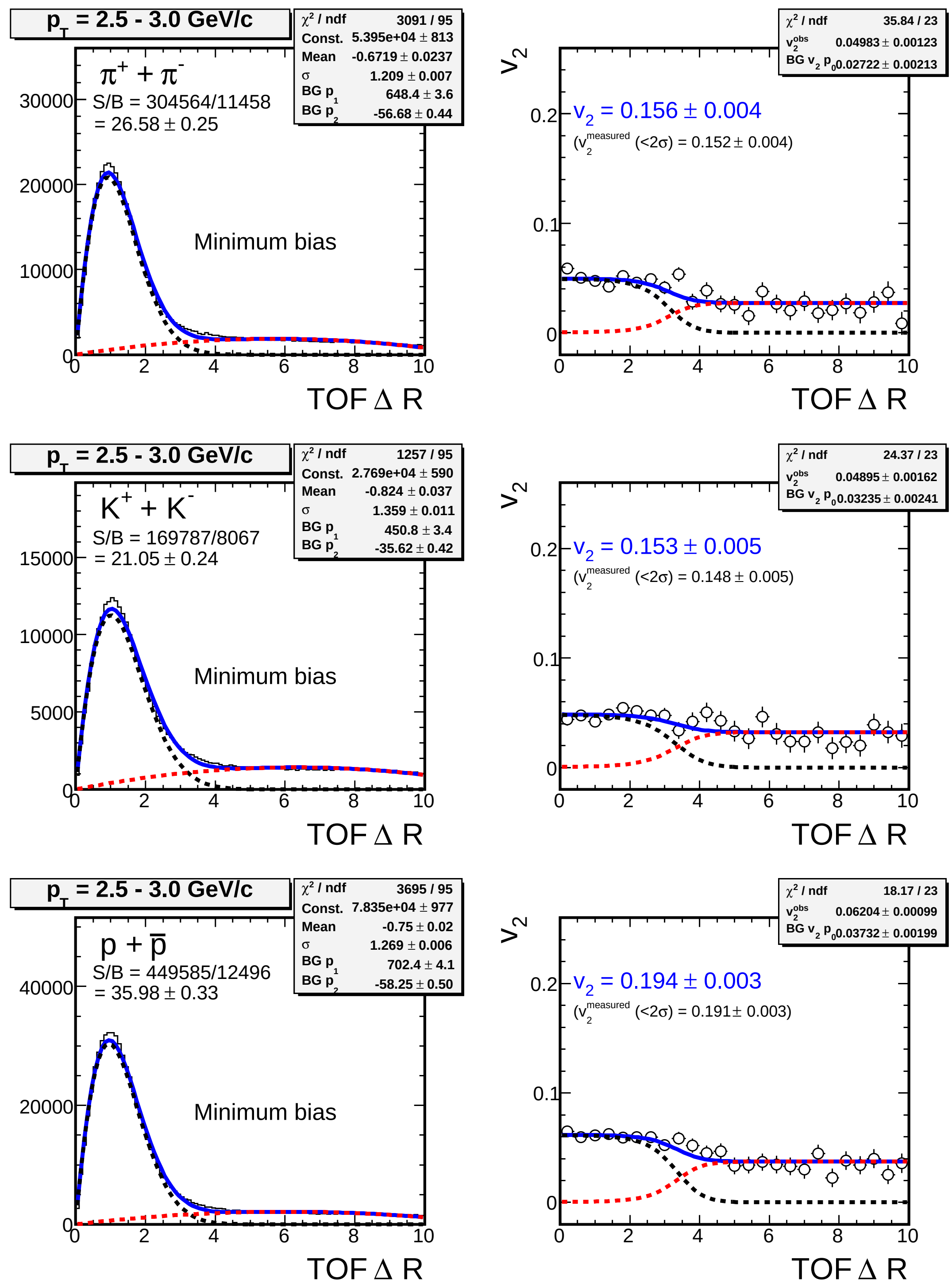

Figure 3.38: (Left) TOF ΔR distribution for π (top), K (middle), and p (bottom) at $p_{\rm T} = 2.5 - 3$ GeV/c in minimum bias event. Solid blue lines represent the fitting result, and dashed black (red) lines are signal (background) contribution. (Right) Measured v_2 vs ΔR for π, K, and p. Solid blue lines are the result of fitting by Eq. (3.57). Dashed black (red) lines are $v_2^S \times N^S/(N^S + N^B)$ ($v_2^B \times N^B/(N^S + N^B)$).

Fig. 3.38 demonstrates v_2 extraction from ΔR distribution. We confirm that the result are unchanged by using the different background shape, such as 3^{rd} or 4^{th} polynominal, for the fitting of ΔR and v_2.

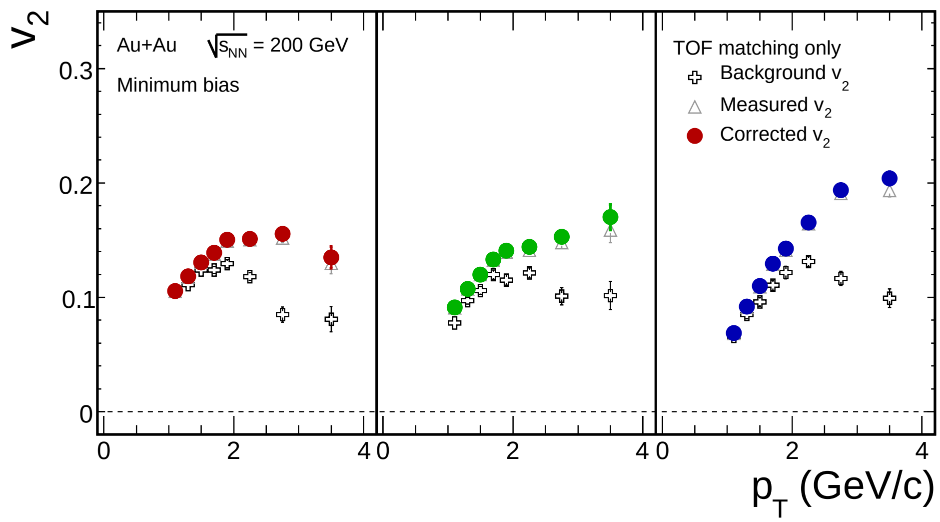

Figure 3.39: v_2 as a function of p_{T} in minimum bias event for π, K, and p. Open triangle is background v_2 (v_2^B), open cross is measured v_2 ($v_2^{measured}$), and solid circle is corrected v_2 (v_2^S).

Fig. 3.39 show the result of v_2 with background correction for π, K, and p. Since the background v_2 is usually smaller than observed v_2 due to the smearing of track or random association, corrected v_2 become larger than measured v_2. One can see such a trend for all particles species in the measured p_{T} range. Thus, we take upper systematic error from background contributions.

Fig. 3.40 shows the systematic error of background contribution as a function of p_{T} in different centrality bins. Systematic error is larger in higher p_{T} bin as we expected, but the magnitude of error is relatively smaller than that of non-identified hadrons. This is mainly because S/B ratio is enhanced by requiring the particle identification in TOF.

Table 3.5 shows the summary of systeamtic error of background contribution for π, K, and p.

Systematic error of mis-identification

It is important to understand the contribution of mis-identified particles, especially for higher p_{T}. Because of the finite timing resolution particles become overlapping each other for high p_{T} in mass square. For example, π and K cannot be well separated for $p_{\mathrm{T}} > 2$ GeV/c.

Fig. 3.41 demonstrates how to evaluate the yield of contamination for each particle species in minimum bias events. We perform fitting the mass square distribution by (3+1) gaussian, where the extra gaussian is used for background. Then we compare

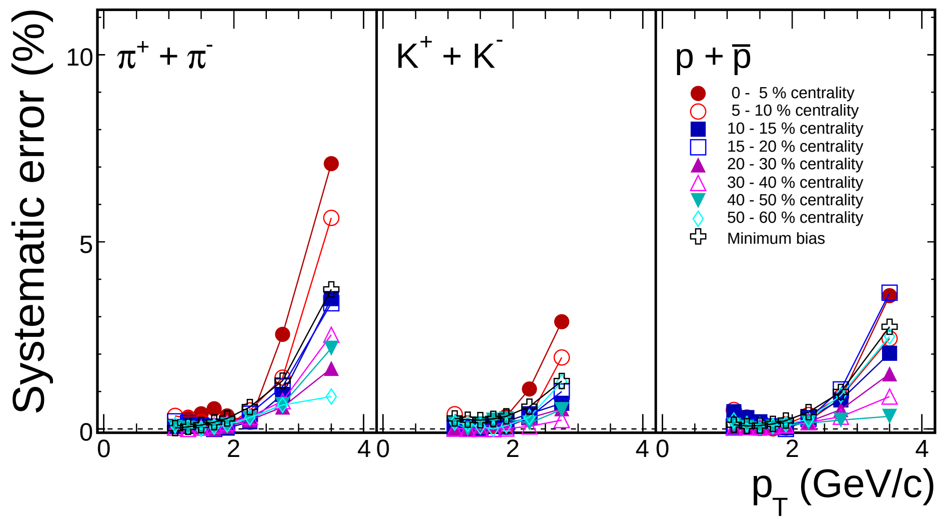

Figure 3.40: Systematic error from background contribution for $\pi^+ + \pi^-$ (left), $K^+ + K^-$, $p + \bar{p}$ in $0 - 60$ % centrality bin, and minimum bias.

Table 3.5: Summary of background systematic error for π, K and p. In $p_{\mathrm{T}} = 2 - 2.5$ GeV/c, 1 % systematic error is added for π, K and p.

	π		K	p	
	p_{T}(GeV/c)				
centrality (%)	2.5 - 3	3 - 4	3 - 4	2.5 - 3	3 - 4
0 - 5 %	3 %	7 %	3 %	1 %	4 %
5 - 10 %	1 %	6 %	2 %	1 %	2 %
10 - 15 %	1 %	4 %	1 %	1 %	2 %
15 - 20 %	1 %	3 %	1 %	1 %	4 %
20 - 30 %	1 %	2 %	1 %	1 %	2 %
30 - 40 %	1 %	3 %	1 %	1 %	1 %
40 - 50 %	1 %	2 %	1 %	1 %	1 %
50 - 60 %	1 %	1 %	1 %	1 %	3 %
60 - 92 %	1 %	21 %	1 %	2 %	3 %
0 - 10 %	2 %	7 %	3 %	1 %	3 %
10 - 20 %	1 %	4 %	1 %	1 %	3 %
0 - 20 %	2 %	5 %	2 %	1 %	4 %
20 - 40 %	1 %	2 %	1 %	1 %	1 %
40 - 60 %	1 %	2 %	1 %	1 %	1 %
20 - 60 %	1 %	2 %	1 %	1 %	1 %
0 - 50 %	1 %	4 %	2 %	1 %	3 %
Minimum bias	1 %	4 %	1 %	1 %	3 %

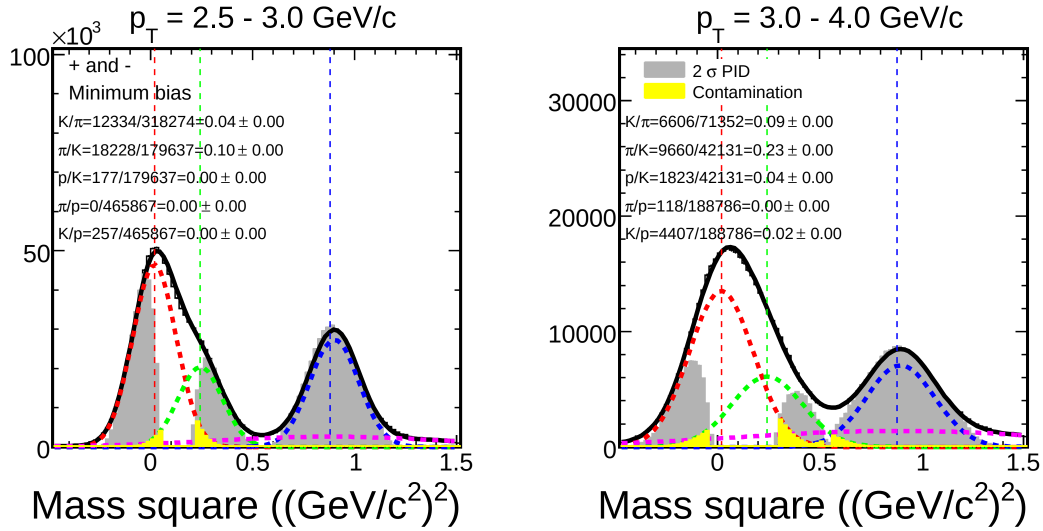

Figure 3.41: Mass square distribution for $p_{\mathrm{T}} = 2.5 - 3$ GeV/c (left), and $p_{\mathrm{T}} = 3 - 4$ GeV/c (right) in minimum bias event. Solid black line shows fitting result by 4 gaussian (3 for π, K and p, 1 for background). We perform fitting by fixing mean value of π, K, p mass square, and constrain σ to the expected width in the measured p_{T} range. Dashed red, green, blue lines are the contribution of each π, K, and p. Shaded grey histograms show the yield of each particle with 2 σ PID cuts. The yellow histograms are the contamination for each particle.

;

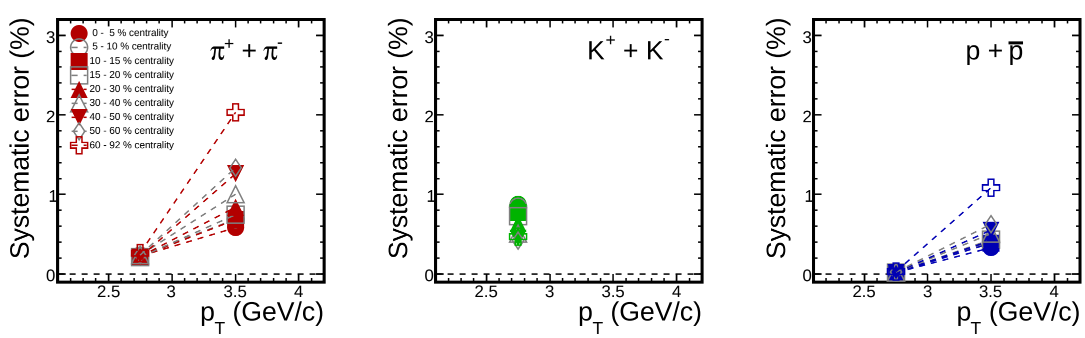

Figure 3.42: Systematic error from mis-identification for $\pi^{\pm}$ (left), $K^{\pm}$ (middle) and $p(\bar{p})$ (right) in each centrality bin.

extracted gaussian of each particle species (dashed line in the figure) with measured particles with 2 σ PID cuts (grey histograms), and evaluate the contamination (yellow histograms). The contribution from contamination are negligible below 2.5 GeV/c, so we do not take into account the systematic error below that p_{T} range. The contamination for each particle species are evaluated for each centrality bin.

The systematic error on v_2 from the contribution of contaminations are mostly centrality independent and the magnitude of errors are 1 % for 0 − 60 % centrality bins, and 2 % for 60 − 92 % (see Fig. 3.42).

3.7.3 Systematic error on v_2 for $d + \bar{d}$, and ϕ

Systematic error on v_2 for $d + \bar{d}$

Fig. 3.43 shows the ratio of v_2 for deuterons as a function of p_{T} from different method and cuts. The sysyetematic error values are calculated for each (p_{T}, centrality) bin by taking the quadratic sum of deviation of v_2 value.

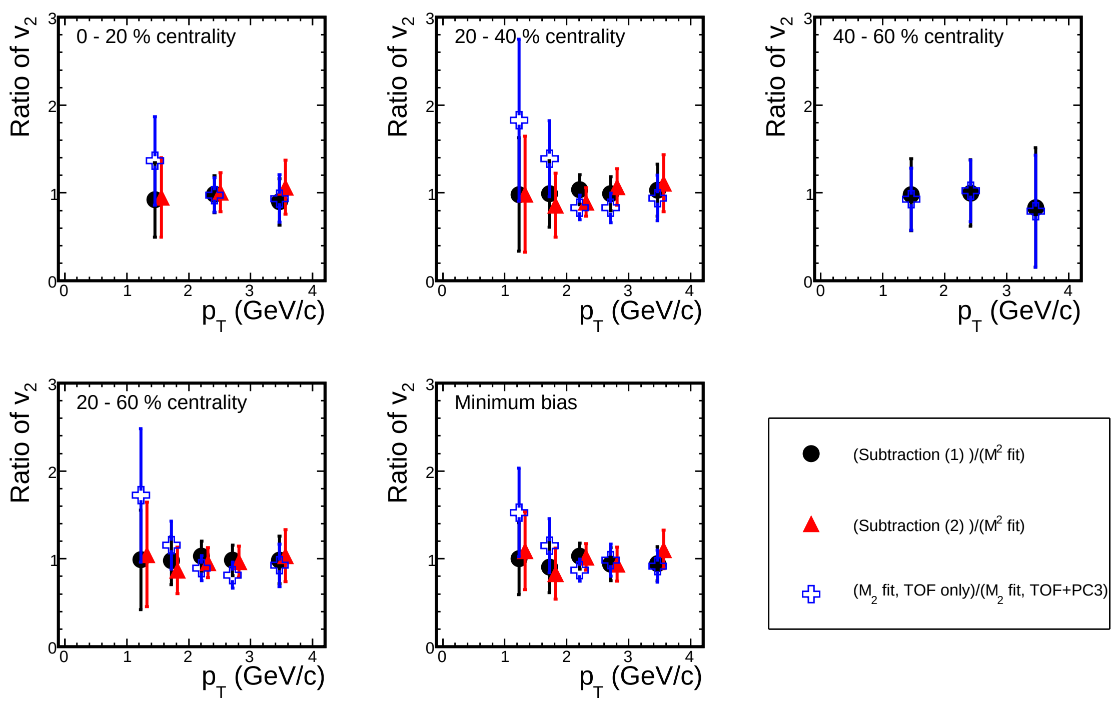

Figure 3.43: The ratio of v_2 for deuterons as a function of p_{T} for different centrality bins. The denominator is v_2 values from mass square fit method with TOF + PC3 matching cuts.

Systematic error on v_2 for ϕ

The systematic error on ϕ meson v_2 are estimated from Fig. 3.34 and summalized in Table 3.7.

Table 3.6: Summary of the relative systematic error on $d + \bar{d}$ v_2 for each (p_{T}, centrality)

centrality (%)	p_{T} (GeV/c)				
	1 - 1.5	1.5 - 2	2 - 2.5	2.5 - 3	3 - 4
0 - 20 %	37.7 (%)		3.0 (%)		13.7 (%)
20 - 40 %	82.9 (%)	41.4 (%)	20.0 (%)	18.4 (%)	12.9 (%)
40 - 60 %	7.4 (%)		2.4 (%)		26.8 (%)
20 - 60 %	72.4 (%)	20.3 (%)	11.9 (%)	19.1 (%)	8.3 (%)
Minimum bias	53.4 (%)	24.4 (%)	13.7 (%)	8.8 (%)	14.5 (%)

Table 3.7: Summary of the relative systematic error on ϕ v_2 for each (p_{T}, centrality)

centrality (%)	p_{T} (GeV/c)			
	1 - 2		2 - 3	
0 - 20 %	34.9 (%)		44.7 (%)	
20 - 40 %	12.6 (%)		6.8 (%)	
40 - 60 %	10.6 (%)		12.3 (%)	
	1 - 1.5	1.5 - 1.9	1.9 - 2.4	2.4 - 3.5
20 - 60 %	74.5 (%)	6.9 (%)	3.2 (%)	23.4 (%)
Minimum bias	137.5 (%)	2.3 (%)	8.2 (%)	21.1 (%)

Chapter 4

Experimental Results

In this chapter, we present the experimental results of v_2 for identified hadrons in Au + Au collisions at $\sqrt{s_{\mathrm{NN}}} = 200$ GeV. In Section 4.1, transverse momentum dependence of v_2 for π, K and p in minimum bias trigger are shown and the validity of our results are examined. Centrality dependence of $v_2(p_{\mathrm{T}})$ for π, K and p are shown in Section 4.2. The results of average v_2 and their evaluation are presented in Section 4.3. And in Section 4.4, the results of v_2 for deuterons and ϕ mesons are shown and compared to that for other hadrons.

4.1 Transverse momentum dependence of v_2 for π, K and p in Minimum bias events

In Run4, the total number of events is about 600 M events, by a factor 20 larger compared to Run2 (30 M events). This significant increase of statistics enable us to study the detail centrality dependence of v_2 for identified hadrons as we will show in the next section.

Fig. 4.1 shows v_2 for π, K and p as a function of transverse momentum p_{T} in minimum bias events. Comparing the Run2 results as already shown in Fig. 1.9, we can extend the p_{T} reach for π and p up to 4 GeV/c by estimating the contamination for each particle carefully. And we can also significantly reduce the statistical error with the high statistics Run-4 data set. For $p_{\mathrm{T}} < 2$ GeV/c, measured v_2 values are smaller for heavier particle species, i.e., $v_2(\pi) > v_2(K) > v_2(p)$. For $p_{\mathrm{T}} > 2$ GeV/c, however, $v_2(\pi)$ and $v_2(K)$ are saturated while $v_2(p)$ is still increasing (and saturating) with p_{T}, i.e., $v_2(p) > v_2(\pi) \sim v_2(K)$.

As we discussed in 3.2.1, azimuthal distributions related to the event plane are symmetric with $2(\phi_{lab} - \Psi_2^{BBC}) \to -2(\phi_{lab} - \Psi_2^{BBC})$, so that the $\left\langle \sin\left(2[\phi_{lab} - \Psi_2^{BBC}]\right)\right\rangle$ values are expected to be zero. If there are experimental bias and fluctuations, it could be deviated from zero. Thus, one could use $\left\langle \sin\left(2[\phi_{lab} - \Psi_2^{BBC}]\right)\right\rangle$ values for checking the validity of the analysis. As one can see that the $\left\langle \sin\left(2[\phi - \Psi_2^{BBC}]\right)\right\rangle$ for all particle species are zero in Fig. 4.1, we confirm that our procedure to extract v_2 with respect to the BBC event plane are correct.

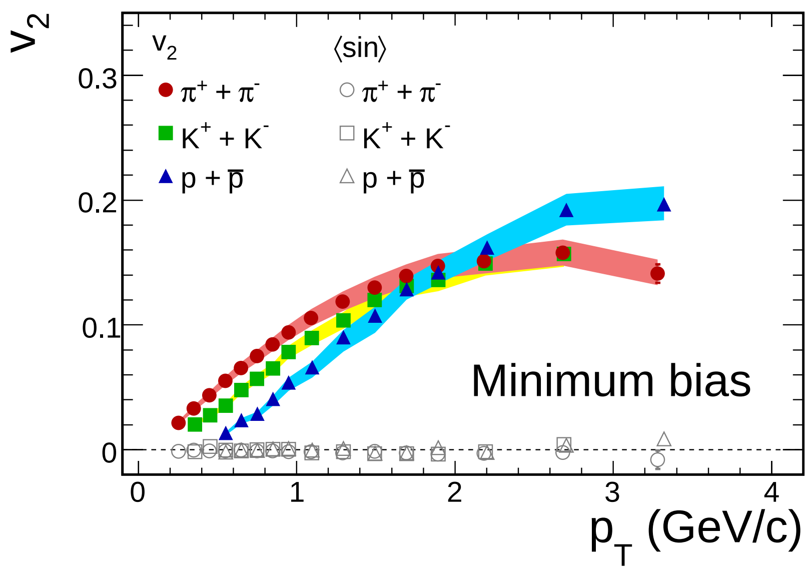

Figure 4.1: v_2 as a function of p_{T} for π, K and p in minimum bias events. Shaded bands indicates systematic errors for each particle. Open symbols around $v_2 = 0$ represent $\left\langle \sin\left(2[\phi_{lab} - \Psi_2^{BBC}]\right)\right\rangle$.

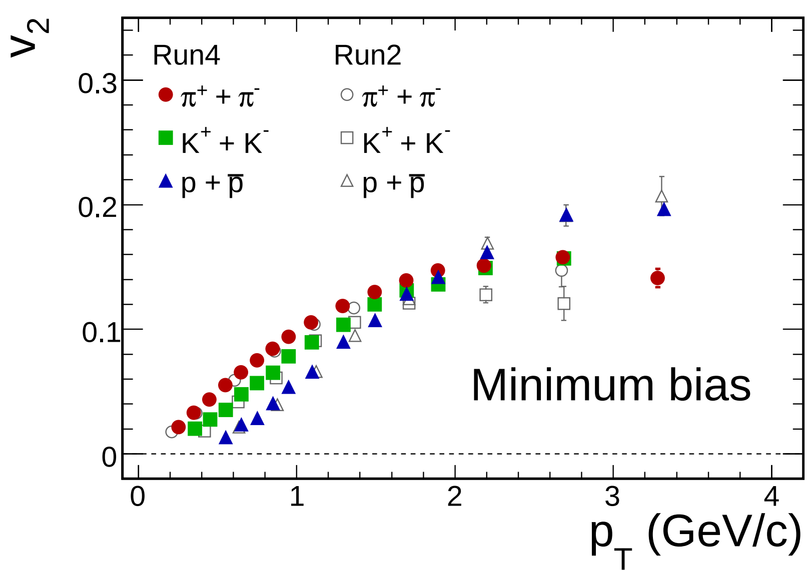

Figure 4.2: Comparison between Run4 and previous Run2 results of $v_2(p_{\mathrm{T}})$ in minimum bias events. Open symbols show the results obtained in Run2 [14]. Only statistical errors are shown.

The consistency are also checked by comparing the previous Run2 results. Fig. 4.2 shows comparison of the $v_2(p_T)$ between Run4 and Run2 [14] (same as Fig. 1.9) in minimum bias events. One can see that the both results agrees well within the error bars.

4.2 Centrality dependence of $v_2(\pi, K, p)$

Centrality dependence of $v_2(p_T)$ and $\langle \sin(2[\phi_{lab} - \Psi_2^{BBC}]) \rangle$ values for π, K and p are shown in Fig. 4.3 - 4.5. Average sine values are consistent with zero for all particle species and all centrality bins as we expected. Clear increase of $v_2(p_T)$ can be observed for all particle species, that is, the magnitude of v_2 increase with increasing centrality.

Fig. 4.6 - 4.8 show the ratio of v_2 for negative to positive particles as a function of p_T. One can see that the ratio of v_2 for π and K is consistent with unity for all centrality bins. On the other hand, $v_2(\bar{p})/v_2(p)$ is smaller than unity for mid-central collisions. In order to see the difference of v_2 between positive and negative particles, the average values of the ratio of v_2 in $p_T = 0.5 - 3$ GeV/c is plotted as a function of centrality as shown in Fig. 4.9. The average values of the ratio's are 0.992 ± 0.002, 1.001 ± 0.006, and 0.966 ± 0.005 for π, K and p respectively. The average value for p is 3.4 ± 0.5 % smaller than 1 in the measured p_T range. There are several sources which induce the difference of v_2 between anti-proton and proton;

- Feed-down decays from resonances (Λ, Ξ etc)
- Baryon transport or baryon stopping in the very beginning of collisions.

The effect of Λ feed down decays on proton v_2 has been studied by a fast MC simulation. In this simulation, we have assumed that total yield of protons is the sum of direct protons and protons from feed down decays of Λ, and that v_2 for direct protons are equal to that of anti-protons. We have also assumed the v_2 for Λ and $\bar{\Lambda}$ is equal. Resulting v_2 for p and $\bar{p}$ can be expressed as

$$v_2(p) = (1 - R_f)v_2(p)^{dir} + R_f v_2(p)^{feed} \tag{4.1}$$

where R_f is the fraction of protons from Λ feed down in all measured protons, $v_2(p)^{dir}$ is the v_2 for direct protons, and $v_2(p)^{feed}$ is the v_2 for protons from Λ feed down decays. The value of R_f is taken from [10]. We have added 10 % uncertainties in the v_2 for direct protons, and also taken into account the systematic error from R_f (~ 12 %).

Top panel in Fig. 4.10 shows the v_2 for p and $\bar{p}$ from the fast MC simulation. We found that the difference of v_2 between p and $\bar{p}$ can be explained by the feed down decays from Λ due to the large systematic errors from direct protons and R_f. In our current assumptions, R_f is the only source to cause the difference between p and $\bar{p}$. However, v_2 for Λ and $\bar{\Lambda}$ could be different from eath other. It is difficult to study more quantitatively how the v_2 for p and $\bar{p}$ are different due to the large systematic uncertainties for v_2 of direct proton and for R_f.

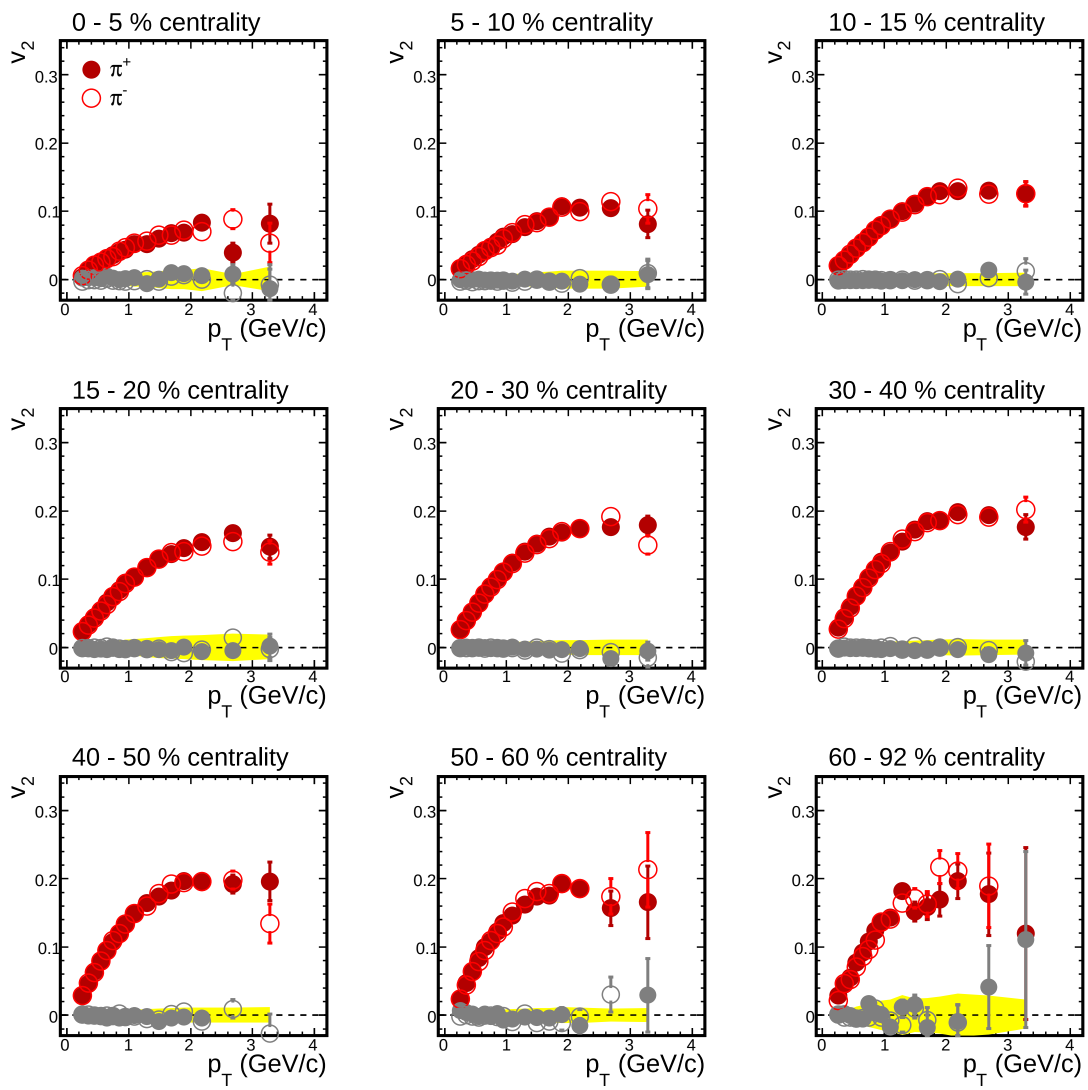

Figure 4.3: v_2 vs p_{T} for different centrality bins for π^+ (solid circles) and π^- (open circles). Yellow band around $v_2 = 0$ shows the absolute systematic errors. $\left\langle \sin\left(2[\phi_{lab} - \Psi_2^{BBC}]\right)\right\rangle$ are also plotted by grey symbols.

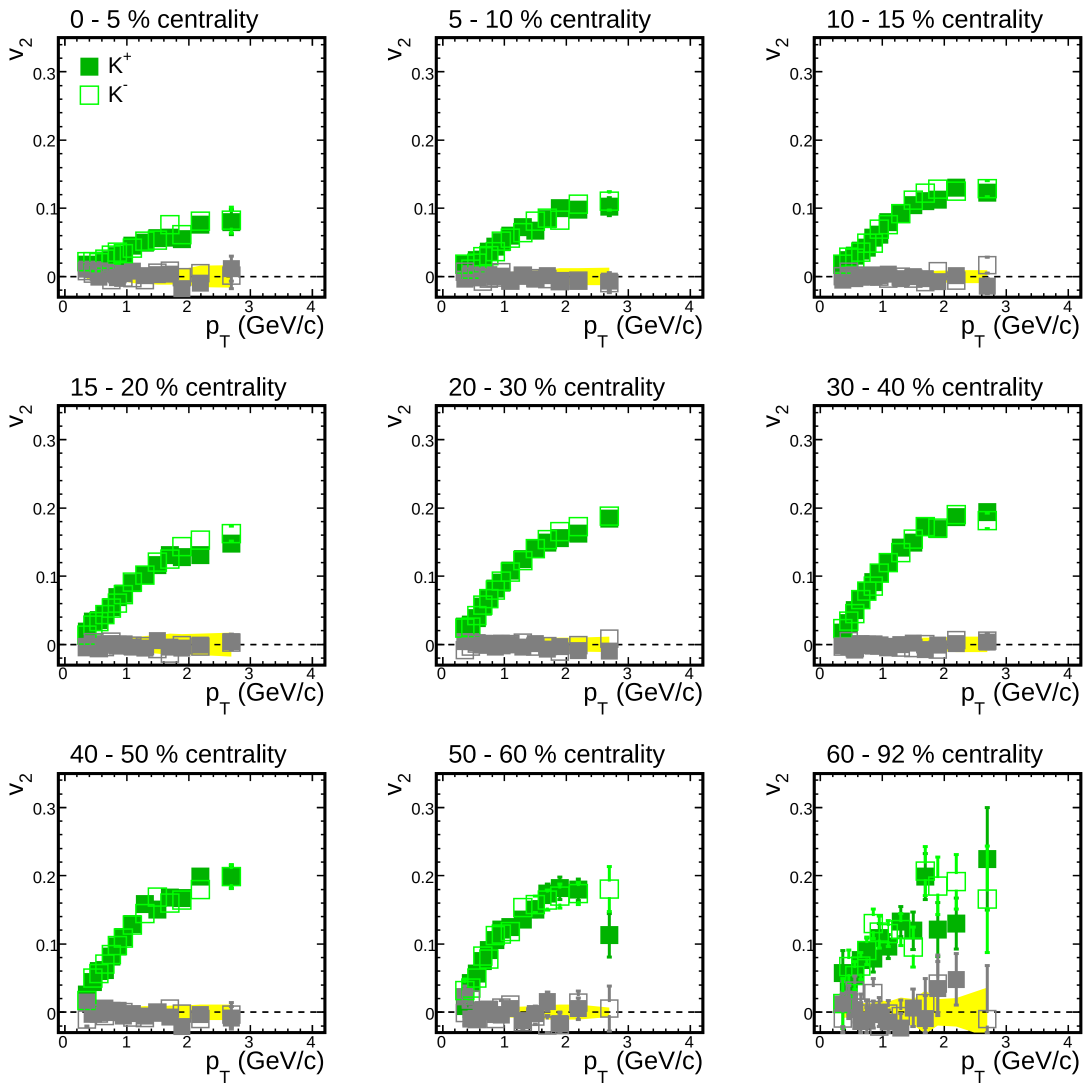

Figure 4.4: v_2 vs p_{T} for different centrality bins for K^+ (solid squares) and K^- (open squares). Yellow band around $v_2 = 0$ shows the absolute systematic errors. $\left\langle \sin\left(2[\phi_{lab} - \Psi_2^{BBC}]\right)\right\rangle$ are also plotted by grey symbols.

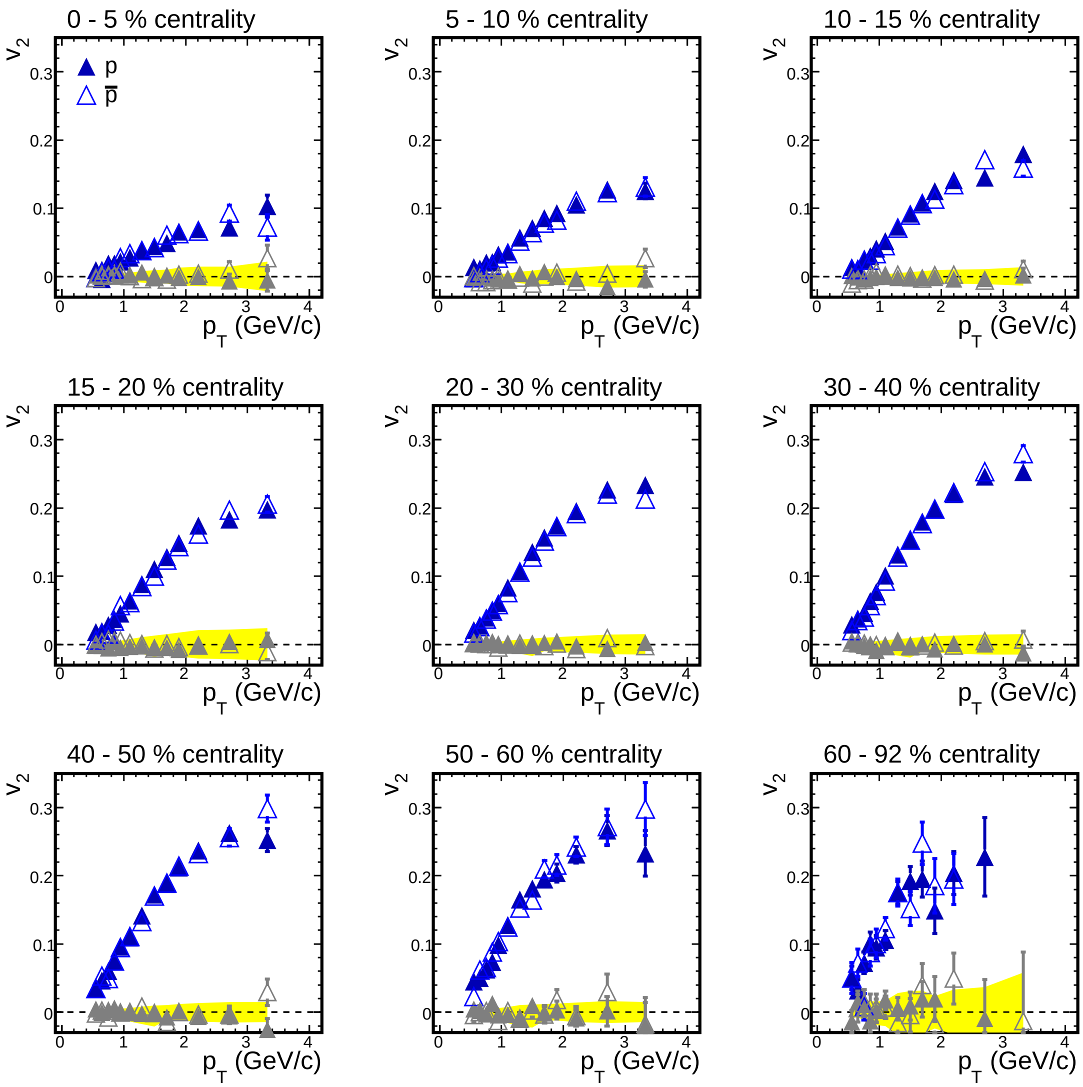

Figure 4.5: v_2 vs p_T for different centrality bins for p (solid triangles) and $\bar{p}$ (open triangles). Yellow band around $v_2 = 0$ shows the absolute systematic errors. $\left\langle \sin\left(2[\phi_{lab} - \Psi_2^{BBC}]\right) \right\rangle$ are also plotted by grey symbols.

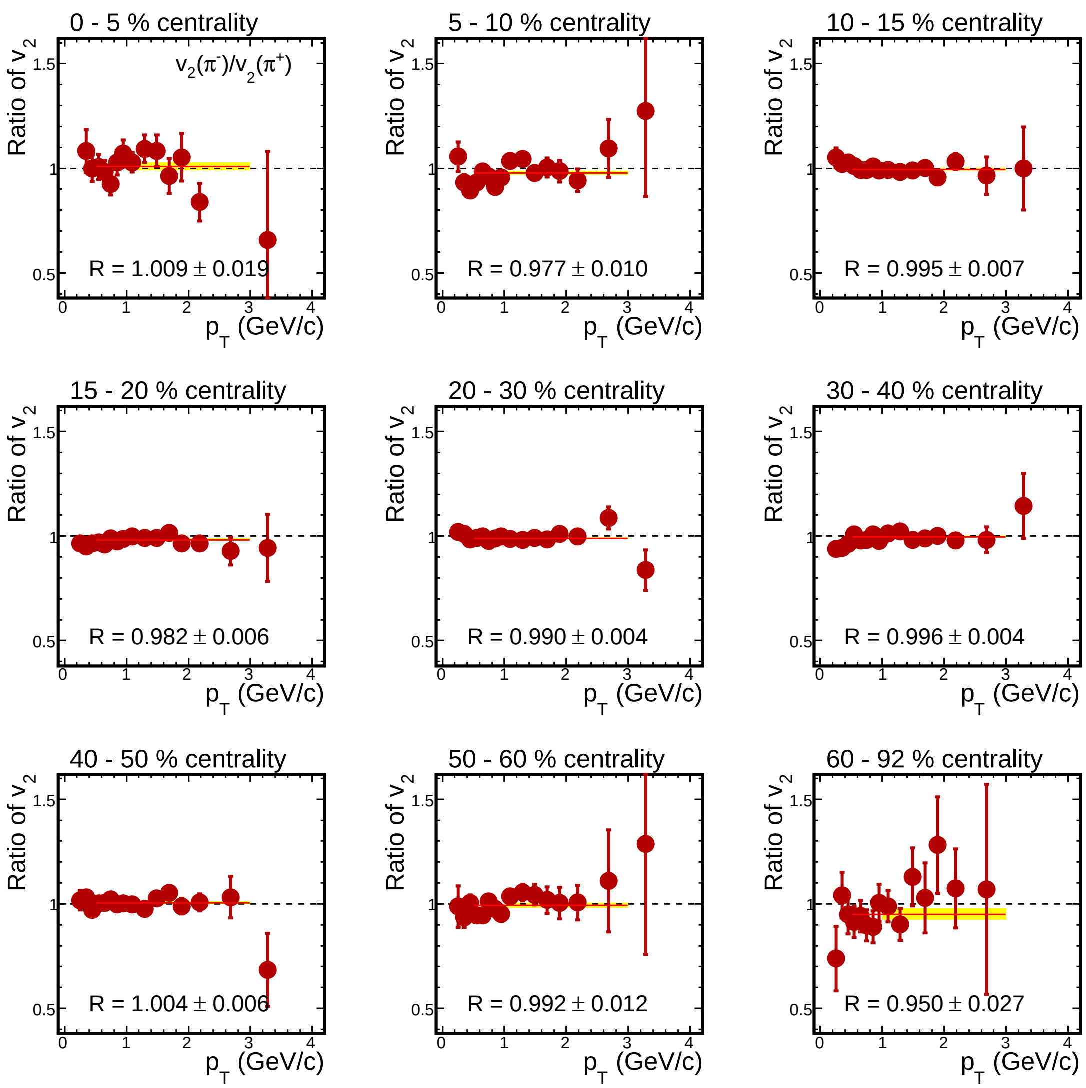

Figure 4.6: Ratio of v_2 ($v_2(\pi^-)/v_2(\pi^+)$) vs p_T for different centrality bins. Solid lines show the average values of the ratios in $p_\mathrm{T} = 0.5 - 3$ GeV/c, and yellow bands show the statistical error from the fittng. Only statistical errors are shown.

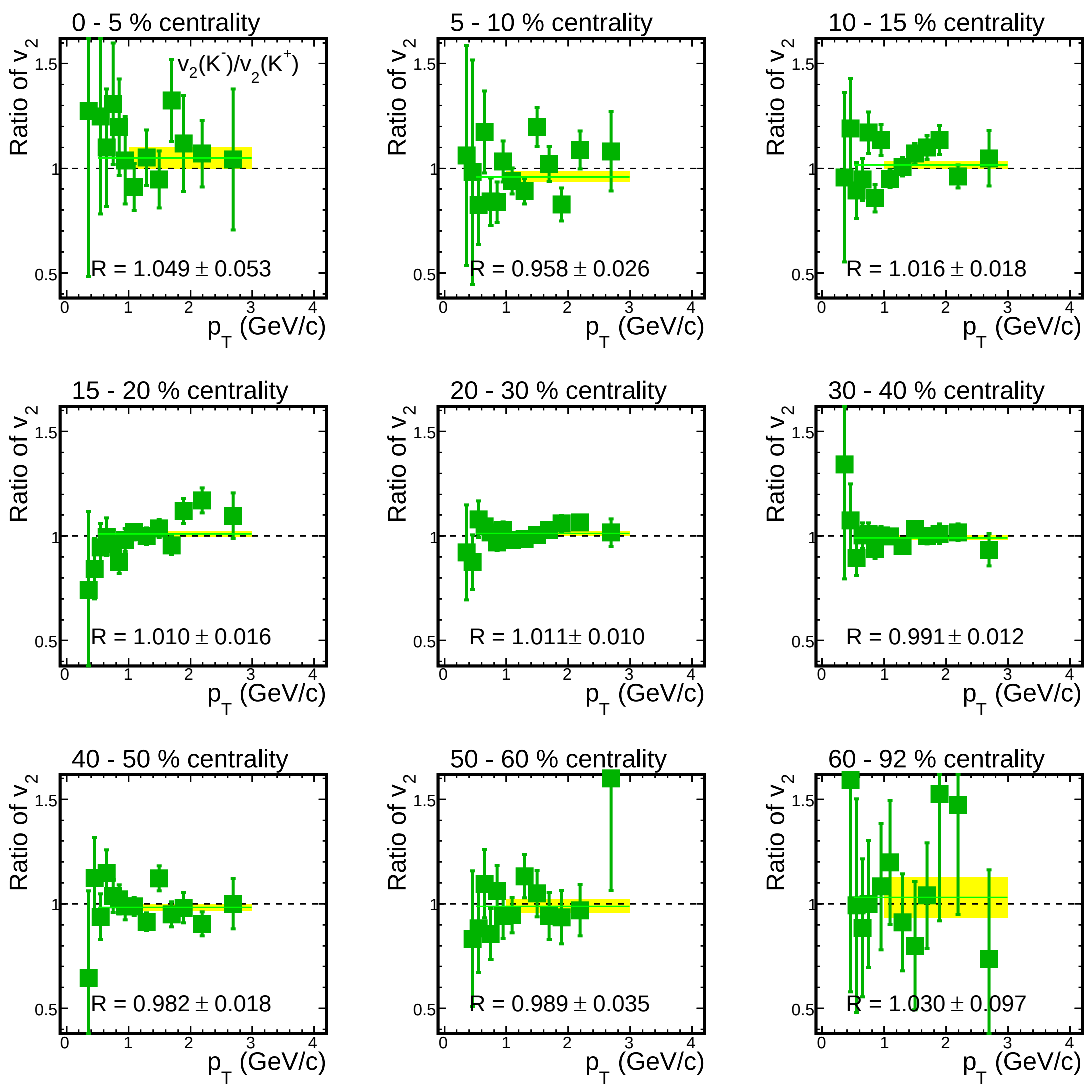

Figure 4.7: Ratio of v_2 ($v_2(K^-)/v_2(K^+)$) vs p_T for different centrality bins. Solid lines show the average values of the ratios in $p_\mathrm{T} = 0.5 - 3$ GeV/c, and yellow bands show the statistical error from the fittng. Only statistical errors are shown.

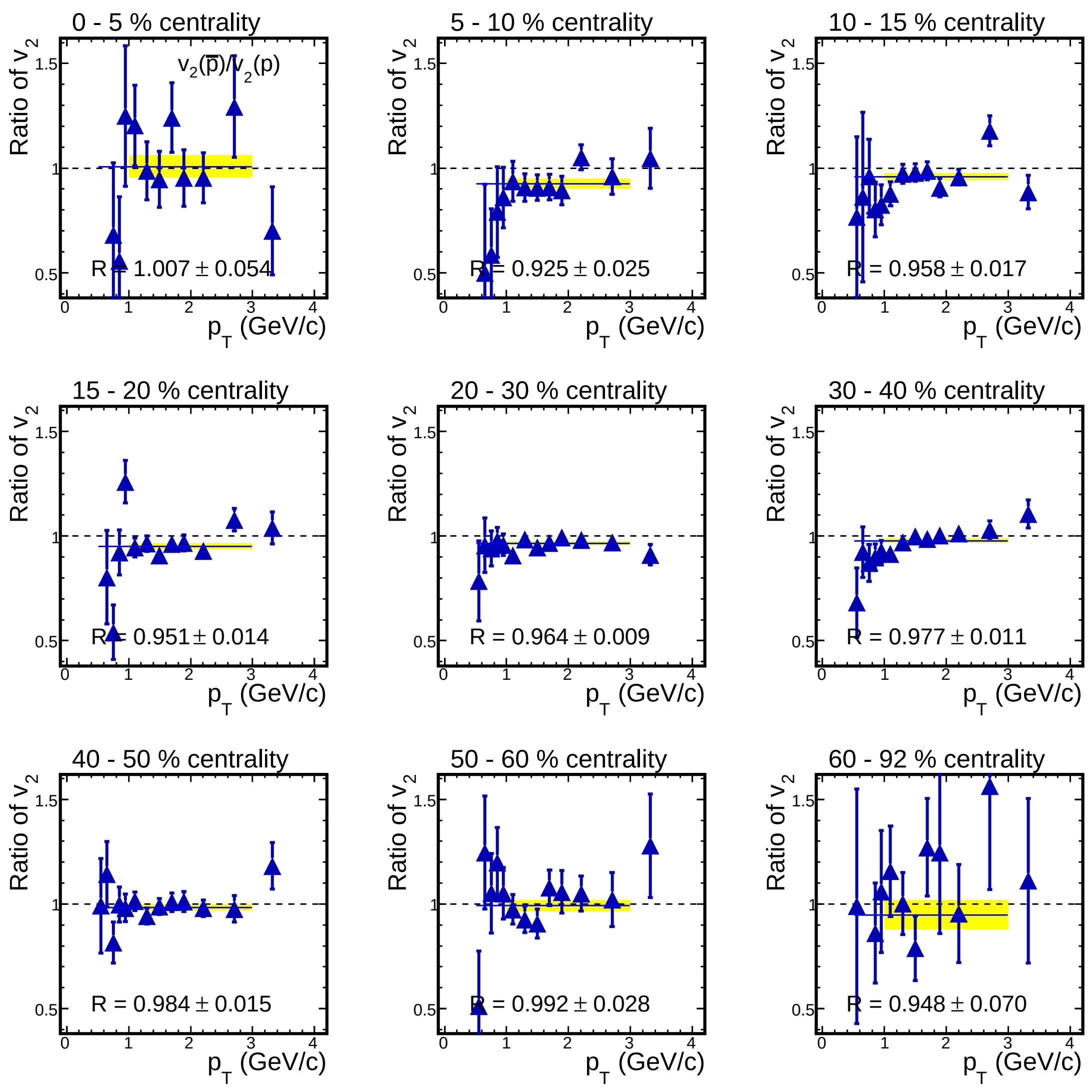

Figure 4.8: Ratio of v_2 ($v_2(\bar{p})/v_2(p)$) vs $p_{\rm T}$ for different centrality bins. Solid lines show the average values of the ratios in $p_{\rm T} = 0.5 - 3$ GeV/c, and yellow bands show the statistical error from the fittng. Only statistical errors are shown.

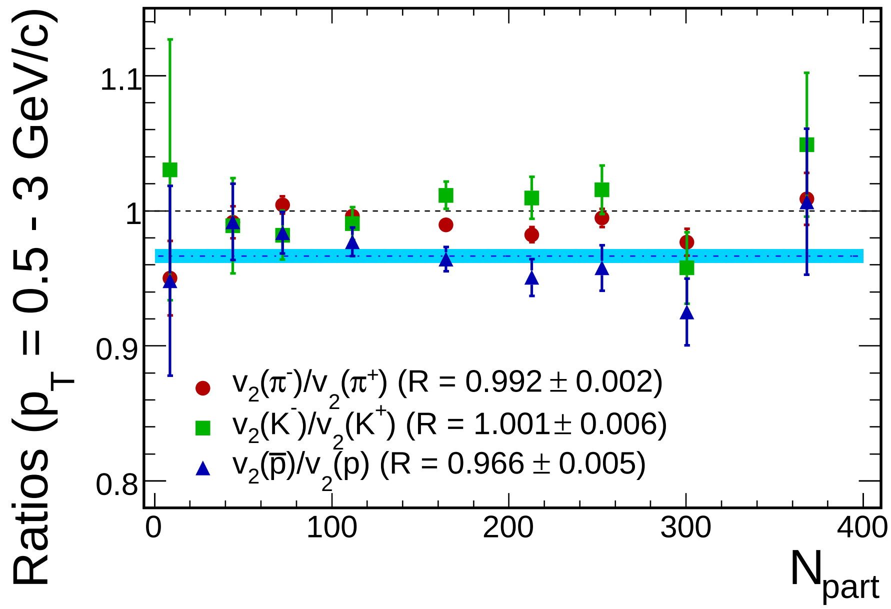

Figure 4.9: Average values of the ratio of v_2 in $p_{\mathrm{T}} = 0.5 - 3$ GeV/c as a function of N_{part}. The average ratio value on $v_2(p)$ is shown by light blue bands. R values in the figure denote the fitting results of the ratio over entire N_{part} for each particle.

One can estimate the v_2 for net proton by assuming that the v_2 is same for the pair producing proton and anti-proton. The v_2 for the net protons is given by

$$v_2^{net}(p) = \frac{1}{N_p - N_{\bar{p}}} \left(N_p v_2(p) - N_{\bar{p}} v_2(\bar{p}) \right). \tag{4.2}$$

Fig. 4.11 shows the extracted v_2 for the net proton. We found that v_2 for the net proton is 9 ± 5 % larger than that of $\bar{p}$ in $5 - 40$ % centrality. Baryon transport is one of the scenario which lead to the difference of v_2 between p and $\bar{p}$. Larger v_2 for baryons may evolve with the multiple scattering through they are transported to mid-rapidity. While v_2 is typically smaller in forward rapidity, it is unknown what the mechanism produce large v_2 in that very short time scale.

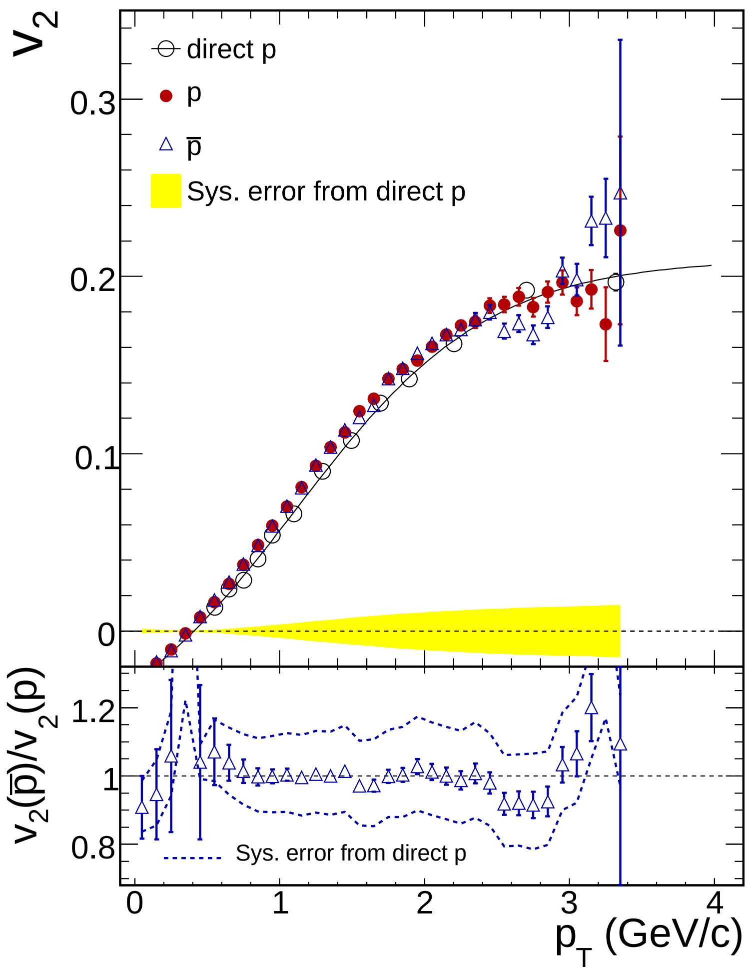

Figure 4.10: (Top) v_2 as a function of p_{T} for p (red circles) and $\bar{p}$ (blue triangles) calculated from v_2 from direct proton and protons from Λ feed down decays. Solid black lines (and open black circles) is the input v_2 for direct protons. Yellow bands include the systematic error which is estimated by allowing for 10 % variation for v_2 of direct protons. (Bottom) Ratio of $v_2(\bar{p})/v_2(p)$ as a function of p_{T}. Dashed lines represent 10 % systematic errors from direct protons, and systematic errors are assmed to be uncorrelated. We do not plot the additional 12 % systematic error from R_f (see text).

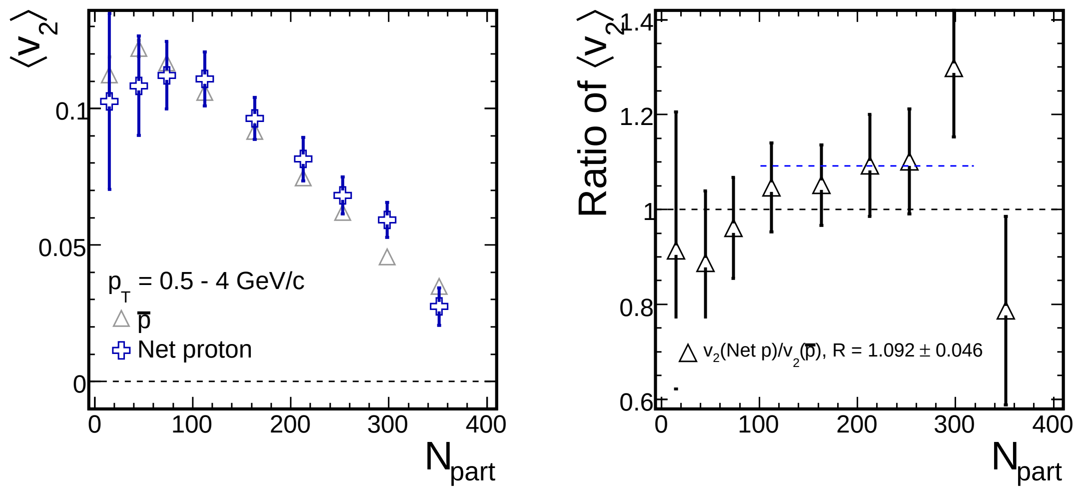

Figure 4.11: (Left) Comparison of v_2 for net proton, p and $\bar{p}$ as a function of N_{part}. Average v_2 is extracted in $p_{\rm T} = 0.5 - 4$ GeV/c. (Right) The ratio of v_2 (v_2(net p)/$v_2(\bar{p})$) as a function of N_{part}. Dashed lines represent the fitting results of the ratio by a straight line. Only statistical errors are shown.

4.3 Average v_2, $\langle v_2 \rangle$, for π, K and p

Average v_2 over measured $p_{\rm T}$ range, which we denote $\langle v_2 \rangle$, of π, K and p are calculated as

$$\langle v_2 \rangle = \frac{\int_0^\infty dp_T \; dN/dp_T \times v_2(p_T)}{\int_0^\infty dp_T \; dN/dp_T} = \frac{\sum_i \; dN^i/dp_T \times v_2^i(p_T)}{\sum_i \; dN^i/dp_T} \tag{4.3}$$

where dN/dp_T is the transverse momentum distributions, and $v_2(p_T)$ is the differential v_2 as a function of $p_{\rm T}$. Since we measure both $p_{\rm T}$ spectra and v_2 in the limited $p_{\rm T}$ range ($0.2 < p_{\rm T} < 4$ GeV/c for π, $0.3 < p_{\rm T} < 3$ GeV/c for K, $0.5 < p_{\rm T} < 4$ GeV/c for p), the integral in Eq. (4.3) are replaced to the sum of data points as one see in the 3^{rd} term. We estimate v_2 and dN/dp_T for lower $p_{\rm T}$ region by extrapolating the fitting results (see below) to $p_{\rm T} \to 0$. Higher $p_{\rm T}$ range are also extrapolated for both v_2 and dN/dp_T but they do not contribute the $\langle v_2 \rangle$ for all particle species, thus we just integrate the results up to the maximum of measured $p_{\rm T}$.

Fig. 4.12 – 4.14 show transverse momentum spectra for π, K and p as a function of centrality [10]. We parameterize the $p_{\rm T}$ spectra by the following functions;

$$f^\pi(p_T) = A \cdot \left(\frac{p_0}{p_T + p_0}\right)^n \quad \text{(for } \pi\text{)} \tag{4.4}$$

$$f^K(p_T) = A \cdot e^{-m_T/T} \quad \text{(for } K\text{)} \tag{4.5}$$

where A, p_0, n, and T are the free parameters. For protons, blast-wave model (Eq. (1.13)) is used to parameterize their $p_{\rm T}$ spectra. Different parameterizations of $p_{\rm T}$ spectra are also used to evaluate the systematic error on $\langle v_2 \rangle$, i.e. the $p_{\rm T}$ spectra for π

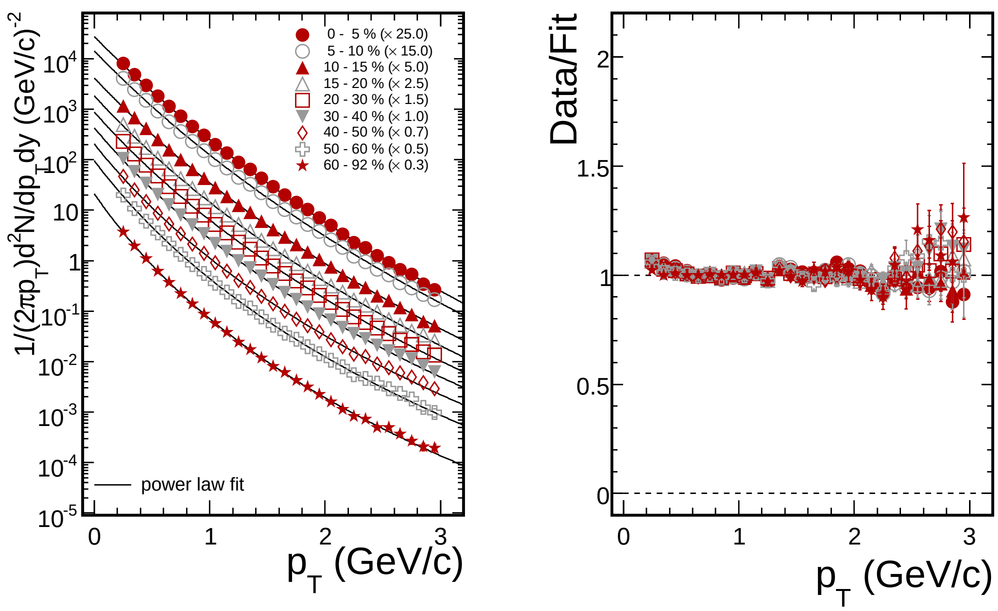

Figure 4.12: (Left) p_{T} spectra for $\pi^+ + \pi^-$ from central (top) to peripheral (bottom) collision. Solid black lines represent power-law fitting results by Eq. (4.4). (Right) The ratio of data to fitting results as a function of p_{T}.

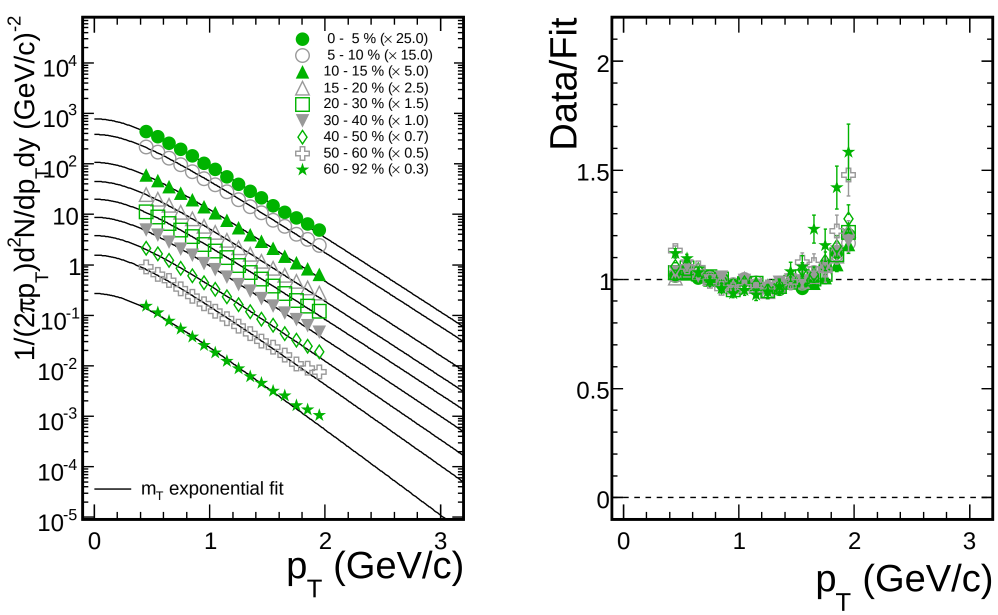

Figure 4.13: (Left) p_{T} spectra for $K^+ + K^-$ from central (top) to peripheral (bottom) collision. Solid black lines represent m_{T} exponential fitting results by Eq. (4.5). (Right) The ratio of data to fitting results as a function of p_{T}.

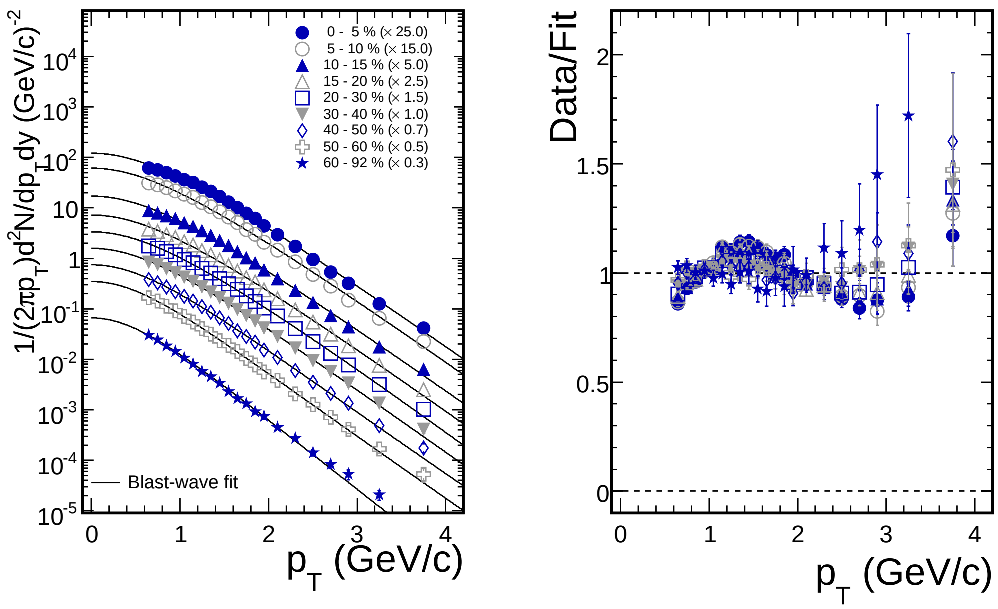

Figure 4.14: (Left) p_{T} spectra for p+$\bar{p}$ from central (top) to peripheral (bottom) collision. Solid black lines represent blast-wave fitting results by Eq. (1.13). (Right) The ratio of data to fitting results as a function of p_{T}.

and p are fitted by m_{T} exponential function, and that for K is fitted by p_{T} exponential function.

Fig. 4.15 shows the fitting results of $v_2(\pi)$, $v_2(K)$ and $v_2(p)$ as a function of p_{T} for difference centrality classes. To extrapolate the data to low and high p_{T}, we use the following functions

$$f(p_T) = a \cdot n_q \left(\frac{1}{1 + e^{-(p_T/n_q - b)/c}} - \frac{1}{1 + e^{b/c}} \right) \tag{4.6}$$

$$f(p_T) = a \cdot p_T^n \tag{4.7}$$

where a, b, c and n are the free parameters, and n_q is the number of quarks for each hadrons (2 for mesons, 3 for baryons). The empirical formula from Eq. (4.6) well describe the p_{T} dependence of v_2 from low to intermediate p_{T} [18]. As we already mentioned, the contributions from high p_{T} does not change the final results of $\langle v_2 \rangle$, Eq. (4.7) gives reasonable estimate of v_2 at low p_{T}.

Fig. 4.16 shows the results of $\langle v_2 \rangle$ as a function of N_{part}. In the measured p_{T} range, measured v_2 values are used to calculate $\langle v_2 \rangle$, and in the lower p_{T} range where we don't have the data points of v_2 extorapolated values from Eq. (4.6) is used. One can see $\langle v_2 \rangle$ values are increasing in smaller N_{part} region (peripheral events) and are saturating in $N_{part} < 100$.

Fig. 4.17 shows the ratio of $\langle v_2 \rangle$ as a function of N_{part} for π, K and p. Systematic errors are evaluated from the maximum difference of $\langle v_2 \rangle$ for each centrality. Systematic

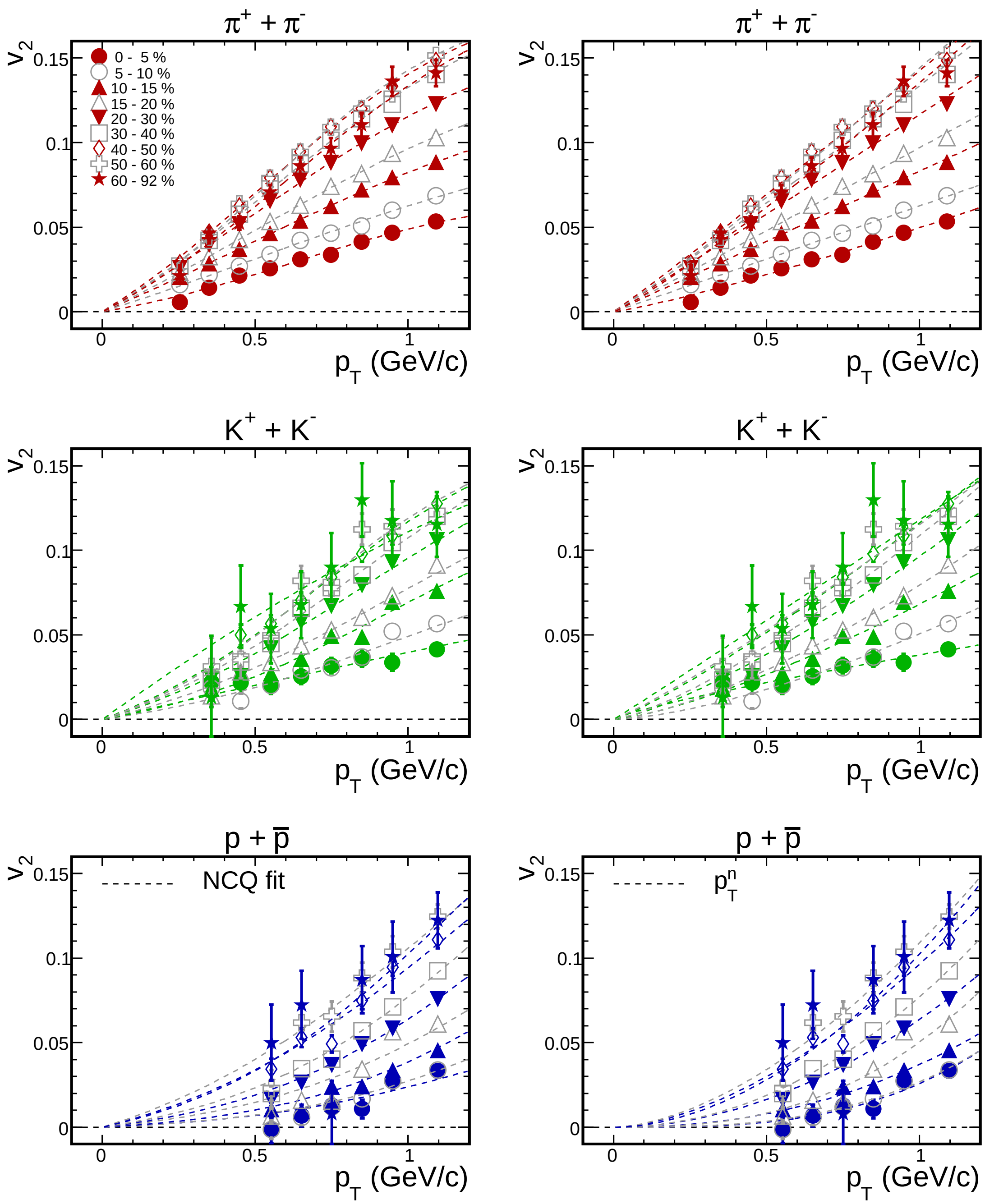

Figure 4.15: $v_2(p_{\mathrm{T}})$ for π, K and p in different centrality bins. Fitting results by Eq. (4.6) and (4.7) are plotted in left and right panels, respevtively.

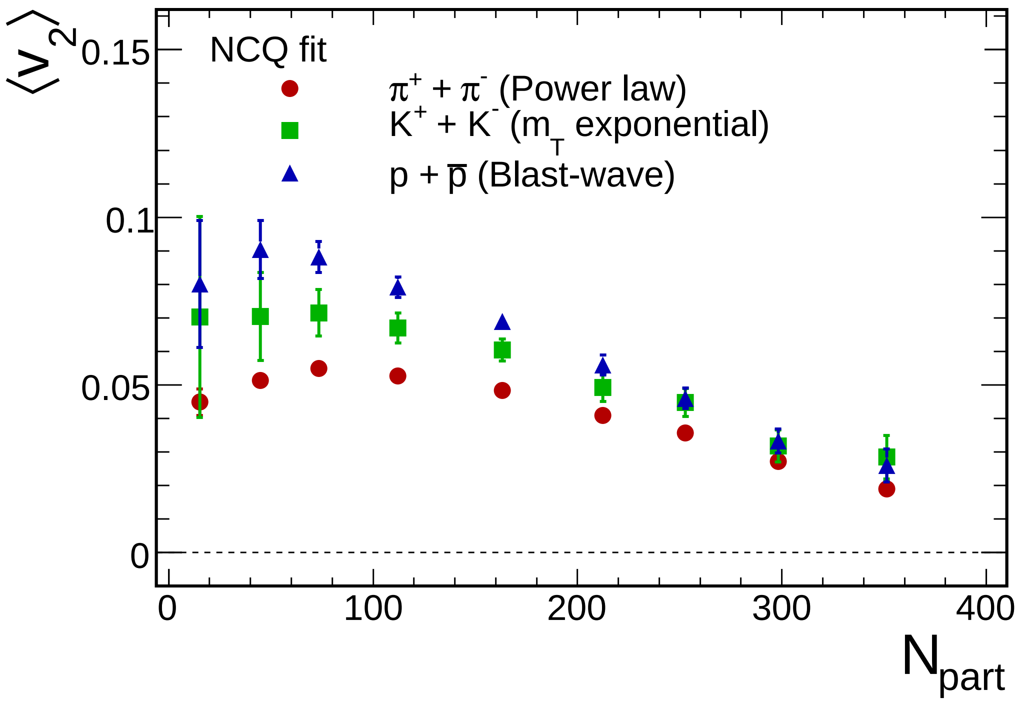

Figure 4.16: N_{part} dependence of $\langle v_2 \rangle$ for π, K and p.

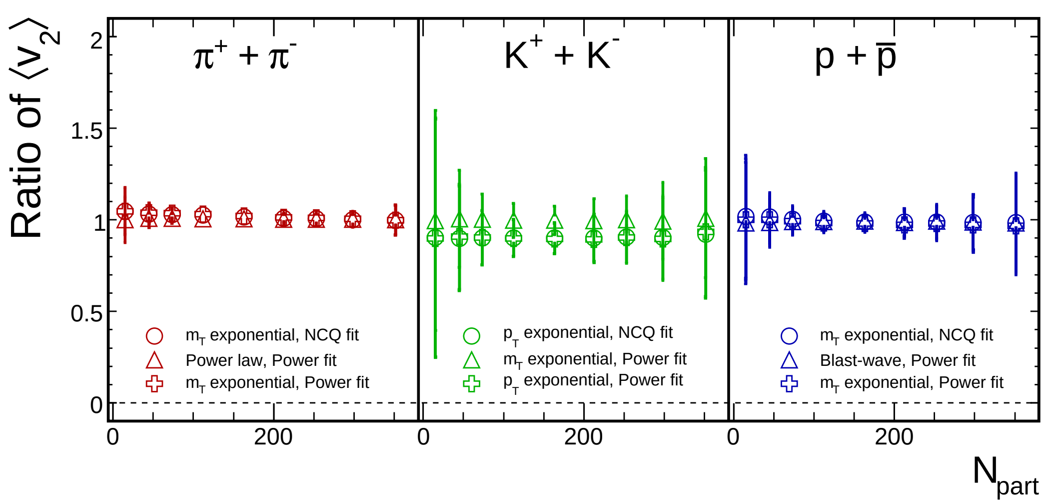

Figure 4.17: Ratio of $\langle v_2 \rangle$ as a function of N_{part} for different parameterizations of $v_2(p_{\mathrm{T}})$ and p_{T} spectra.

errors are summalized in table 4.1. We assume the flat distribution of $\langle v_2 \rangle$ for each centrality bin and then evaluate the systematic error as

$$\sigma^{sys}(\langle v_2 \rangle) = \frac{2 \times |D_{max}|}{\sqrt{12}} \tag{4.8}$$

where $|D_{max}|$ is the maximum difference of between the measured $\langle v_2 \rangle$ and the reference $\langle v_2 \rangle$.

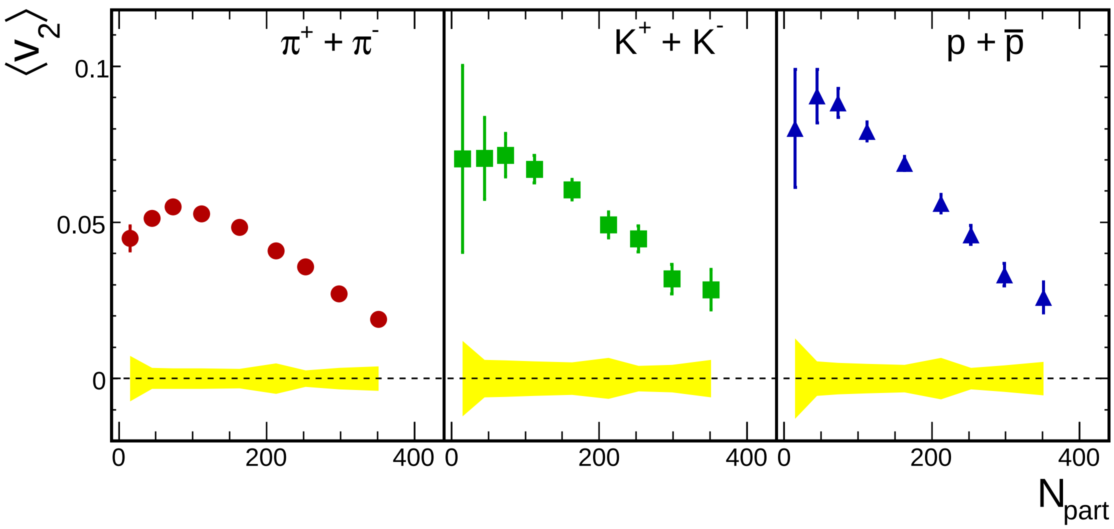

Figure 4.18: $\langle v_2 \rangle$ as a function of N_{part} for π (left), K (middle) and p (right) with absolute systematic error (yellow bands around $v_2 = 0$). Systematic error is calculated by quadratic sum of systematic error from the different procedures to extract $\langle v_2 \rangle$ and errors from Section 3.7.

Table 4.1: Summary of systematic error on $\langle v_2 \rangle$. $|D_{max}|$ is given by the maximum difference of $\langle v_2 \rangle$.

Centrality	$\pi^+ + \pi^-$		$K^+ + K^-$		$p + \bar{p}$	
	$\lvert D_{max} \rvert$	Sys. error	$\lvert D_{max} \rvert$	Sys. error	$\lvert D_{max} \rvert$	Sys. error
0 - 5 %	0.0016	0.1 %	0.0791	4.6 %	0.0323	1.9 %
5 - 10 %	0.0048	0.3 %	0.1052	6.1 %	0.0274	1.6 %
10 - 15 %	0.0106	0.6 %	0.0953	5.5 %	0.0207	1.2 %
15 - 20 %	0.0137	0.8 %	0.1053	6.1 %	0.0275	1.6 %
20 - 30 %	0.0202	1.2 %	0.1033	6.0 %	0.0202	1.2 %
30 - 40 %	0.0319	1.8 %	0.1010	5.8 %	0.0176	1.0 %
40 - 50 %	0.0370	2.1 %	0.1000	5.8 %	0.0104	0.6 %
50 - 60 %	0.0397	2.3 %	0.1008	5.8 %	0.0154	0.9 %
60 - 92 %	0.0477	2.8 %	0.1011	5.8 %	0.0177	1.0 %

4.4 Centrality and p_{T} dependence of v_2 for $d + \bar{d}$ and ϕ

Fig. 4.19 shows v_2 as a function of p_{T} for $d + \bar{d}$ in minimum bias events. For $p_{\mathrm{T}} < 2$ GeV/c, the magnitude of v_2 for deuterons is smaller than that of other hadrons. This trend of v_2 is consistent with the picture of hydrodynamic calculation with common velocity field, that is v_2 of heavier particles become smaller for a given p_{T}. For $p_{\mathrm{T}} > 2$ GeV/c, on the other hand, one can see that $v_2(d)$ is consistent with v_2 for other hadrons.

Fig. 4.20 shows v_2 as a function of p_{T} for ϕ mesons in minimum bias events. The magnitude of v_2 for ϕ mesons is smaller than that of other hadrons in $p_{\mathrm{T}} < 1.5$ GeV/c, while v_2 is consisteht with that for other hadrons in $p_{\mathrm{T}} > 1.5$ GeV/c.

Fig. 4.21 shows centrality dependence of $v_2(d)$ and $v_2(\phi)$ as a function of p_{T}. Similar trend of v_2 are observed for the data in 20 % centrality steps as in minimum bias events, while the statistical errors are large especially for higher p_{T} bins.

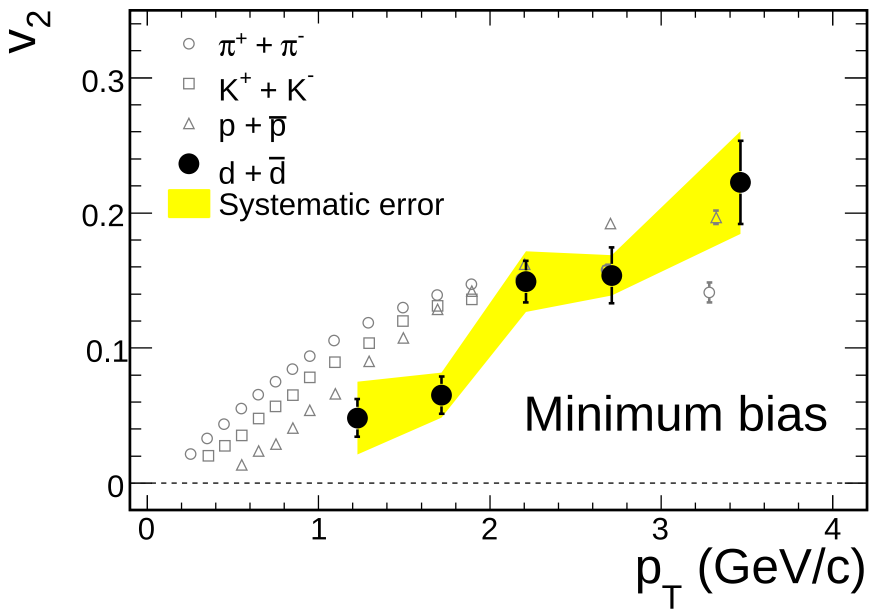

Figure 4.19: v_2 as a function of p_T for $d + \bar{d}$ in minimum bias events. v_2 of π, K and p are also plotted for comparison. Yellow bands show the systematic error on $v_2(d)$.

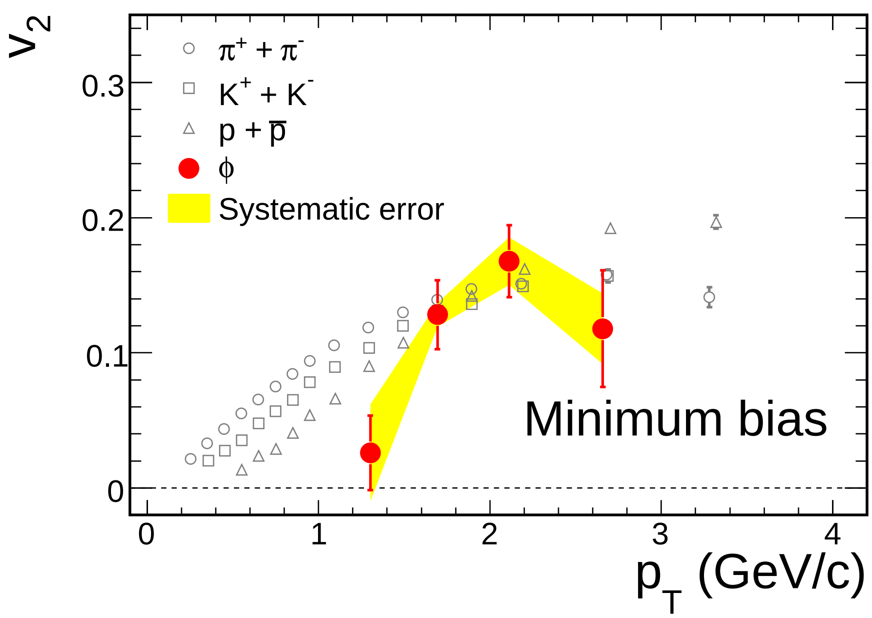

Figure 4.20: v_2 as a function of p_T for ϕ mesons in minimum bias events. v_2 of π, K and p are also plotted for comparison. Yellow bands show the systematic error on $v_2(\phi)$.

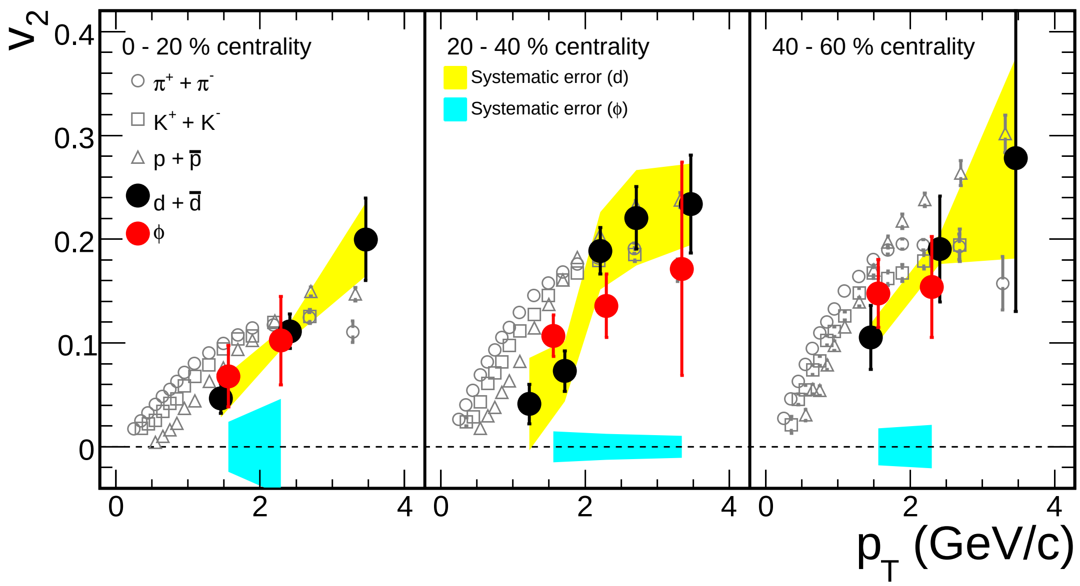

Figure 4.21: Comparison of $v_2(p_\mathrm{T})$ between $d + \bar{d}$ and ϕ in different centrality bins. Yellow bands show the systematic error on $v_2(d)$, and light blue bands around $v_2 = 0$ show the systematic error on $v_2(\phi)$.

Chapter 5

Discussions

In the presious chapter, we have found that;

- Mass ordering of v_2, i.e. v_2 for heavier particles is larger for a given p_{T} at $p_{\mathrm{T}} < 2$ GeV/c, which is consistent with the hydrodynamical model calculations.
- For $p_{\mathrm{T}} > 2$ GeV/c, v_2 for heavier particle species, such as protons, deuterons are larger compared to those for mesons.
- v_2 increases from central to peripheral collisions. Centrality dependence of v_2 is qualitatively consistent with that of the eccentricity.

In Section 5.1, we discuss degree of thermalization and its relation between spatial eccentricity and elliptic flow more quantitatively with the eccentricity estimated by the Monte Carlo simulation with Glauber model. In Section 5.2, the sensitivity of initial density profile to measured v_2 is discussed by using extended Blast-wave parameterization. Finally, in Section 5.3, we discuss the partonic collectivity with the quark number scaling of v_2.

5.1 Eccentricity Scaling of v_2

As we discussed in Section 1.3.3, final momentum anisotropy is sensitive to the degree of thermalization. In peripheral collisions, where the emitted particles can escape from the overlap zone without interacting with other particles, the system is close to free streaming. In the case of free streaming (collisionless limit: $\lambda \to \infty$), the magnitude of elliptic flow is [49]

$$\langle v_2 \rangle \propto \frac{\langle \varepsilon \rangle}{\langle S \rangle} \frac{dN}{dy} \tag{5.1}$$

where $\langle \varepsilon \rangle$ is the spatial eccentricity (several definitions of eccentricity can be used, see Appendix A.2), $\langle S \rangle$ is the transverse area of collision zone, and dN/dy is the rapidity density of total (charged + neutral) produced particles. Bracket $\langle\rangle$ for v_2, ε and S denote the average over all events for all particles. In this free streaming limit, the ratio of $\langle v_2 \rangle / \langle \varepsilon \rangle$ linearly increase with the transverse number density $(1/\langle S \rangle dN/dy)$. Since

dN/dy increases in more central collisions, the ratio of $\langle v_2\rangle/\langle\varepsilon\rangle$ increases with more central events for a fixed collision system.

The transverse number density can be related to the degree of thermalization, i.e. the Knudsen number K [50]

$$\frac{1}{K} = \frac{R}{\lambda} = R\sigma n(\tau) \sim \frac{c_s\sigma}{c\,\langle S\rangle}\frac{dN}{dy} \tag{5.2}$$

where λ is the mean free path of produced particles, R is the transverse size of the system, σ is the cross section among the produced particles, $n(\tau)$ is the number density of produced particles at "time" τ, and c, c_s are the speed of light and speed of sound, respectively. The above equation is valid for $\tau \leq R/c_s$, where the transverse size of the system does not change significantly [50]. In the hydrodynamical limit: $\lambda \to 0$, that is $1/K \gg 1$, the ratio $\langle v_2\rangle/\langle\varepsilon\rangle$ becomes constant [51]. The relation between the measured v_2 and Knudsen number can be given by [50]

$$\frac{\langle v_2\rangle}{\langle\varepsilon\rangle} = \frac{\langle v_2^h\rangle}{\langle\varepsilon\rangle}\frac{1}{1+K/K_0} \tag{5.3}$$

where $\langle v_2^h\rangle$ is the limitting values of v_2 when $K \to 0$, which corresponds to the v_2 from hydrodynamics, and K_0 is the parameter of order unity, whose precise value can only be determined through a transport calculation.

Therefore, the possible thermalization achieved in the early stage of heavy ion collisions could be investigated with detailed comparison between spatial eccentricity in initial coordinate space and elliptic flow in final momentum space.

First, we discuss the eccentricity scaling of $\langle v_2\rangle$ (average v_2) by using standard eccentricity among the Au + Au and Cu + Cu collisions. Second, we introduce the more accurate definitions of eccentricity (participant eccentricity), which is taking into account the fluctuation of positions for participating nucleons, and discuss the scaling relation between $\langle v_2\rangle$ and participant eccentricity in Au + Au and Cu + Cu collisions. Last, we discuss the difference of eccentricity between different averaging and compare the results of scaled $\langle v_2\rangle$ for different definitions of eccentricity.

5.1.1 $\langle v_2\rangle$ in Au + Au and Cu + Cu Collisions and Standard Eccentricity

Fig. 5.1 shows the $\langle v_2\rangle$ for charged hadrons as a function of N_{part} in Au + Au and Cu + Cu collisions at $\sqrt{s_{\rm NN}} = 200$ GeV. The behavior of $\langle v_2\rangle$ is qualitatively similar to that of eccentricity, that is the magnitude of $\langle v_2\rangle$ is smaller for larger N_{part} and $\langle v_2\rangle$ in Au + Au is larger than that of Cu + Cu for a given N_{part} (see Fig. A.3).

In order to study the relation between the $\langle v_2\rangle$ and the eccentricity more quantitatively, the eccentricity scaling of v_2 is examined for both Au + Au and Cu + Cu collisions. We first use **standard eccentricity** $\langle\varepsilon_{std}\rangle$, which is defined by the fixed axes in the coordinate space, as defined in Eq. (A.7) and (A.8). Fig. 5.2 show the N_{part} dependence of the ratio $\langle v_2\rangle/\langle\varepsilon_{std}\rangle$. One can clearly see that the scaled $\langle v_2\rangle$ rapidly

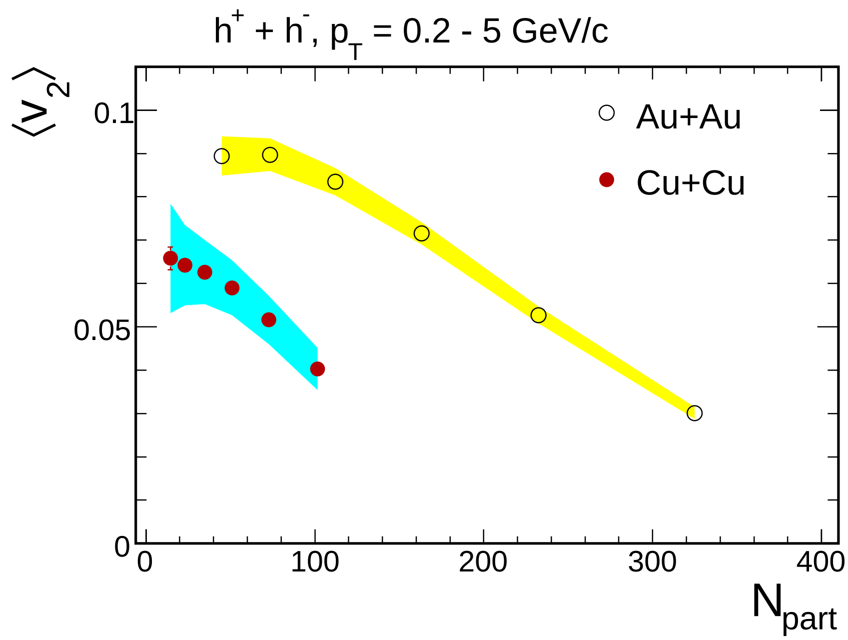

Figure 5.1: $\langle v_2 \rangle$ for charged hadrons as a function of N_{part} in Au + Au and Cu + Cu collisions (corresponding centrality range is 0 - 60 %) at $\sqrt{s_{\rm NN}} = 200$ GeV. Average v_2 values are obtained by integrating $v_2(p_{\rm T})$ over $p_{\rm T} = 0.2 - 5.0$ GeV/c. Yellow and light blue bands represent the systematic errors on v_2 in Au + Au and Cu + Cu, respectively.

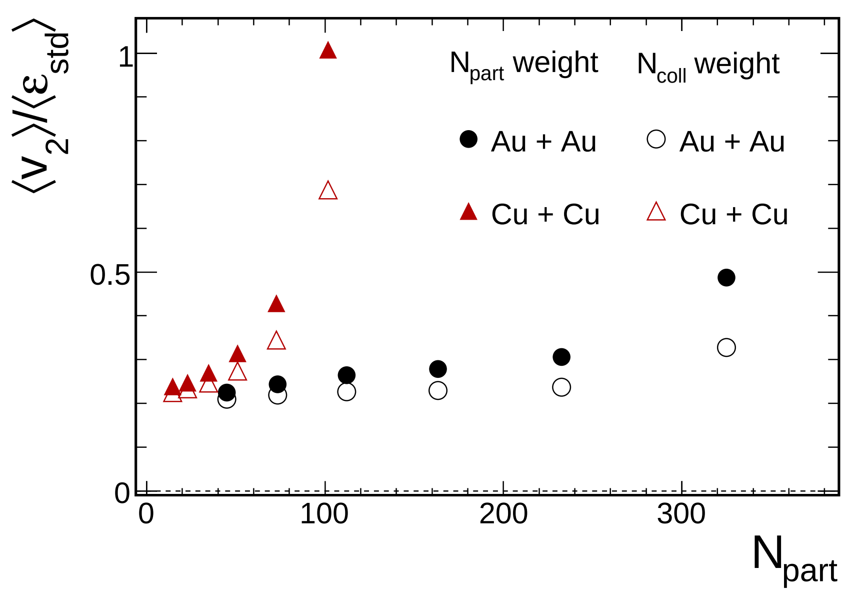

Figure 5.2: $\langle v_2 \rangle / \langle \varepsilon_{std} \rangle$ as a function of N_{part} in Au + Au and Cu + Cu collisions. Solid (open) data points show the results of $\langle v_2 \rangle$ divided by $\langle \varepsilon_{std} \rangle$ weighting with N_{part} (N_{coll}) density profile.

increase around $N_{part} \sim 100$ especially for Cu + Cu and $\langle v_2\rangle/\langle\varepsilon_{std}\rangle$ is not scaled among the different colliding systems. Since $\langle\varepsilon_{std}\rangle$ is defined with the fixed axes in coordinate space, it does not take into account the event-by-event position fluctuations of participating nucleons in principle. Such fluctuations lead to the difference between fixed axes in the reference frame and the principal axes determined by the participant nucleons. Therefore, $\langle\varepsilon_{std}\rangle$ could underestimate the magnitude of eccentricity. The scaling breaks between Au + Au and Cu + Cu with $\langle\varepsilon_{std}\rangle$ suggest that such fluctuations are dominant especially for Cu + Cu collisions.

Such a behavior is also found for $\left\langle\varepsilon_{std}^{coll}\right\rangle$ as shown by the open data points in Fig. 5.2. One also see relatively smaller $\langle v_2\rangle/\left\langle\varepsilon_{std}^{coll}\right\rangle$ compared to $\langle v_2\rangle/\left\langle\varepsilon_{std}^{part}\right\rangle$. This is simply because the steeper N_{coll} density distribution gives larger eccentricity (about $1.5-2$ times larger in most central, close to unity in most peripheral, see Fig. A.7 and A.8).

5.1.2 Eccentricity Scaling of $\langle v_2\rangle$ with Participant Eccentricity

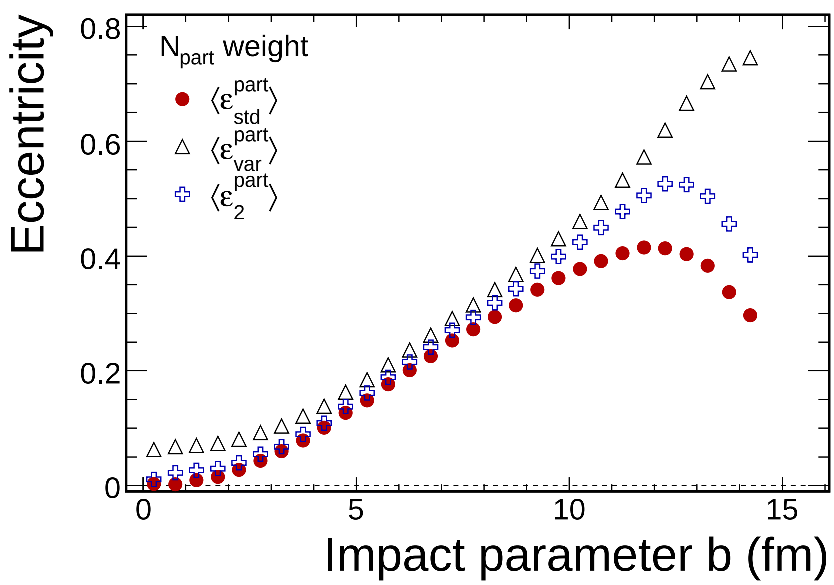

Figure 5.3: Comparison of $\langle\varepsilon\rangle$ as a function of impact parameter in Au + Au. Red circles, black triangles and blue crosses are $\langle\varepsilon_{std}\rangle$, $\langle\varepsilon_{var}\rangle$, and $\langle\varepsilon_2\rangle$, respectively. Eccentricity is calculated with N_{part} weight.

To take into account the position fluctuations of participant nucleons, we calculate $\langle\varepsilon_{var}\rangle$ (**participant eccentricity**) which is defined by the axes determined with the distributions of participant nucleons. We also consider $\langle\varepsilon_2\rangle$ (**event plane eccentricity**) which is basically same as $\langle\varepsilon_{var}\rangle$ but is defined by subtracting auto-correlation between participating nucleons and the event plane. Details definitions of these $\langle\varepsilon\rangle$ can be found in Appendix A.2.

Fig. 5.3 compare the eccentricity as a function of impact parameter in Au + Au collisions. $\langle\varepsilon_{std}\rangle$ becomes zero at most central since the radius of x and y is equal. $\langle\varepsilon_{std}\rangle$ increase with increasing impact parameter, and become decreasing from $b \geq 2R_{\rm Au}$ due to the effect of surface diffuseness. On the other hand, $\langle\varepsilon_{var}\rangle$ and $\langle\varepsilon_2\rangle$ have finite value even at most central since they include the event-by-event position fluctuations. Because $\langle\varepsilon_{var}\rangle$ is defined by the event plane determined with the participating nucleons, it becomes unity in the limit of $N_{part} \to 1$ due to the auto-correlation. For $\langle\varepsilon_2\rangle$, the effect of auto-correlation is strongly suppressed at most peripheral, and the magnitude is approaching to the $\langle\varepsilon_{std}\rangle$.

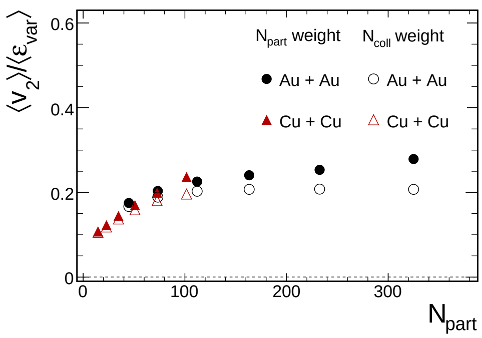

(a)

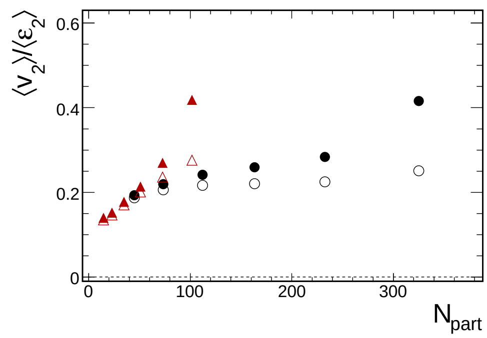

(b)

Figure 5.4: Eccentricity scaling of $\langle v_2\rangle$ as a function of N_{part}. (a) with $\langle\varepsilon_{var}\rangle$, (b) with $\langle\varepsilon_2\rangle$. Note that the scale of vertical axis is different from Fig. 5.2.

Fig. 5.4 show the $\langle v_2\rangle/\langle\varepsilon_{var}\rangle$ (left) and $\langle v_2\rangle\langle\varepsilon_2\rangle$ (right) as a function of N_{part}. As one can see that eccentricity scaling works for Au + Au and Cu + Cu with $\langle\varepsilon_{var}\rangle$ as shown in left figure. However, if one takes $\langle\varepsilon_2\rangle$, eccentricity scaling seems to break at most central Cu + Cu bin. There might be several reasons why the eccentricity scaling of $\langle v_2\rangle$ with $\langle\varepsilon_2\rangle$ breaks; first there may be remaining auto-correlations in the measured $\langle v_2\rangle$, and second we may oversubtract auto-correlations from $\langle\varepsilon_{var}\rangle$.

5.1.3 $\langle\varepsilon\rangle$ vs $\varepsilon\{2\}$

We measured the magnitude of v_2 by the event plane method, $v_2\{EP_2\} = \langle\cos 2[\phi - \Psi]\rangle$, which is equivalent to that by two-particle azimuthal correlations between emitted particles $v_2\{2\} = \sqrt{\cos 2[\phi_1 - \phi_2]}$ [52]. Both methods yield $v_2\{EP_2\} \simeq v_2\{2\} = \sqrt{\langle v_2^2\rangle}$ when v_2 fluctuate event-by-event. If we assume v_2 in each event is proportional to ε, one expects $v_2\{EP_2\} \simeq v_2\{2\} = \sqrt{\langle\varepsilon^2\rangle}$ [53]. Therefore, $\varepsilon\{2\} \equiv \sqrt{\langle\varepsilon^2\rangle}$ is thought to be more natural choice of eccentricity compared to the $\langle\varepsilon\rangle$, as long as v_2 is determined by the event plane determined with the emitted parricles from the participant nucleons.

Fig. 5.5 show eccentricity scaling of $\langle v_2\rangle$ with $\varepsilon\{2\}$ as a function of N_{part}. Since the magnitude of $\varepsilon\{2\}$ is almost independent of the definitions of eccentricity (see Fig. A.5 and A.6), scaled $\langle v_2\rangle$ is almost same with different definitions of eccentricity for a given

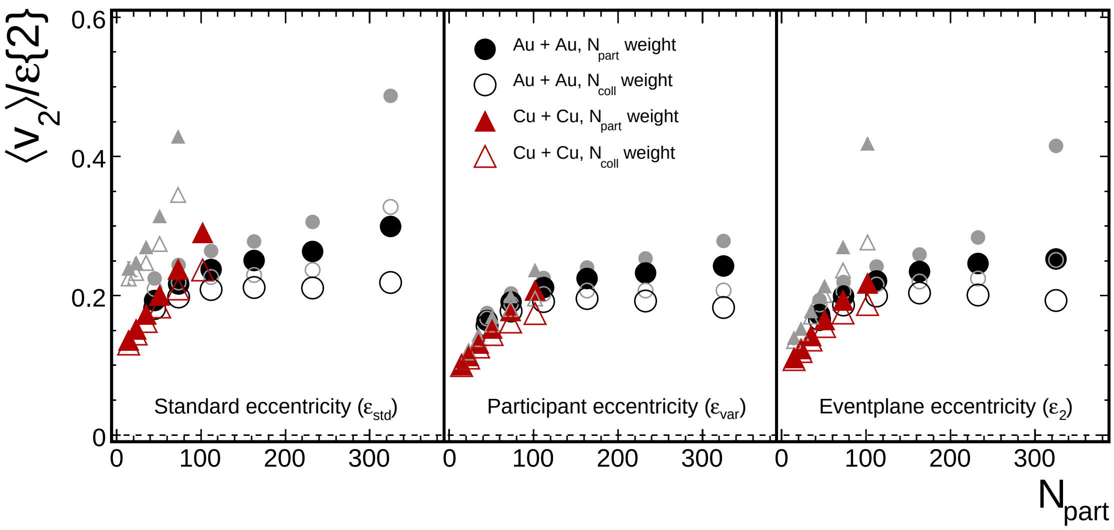

Figure 5.5: Comparison of $\langle v_2\rangle/\varepsilon\{2\}$ as a function of N_{part}. From left to right figures, $\langle\varepsilon_{std}\rangle$, $\langle\varepsilon_{var}\rangle$, and $\langle\varepsilon_2\rangle$ are used for scaling, respectively. Grey data points show the $\langle v_2\rangle/\langle\varepsilon\rangle$ (standard averaging).

centrality. One can also see that the $\langle v_2\rangle/\varepsilon\{2\} < \langle v_2\rangle/\langle\varepsilon\rangle$ (grey data points), which is due to $\varepsilon\{2\} > \langle\varepsilon\rangle$ (see Fig. A.5 and A.6). In our current systematic error on $\langle v_2\rangle$ and ε, it is difficult to conclude which is the best quantity to explain the scaling of $\langle v_2\rangle$.

For all defenitions of eccentricity, scaled v_2 is relatively smaller and flatter by $\langle\varepsilon\rangle$ weighting with N_{coll} density profile. Since the hydrodynamics is scale invariant, $\langle v_2\rangle/\langle\varepsilon\rangle$ becomes independent of the system size if the complete local thermal equilibrium is established. Therefore, flatter $\langle v_2\rangle/\langle\varepsilon\rangle$ with N_{coll} density might suggest that the local thermal equilibrium is attained, although there is a possibility that this flatter behavior of $\langle v_2\rangle/\langle\varepsilon\rangle$ is just a coincidence.

5.2 Interpretation with Blast-wave Picture

The elliptic flow could be one of the most sensitive signatures in the early stage of heavy ion collisions. Therefore, detaild comparison between measured v_2 and hydrodynamical model can shed light on the thermodynamic bulk properties of the system and the collision dynamics.

Blast-wave model parameterization is similar to the freeze-out configuration obtained from hydrodynamical model but the physical parameters of the configuration are treated as free parameters. It is widely used to describe the temperature and common velocity field at the kinetic freeze-out by comparing with the measured single particle spectra and v_2. However, one could expect v_2 is more sensitive to the early stage before the kinetic freeze-out takes place so that the transverse momentum spectra and v_2 may have different sensitivities to the dynamics in the heavy ion collisions.

In this section, we show the independent fitting results of single particle spectra and v_2 by extended Blast-wave model, and discuss the extracted parameters and its relation of collision dynamics.

5.2.1 Extended Blast-wave Model

In order to study the sensitivity of initial density profile to measured v_2, we perform the fitting with Blast-wave parameterization. In the standard Blast-wave framework, density distribution is assumed to be constant and velocity profile is linear as a function of radius in the transverse directions. In our extended Blast-wave model, we use more realistic density and veloicty distributions inspired from the Hydrodynamical model. That is, the density distribution is detemined by the initial overlap density (N_{part} or N_{coll} density profile), and the velocity distribution is calculated by its gradient distributions. As we already discussed in Section 5.1, N_{coll} density profile is more closely related to the degrees of thermalization, one could expect that v_2 may be described in N_{coll} density distributions than in N_{part} density profile.

The basic assumptions of our Blast-wave model are listed below;

- Longitudinal boost invariance
- An instant freeze-out takes place just after the collision on a hyper-surface Σ at a proper time τ
- An instant freeze-out is independent of r at τ = const.
  - Use N_{part} or N_{coll} overlap density distributions from Glauber model
  - Initial spatial eccentricity ε is fixed by inital overlap geometry, and ε is calculated by

$$\varepsilon = \frac{\sum_i N_i(y_i^2 - x_i^2)}{\sum_i N^i(x_i^2 + y_i^2)} \tag{5.4}$$

    where N_i is the number density (N_{part} or N_{coll}) at (x, y), and x_i, y_i are the x and y positions for i^{th} participant.

- Radial boost velocity is assumed to be proportional to the density gradient distributions
  - The magnitude of radial boost velocity is fixed by the magnitude of density gradient
  - The boost direction (azimuthal angle of boost) is fixed by the direction of density gradient, thus the azimuthal dependence of boost β_n (n^{th} fourier harmonics, $n = 2, 4, ...$) is automatically determined by the gradient of density distributions. β_n is obtained by

$$\beta_n = \frac{\sum_i N_i G_i \cos(n\phi_i)}{\sum_i N_i G_i} \tag{5.5}$$

    where G_i is the gradient of the density profile at (x, y) and ϕ_i is the azimuthal angle with respect to the reaction plane for i^{th} participant. We only consider β_2 since the higher harmonics ($n \geq 4$) is negligible.

- No chemical freeze-out
- Freeze-out temperature is independent of the position for particles (x, y), $T(x, y) = T$, that is kinetic freeze-out takes place for all hadrons at the same time

There are 2 free parameters in our model: 1) freeze-out temperature (T), and 2) surface radial boost velocity (β_T).

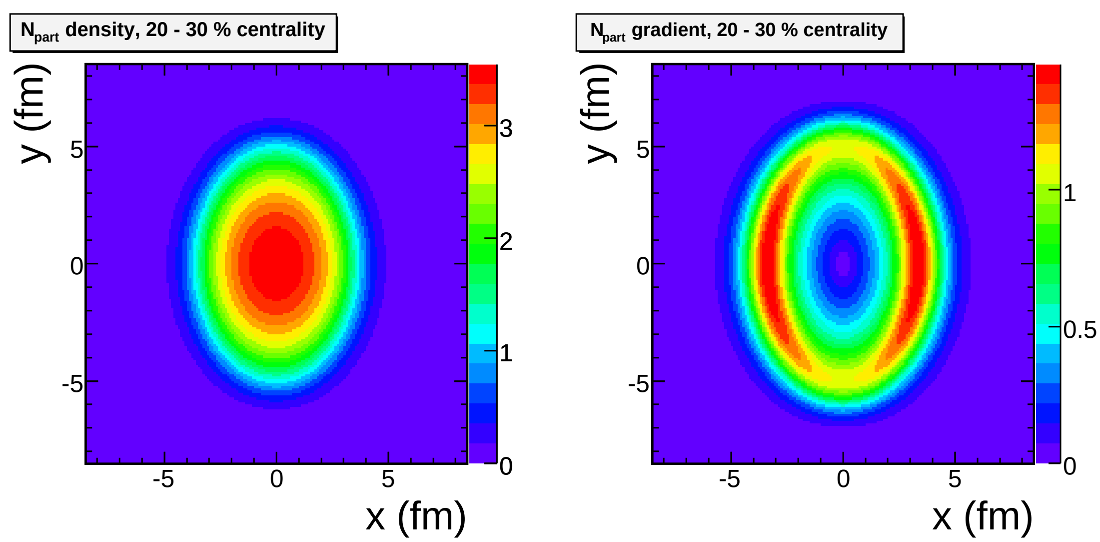

Figure 5.6: (Left) N_{part} density distribution in 20 - 30 % centrality. (Right) N_{part} gradient distribution in 20 - 30 % centrality.

Fig. 5.6 and 5.7 show N_{part} and N_{coll} density distributions (left), gradient of density (right) in 20 - 30 % centrality, respectively used in our model. One can see that the

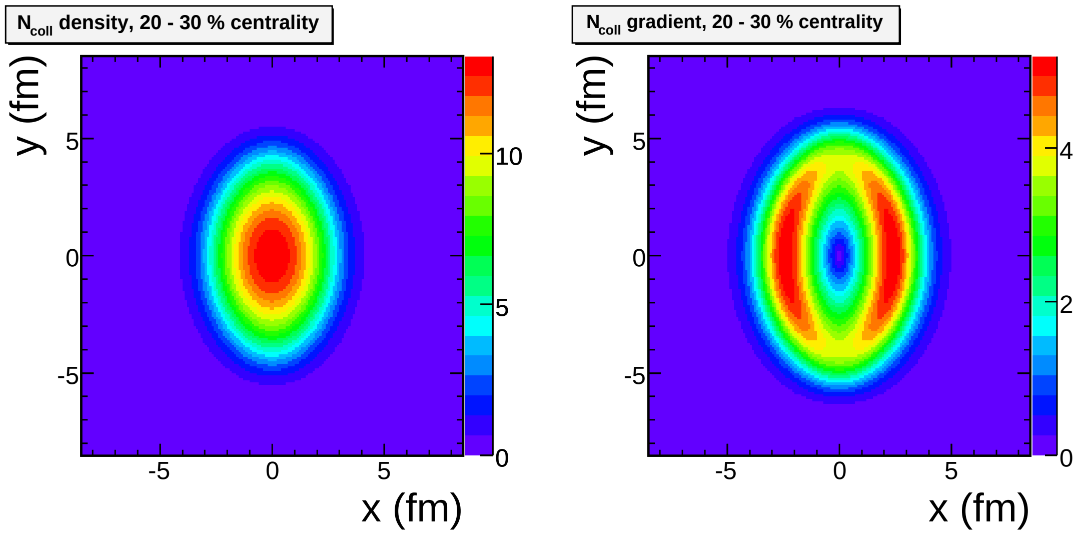

Figure 5.7: (Left) N_{coll} density distribution in 20 - 30 % centrality. (Right) N_{coll} gradient distribution in 20 - 30 % centrality.

width of x direction in N_{coll} distribution is smaller than that of N_{part} distribution. Since the density is larger in the smaller r, number of collisions for each participant nucleon become larger in small r. That is why N_{coll} distribution become steeper compared to the N_{part} distribution.

Fig. 5.8 show the N_{part} and N_{coll} density distributions and gradient arrows in 20 - 30 % centrality bin. As one already sees in Fig. 5.6 and 5.7, the steeper N_{coll} distribution lead to larger gradient, i.e. larger velocity, for a given $(x,\ y)$ position compared to N_{part} distributions. The direction of arrows are used as the azimuthal angles of boost direction.

Fig. 5.9 show the projections of N_{part} density and its gradient as a function of r for several centrality classes. One can see that the density distributions in in-plane are steeper than out-of-plane and that trend is more visible for peripheral collisions.

The more details of our Blast-wave parameterization are described in Appendix C.

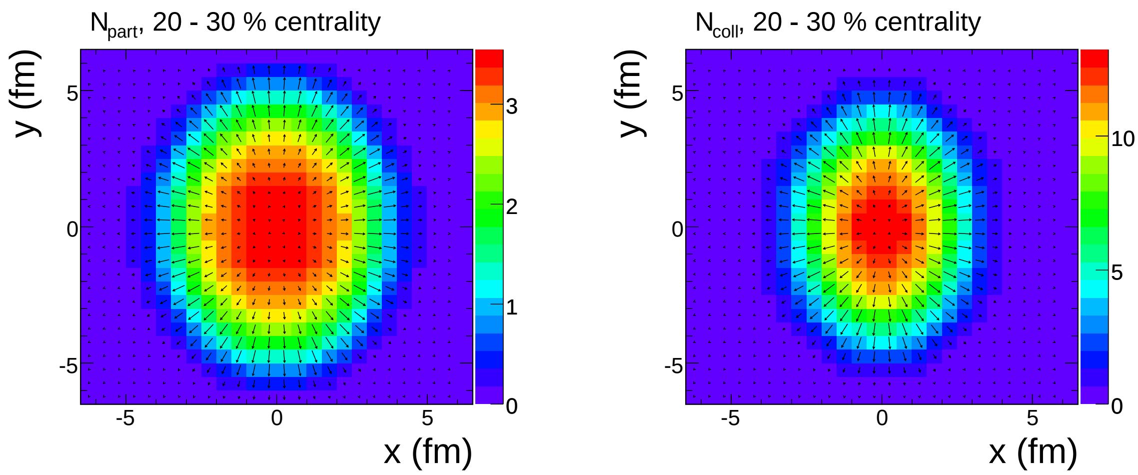

(a) (b)

Figure 5.8: (a) N_{part} density distributions, and (b) N_{coll} density distributions in 20 - 30 % centrality. The direction of arrows indicates the direction of gradient, and the length of arrows is the magnitude of gradient. The maximum value of gradient is normalized to 1 in these figures.

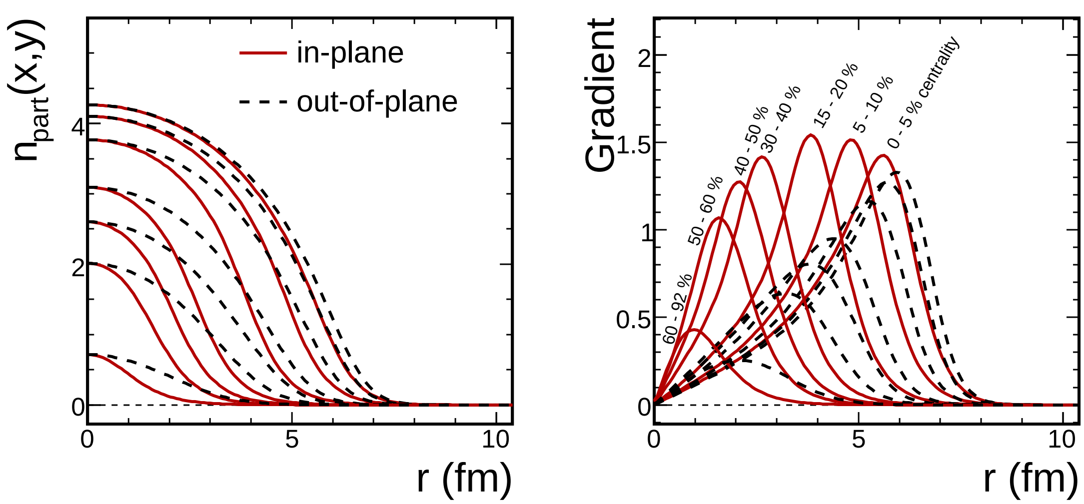

Figure 5.9: (Left) Centrality dependence of projections of N_{part} density distributions into x-axis (solid red) and y-axis (dashed black). (Right) Centrality dependence of projections of N_{part} gradient distributions, i.e. velocity distributions, into x-axis (solid red) and y-axis (dashed black).

5.2.2 Fitting Results

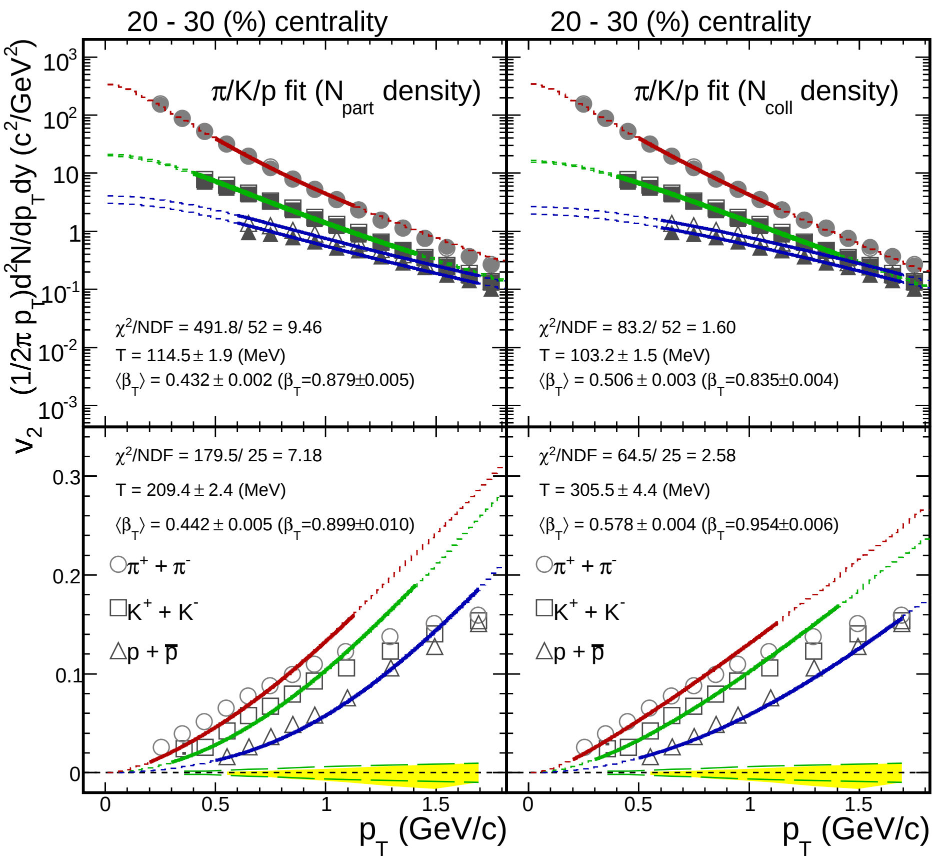

Figure 5.10: Fitting results for π, K and p by Blast-wave model in $20-30$ % centrality. Single particle spectra and v_2 are fitted independently. Fitting is performed by minimizing χ^2 for π, K and p simultaneously. Left and right panel show the results with N_{part} and N_{coll} density, respectively. Yellow bands represents the systematic error on $v_2(p)$, and green dashed lines are the systematic error on $v_2(K)$. Solid lines on the data points represent the fitting results in the p_{T} range denoted in Table 5.1, and doted lines extrapolate fitting results in lower and higher p_{T} range.

Fig. 5.10 show the fitting results for both spectra and v_2 in $20-30$ % centrality bin by Blast-wave model. The data points of p_{T} spectra is taken from [10], and results of v_2 are obtained in this thesis. Fitting is performed for π, K and p simultaneously. Fitting range for each particle species are summarized in Table 5.1. Higher p_{T} values are determined by requiring $m_{\mathrm{T}} - m_0 < 1$ GeV/c. We exclude the low p_{T} pions from spectra because there are significant contributions from resonance decays. Minimization of χ^2 is performed including the systematic error. The systematic error on $v_2(\pi)$ are not plotted in the figure but the magnitude of the error is comparable to that of K. One can see that the fitting for π is not so good especially by using N_{part} density distribution, so we also fit the spectra and v_2 for K and p excluding π as shown in Fig. 5.11.

Table 5.2 summarize the extracted parameters. Average radial flow velocity, $\langle\beta_T\rangle$, is

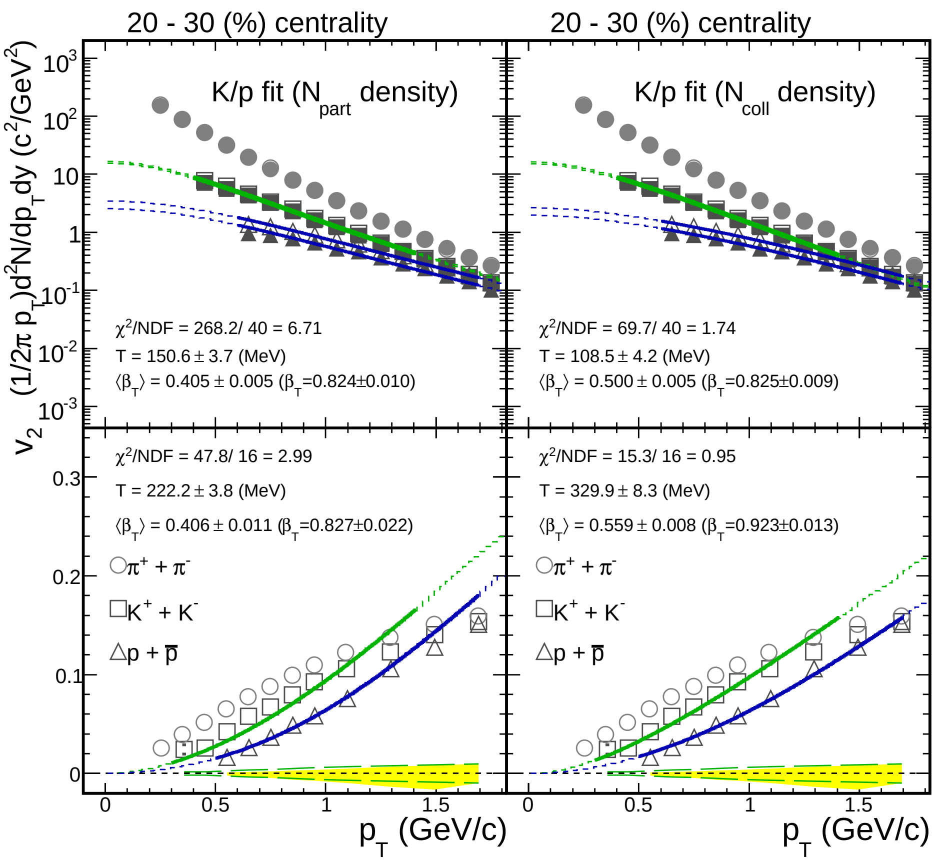

Figure 5.11: Fitting results for K and p by Blast-wave model in $20-30$ % centrality.

Table 5.1: Fitting range used in the Blast-wave fit.

	Fitting range	
Particle species	spectra	v_2
π	0.5 - 1.13 GeV/c	0.2 - 1.13 GeV/c
K	0.4 - 1.40 GeV/c	0.3 - 1.40 GeV/c
p	0.6 - 1.70 GeV/c	0.5 - 1.70 GeV/c

Table 5.2: Summary of extracted T, $\langle \beta_T \rangle$ and χ^2/NDF in $20 - 30$ % centrality.

Parameters	$\pi + K + p$		$K + p$	
Density profile	N_{part}	N_{coll}	N_{part}	N_{coll}
Statistical error only : spectra fit				
T (MeV)	114.5 ± 1.9	103.2 ± 1.5	150.6 ± 3.7	108.5 ± 4.2
$\langle \beta_T \rangle$	0.432 ± 0.002	0.506 ± 0.003	0.405 ± 0.005	0.500 ± 0.005
χ^2/NDF	$491.8/52 = 9.5$	$83.2/52 = 1.6$	$268.2/40 = 6.7$	$69.7/40 = 1.7$
Statistical error only : v_2 fit				
T (MeV)	213.2 ± 2.4	311.8 ± 0.7	231.9 ± 2.4	341.4 ± 2.5
$\langle \beta_T \rangle$	0.450 ± 0.005	0.582 ± 0.001	0.404 ± 0.005	0.547 ± 0.004
χ^2/NDF	$4761.1/25 = 190.4$	$1836.2/25 = 73.5$	$270.5/16 = 16.9$	$82.7/16 = 5.2$
Include systematic error on v_2 for χ^2 minimization				
T (MeV)	209.4 ± 2.4	305.5 ± 4.4	222.2 ± 3.8	329.9 ± 8.3
$\langle \beta_T \rangle$	0.442 ± 0.005	0.578 ± 0.004	0.406 ± 0.011	0.559 ± 0.008
χ^2/NDF	$179.5/25 = 7.2$	$64.5/25 = 2.6$	$47.8/16 = 3.0$	$15.3/16 = 1.0$

calculated by integrating the gradient distribution weighted with density profile. Several features are listed below.

- Temperature
  - For spectra, consistent values are obtained from both N_{part} and N_{coll} density
  - For v_2, temperature in N_{coll} density is about 100 MeV larger than N_{part} density.
  - Temperatures obtained from v_2 fitting are about 100 - 200 MeV higher than that from spectra.
- $\langle \beta_T \rangle$
  - Larger $\langle \beta_T \rangle$ in N_{coll} density for both spectra and v_2.
- χ^2/NDF
  - Better χ^2/NDF in N_{coll} density profile for both spectra and v_2.
  - Better χ^2/NDF if one exclude π from fitting.

As one can see that the results obtained from K and p fit give always better χ^2/NDF compared to that from π, K and p fit. Larger temperature from the fitting of v_2 could suggest that the magnitude of v_2 saturate in early time compared to the time scale of kinetic freeze-out which can be obtained by the spectra fit only. In order to see

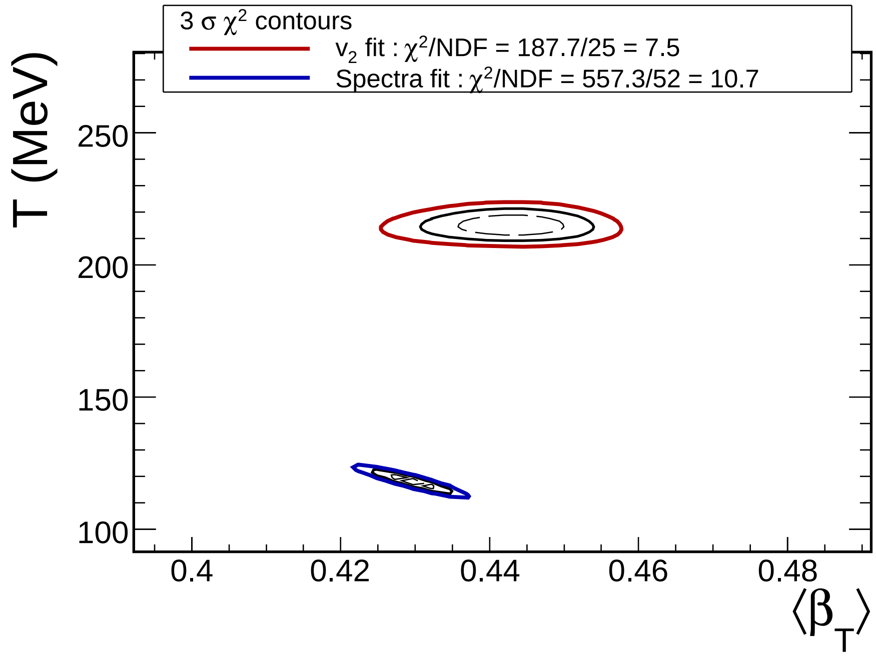

Figure 5.12: 3 σ χ^2 contour for temperature vs average radial flow velcoity with N_{part} density profile. Dashed and solid black line show the 1 and 2 σ contour, and solid red (blue) line represent 3 σ contour line for v_2 (spectra).

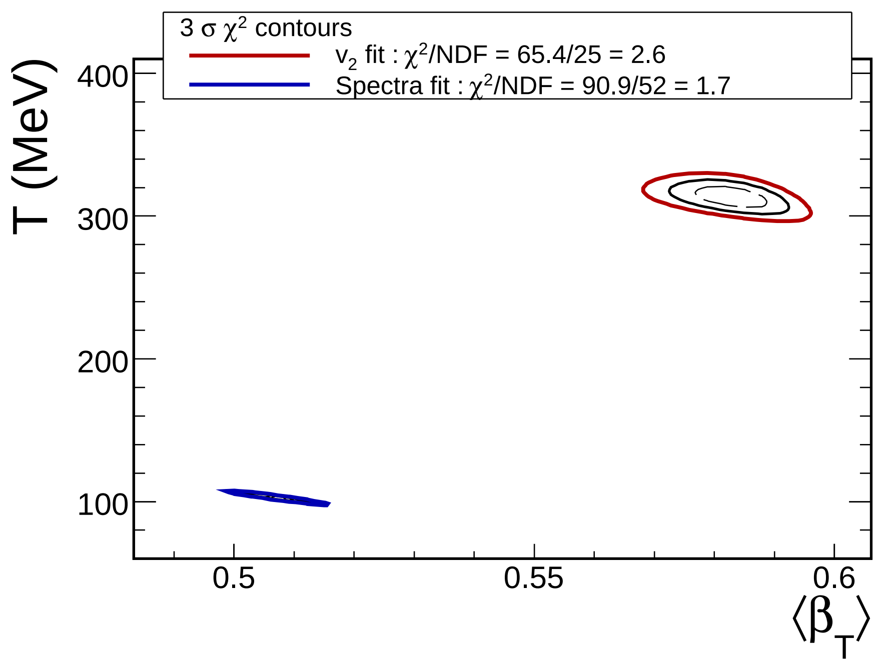

Figure 5.13: 3 σ χ^2 contour for temperature vs average radial flow velcoity with N_{coll} density profile.

the difference of temperature and radial flow velocity between spectra and v_2 visually, contour lines of χ^2 are plotted in temperature with respect to the radial flow velocity.

Fig. 5.12 and 5.13 show the 3 σ contour lines for temperature with respect to the average radial flow velocity for both spectra (blue) and v_2 (red) with N_{part} and N_{coll} density profile. The contours of χ^2 are obtained from π, K and p fitting. Slightly different minimum χ^2 positions are due to the finite bin size of temperature and $\langle \beta_T \rangle$. One clearly sees that the minimum position of χ^2 is quite different between spectra and v_2 for both results.

From the next section, we only consider the results from K and p fitting since the shape of $v_2(p_{\mathrm{T}})$ for π from Blast-wave model does not well reproduce the data, and it gives better χ^2/NDF for both spectra and v_2 compared to that from π, K and p fitting.

5.2.3 Sensitivity to the Eccentricity

In order to study the effective dynamical evolution of the system, the eccentricity value is varied by expanding the initial density distribution given from Glauber model. For the sake of simplicity, we only consider the expansion of x-direction, i.e. the direction of reaction plane. Since the pressure gradient is largest in that direction, this simple expansion gives naively correct picture of the system evolution.

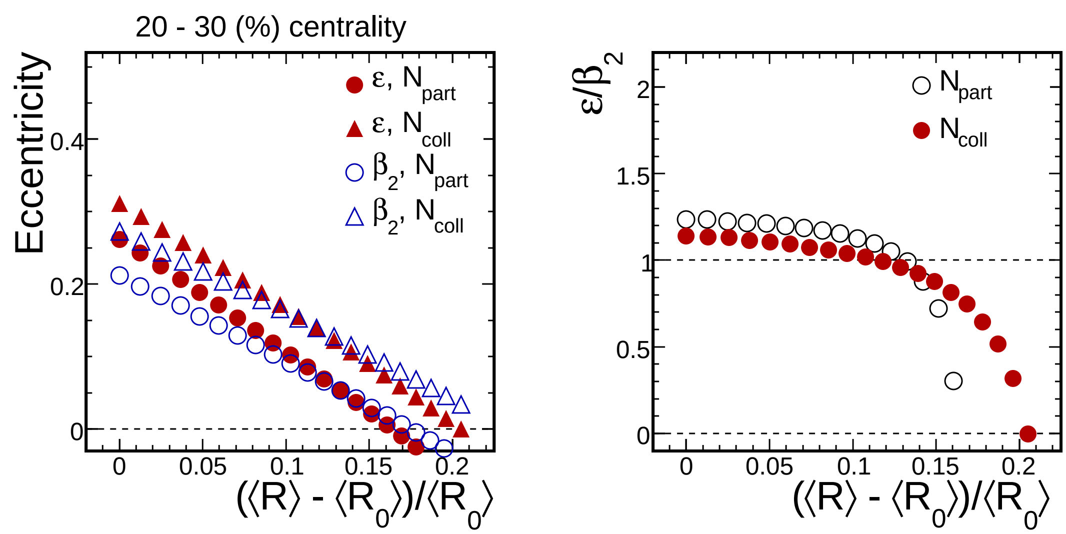

Figure 5.14: Transverse length dependence of eccentricity and β_2 in $20-30$ % centrality (left). Right figure shows the ratio of ε to β_2 as a function of $(\langle R\rangle - \langle R_0\rangle)/\langle R_0\rangle$.

Fig. 5.14 shows the eccentricity weighted by N_{part} (solid red circles) and N_{coll} (solid red triangles) as a function of normalized transverse length. $\langle R\rangle$ variable is defined as

$$\frac{1}{\langle R\rangle^2} = \frac{1}{\langle x^2\rangle} + \frac{1}{\langle y^2\rangle} \tag{5.6}$$

$\langle R\rangle$ is more natural choice than the rms radius of the system since v_2 is driven by the pressure gradient [50]. $\langle R_0\rangle$ value is the average transverse length in the initial density profile given by the Glauber model.

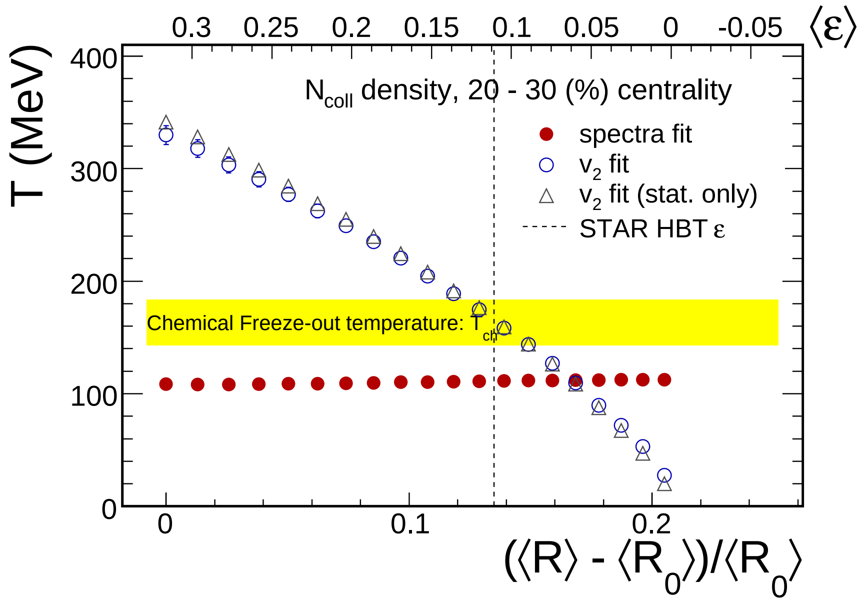

Figure 5.15: Temperature T as a function $(\langle R\rangle - \langle R_0\rangle)/\langle R_0\rangle$ obtained from N_{coll} density profile. Solid red and open black symbols show the results from spectra and v_2, respectively. Open triangles show the result from v_2 fitting with statistical error only. Yellow band represent the lower and upper values of chemical freeze-out temperature $T_{ch} = 143 - 184$ (MeV) [56, 57]. Black dashed line show the $\langle\varepsilon\rangle$ value taken from azimuthal HBT analysis at STAR experiment [58]. Top x-axis denote the corresponding values of $\langle\varepsilon\rangle$.

Fig. 5.15 shows the temperature T as a function of $(\langle R\rangle - \langle R_0\rangle)/\langle R_0\rangle$ in $20-30$ % centrality with N_{coll} deisnty profile. The temperature from spectra fit are unchanged with $\langle R\rangle$ as it should since transverse momentum spectra does not depend on the eccentricity. And the temperature values are smaller than that at chemical freeze-out temperature which is given in [56, 57]. This result support that the temperature obtained from spectra fit could reflect the conditions where the kinetic freeze-out takes place. If one look at the Fig. 5.16 and 5.17, average radial flow velocity $\langle\beta_T\rangle$ and χ^2/NDF are also unchanged so much for spectra fit.

However, the result of temperature from v_2 fit significantly decrease with $(\langle R\rangle - \langle R_0\rangle)/\langle R_0\rangle$ and become same temperature value from spectra fit around $\langle\varepsilon\rangle \sim 0.06$. For $\langle\beta_T\rangle$ values, it initially 0.1 larger than that from spectra fit, and coincide in large $(\langle R\rangle - \langle R_0\rangle)/\langle R_0\rangle$. The χ^2/NDF values are slowly decreasing with $(\langle R\rangle - \langle R_0\rangle)/\langle R_0\rangle$ and take the minimum value around $(\langle R\rangle - \langle R_0\rangle)/\langle R_0\rangle \sim 0.22$ ($\langle\varepsilon\rangle \sim 0.06$). One also see that the results about temperature and average radial flow velocity from χ^2 minimization with statistical error unchanged compared to that obtained with statistical and systematic error.

Dashed lines in Fig. 5.15 − 5.17 represent the $\langle \varepsilon \rangle$ value obtained from azimuthal HBT analysis at STAR [58]. We define its value as the time when the kinetic freeze-out takes place. Corresponding $(\langle R \rangle - \langle R_0 \rangle)/\langle R_0 \rangle$ value at kinetic freeze-out is about 0.13. If one compare the temperature of v_2 and spectra at the kinetic freeze-out, the temeperature from v_2 is as large as T_{ch}, and larger than that of spectra. This result suggest that the "freeze-out" of v_2 could occur at the chemical freeze-out and its freeze-out is earlier than that of spectra. The result obtained by changing the eccentricity is consistent with the picuture of the collective in-plane expansion, where the initial eccentricity is quenched and the v_2 is developed through the expansion of the system with time.

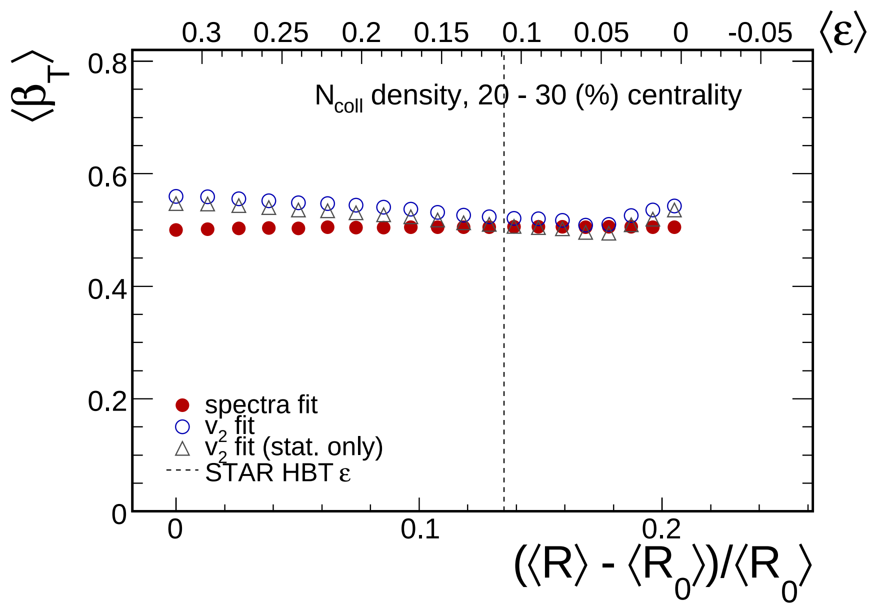

Figure 5.16: Average radial flow velocity $\langle \beta_T \rangle$ as a function $(\langle R \rangle - \langle R_0 \rangle)/\langle R_0 \rangle$ obtained from N_{coll} density profile.

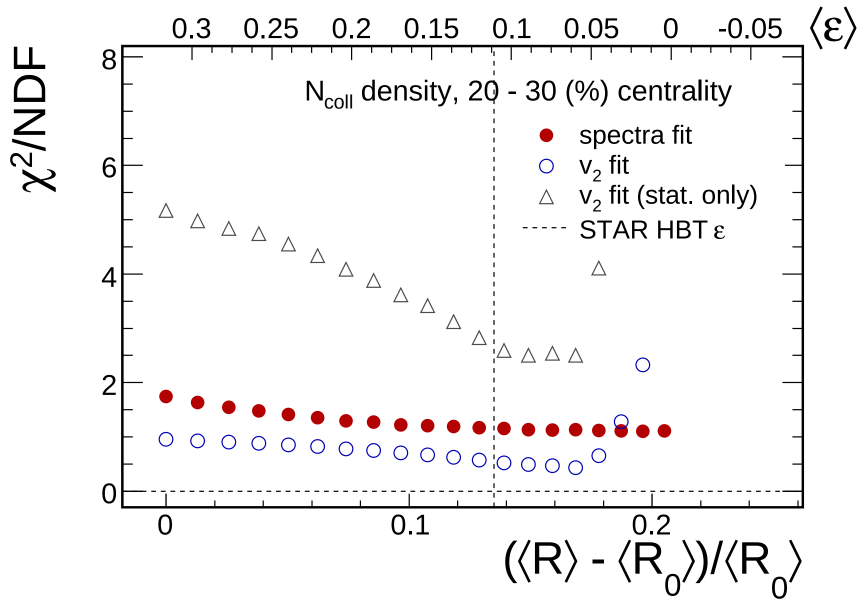

Figure 5.17: χ^2/NDF as a function $(\langle R\rangle - \langle R_0\rangle)/\langle R_0\rangle$ obtained from N_{coll} density profile.

5.2.4 Robustness of Fitting Results

In order to check the robustness of the fitting, we have checked several systematics of the fitting resutls as follows;

- Vary the size of system
- Vary velocity profile for a given density distribution.
- Use different parameterization for Woods-saxon density profile
  - $\sigma_{NN} = 42$ mb, $a = 0.53$ fm (default)
  - $\sigma_{NN} = 37$ mb, $a = 0.53$ fm
  - $\sigma_{NN} = 47$ mb, $a = 0.53$ fm
  - $\sigma_{NN} = 42$ mb, $a = 0.43$ fm
  - $\sigma_{NN} = 42$ mb, $a = 0.63$ fm
- Different centrality window, $10 - 20$ % and $30 - 40$ %.

System Size

Since v_2 does not depend on the absolute scale of R_x and R_y, where $R_x(_y)$ denote the radius of x (y) direction, only depends on the ratio of size for x and y (R_y/R_x), fitting results should not be changed with the system size. We confirmed that the results are unchanged for both spectra and v_2 with reasonable range of the system size.

Parameterization of Woods-saxon density profile

Table 5.3: Summary of temperatures and average velocity for different parameterizations from v_2 fit

Type	N_{part} weight				
	$\langle\varepsilon\rangle$	β_2	T (MeV)	$\langle\beta_T\rangle$	χ^2/NDF
default	0.262	0.212	222.2 ± 3.8	0.436 ± 0.012	47.8/16 = 3.0
(1)	0.270	0.220	232.5 ± 3.9	0.444 ± 0.011	42.4/16 = 2.7
(2)	0.254	0.204	213.2 ± 3.7	0.427 ± 0.012	53.3/16 = 3.3
(3)	0.311	0.245	234.8 ± 3.9	0.441 ± 0.012	63.0/16 = 4.0
(4)	0.216	0.180	202.9 ± 3.6	0.423 ± 0.011	38.5/16 = 2.4
	N_{coll} weight				
	$\langle\varepsilon\rangle$	β_2	T (MeV)	$\langle\beta_T\rangle$	χ^2/NDF
default	0.311	0.272	329.9 ± 8.3	0.582 ± 0.008	15.3/16 = 1.0
(1)	0.311	0.272	329.9 ± 8.3	0.582 ± 0.008	15.3/16 = 1.0
(2)	0.311	0.272	329.9 ± 8.3	0.582 ± 0.008	15.3/16 = 1.0
(3)	0.354	0.300	330.6 ± 8.0	0.587 ± 0.009	19.8/16 = 1.2
(4)	0.269	0.248	320.2 ± 8.2	0.575 ± 0.008	12.9/16 = 0.8

Different parameterizations of Woods-saxon density distribution are used to check the stability of the extracted parameters. Table 5.3 summarize the results of extracted parameters from v_2 fit from different parameterizations for the Glauber model, where (1) $\sigma_{NN} = 37$ mb, (2) $\sigma_{NN} = 47$ mb, (3) $a = 0.43$ fm, and (4) $a = 0.63$ fm. σ_{NN} and a denote the inelastic $p+p$ cross sections and surface diffuseness parameters, respectively. Comparing the results from default parameterization given in Table 5.2, the temperature (average velocity) is about 10 (6) % changed for N_{part} weight, while for N_{coll} weight the difference is relatively smaller, about 4 % for both T and $\langle\beta_T\rangle$. The difference obtained from this study are included in the systematic errors on extracted parameters.

Velocity Profile

The sensitivity of the extracted parameters are studied by varying the velocity profile distribution for the density distribution where the χ^2/NDF is miniumum, $(\langle R\rangle - \langle R_0\rangle)/\langle R_0\rangle \sim 0.22$. The velocity distribution is modified by adding $1 \pm 2\beta_2 \cos(2\phi)$ to the original velocity profile in Glauber model, where β_2 is 2^{nd} harmonics of radial flow velocity introduced in Eq. (5.5) for $n = 2$. We found that χ^2/NDF become larger if the velocity profile varied by the β_2 parameter for both N_{part} and N_{coll} density, i.e. the minimum χ^2/NDF is obtained at the initial velocity profile given by Glauber model. This result could suggest that the v_2 is sensitive to the velocity profile which is determined by the initial density overlap.

Different centrality

Other centrality bins, namely $10 - 20$ % and $30 - 40$ % centrality bins, are also fitted to see the centrality dependence of extracted parameters, and the results are shown in Table 5.4. $\langle \varepsilon \rangle$ and β_2 is calculated by Eq. (5.4) and Eq. (5.5), respectively.

Table 5.4: Summary of temperatures and average velocity for different centrality classes. Results of $20 - 30$ % centrality are taken from Table 5.2.

Centrality (%)	N_{part} weight				
	$\langle \varepsilon \rangle$	β_2	T (MeV)	$\langle \beta_T \rangle$	χ^2/NDF
0 - 10 %	0.061	0.049	126.2 ± 7.9	0.410 ± 0.016	$15.0/16 = 0.9$
10 - 20 %	0.178	0.141	201.0 ± 3.9	0.397 ± 0.009	$48.0/16 = 3.0$
20 - 30 %	0.262	0.212	222.2 ± 3.8	0.436 ± 0.012	$47.8/16 = 3.0$
30 - 40 %	0.331	0.276	261.5 ± 4.6	0.444 ± 0.012	$31.2/16 = 2.0$

	N_{coll} weight				
	$\langle \varepsilon \rangle$	β_2	T (MeV)	$\langle \beta_T \rangle$	χ^2/NDF
0 - 10 %	0.082	0.069	185.7 ± 11.3	0.517 ± 0.012	$11.9/16 = 0.8$
10 - 20 %	0.221	0.186	285.7 ± 9.1	0.549 ± 0.006	$19.4/16 = 1.2$
20 - 30 %	0.311	0.272	329.9 ± 8.3	0.582 ± 0.008	$15.3/16 = 1.0$
30 - 40 %	0.379	0.347	386.7 ± 9.5	0.581 ± 0.010	$15.6/16 = 1.0$

5.3 Partonic Collectivity

Hadron production via quark coalescence mechanism predicts the universal scaling of v_2 from thermalized partons

$$v_2^h(p_T) \simeq n_q \times v_2^q\,(p_T/n_q) \tag{5.7}$$

where n_q is the number of constituent quarks in hadrons, v_2^h and v_2^q are hadron v_2 at p_T and quark v_2 at p_T/n_q, respectively. This quark number scaling indicates that the elliptic flow is developed in the early partonic stage of heavy ion collisions.

In Section 5.3.1, we first discuss the quark number scaling of v_2 for several different particle species in minimum bias events. Second, the validity of quark number scaling of v_2 is also discussed for different centrality classes in Section 5.3.2.

5.3.1 Quark Number Scaling in Minimum Bias Events

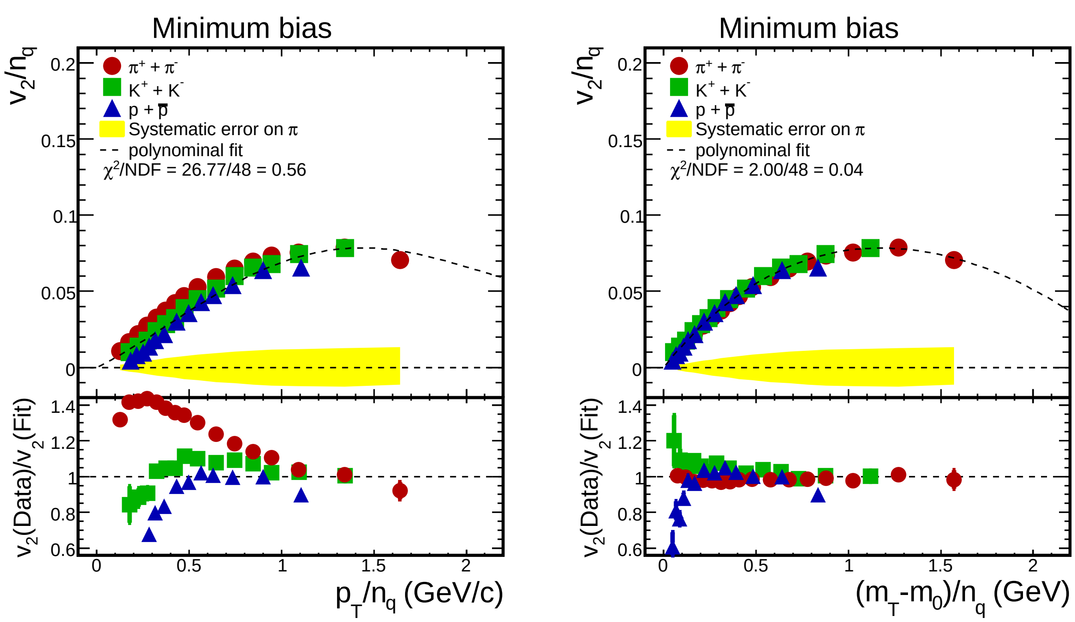

Figure 5.18: v_2 as a function of p_T (left) and $m_\mathrm{T} - m_0$ (right) divided by number of quarks for each hadrons ($n_q = 2$ for mesons and $n_q = 3$ for protons) in minimum bias events. Yelllow bands show the absolute systematic error on $\pi^+ + \pi^-$ Dashed lines represent the simultaneous fitting results for π, K and p by 4^{th} polynominal functions. Bottom figures show the ratios of data to fitting results of v_2.

Fig. 5.18 shows the v_2/n_q as a function of p_T/n_q (left) and KE_T/n_q (right) for identified hadrons in minimum bias events. The scaled v_2 values are fitted by polynominal function in order to test the validity of the quark number scaling. The ratio of data to fitting result is plotted in the bottom panels. One immediately find that the scaling breaks at $p_{\mathrm{T}}/n_q < 1$ GeV/c, and the ratio is larger for lighter hadrons (i.e., $\pi > K > p$). As we already discussed in Section 1.3.3, the resonance decay contributions could be one of the possible explanations about the deviation of π from the quark number scaling [18].

Recently, the PHENIX collaboration found that the quark number scaling of v_2 with transverse kinetic energy $KE_{\mathrm{T}} = m_{\mathrm{T}} - m_0$ (GeV) holds full measured KE_{T} range [54]. If the elliptic flow is driven by the hydrodynamical pressure gradient, the magnitude of v_2 is expected to scale with KE_{T} since the pressure gradient is directly linked to the collective kinetic energy of the emitted particles.

The scaling of v_2 with KE_{T} is plotted in the right panel. The fitting is also performed by polynominal function and take the ratio as shown in right bottom panel. The ratio shows excellent scaling in the measured KE_{T} range compared to the p_{T} scaling in left panel, except for very low KE_{T}. This result support the picture that the elliptic flow is driven by the hydrodynamical collective pressure gradient.

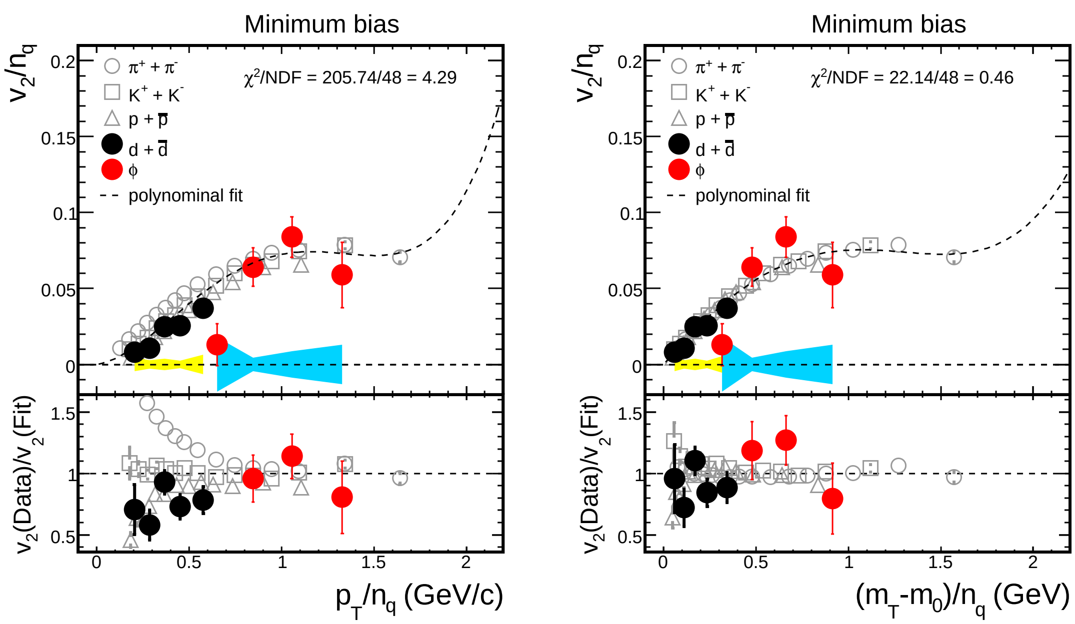

Figure 5.19: Quark number scaling of v_2 for d ($n_q = 6$) and ϕ ($n_q = 2$) as a function of p_{T} (left) and $m_{\mathrm{T}} - m_0$ (right) in minimum bias events. Yellow and blue bands around $v_2 = 0$ represent the absolute systematic error on v_2 for d and ϕ, respectively. Dashed lines are the fitting results by 4^{th} polynominal functions. Bottom figures show the ratio of data to fitting of v_2.

Elliptic flow for ϕ mesons could provide the evidence of partonic collectivity in the early pre-hadronic stage of heavy ion collisions. Because of their small hadronic cross sections with non-strange hadrons and their relatively longer lived life time, ϕ meson is expected to reach the detector with almost no interactions with the other hadrons in the later hadronic stage. Thus, if quark number scaling holds to v_2 for ϕ meson, it should reflect the elliptic flow of thermal s-quark which is developed in the partonic stage of the system.

One could test the validity of this hypothesis that v_2 of each constituent quark is additive in the coalescence mechanism by measuring deuteron v_2. At RHIC energies, the dominant production mechanism of deuterons is considered as hadron coalescence with p and n, and in fact the measurement of the yield for d and $\bar{d}$ support the hadron coalescence of p and n [55]. Thus, the measurement of v_2 for deuterons could be a good probe to test the additive scaling relations among the constituents, i.e. first with respect to the v_2 of its constituent of hadrons, and second with respect to the v_2 of the constituent quarks of those hadrons ($n_q = 2 \times 3$).

Fig. 5.19 show the comparison between quark number scaling of v_2 for ϕ mesons and deuterons and those for π, K and p as a function of p_{T} and $m_{\mathrm{T}} - m_0$ in minimum bias events. Scaled v_2 of deuterons are in good agreement with the protons as shown in left panel. This result support that $v_2(d)$ is additive with respect to their constituent hadrons. And scaled v_2 for ϕ mesons are also consistent with the other hadrons within the errors. Right panel shows universal scaling of v_2 with KE_{T} and d and ϕ lie on the same line together with the other hadrons, although the statistical and systematic errors on ϕ mesons are large. This results are the strong indication that the elliptic flow is established under the conditions where the partonic degrees of freedom is relevant.

5.3.2 Centrality Dependence of Quark Number Scaling of v_2

The validity of quark number scaling has also studied in measured centrality classes. Fig. 5.20 show the quark number scaling of $v_2(KE_{\mathrm{T}})$ from central to peripheral events. And Fig. 5.21 show the ratio of v_2(Data) to v_2(Fit) as a function of KE_{T}/n_q. One can see that the quark number scaling of v_2 holds for all centrality bin within the systematic errors, except for below $KE_{\mathrm{T}}/n_q \simeq 0.3$ GeV, which is corresponds to $KE_{\mathrm{T}} \simeq 0.6$ (0.9) GeV for mesons (protons). Large deviations at low KE_{T}/n_q from central to mid-central show the similar mass dependence as we see in $v_2(p_{\mathrm{T}})$ at low p_{T}, i.e. $v_2(\pi) \geq v_2(K) > v_2(p)$. This deviations could be due to the radial flow in the hadronic stage after the chemical freeze-out.

Fig. 5.22 show the quark number scaling of v_2 for d and ϕ compared to π, K and p in 3 different centrality bins. Although the statistical error bars on d and ϕ mesons are large, the quark number scaling of v_2 with KE_{T} also holds for d and ϕ in $0 - 60$ % centrality.

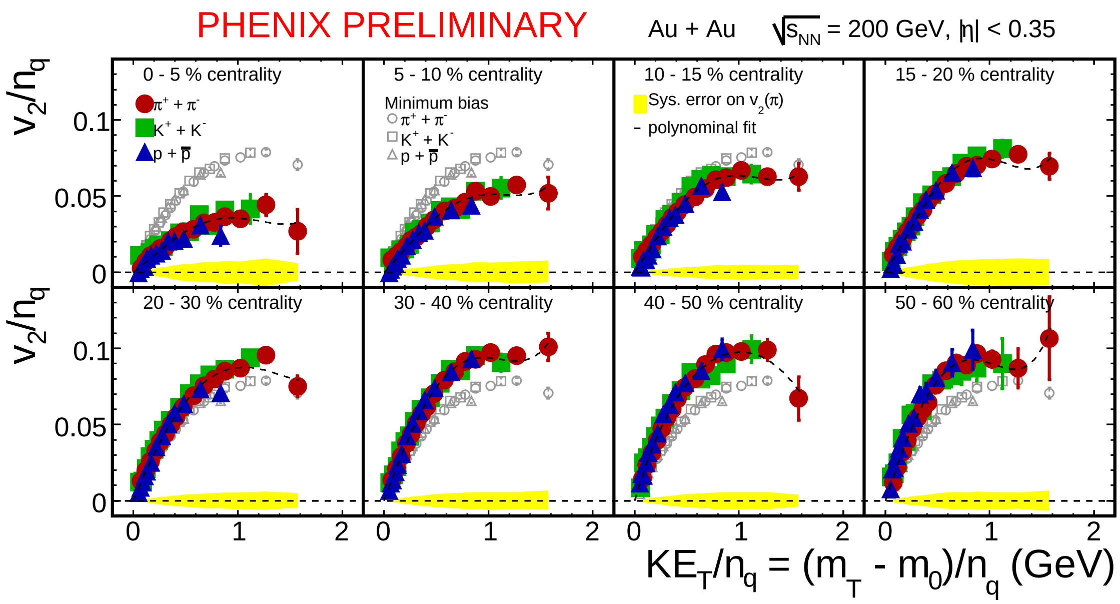

Figure 5.20: v_2/n_q vs $(KE_{\mathrm{T}})/n_q$ for π, K and p in different centrality classes. Yellow bands around $v_2/n_q = 0$ denote the systematic error on $v_2(\pi)$. Dashed lines represent the simultaneous fitting results for π, K and p by 4^{th} polynominal functions. Open data symbols in each panel show the v_2 in minimum bias event.

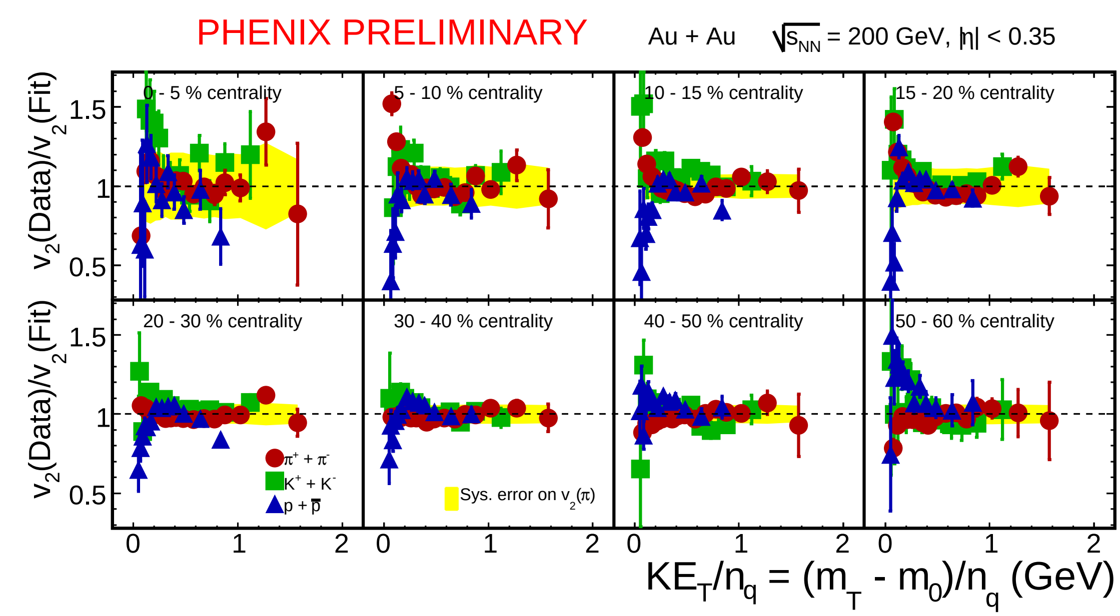

Figure 5.21: Ratio v_2(Data)/v_2(Fit) as a function of KE_{T}/n_q in different centrality classes. Yellow bands around $v_2/n_q = 0$ denote the systematic error on $v_2(\pi)$.

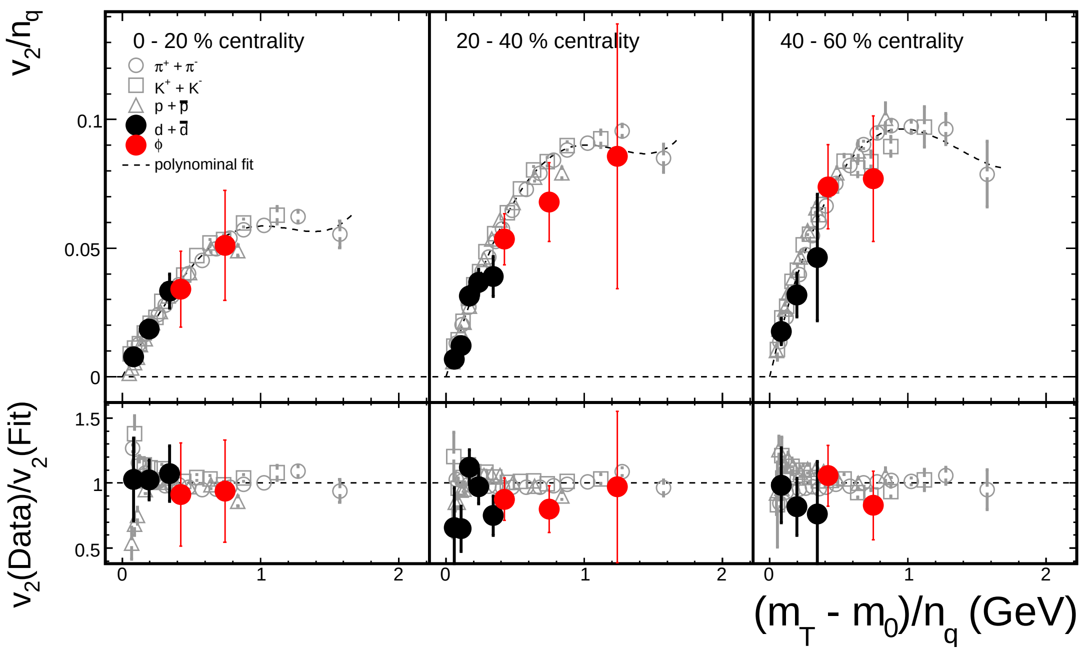

Figure 5.22: v_2/n_q vs $(m_{\rm T} - m_0)/n_q$ (top), and v_2(Data)/v_2(Fit) vs $(m_{\rm T} - m_0)/n_q$ (bottom) for d and ϕ in different centrality classes. Dashed lines represent the simultaneous fitting results by the 4^{th} polynominal functions.

5.4 Summary

From the discussions, we conclude that

- Eccentricity Scaling
  - $\langle \varepsilon_{var} \rangle$, which is taking into account the position fluctuations of participant nucleons, is the relevant quantity to explain the relation between initial geometry overlap and v_2.
  - Eccentricity scaling works in both Au + Au and Cu + Cu collisions with $\langle \varepsilon_{var} \rangle$. This result suggest that the ratio $\langle v_2 \rangle / \langle \varepsilon \rangle$ is determined by the number density even in the different systems.
- Blast-wave fit
  - For the initial density profile, T from v_2 fit is $100 - 200$ MeV larger than that from spectra fit, whereas $\langle \beta_T \rangle$ is almost unchanged between v_2 and spectra fit.
  - Better fitting resutls, i.e. smaller χ^2, are obtained from N_{coll} density profile than N_{part} density profile for both v_2 and spectra.
  - By considering in-plane 1D expansion, T from v_2 fit strongly decreases with the expansion while that from spectra fit remains constant. $\langle \beta_T \rangle$ does not changed so much with the expansion for both spectra and v_2.

  - If the kinetic freeze-out is defined at the $\langle \varepsilon \rangle$ estimated by azimuthal HBT, T from v_2 fit is as large as the chemical freeze-out temperature ($\sim$ 150 MeV).
  - The results from the simple expansion are consistent with the picture of the collective in-plane expansion, where the initial eccentricity is decreasing with time and the magnitude of v_2 is developed through the expansion of the system.

- Quark number scaling of v_2
  - Scaling of v_2 with p_T holds above $p_\mathrm{T} = 1$ GeV/c, but it breaks for $p_\mathrm{T} < 1$ GeV/c.
  - Scaling of v_2 with KE_T holds for all centrality bins within systematic errors, except for $KE_\mathrm{T}/n_q < 0.3$ GeV.
  - ϕ mesons are also follow the quark number scaling of v_2. This result support the picutre that the v_2 for ϕ meson is established at the pre-hadronic stage where the partonic degrees of freedom is relevant.

Chapter 6

Conclusions

We have measured the elliptic flow v_2 for identified $\pi^+ + \pi^-$, $K^+ + K^-$, $p + \bar{p}$, $d + \bar{d}$ and ϕ in a broad range of p_{T} (up to 4 GeV/c) and in detailed centrality in Au + Au collisions at $\sqrt{s_{\mathrm{NN}}} = 200$ GeV.

The main goal of ultra-relativistic heavy ion collisions is to find the quark-gluon plasma (QGP) and to study its properties under extreme conditions. Elliptic flow is one of the observables to probe the properties of QGP possibly created in the early stage of heavy ion collisions. If the local thermal equilibrium is reached, elliptic flow is determined through the initial geometry overlap (eccentricity) and the initial density profile. Therefore, elliptic flow could shed light on the possible local thermal equilibrium in the produced matter.

Using the data set taken in Run-4 period by the PHENIX experiment, the statistics increase by a factor 20 compared to the previous Run-2 data set. This allow us to extend the p_{T} reach for π and p with the carefull estimate of contamination, and to study the detailed centrality dependence of v_2. With the excellent capability of particle identification by Time-Of-Flight Counter ($\sigma_t \sim 120$ ps) and Electro-Magnetic Calorimeter ($\sigma_t \sim 400$ ps), and also with the good resolution of event plane at Beam-Beam Counter, we found the following important features;

- For $p_{\mathrm{T}} < 2$ GeV/c, v_2 shows the mass ordering, i.e. $(v_2(\pi) > v_2(K) > v_2(p) \geq v_2(\phi) > v_2(d))$. This characteristic p_{T} dependence of v_2 is consistent with hydrodynamical model calculations.

- For $p_{\mathrm{T}} > 2$ GeV/c, v_2 for mesons saturate earlier than that for baryons, i.e. $(v_2(\pi) \approx v_2(K) \approx v_2(\phi) < v_2(p) \approx v_2(d))$.

- v_2 increase from central to peripheral collisions. This behavior of v_2 is qualitatively consistent with the centrality dependence of the eccentricity.

The relation between $\langle \varepsilon \rangle$ (initial eccentricity) and final elliptic flow has been studied by eccentricity scaling of v_2. We have used $\langle \varepsilon_{var} \rangle$ (participant eccentricity) which is taking into account the position fluctuations for the participant nucleons, instead of the standard eccentricity. The average v_2, $\langle v_2 \rangle$, among Au + Au and Cu + Cu collisions are scaled together with $\langle \varepsilon_{var} \rangle$. This result suggest that the $\langle v_2 \rangle / \langle \varepsilon \rangle$ is determined by the number density of participant nucleons even in the different colliding system.

We have developed an extended Blast-wave model in which the effect of initial density profile has been investigated for both number of participant (N_{part}) and number of collision (N_{coll}) density distributions. Thermodynamic quantities, such as the freeze-out temperature T and the radial flow velocity β_T, have been extracted for both single particle spectra and v_2 independently. Extracted T's from v_2 fit are $100-200$ MeV larger than that from spectra fit, and the results obtained from N_{coll} density profile have always smaller χ^2/NDF for both spectra and v_2. This result could be attributed that the v_2 is developed by the number of collisions among the constituents not the number density of participant nucleons since the number of collisions are closely related to the degrees of thermalization. By studying the 1D in-plane expansion of the system, i.e. changing the eccentricity of the system, we have found that T from v_2 fit significantly decreases with the eccentricity, while those from spectra fit are unchanged. $\langle\beta_T\rangle$ for both spectra and v_2 remain constant with respect to the eccentricity. T from v_2 fit is as large as the chemical freeze-out temperature if we assume that the kinetic freeze-out takes place at the $\langle\varepsilon\rangle$ obtained by the azimuthal HBT analysis. Larger T from v_2 fit than that from spectra fit at the kinetic freeze-out may suggest that the freeze-out of v_2 could be earlier than that of spectra. These results are consistent with the picture of the collective in-plane expansion, where the initial eccentricity is quenched and the magnitude of v_2 is developed through the expansion with time.

The quark number scaling of v_2 has been examined for measured centrality range. The scaling works well for all particle species at $p_{\mathrm{T}}/n_q > 1$ GeV/c, however, it breaks at lower p_{T}. By assuming the v_2 is determined by the transverse kinetic energy $KE_{\mathrm{T}} = m_{\mathrm{T}} - m_0$, the quark number scaling of v_2 with KE_{T} lie on the universal curve for π, K and p in all centrality bins within the systematic errors, whereas the scaling of v_2 breaks for $KE_{\mathrm{T}}/n_q < 0.3$ GeV. Since the pressure gradient is directly linked to the transverse kinetic energy, this results could suggest that the collective pressure gradient is the driving force of elliptic flow. We have also observed that the quark number scaling of v_2 with KE_{T} holds for ϕ and d in different centrality selections. The cross section (mean free parth) of ϕ meson with the system is small (large) compared to the non-strange hadrons, so that ϕ mesons do not suffer from the hadronic interactions. Therefore, the observation of the quark number scaling of v_2 for ϕ mesons could indicate the partonic collectivity in the pre-hadronic phase of heavy ion collisions.

Appendix A

Glauber Model

A.1 Parameterization

The Glauber model, which is a semi-classical model treating the nucleus-nucleus collisions as the superposition of the nucleon-nucleon collisions, has been successufully applied in the description of high-energy nuclear reactions. Nucleons are assumed to travel in straight lines, and are not deflected after the collisions, which holds as a good approximation at very high energies. Also, the nucleon-nucleon inelastic cross-section σ_{NN}^{in}, is assumed to be the same as that in the vacuum. In other words, secondary particle production and possible excitation of nucleons are not considered in this model.

The density distribution of the two nuclei with mass number A (here we consider Au nucleus $A = 197$), is described by a Woods-Saxon parameterization

$$\rho^{Au}(r) = \frac{\rho_0^{Au}}{1 + e^{(r-R_{Au})/a^{Au}}} \tag{A.1}$$

where $R_{Au} = 6.38$ fm is the radius of Au nucleus and $a^{Au} = 0.54$ fm is the surface diffuseness parameter. The normalization factor $\rho_0^{Au} = 0.17$ fm^{-3} is set to give $\int d^3r\rho^{Au}(r) = A = 197$.

The relavant quantity for the following considerations is the nuclear thickness function, which integrates the nuclear density function over the longitudinal coordinate z;

$$T_A(x, y) = \int_{-\infty}^{\infty} dz\rho^{Au}(x, y, z) \tag{A.2}$$

The opacity of the nucleus is obtained simply by multiplying the thickness function with the total inelastic cross section σ_0 of a nucleon-nucleon collsions. We use $\sigma_0 = 42$ mb at $\sqrt{s_{\rm NN}} = 200$ GeV [60].

Number of participant nucleons (N_{part}), which is defined by the number of nucleons participate in inelastic collisions at least once, for two colliding nucei with mass number

A and B is given by

$$\begin{aligned} n_{part}(x,y;b) &= T_A(x+b/2,y)\left(1-\left(1-\frac{\sigma_0 T_B(x-b/2,y)}{B}\right)^B\right) \\ &+ \quad T_B(x-b/2,y)\left(1-\left(1-\frac{\sigma_0 T_A(x+b/2,y)}{A}\right)^A\right) \qquad \text{(A.3)} \\ N_{part}(b) &= \int dxdy\ n_{part}(x,y;b) \qquad \text{(A.4)} \end{aligned}$$

where A and B is the mass number, b is the impact parameter. The thickness function of each nucleus is simply shifted by $\pm b/2$ to the left or to the right along the x-axis to meet the thickness function of the other nucleus shifted in the other direction. Integrating the Eq. (A.3) over the transverse plane yields the total number of participant nucleons as a function of the impact parameter as shown in Eq. (A.4).

Number of nucleon-nucleon collisions (N_{coll}) in non-central $A+B$ collisions is expressed by the product of the thickness function of one nucleus with the encountered opacity ot the other nucleus

$$\begin{aligned} n_{coll}(x,y;b) &= \sigma_0 T_A(x+b/2,y)T_B(x-b/2,y) \qquad \text{(A.5)} \\ N_{coll}(b) &= \int dxdy\ n_{coll}(x,y;b) \qquad \text{(A.6)} \end{aligned}$$

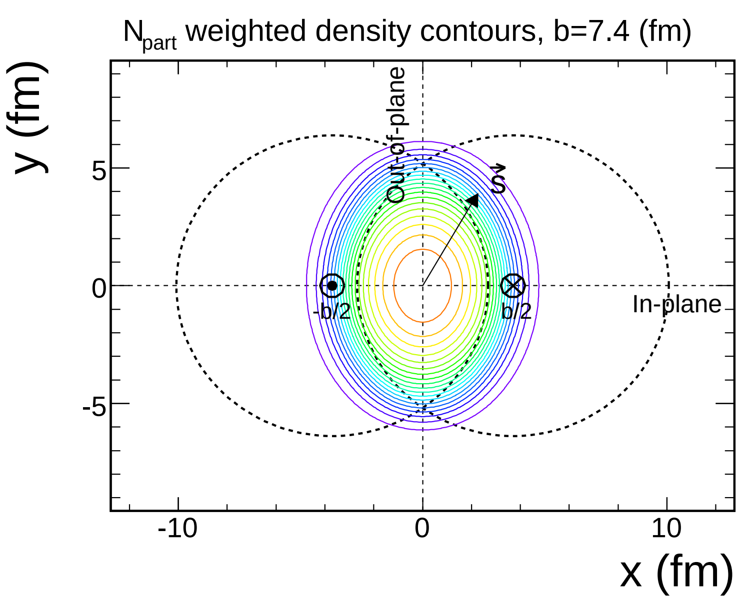

Figure A.1: Contours of constant densities of N_{part} in Au + Au collisions with $b = 7.4$ fm at $\sqrt{s_{\mathrm{NN}}} = 200$ GeV. The contours are given by 5 % step of the maximum value of the density. The dashed line indicate the radius of the colliding nuclei.

Fig. A.1 show the contours of overlap density distribution weighted by number of nucleon-nucleon collisions at $b = 7.4$ fm obtained from Monte Carlo simulation by Glauber model.

N_{part} and N_{coll} value from Glauber Monte Calro simulation are plotted as a function of centrality in Fig. A.2.

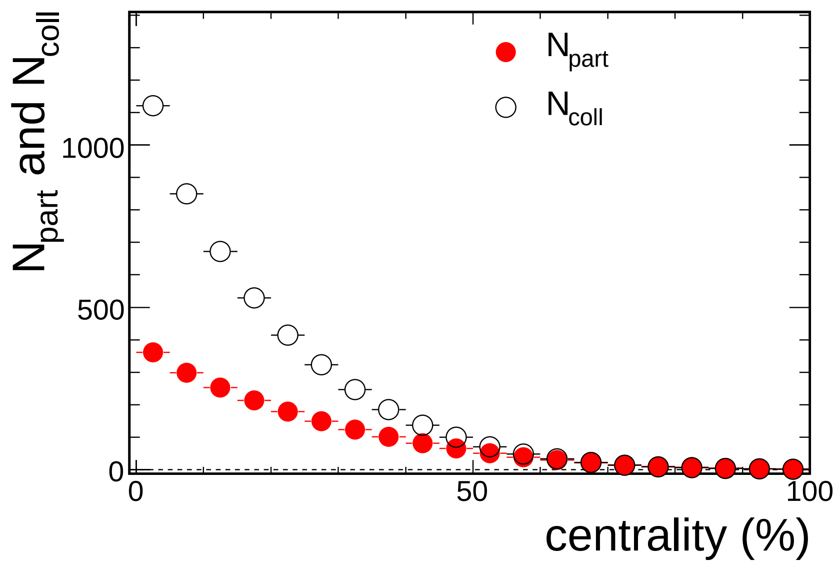

Figure A.2: Number of participant nucleons (N_{part}) and number of nucleon-nucleon collisions (N_{coll}) as a function of centrality from Glauber Monte Calro simulation.

A.2 Participant Eccentricity (ε_{var})

Initial spatial anisotropy (**eccentricity**) for a given impact parameter is also calculated. In the Glauber Monte Carlo simulations, the standard eccentricity is calculated in a reference frame that is defined by the center of the two colliding nuclei, and is given by

$$\varepsilon_{std}^{part} \equiv \frac{\{n_{part} \times (y^2 - x^2)\}}{\{n_{part} \times (y^2 + x^2)\}} = \frac{\sum_i n_{part}^i \times (y_i^2 - x_i^2)}{\sum_i n_{part}^i \times (y_i^2 + x_i^2)} \quad \text{(A.7)}$$

$$\varepsilon_{std}^{coll} \equiv \frac{\{n_{coll} \times (y^2 - x^2)\}}{\{n_{coll} \times (y^2 + x^2)\}} = \frac{\sum_i n_{coll}^i \times (y_i^2 - x_i^2)}{\sum_i n_{coll}^i \times (y_i^2 + x_i^2)} \quad \text{(A.8)}$$

where $(x,\ y)$ is the position of a participant nucleon in the coordinate system (x and y axes are defined as shown in Fig. A.1), and superscript of *part* and *coll* represent that average is taken by weighting with n_{part} and n_{coll} density, respectively. Brackets $\{...\}$ denotes an sample average, it means an average over all participant nucleons in one collision event.

Because of the event-by-event fluctuations in the participant nucleon positions [61], the eccentricity in a given event is shifted and tilted with respect to the (x, y) frame. The center-of-gravity of the participant nucleons is given by

$$\{x\} \equiv x_c = \frac{1}{N_{part}} \sum_i x_i \tag{A.9}$$

$$\{y\} \equiv y_c = \frac{1}{N_{part}} \sum_i y_i \tag{A.10}$$

We denote the position of participant i in the shifted reference frame S, in which the center-of-gravity is at the origin, as $(x_i^s, y_i^s) = (x_i - x_c, y_i - y_c)$. We can now determine as reference frame S^r which is rotated relative to S by an angle Ψ and in which the eccentricity is maximal. The coordinate in the rotated system is given by

$$\begin{pmatrix} x_i^r \\ y_i^r \end{pmatrix} = \begin{pmatrix} \cos\Psi & -\sin\Psi \\ \sin\Psi & \cos\Psi \end{pmatrix} \begin{pmatrix} x_i^s \\ y_i^s \end{pmatrix} \tag{A.11}$$

The eccentricity in the rotated frame (**participant eccentricity**) is given by

$$\varepsilon_{var}^{part} \equiv \frac{\{n_{part} \times (y_r^2 - x_r^2)\}}{\{n_{part} \times (y_r^2 + x_r^2)\}} \tag{A.12}$$

$$\varepsilon_{var}^{coll} \equiv \frac{\{n_{coll} \times (y_r^2 - x_r^2)\}}{\{n_{coll} \times (y_r^2 + x_r^2)\}} \tag{A.13}$$

with

$$\begin{aligned} x_r^2 &= (x_s \cos\Psi - y_s \sin\Psi)^2 \\ &= x_s^2 \cos^2\Psi - 2x_s y_s \cos\Psi \sin\Psi + y_s^2 \sin^2\Psi \end{aligned} \tag{A.14}$$

$$\begin{aligned} y_r^2 &= (x_s \sin\Psi + y_s \cos\Psi)^2 \\ &= x_s^2 \sin^2\Psi + 2x_s y_s \cos\Psi \sin\Psi + y_s^2 \cos^2\Psi \end{aligned} \tag{A.15}$$

Participant eccentricity for a given event can be rewritten by using Eq. (A.14), (A.15),

$$\begin{aligned} \varepsilon_{var} &= \frac{\{(y_s^2 - x_s^2)\cos^2\Psi + (x_s^2 - y_s^2)\sin^2\Psi + 4x_s y_s \cos\Psi \sin\Psi\}}{\{x_s^2 + y_s^2\}} \\ &= \frac{\{y_s^2 - x_s^2\}\cos(2\Psi) + 2\{x_s y_s\}\sin(2\Psi)}{\{x_s^2 + y_s^2\}} \\ &\equiv \frac{(\sigma_y^2 - \sigma_x^2)\cos(2\Psi) + 2\sigma_{xy}\sin(2\Psi)}{\sigma_y^2 + \sigma_x^2} \end{aligned} \tag{A.16}$$

where σ_x, σ_y and σ_{xy} are defined as follows

$$\sigma_x^2 \equiv \{x^2\} - \{x\}^2 \tag{A.17}$$

$$\sigma_y^2 \equiv \{y^2\} - \{y\}^2 \tag{A.18}$$

$$\sigma_{xy} \equiv \{xy\} - \{x\}\{y\} \tag{A.19}$$

$\{y_s^2 - x_s^2\}$, $\{x_s y_s\}$ and $\{y_s^2 + x_s^2\}$ in Eq. (A.16) can be expressed by making use of Eq. (A.17) - (A.19)

$$\begin{aligned}
\{y_s^2 - x_s^2\} &= \{(y_i - \{y\})^2 - (x_i - \{x\})^2\} \\
&= \{y_i^2 - 2y_i\{y\} + \{y\}^2 - (x_i^2 - 2x_i\{x\} + \{x\}^2)\} \\
&= \{y^2\} - \{y\}^2 - (\{x^2\} - \{x\}^2) = \sigma_y^2 - \sigma_x^2 \qquad \text{(A.20)} \\
\{x_s y_s\} &= \{(x_i - \{x\})(y_i - \{y\})\} \\
&= \{x_i y_i - \{x\}y_i - x_i\{y\} + \{x\}\{y\}\} \\
&= \{xy\} - \{x\}\{y\} = \sigma_{xy} \qquad \text{(A.21)} \\
\{y_s^2 + x_s^2\} &= \sigma_y^2 + \sigma_x^2 \qquad \text{(A.22)}
\end{aligned}$$

The rotation angle Ψ which maximize the eccentricity is given by the following condition

$$\frac{d\varepsilon_{var}}{d\Psi} = 0 \qquad \text{(A.23)}$$

Ψ can be determined by

$$\begin{aligned}
\frac{d\varepsilon_{var}}{d\Psi} &= -2(\sigma_y^2 - \sigma_x^2)\sin(2\Psi) + 4\sigma_{xy}\cos(2\Psi) = 0 \\
\therefore \tan(2\Psi) &= \frac{2\sigma_{xy}}{\sigma_y^2 - \sigma_x^2} \\
\cos(2\Psi) &= \frac{1}{\sqrt{1 + \tan^2(2\Psi)}} = \frac{\sigma_y^2 - \sigma_x^2}{\sqrt{(\sigma_y^2 - \sigma_x^2)^2 + 4\sigma_{xy}^2}} \qquad \text{(A.24)} \\
\sin(2\Psi) &= 1 - \cos^2(2\Psi) = \frac{2\sigma_{xy}}{\sqrt{(\sigma_y^2 - \sigma_x^2)^2 + 4\sigma_{xy}^2}} \qquad \text{(A.25)}
\end{aligned}$$

Therefore

$$\begin{aligned}
\varepsilon_{var} &= \frac{1}{\sigma_y^2 + \sigma_x^2}\left((\sigma_y^2 - \sigma_x^2)\frac{\sigma_y^2 - \sigma_x^2}{\sqrt{(\sigma_y^2 - \sigma_x^2)^2 + 4\sigma_{xy}^2}} + 2\sigma_{xy}\frac{2\sigma_{xy}}{\sqrt{(\sigma_y^2 - \sigma_x^2)^2 + 4\sigma_{xy}^2}}\right) \\
&= \frac{\sqrt{(\sigma_y^2 - \sigma_x^2)^2 + 4\sigma_{xy}^2}}{\sigma_y^2 + \sigma_x^2} \qquad \text{(A.26)}
\end{aligned}$$

If the event-by-event fluctuations in the position of participant nucleons are small, participant eccentricity become standard eccentricity. Since $\sigma_x \sim \sqrt{\{x^2\}}$, $\sigma_y \sim \sqrt{\{y^2\}}$ ($\{x\} \sim 0$, $\{y\} \sim 0$) and $\sigma_{xy} \sim 0$

$$\begin{aligned}
\varepsilon_{var} &\approx \frac{\sigma_y^2 - \sigma_x^2}{\sigma_y^2 + \sigma_x^2} \\
&\approx \frac{\{y^2\} - \{x^2\}}{\{y^2\} + \{x^2\}} = \varepsilon_{std} \qquad \text{(A.27)}
\end{aligned}$$

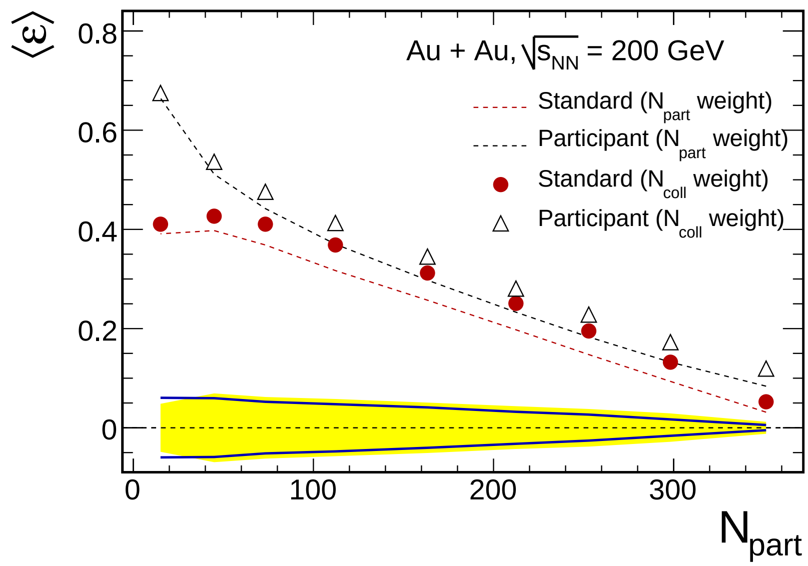

Figure A.3: Standard and participant eccentricity as a function of N_{part}. Lines and symbolds represent the results with N_{part} and N_{coll} weighted eccentricity, respectively. Yellow bands and solid lines around denote the absolute systematic error on $\langle\varepsilon\rangle$ for standard and participant eccentricity.

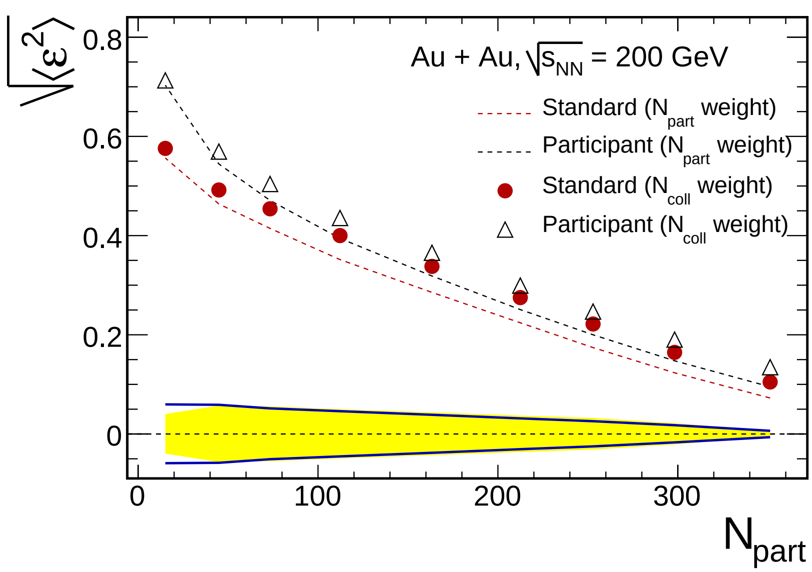

Figure A.4: Standard and participant eccentricity as a function of N_{part}. Different definition of eccentricity ($\varepsilon\{2\} \equiv \sqrt{\langle\varepsilon^2\rangle}$) is used.

Fig. A.3 and A.4 show N_{part} dependence of the standard and participant eccentricity calculated in Glauber MC model.

The participant eccentricity is defined by the principal axes (or event plane) which is determined by the position of all participating nucleons. It always includes auto-correlations between participants and the event plane, so that the $\langle \varepsilon_{var} \rangle$ goes 1 in peripheral events due to such correlations. In order to take into account the effect of auto-correlations, we subtract the auto-correlation from participant eccentricity event-by-event basis. We define **event plane eccentricity**, $\langle \varepsilon_2 \rangle$, and calculate it by using following redefined event plane angle Ψ^i for i-th event

$$x_s^i = r_s^i \cos(2\phi_s^i) \tag{A.28}$$

$$y_s^i = r_s^i \sin(2\phi_s^i) \tag{A.29}$$

$$\phi_s^i = \tan^{-1}\left(\frac{y_s^i}{x_s^i}\right) \tag{A.30}$$

$$\tan(2\Psi^i) = -\frac{\sum_j (r_s^j)^2 \sin(2\phi_s^j) - (r_s^i)^2 \sin(2\phi_s^i)}{\sum_j (r_s^j)^2 \cos(2\phi_s^j) - (r_s^i)^2 \cos(2\phi_s^i)} \tag{A.31}$$

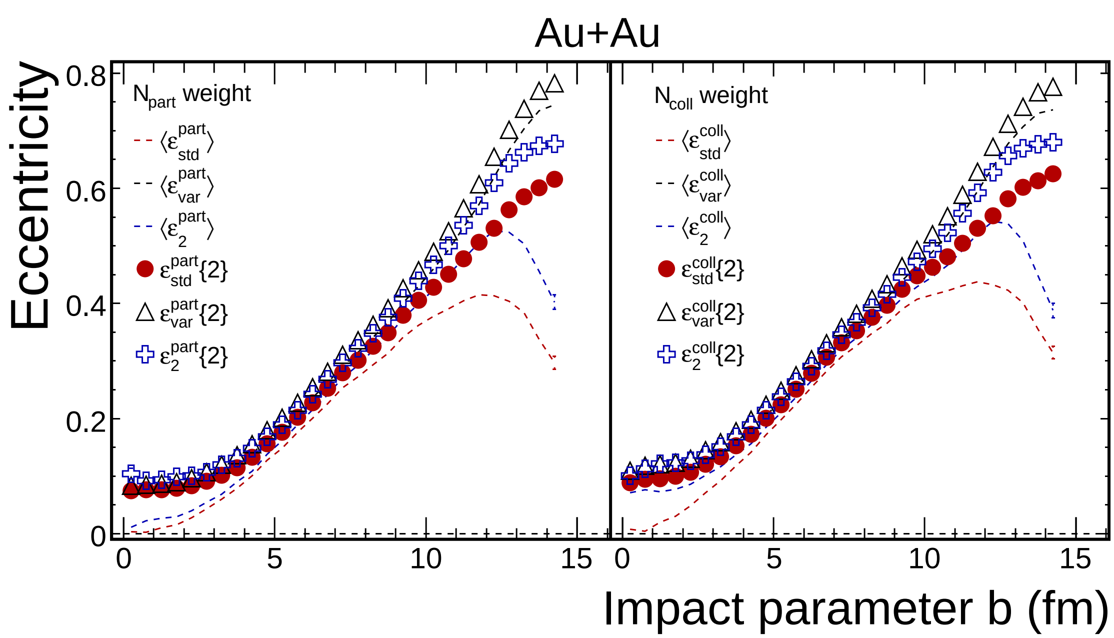

Figure A.5: Comparison of eccentricity as a function of impact parameter in Au + Au collisions. Left (right) figure shows the eccentricity calculated with N_{part} (N_{coll}) density profile.

Fig. A.5 and A.6 show the comparison of eccentricity in Au + Au and Cu + Cu collisions (dashed lines). The event plane eccentricity takes almost intermidiate value between standard and participant eccentricity. We also compare that the different averaging, $\varepsilon\{2\} \equiv \sqrt{\langle \varepsilon^2 \rangle}$, to the standard calculation as shown in the data symbols in Fig.

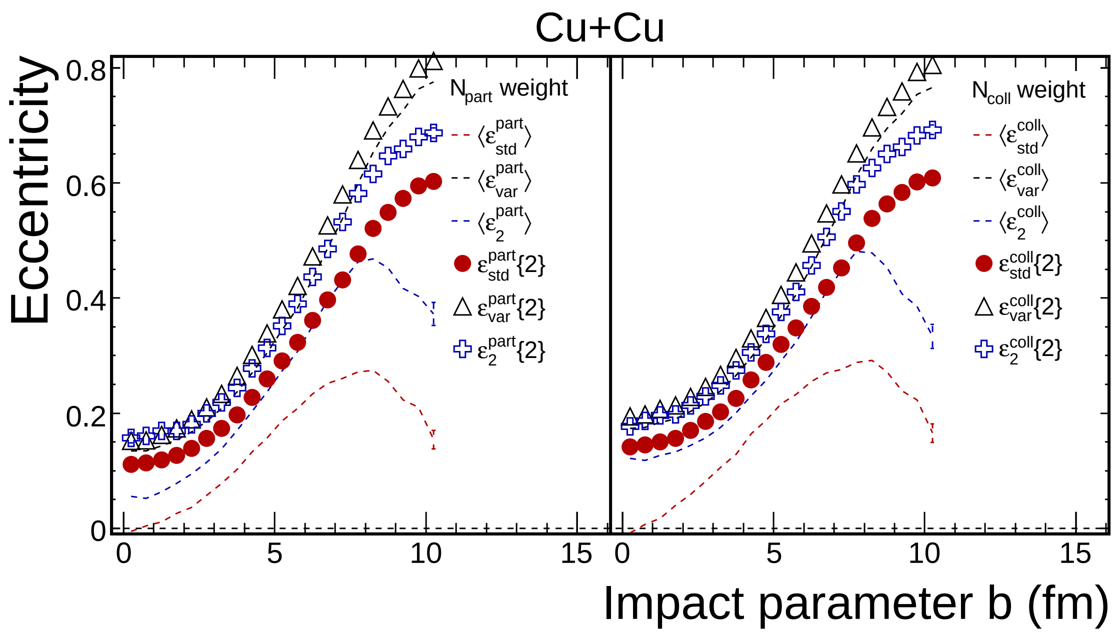

Figure A.6: Comparison of eccentricity as a function of impact parameter in Cu + Cu collisions. Left (right) figure shows the eccentricity calculated with N_{part} (N_{coll}) density profile.

A.5 and A.6. In the $\varepsilon\{2\}$, the difference of ε between different definitions of eccentricity is relatively smaller than the ε.

Fig. A.7 and A.8 show the ratio of ε^{coll} to ε^{part} as a function of impact parameter in Au + Au and Cu + Cu collisions. ε^{coll} is about $1.5 - 2$ times larger in most central collision and close to unity in most peripheral collisions than ε^{part}.

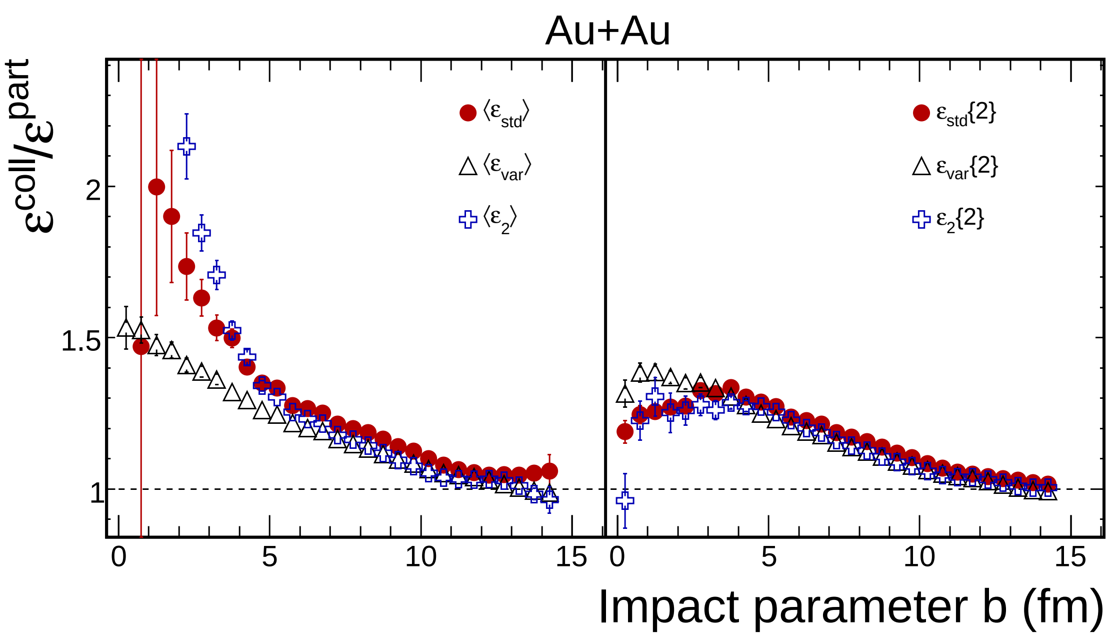

Figure A.7: $\langle\varepsilon^{coll}\rangle / \langle\varepsilon^{part}\rangle$ (left) and $\varepsilon^{coll}\{2\}/\varepsilon^{part}\{2\}$ (right) as a function of impact parameter in Au + Au.

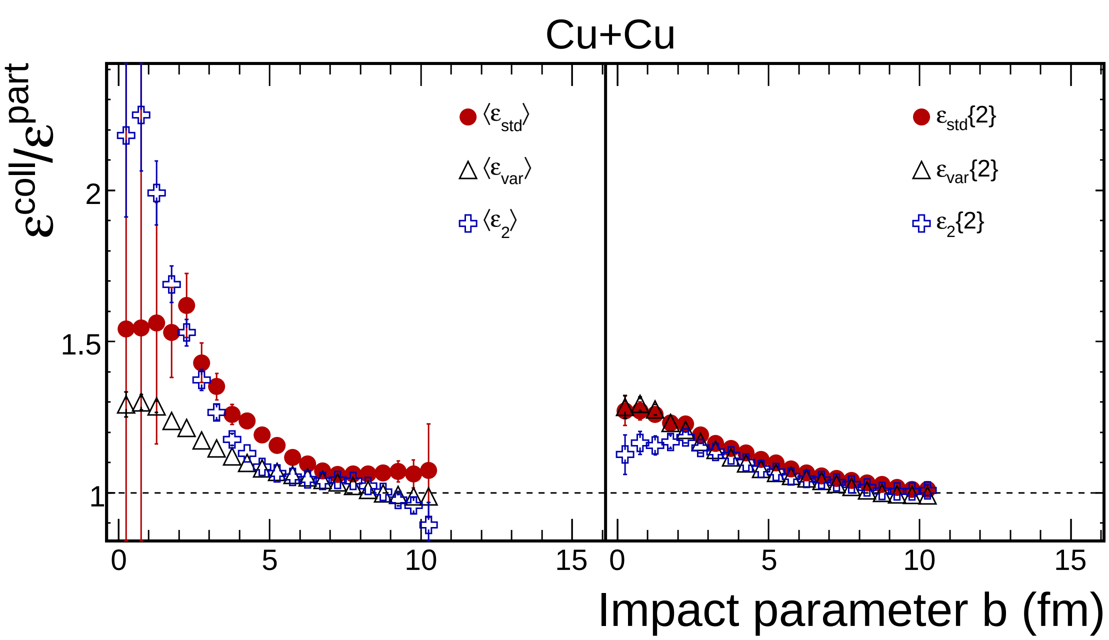

Figure A.8: $\langle\varepsilon^{coll}\rangle / \langle\varepsilon^{part}\rangle$ (left) and $\varepsilon^{coll}\{2\}/\varepsilon^{part}\{2\}$ (right) as a function of impact parameter in Cu + Cu.

A.3 Results and Systematic Errors

Results of Glauber Monte Carlo simulation are summarized in Table A.1 and A.2. The variables are calculated under the default condition (see below). Centrality classes are defined as: (0) :0 – 5 %, (1) :5 – 10 %, (2) :10 – 15 %, (3) :15 – 20 %, (4) :20 – 30 %, (5) :30 – 40 %, (6) :40 – 50 %, (7) :50 – 60 %, and (8) :60 – 92 %.

Systematic errors for calculated quantities are evaluated by varying the input parameters

1. $\sigma_{NN} = 42$ mb, $R_{Au} = 6.38$ fm, $a = 0.53$ fm ($R_{Cu} = 4.27$ fm) : default
2. $\sigma_{NN} = 37$ mb, $R_{Au} = 6.38$ fm, $a = 0.53$ fm
3. $\sigma_{NN} = 47$ mb, $R_{Au} = 6.38$ fm, $a = 0.53$ fm
4. $\sigma_{NN} = 42$ mb, $R_{Au} = 6.08$ fm, $a = 0.53$ fm ($R_{Cu} = 4.07$ fm)
5. $\sigma_{NN} = 42$ mb, $R_{Au} = 6.68$ fm, $a = 0.53$ fm ($R_{Cu} = 4.47$ fm)
6. $\sigma_{NN} = 42$ mb, $R_{Au} = 6.38$ fm, $a = 0.43$ fm
7. $\sigma_{NN} = 42$ mb, $R_{Au} = 6.38$ fm, $a = 0.63$ fm

where the radius inside () represent the values in Cu + Cu. Relative systematic errors on each quantity are summarized in Table A.3 and A.4.

Table A.1: Summary of results in Au + Au at $\sqrt{s_{\rm NN}} = 200$ GeV

Centrality	(0)	(1)	(2)	(3)	(4)	(5)	(6)	(7)	(8)
N_{part}	351.3	298.2	252.9	212.5	163.2	112.2	73.3	44.9	15.1
N_{coll}	1071.4	847.0	671.0	528.7	366.4	215.6	119.1	59.9	15.4
$\left\langle \varepsilon_{std}^{part} \right\rangle$	0.031	0.093	0.147	0.198	0.257	0.316	0.368	0.398	0.391
$\left\langle \varepsilon_{var}^{part} \right\rangle$	0.084	0.132	0.183	0.233	0.297	0.370	0.442	0.511	0.664
$\left\langle \varepsilon_{2}^{part} \right\rangle$	0.043	0.102	0.159	0.212	0.276	0.345	0.409	0.462	0.527
$\varepsilon_{std}^{part}\{2\}$	0.072	0.123	0.174	0.224	0.285	0.351	0.414	0.463	0.556
$\varepsilon_{var}^{part}\{2\}$	0.095	0.148	0.200	0.251	0.318	0.394	0.470	0.544	0.703
$\varepsilon_{2}^{part}\{2\}$	0.095	0.140	0.187	0.238	0.304	0.378	0.450	0.517	0.651
$\left\langle \varepsilon_{std}^{coll} \right\rangle$	0.052	0.132	0.195	0.250	0.312	0.368	0.410	0.426	0.410
$\left\langle \varepsilon_{var}^{coll} \right\rangle$	0.119	0.172	0.228	0.280	0.345	0.412	0.475	0.536	0.675
$\left\langle \varepsilon_{2}^{coll} \right\rangle$	0.091	0.149	0.207	0.262	0.325	0.386	0.436	0.478	0.537
$\varepsilon_{std}^{coll}\{2\}$	0.104	0.164	0.221	0.275	0.338	0.400	0.454	0.492	0.575
$\varepsilon_{var}^{coll}\{2\}$	0.134	0.190	0.246	0.299	0.365	0.436	0.503	0.569	0.712
$\varepsilon_{2}^{coll}\{2\}$	0.127	0.180	0.236	0.287	0.352	0.418	0.481	0.539	0.663

Table A.2: Summary of results in Cu + Cu at $\sqrt{s_{\mathrm{NN}}}$ = 200 GeV

Centrality	(0)	(1)	(2)	(3)	(4)	(5)	(6)	(7)	(8)
N_{part}	109.3	93.2	79.0	66.7	50.9	34.8	23.0	14.5	5.8
N_{coll}	220.2	174.1	137.6	108.7	74.7	44.3	25.5	14.1	4.8
$\left\langle \varepsilon_{std}^{part} \right\rangle$	0.021	0.062	0.102	0.138	0.188	0.232	0.259	0.275	0.240
$\left\langle \varepsilon_{var}^{part} \right\rangle$	0.151	0.191	0.236	0.280	0.348	0.434	0.523	0.611	0.737
$\left\langle \varepsilon_{2}^{part} \right\rangle$	0.075	0.120	0.169	0.213	0.276	0.353	0.421	0.471	0.520
$\varepsilon_{std}^{part}\{2\}$	0.121	0.156	0.195	0.236	0.294	0.361	0.422	0.484	0.560
$\varepsilon_{var}^{part}\{2\}$	0.171	0.216	0.264	0.312	0.384	0.475	0.564	0.652	0.774
$\varepsilon_{2}^{part}\{2\}$	0.167	0.203	0.243	0.287	0.356	0.439	0.519	0.593	0.711
$\left\langle \varepsilon_{std}^{coll} \right\rangle$	0.033	0.087	0.130	0.169	0.215	0.254	0.276	0.293	0.255
$\left\langle \varepsilon_{var}^{coll} \right\rangle$	0.189	0.223	0.265	0.306	0.371	0.456	0.542	0.623	0.735
$\left\langle \varepsilon_{2}^{coll} \right\rangle$	0.132	0.161	0.200	0.237	0.294	0.368	0.439	0.487	0.517
$\varepsilon_{std}^{coll}\{2\}$	0.153	0.187	0.224	0.265	0.322	0.384	0.443	0.504	0.572
$\varepsilon_{var}^{coll}\{2\}$	0.213	0.251	0.295	0.340	0.409	0.497	0.582	0.662	0.773
$\varepsilon_{2}^{coll}\{2\}$	0.198	0.233	0.272	0.315	0.379	0.459	0.538	0.608	0.715

Table A.3: Summary of relative systematic errors (%) in Au + Au at $\sqrt{s_{\mathrm{NN}}}$ = 200 GeV

Centrality classes	(0)	(1)	(2)	(3)	(4)	(5)	(6)	(7)	(8)
N_{part}	1.6	3.3	5.0	6.9	10.1	16.2	23.9	34.2	59.4
N_{coll}	20.2	18.6	17.7	16.7	17.0	20.8	29.5	42.1	69.1
$\left\langle \varepsilon_{std}^{part} \right\rangle$	38.7	31.0	25.9	21.8	19.7	18.3	16.8	17.4	12.4
$\left\langle \varepsilon_{var}^{part} \right\rangle$	6.4	12.6	14.3	13.9	13.7	12.8	11.8	11.6	9.1
$\left\langle \varepsilon_{2}^{part} \right\rangle$	14.3	20.6	18.8	16.6	16.1	14.5	12.7	11.2	3.9
$\varepsilon_{std}^{part}\{2\}$	9.3	17.4	18.2	16.3	15.1	14.1	13.3	12.3	7.2
$\varepsilon_{var}^{part}\{2\}$	6.7	11.6	12.8	12.4	12.0	11.6	10.9	10.8	8.4
$\varepsilon_{2}^{part}\{2\}$	12.7	12.3	14.2	13.8	12.7	12.2	11.1	10.5	8.1
$\left\langle \varepsilon_{std}^{coll} \right\rangle$	23.5	20.9	17.4	17.4	16.4	16.0	16.5	18.1	12.7
$\left\langle \varepsilon_{var}^{coll} \right\rangle$	5.3	10.1	12.2	13.1	13.2	12.4	12.1	12.0	7.9
$\left\langle \varepsilon_{2}^{coll} \right\rangle$	9.4	13.0	15.0	15.2	15.1	14.3	13.8	13.2	3.5
$\varepsilon_{std}^{coll}\{2\}$	7.2	12.8	13.6	14.4	13.6	13.1	13.4	12.9	7.3
$\varepsilon_{var}^{coll}\{2\}$	5.3	9.2	11.0	12.0	11.8	11.3	11.1	11.0	7.4
$\varepsilon_{2}^{coll}\{2\}$	5.9	10.8	11.8	13.1	12.6	12.1	11.7	11.2	7.2

Table A.4: Summary of relative systematic errors (%) in Cu + Cu at $\sqrt{s_{\mathrm{NN}}} = 200$ GeV

Centrality classes	(0)	(1)	(2)	(3)	(4)	(5)	(6)	(7)	(8)
N_{part}	3.3	3.9	5.2	7.7	11.2	18.2	25.6	35.3	58.3
N_{coll}	21.4	19.2	18.2	16.7	17.4	21.0	29.1	40.2	62.7
$\left\langle\varepsilon_{std}^{part}\right\rangle$	53.0	46.1	46.9	39.1	31.0	30.7	28.8	25.8	20.4
$\left\langle\varepsilon_{var}^{part}\right\rangle$	4.3	4.0	8.5	10.1	8.7	9.8	10.2	8.9	6.5
$\left\langle\varepsilon_{2}^{part}\right\rangle$	11.2	7.1	14.9	16.5	11.8	11.3	9.2	6.3	7.0
$\varepsilon_{std}^{part}\{2\}$	4.5	7.7	12.4	13.0	12.3	12.1	12.0	10.1	5.4
$\varepsilon_{var}^{part}\{2\}$	4.2	3.8	8.0	9.3	8.0	9.0	9.4	8.1	5.8
$\varepsilon_{2}^{part}\{2\}$	3.7	4.4	8.2	8.5	8.0	9.0	8.8	7.3	6.5
$\left\langle\varepsilon_{std}^{coll}\right\rangle$	37.7	34.3	39.8	38.4	30.4	32.0	31.2	28.3	20.7
$\left\langle\varepsilon_{var}^{coll}\right\rangle$	2.4	4.6	9.7	10.8	10.0	10.4	9.9	7.8	5.8
$\left\langle\varepsilon_{2}^{coll}\right\rangle$	5.3	9.7	15.3	16.3	14.7	13.5	10.6	6.5	7.5
$\varepsilon_{std}^{coll}\{2\}$	2.6	9.3	14.2	15.4	13.5	13.4	13.2	10.4	5.1
$\varepsilon_{var}^{coll}\{2\}$	1.9	4.0	9.3	9.9	9.0	9.4	8.9	7.1	5.3
$\varepsilon_{2}^{coll}\{2\}$	2.3	3.0	10.4	10.7	9.5	9.7	8.9	6.5	5.9

Appendix B

Event Plane Resolution

In this chapter, we derive the formula of the event plane resolution under the assumptions introduced in the Section 3.2.4.

Starting from the assumptions in Section 3.2.4, the probability distribution can be given by the gaussian as

$$
\begin{aligned}
\frac{dP}{dv_n d\theta_n} &= \frac{v_n}{2\pi\sigma_n^2} \exp\left(-\frac{|v_n - \bar{v}_n|^2}{2\sigma_n^2}\right) = \frac{v_n}{2\pi\sigma_n^2} \exp\left(-\frac{v_n^2 + \bar{v}_n^2 - 2v_n\bar{v}_n \cos(\theta_n)}{2\sigma_n^2}\right) \\
&= \frac{\chi_n}{\sqrt{2}\pi\sigma_n} \exp\left(-\chi_n^2 - \bar{\chi}_n^2 + 2\chi_n\bar{\chi}_n \cos(\theta_n))\right) \qquad \text{(B.1)}
\end{aligned}
$$

where $\theta_n = n\Delta\Psi = n(\Psi_n - \Psi)$, and $\chi_n = v_n/(\sqrt{2}\sigma_n)$, $\bar{\chi}_n = \bar{v}_n/(\sqrt{2}\sigma_n)$. For isotropic probability distribution ($\bar{v}_n = 0$), the variance σ_n is same for any n-th moment,

$$
\begin{aligned}
\sigma^2 \equiv \sigma_n^2 &= \left\langle (v_n - \bar{v}_n)^2 \right\rangle = \left\langle v_n^2 \right\rangle \quad (\because \bar{v}_n = 0) \\
&= \left\langle \frac{x_n^2}{x_0^2} \right\rangle \\
&= \frac{M \langle w^2 \rangle \langle \cos^2(n\phi) \rangle}{M^2 \langle w \rangle^2} \\
&= \frac{\langle w^2 \rangle}{2M \langle w \rangle^2} \qquad \text{(B.2)}
\end{aligned}
$$

where $\langle \cos(n\phi) \rangle = 1/2$ for isotropic probability distribution.

Eq. (B.1) can be integrated over dimensionless parameter χ_n.

$$\begin{aligned}
\frac{dP}{d\theta_n} &= \frac{1}{\pi}\int_0^\infty \chi_n d\chi_n \ \exp\left(-\chi_n^2-\bar{\chi}_n^2+2\chi_n\bar{\chi}_n\cos\left(\theta_n\right)\right) \\
&= \frac{e^{-\bar{\chi}_n^2}}{\pi}\int_0^\infty \chi_n d\chi_n \ \exp\left(-\chi_n^2+2\chi_n\bar{\chi}_n\cos\left(\theta_n\right)\right) \\
&= \frac{e^{-\bar{\chi}_n^2}}{\pi}\int_0^\infty \chi_n d\chi_n \ \exp\left(-(\chi_n-a_n)^2\right)\times\exp\left(a_n^2\right) \quad \left(a_n\equiv\bar{\chi}_n\cos\left(\theta_n\right)\right) \\
&= \frac{e^{-\bar{\chi}_n^2}e^{a_n^2}}{\pi}\int_{-a_n}^\infty (y_n+a_n)dy_n \ \exp\left(-y_n^2\right) \quad \left(y_n=\chi_n-a_n\right) \\
&= \frac{e^{-\bar{\chi}_n^2}e^{a_n^2}}{\pi}\left[\int_{-a_n}^\infty y_n dy_n \ \exp\left(-y_n^2\right)+a_n\int_{-a_n}^\infty dy_n \ \exp\left(-y_n^2\right)\right] \qquad \text{(B.3)}
\end{aligned}$$

1^{st} term of Eq. (B.3) can be calculated by using integration by parts:

$$\begin{aligned}
\int_{-a_n}^\infty y_n dy_n \ \exp\left(-y_n^2\right) &= \left[-\frac{1}{2}e^{-y_n^2}\right]_{-a_n}^\infty \\
&= \frac{1}{2}e^{-a_n^2} \qquad \text{(B.4)}
\end{aligned}$$

2^{nd} term of Eq. (B.3) can be expressed by using standard error function erf(x):

$$\begin{aligned}
\int_{-a_n}^\infty dy_n \ \exp\left(-y_n^2\right) &= \int_{-a_n}^0 dy_n \ \exp\left(-y_n^2\right)+\int_0^\infty dy_n \ \exp\left(-y_n^2\right) \\
&= \frac{\sqrt{\pi}}{2}\mathrm{erf}(a_n)+\frac{\sqrt{\pi}}{2} \qquad \text{(B.5)}
\end{aligned}$$

Therefore, Eq. (B.3) reduces to:

$$\begin{aligned}
\frac{dP}{d\theta_n} &= \frac{e^{-\bar{\chi}_n^2}e^{a_n^2}}{\pi}\left[\frac{1}{2}e^{-a_n^2}+\frac{a_n\sqrt{\pi}}{2}\left(1+\mathrm{erf}(a_n)\right)\right] \\
&= \frac{e^{-\bar{\chi}_n^2}}{2\pi}\left[1+\sqrt{\pi}\bar{\chi}_n\cos\theta_n e^{\bar{\chi}_n^2\cos^2\left(\theta_n\right)}\left[1+\mathrm{erf}(\bar{\chi}_n\cos\left(\theta_n\right))\right]\right] \qquad \text{(B.6)}
\end{aligned}$$

Fig. B.1 shows the distribution of θ_n for different value of χ (χ = 0.5, 1, 1.5, 2). As one can see in Eq. (B.6), the distribution of θ_n is symmetric under the transformation $\theta_n \rightarrow -\theta_n$. If $\chi_n \ll 1$, statistical fluctuations are large compared to the dynamical anisotropy, Eq. (B.6) becomes:

$$\frac{dP}{d\theta_n} \approx \frac{1}{2\pi}\left[1+\sqrt{\pi}\bar{\chi}_n\cos\left(\theta_n\right)\right] \qquad \text{(B.7)}$$

On the other hand, if $\chi_n \gg 1$, one can expand the cosine and sine as $\cos\theta_n \approx 1$ and

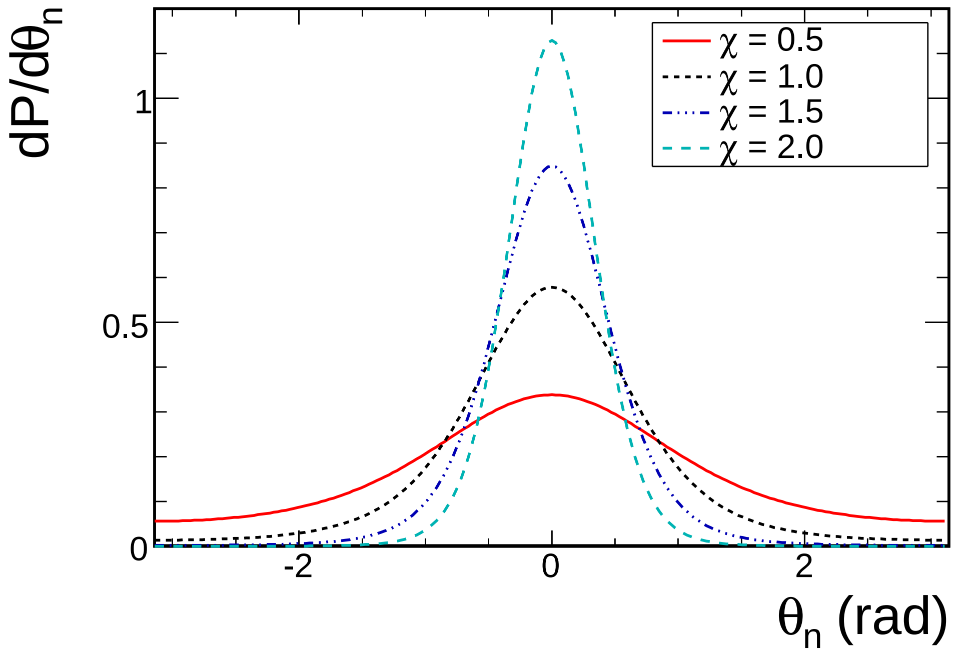

Figure B.1: The distribution of θ_n for $\chi = 0.5$, 1, 1.5 and 2.

$\sin\theta_n \approx \theta_n$. Eq. (B.6) becomes:

$$\begin{aligned}
\frac{dP}{d\theta_n} &= \frac{e^{-\bar{\chi}_n^2}}{2\pi} + \frac{1}{2\sqrt{\pi}}\bar{\chi}_n \cos\theta_n e^{-\bar{\chi}_n^2 \sin^2(\theta_n)}\left[1 + \mathrm{erf}(\bar{\chi}_n \cos(\theta_n))\right] \\
&\approx \frac{e^{-\bar{\chi}_n^2}}{2\pi} + \frac{1}{2\sqrt{\pi}}\bar{\chi}_n e^{-\bar{\chi}_n^2\theta_n^2}\left[1 + \mathrm{erf}(\bar{\chi}_n)\right] \\
&\approx \frac{\bar{\chi}_n}{\sqrt{\pi}} e^{-\bar{\chi}_n^2\theta_n^2} \quad (\because e^{-\bar{\chi}_n^2} \to 0, \quad \mathrm{erf}(\bar{\chi}_n) \to 1) \qquad \text{(B.8)}
\end{aligned}$$

We can measure n-th Fourier coefficient v_n by using the event planes determined from any harmonic k, with $n \geq k$. Thus, it is convenient to introduce the **event plane resolution** by $\langle \cos k\theta_n \rangle$ [13]:

$$\begin{aligned}
\langle \cos(k\theta_n) \rangle &= \int_0^\infty d\chi_n \int_0^{2\pi} d\theta_n \ \cos(k\theta_n) \frac{dP}{d\chi_n d\theta_n} \\
&= \frac{e^{-\bar{\chi}_n^2}}{\pi} \int_0^\infty d\chi_n \ \chi_n e^{-\chi_n^2} \int_0^{2\pi} d\theta_n \ \cos(k\theta_n) e^{2\chi_n\bar{\chi}_n \cos(\theta_n)} \\
&= 2e^{-\bar{\chi}_n^2} \int_0^\infty d\chi_n \ \chi_n e^{-\chi_n^2} I_k(2\chi_n\bar{\chi}_n) \\
&= 2e^{-\bar{\chi}_n^2} \left(\left[-\frac{1}{2} e^{-\chi_n^2} I_k(2\chi_n\bar{\chi}_n) \right]_0^\infty + \frac{1}{2} \int_0^\infty d\chi_n \ e^{-\chi_n^2} \frac{dI_k}{d\chi_n}(2\chi_n\bar{\chi}_n) \right) \\
&= e^{-\bar{\chi}_n^2} \int_0^\infty d\chi_n \ e^{-\chi_n^2} \frac{dI_k}{d\chi_n}(2\chi_n\bar{\chi}_n)
\end{aligned}$$

where 1^{st} term becomes 0, and $dI_k/d\chi_n$ is given by the following recurrence relation:

$$
\begin{aligned}
\frac{dI_k}{d\chi_n}(2\chi_n\bar{\chi}_n) &= \frac{1}{2\pi}\frac{d}{d\chi_n}\left(\int_0^{2\pi} d\theta_n \;\cos(k\theta_n)e^{2\chi_n\bar{\chi}_n\cos(\theta_n)}\right) \\
&= \frac{\bar{\chi}_n}{\pi}\int_0^{2\pi} d\theta_n \;\cos(k\theta_n)\cos(\theta_n)e^{2\chi_n\bar{\chi}_n\cos(\theta_n)} \\
&= \frac{\bar{\chi}_n}{2\pi}\int_0^{2\pi} d\theta_n \;\left[\cos((k+1)\theta_n)+\cos((k-1)\theta_n)\right]\times e^{2\chi_n\bar{\chi}_n\cos(\theta_n)} \\
&= \bar{\chi}_n\left[I_{k+1}(2\chi_n\bar{\chi}_n)+I_{k-1}(2\chi_n\bar{\chi}_n)\right]
\end{aligned}
$$

Therefore

$$
\begin{aligned}
\langle\cos(k\theta_n)\rangle &= \bar{\chi}_n e^{-\bar{\chi}_n^2}\int_0^{\infty} d\chi_n \; e^{-\chi_n^2}\left[I_{k+1}(2\chi_n\bar{\chi}_n)+I_{k-1}(2\chi_n\bar{\chi}_n)\right] \\
&= \frac{\sqrt{\pi}}{2}\bar{\chi}_n e^{-\bar{\chi}_n^2/2}\left[I_{(k-1)/2}\left(\frac{\bar{\chi}_n^2}{2}\right)+I_{(k+1)/2}\left(\frac{\bar{\chi}_n^2}{2}\right)\right] \\
&\left(\int_0^{\infty} e^{-\bar{\chi}_n^2}I_k(2\chi_n\bar{\chi}_n)d\chi_n = \frac{\sqrt{\pi}}{2}e^{\bar{\chi}_n^2/2}I_{k/2}\left(\frac{\bar{\chi}_n^2}{2}\right)\right)
\end{aligned} \tag{B.9}
$$

If $\chi \ll 1$, Eq. (B.9) reduces to

$$
\begin{aligned}
\langle\cos(k\theta_n)\rangle &\approx \frac{\sqrt{\pi}}{2}\bar{\chi}_n\left[\frac{1}{\Gamma\left(\frac{k+1}{2}\right)}\left(\frac{\bar{\chi}_n^2}{4}\right)^{(k-1)/2}+\frac{1}{\Gamma\left(\frac{k+3}{2}\right)}\left(\frac{\bar{\chi}_n^2}{4}\right)^{(k+1)/2}\right] \\
&= \frac{\sqrt{\pi}}{2}\bar{\chi}_n\frac{1}{\Gamma\left(\frac{k+1}{2}\right)}\left(\frac{\bar{\chi}_n^2}{4}\right)^{(k-1)/2}\left[1+\frac{2}{k+1}\left(\frac{\bar{\chi}_n^2}{4}\right)^2\right] \\
&\approx \frac{\sqrt{\pi}}{2^k}\frac{\bar{\chi}_n^k}{\Gamma\left(\frac{k+1}{2}\right)}
\end{aligned} \tag{B.10}
$$

If $\chi \gg 1$, Eq. (B.9) reduces to

$$
\begin{aligned}
\langle\cos(k\theta_n)\rangle &= \int_{-\pi}^{\pi} d\theta_n \;\cos k\theta_n\frac{dP}{d\theta_n} \\
&\approx \frac{\bar{\chi}_n}{\sqrt{\pi}}\int_{-\pi}^{\pi} d\theta_n \;\cos k\theta_n e^{-\bar{\chi}_n^2\theta_n^2} \\
&= \frac{1}{\sqrt{\pi}}\int_{-\bar{\chi}_n\pi}^{\bar{\chi}_n\pi} da_n \;\cos\left(\frac{ka_n}{\bar{\chi}_n}\right)e^{-a_n^2} \quad (a_n = \bar{\chi}_n\theta_n) \\
&= \frac{1}{\sqrt{\pi}}\int_{-\infty}^{\infty} da_n \;\cos\left(\frac{ka_n}{\bar{\chi}_n}\right)e^{-a_n^2} \quad (\bar{\chi}_n \gg 1) \\
&= \exp\left(-\frac{k^2}{4\bar{\chi}_n^2}\right)
\end{aligned} \tag{B.11}
$$

in the last line we use the following integral formula

$$
\int_{-\infty}^{\infty} e^{-ax^2}\cos(kx)dx = \sqrt{\frac{\pi}{a}}e^{-k^2/(4a)} \tag{B.12}
$$

Appendix C

Blast-wave Parameterization

C.1 Transverse Expansion

The invariant momentum spectrum of hadrons emitted at freeze-out is given by a local thermal distribution $f(x,p)$, with the freeze-out temperature T, boosted by a local velocity field u^μ, at the freeze-out hyper-surface Σ [59].

$$E\frac{dN}{d^3p} = \frac{dN}{m_T dm_T dy d\phi_p} = \int_\Sigma f(x,p)\Omega(r,\phi)p^\mu d\Sigma_\mu \quad \text{(C.1)}$$

$$\begin{aligned} p^\mu &= (E, p_x, p_y, p_z) \\ &= (m_T \cosh y, p_T \cos\phi_p, p_T \sin\phi_p, m_T \sinh y) \end{aligned} \quad \text{(C.2)}$$

where p^μ is a four-momentum of the emitted hadrons, $d\Sigma_\mu$ is a normal vector to the hyper-surface Σ, and where transverse momentum (p_T), transverse mass (m_T), rapidity (y), azimiuthal angle (ϕ_p) refer to the momentum of the emitted hadrons. and $\Omega(r,\phi)$ is density distributions from Glauber model. The local thermal distribution $f(x,p)$ is given by

$$f(x,p) = \frac{1}{(2\pi)^3}\frac{1}{e^{(p_\mu u^\mu(x)-\mu(x))/T(x)} \pm 1} \quad \text{(C.3)}$$

where $\mu(x)$ is a local chemical potential, $T(x)$ is a local temperature, $u^\mu(x)$ is a local flow velocity with $u_\mu u^\mu = 1$, and upper (lower) sign is for fermions (bosons). We can omit ± 1 in the denominator in Eq. (C.3) if we assume a Boltzmann distribution for all particles. Freeze-out hyper surface is parameterized as follows:

$$\Sigma^\mu = (t,x,y,z) = (\tau\cosh\eta, r\cos\phi, r\sin\phi, \tau\sinh\eta) \quad \text{(C.4)}$$

$$\eta = \frac{1}{2}\log\left(\frac{t+z}{t-z}\right) \quad \text{(C.5)}$$

where r and ϕ are the usual cilindrical coordinates, and η is space-time rapidity. A normal vector $d\Sigma_\mu$ in Eq. (C.1) to the surface is then given by

$$d\Sigma_\mu = \epsilon_{\mu\nu\lambda\rho}\frac{\partial\Sigma^\nu}{\partial r}\frac{\partial\Sigma^\lambda}{\partial\phi}\frac{\partial\Sigma^\rho}{\partial\eta}drd\phi d\eta = d\sigma_\mu drd\phi d\eta \quad \text{(C.6)}$$

We explicitly calculate the components of $\mathrm{d}\sigma_\mu$:

$$\begin{aligned} d\sigma_0 &= \epsilon_{0\nu\lambda 3}\frac{\partial\Sigma_\nu}{\partial r}\frac{\partial\Sigma_\lambda}{\partial\phi}\tau\cosh\eta \\ &= (\cos\phi\ r\cos\phi - \sin\phi(-r\sin\phi))\tau\cosh\eta = r\tau\cosh\eta \qquad (C.7) \\ d\sigma_1 &= \epsilon_{1\nu\lambda\rho}\frac{\partial\Sigma_\nu}{\partial r}\frac{\partial\Sigma_\lambda}{\partial\phi}\frac{\partial\Sigma_\rho}{\partial\eta} = 0 \qquad (C.8) \\ d\sigma_2 &= \epsilon_{2\nu\lambda\rho}\frac{\partial\Sigma_\nu}{\partial r}\frac{\partial\Sigma_\lambda}{\partial\phi}\frac{\partial\Sigma_\rho}{\partial\eta} = 0 \qquad (C.9) \\ d\sigma_3 &= \epsilon_{3\nu\lambda\rho}\frac{\partial\Sigma_\nu}{\partial r}\frac{\partial\Sigma_\lambda}{\partial\phi}\frac{\partial\Sigma_\rho}{\partial\eta} \\ &= (-\cos\phi\ r\cos\phi + \sin\phi(-r\sin\phi))\tau\sinh\eta = -r\tau\sinh\eta \qquad (C.10) \end{aligned}$$

From Eq. (C.6) - (C.10) $\mathrm{d}\Sigma_\mu$ becomes

$$d\Sigma_\mu = (\cosh\eta, 0, 0, -\sinh\eta)\ r\tau dr d\phi d\eta \qquad (C.11)$$

Thus, we obtain

$$\begin{aligned} p^\mu d\Sigma_\mu &= (m_T\cosh y\cosh\eta - m_T\sinh y\sinh\eta)\ \ r\tau dr d\phi d\eta \\ &= m_T\cosh(y-\eta)\ r\tau dr d\phi d\eta \qquad (C.12) \end{aligned}$$

Local velocity field u^μ can be parameterized as

$$u^\mu = (\cosh\eta_L\cosh\rho, \sinh\rho\cos\phi_b, \sinh\rho\sin\phi_b, \sinh\eta_L\cosh\rho) \qquad (C.13)$$

in cylindrical coordinates, where ϕ_b is azimuthal angle of radial boost velocity, η_L is longitudinal flow rapidity, and $\rho = \rho(r, \phi_s)$ is transvers flow rapidity defined as

$$\rho(r, \phi_s) = \tanh(\beta_T \cdot g(r, \phi_s)) \qquad (C.14)$$

where β_T is the surface radial flow velocity, and $g(r, \phi_s)$ is the density gradient distributions given by Glauber model. In Bjorken scenario [9] η_L is identical to the space-time rapidity η. From Eq. (C.2) and (C.13)

$$\begin{aligned} p_\mu u^\mu &= m_T\cosh y\cosh\eta\cosh\rho - p_T\cos\phi_p\sinh\rho\cos\phi_b \\ &\quad - p_T\sin\phi_p\sinh\rho\sin\phi_b - m_T\sinh y\sinh\eta\cosh\rho \\ &= m_T\cosh\rho\cosh(y-\eta) - p_T\sinh\rho\cos(\phi_b - \phi_p) \qquad (C.15) \end{aligned}$$

We can write the invariant momentum distribution by assuming a Boltzman distribution for all particles and Bjorken scenario as

$$\begin{aligned} E\frac{dN}{d^3p} &= \frac{1}{(2\pi)^3}\int_\Sigma e^{-(p_\mu u^\mu - \mu)/T}\ \Omega(r, \phi_s)\ p^\mu d\Sigma_\mu \\ &= \frac{m_T\tau e^{\mu/T}}{(2\pi)^3}\int_0^\infty r dr\int_0^{2\pi} d\phi_s\int_{-\infty}^{\infty} d\eta\ \cosh(y-\eta) \\ &\quad \times e^{-\beta(r,\phi_s)\cosh(y-\eta)}\ e^{\alpha(r,\phi_s)\cos(\phi_b-\phi_p)}\ \Omega(r, \phi_s) \end{aligned}$$
$$(C.16)$$

where $\alpha(r, \phi_s)$ and $\beta(r, \phi_s)$ are defined as

$$\alpha(r, \phi_s) = \frac{p_T}{T} \sinh \rho(r, \phi_s) \tag{C.17}$$

$$\beta(r, \phi_s) = \frac{m_T}{T} \cosh \rho(r, \phi_s) \tag{C.18}$$

C.2 Transverse Momentum Spectra and v_2

Azimuthally integrated transverse momentum spectra is obtained by integrating over ϕ_p. We can integrate over η with the help of modified Bessel functions of the second kind by assuming $y = 0$ because we only interested in mid-rapidity particles in the center-of-mass frame.

$$\begin{aligned}
\frac{dN}{p_T dp_T} &= \int_0^{2\pi} d\phi_p \; E\frac{dN}{d^3p} \\
&= \frac{m_T \tau e^{\mu/T}}{(2\pi)^3} \int_0^{\infty} rdr \int_0^{2\pi} d\phi_p \int_0^{2\pi} d\phi_s \\
&\quad \times \left(\int_{-\infty}^{\infty} d\eta \;\; \cosh{(\eta)} \; e^{-\beta(r,\phi_s)\cosh{(\eta)}} \right) e^{\alpha(r,\phi_s)\cos{(\phi_b - \phi_p)}} \; \Omega(r, \phi_s) \\
&= \frac{2m_T \tau e^{\mu/T}}{(2\pi)^3} \int_0^{\infty} rdr \int_0^{2\pi} d\phi_p \int_0^{2\pi} d\phi_s \; K_1(\beta(r, \phi_s)) \\
&\quad \times e^{\alpha(r,\phi_s)\cos{(\phi_b - \phi_p)}} \; \Omega(r, \phi_s)
\end{aligned} \tag{C.19}$$

$$K_n(z) = \frac{1}{2} \int_{-\infty}^{\infty} d\eta \;\; \cos{(n\eta)} e^{-z\cosh\eta} \tag{C.20}$$

We can exchange the order of integration in ϕ_p and ϕ_s, and perform a transformation $\psi \equiv \phi_s - \phi_p$. Then the integral in ψ can be performed analytically and lead to the modified Bessel functions of 1st kind

$$\begin{aligned}
\frac{dN}{p_T dp_T} &= \frac{2m_T \tau e^{\mu/T}}{(2\pi)^3} \int_0^{\infty} rdr \int_0^{2\pi} d\phi_s \left(\int_0^{2\pi} d\psi \;\; e^{\alpha(r,\phi_s)\cos{(\psi)}} \right) \\
&\quad \times \;\; K_1(\beta(r, \phi_s)) \; \Omega(r, \phi_s) \\
&= \frac{2m_T \tau e^{\mu/T}}{(2\pi)^2} \int_0^{\infty} rdr \int_0^{2\pi} d\phi_s \\
&\quad \times \;\; I_0(\alpha(r, \phi_s)) \; K_1(\beta(r, \phi_s)) \; \Omega(r, \phi_s)
\end{aligned} \tag{C.21}$$

where I_0 is the modified Bessel functions of the first kind

$$I_n(z) = \frac{1}{2\pi} \int_0^{2\pi} d\phi \;\; \cos{(n\phi)} e^{z\cos\phi} \tag{C.22}$$

Elliptic flow can be calculated as

$$v_2(p_{\rm T}) = \frac{\int_0^{2\pi} d\phi_p \;\; \cos{(2\phi_p)} \; dN/(p_{\rm T} dp_{\rm T} d\phi_p)}{\int_0^{2\pi} d\phi_p \; dN/(p_{\rm T} dp_{\rm T} d\phi_p)} \tag{C.23}$$

The denominator is already calculated as shown in Eq. (C.21). The numerator is obtained in similar way to integrate transverse momentum spectra. Thus,

$$\begin{aligned}
&\int_0^{2\pi} d\phi_p \ \cos(2\phi_p) \ dN/(p_{\mathrm{T}} dp_{\mathrm{T}} d\phi_p) \\
= \ & \frac{2m_T \tau e^{\mu/T}}{(2\pi)^3} \int_0^{\infty} r dr \int_0^{2\pi} d\phi_s \ K_1(\beta(r,\phi_s)) \ \Omega(r,\phi_s) \\
& \times \int_0^{2\pi} d\phi_p \ \cos(2\phi_p) \ e^{\alpha(r,\phi_s)\cos(\phi_s-\phi_p)}
\end{aligned} \tag{C.24}$$

Again, we write $\psi = \phi_s - \phi_p$ and decompose

$$\begin{aligned}
\cos(2\phi_p) &= \cos(2\phi_s - 2\psi) \\
&= \cos(2\phi_s)\cos(2\psi) + \sin(2\phi_s)\sin(2\psi)
\end{aligned} \tag{C.25}$$

The ψ integration with the term proportional to $\sin(2\psi)$ vanishes because of the symmetry in azimuthal direction of ψ. Thus, the numerator becomes

$$\begin{aligned}
&\int_0^{2\pi} d\phi_p \ \cos(2\phi_p) \ dN/(p_{\mathrm{T}} dp_{\mathrm{T}} d\phi_p) \\
= \ & \frac{2m_T \tau e^{\mu/T}}{(2\pi)^3} \int_0^{\infty} r dr \int_0^{2\pi} d\phi_s \ K_1(\beta(r,\phi_s)) \ \Omega(r,\phi_s) \\
& \times \cos(2\phi_s) \left(\int_0^{2\pi} d\psi \ \cos(2\psi) \ e^{\alpha(r,\phi_s)\cos(\psi)} \right) \\
= \ & \frac{2m_T \tau e^{\mu/T}}{(2\pi)^3} \int_0^{\infty} r dr \int_0^{2\pi} d\phi_s \ K_1(\beta(r,\phi_s)) \ \Omega(r,\phi_s) \\
& \times \cos(2\phi_s) \ I_2(\alpha(r,\phi_s))
\end{aligned} \tag{C.26}$$

The integral of ψ leads to a modified Bessel functions of 1st kind I_2 (see, Eq. (C.22)). We finally obtain the expression of $v_2(p_{\mathrm{T}})$ as

$$v_2(p_{\mathrm{T}}) = \frac{\int_0^{\infty} r dr \int_0^{2\pi} d\phi_s \ K_1(\beta(r,\phi_s)) \ \Omega(r,\phi_s)\cos(2\phi_s) \ I_2(\alpha(r,\phi_s))}{\int_0^{\infty} r dr \int_0^{2\pi} d\phi_s \ K_1(\beta(r,\phi_s)) \ \Omega(r,\phi_s) I_0(\alpha(r,\phi_s))} \tag{C.27}$$

Bibliography

[1] Michael Schmelling, Status of the Strong Coupling Constant, hep-ex/9701002 (1997)

[2] F. Karsch, E. Laermann and A. Peikert, The pressure in 2, 2 + 1, and 3 flavour QCD, Phys. Lett. **B478**, 447 (2000)

[3] Michael L. Miller, Klaus Reygers, Stephen J. Sanders, Peter Steinberg, Glauber Modeling in High Energy Nuclear Collisions, nucl-ex/0701025 (2007)

[4] J. E. Elias et al., Projectile Dependence of Multiparticle Production in Hadron-Nucleus Interactions at 100 GeV/c, Phys. Rev. Lett. **41**, 285 (1978)

[5] B. B. Back et al., Centrality and energy dependence of charged-particle multiplicities in heavy ion collisions in the context of elementary reactions, Phys. Rev. Lett. **74**, 021902(R) (2006)

[6] T. Matsui, Dynamical evolution of the quark-gluon plasma and phenomenology, Nucl. Phys. **A461**, 27 (1987)

[7] Larry. McLerran, The Color Glass Condensate and Small x Physics: 4 Lectures., hep-ph/0104285 (2001)

[8] Xinn-Nian Wang. A pQCD-based approach to parton production and equilibration in high-energy nuclear collision, Phys. Rep. 280, 287 (1997)

[9] J. D. Bjorken, Highly relativistic nucleus-nucleus collisions: The central rapidity region, Phys. Rev. **D27**, 140 (1983)

[10] S. S. Adler, et al., Identified charged particle spectra and yield in Au + Au Collisions at $\sqrt{s_{\mathrm{NN}}} = 200$ GeV, Phys. Rev. **C69**, 034909 (2004)

[11] K. Guettler et al., Inclusive production of low-momentum charged pions at $x = 0$ at the CERN intersecting storage rings, Phys. Rev. **D64**, 111 (1976)

[12] Philip J. Siemens and John O. Rasmussen, Evidence for a Blast Wave from Compressed Nuclear Matter , Phys. Rev. **C42**, 880 (1979)

[13] A. M. Poskanzer and S. A. Voloshin, Methods for analyzing anisotropic flow in relativistic nuclear collisions, Phys. Rev. **C58**, 1671 (1998)

[14] S. S. Adler, et al., Elliptic Flow of Identified Hadrons in Au + Au Collisions at $\sqrt{s_{\rm NN}} = 200$ GeV, Phys. Rev. Lett. **91**, 182301 (2003)

[15] Dènes Molnár and Sergei A. Voloshin, Elliptic Flow at Large Transverse Momentum from Quark Coalescence, Phys. Rev. Lett. **91**, 092301 (2003)

[16] A. Schwarzschild and C. Zupancic, Production of Tritons, Deuterons, Nucleons, and Mesons by 30-GeV Protons on Al, Be, and Fe Targets, Phys. Rep. 129, 854 (1963)

[17] J. Adams, et al., Azimuthal anisotropy in Au + Au collisions at $\sqrt{s_{\rm NN}} = 200$ GeV, Phys. Rev. **C72**, 014904 (2005)

[18] X. Dong, S.Esumi, P. Sorensen, N. Xu, Z.Xu, Resonance decay effects on anisotropy parameters, Phys. Lett. **B597**, 328 (2004)

[19] V. Greco and C. M. Ko, Effect of resonance decays on hadron elliptic flows, Phys. Rev. **C70**, 024901 (2004)

[20] R. J. Fries, B. Müller, C. Nonaka and S. A. Bass, Hadron production in heavy ion collisions: Fragmentation and recombination from a dense parton phase, Phys. Rev. **C68**, 044902 (2003)

[21] A. Kiyomichi, Ph-D thesis, Study of Identified Hadron Spectra and Yields at Mid-rapidity in $\sqrt{s_{\rm NN}} = 200$ GeV Au + Au Collisions, (2005)

[22] F. Retière, and M. A. Lisa, Observable implications of geometrical and dynamical aspects of freeze-out in heavy ion collisions, Phys. Rev. **C70**, 044907 (2004)

[23] Asher Shor, ϕ-Meson Production as a Probe of the Quark-Gluon Plasma, Phys. Rev. Lett. **54**, 1122 (1985)

[24] M. Harrison, T. Ludlam, S. Ozaki, RHIC project overview, Nucl. Instr. and Meth. **A499**, 235-244 (2003)

[25] M. Hahn, et al., The RHIC design overview, Nucl. Instr. and Meth. **A499**, 245-263 (2003)

[26] PHENIX Conceptual Design Report, BNL, 1993, unpublished

[27] S.H. Aronson et al., PHENIX Magnet System, Nucl. Instr. and Meth. **A499**, 480 (2003)

[28] C. Adler, et al., The RHIC zero degree calorimeters, Nucl. Instr. and Meth. **A461**, 337 (2001)

[29] K. Ikematsu et al., A start-timing detector for the collider experiment PHENIX at RHIC-BNL, Nucl. Instr. and Meth. **A411**, 238 (1998)

[30] Yuji Tsuchimoto, talk given in PHENIX Run4 Focus seminar for BBC.

[31] K. Adcox et al., PHENIX Detector Overview, Nucl. Instr. and Meth. **A499**, 469 (2003)

[32] K. Adcox et al., PHENIX Central Arm Tracking Detectors, Nucl. Instr. and Meth. **A499**, 489 (2003)

[33] M. Aizawa et al., PHENIX Central Arm Particle I.D. Detectors, Nucl. Instr. and Meth. **A499**, 508 (2003)

[34] Yuriy Riabov, Low-mass Drift Chambers of the PHENIX central spectrometers at RHIC, Nucl. Instr. and Meth. **A494**, 194 (2002)

[35] K. Adcox et al., Construction and performance of the PHENIX pad chambers, Nucl. Instr. and Meth. **A497**, 263 (2003)

[36] Hans-Ake Gustafsson, talk given in PHENIX Run4 Focus seminar for PC.

[37] L. Aphecetche et al., PHENIX Calorimeter, Nucl. Instr. and Meth. **A499**, 521 (2003)

[38] T. Hachiya, et al., Study of BBC trigger efficiency based on simulations for run-2 analysis, PHENIX internal analysis note. AN107

[39] J. L. Nagle, et al., Minimum Bias Trigger Selection and Centrality Note, PHENIX internal analysis note. AN112

[40] X. N. Wang and M. Gyulassy, HIJING: A Monte Carlo model for multiple jet production in pp, pA, and AA collisions, Phys. Rev. **D44**, 3501 (1991)

[41] T. Isobe and S. Esumi, PHENIX internal presentation in Global/Hadron PWG meeting, Centrality function for Run4 Au + Au $\sqrt{s_{\rm NN}} = 200$ GeV status report (https://www.phenix.bnl.gov/WWW/p/draft/isobe/PWG/PWG_TadaAki_20041119.ppt)

[42] J. Barrette et al., Energy and charged particles flow in 10.8A GeV/cAu + Au collisions, Phys. Rev. **C55**, 1420 (1997)

[43] T. Chujo, et al., p/π ratio in Au + Au at $\sqrt{s_{\rm NN}} = 62.4$ GeV, PHENIX internal analysis note. AN289

[44] T. Chujo, PHENIX internal Web page, TOF PID Recalibration Module Documentation (https://www.phenix.bnl.gov/WWW/p/draft/chujo/Pidrecal/)

[45] N. Borghini and J.-Y. Ollitrault, Azimuthally sensitive correlations in nucleus-nucleus collisions, Phys. Rev. **C70**, 064905 (2004)

[46] S. Esumi, et al., Analysis note for PPG022 (π/K/p v_2), PHENIX internal analysis note. AN174

[47] H. Masui, et al., Azimuthal anisotropy (v_2, v_4) of identified hadrons in Au + Au and Cu + Cu collisions at $\sqrt{s_{\rm NN}}$ = 200 GeV, PHENIX internal analysis note. AN445

[48] J. Jia, et al., Study on Charged High $p_{\rm T}$Background in PHENIX , PHENIX internal analysis note. AN177

[49] Henning Heiselberg, Anne-Marie Levy, Elliptic flow and Hanbury-Brown-Twiss correlations in noncentral nuclear collisions, Phys. Rev. **C59**, 2716 (1999)

[50] Rajeev S. Bhalerao, Jean-Paul Blaziot, Nicolas Borghini, Jean-Yves Ollitrault, Elliptic flow and incomplete equilibration at RHIC, Phys. Lett. **B627**, 49 (2005)

[51] Jean-Yves Ollitrault, Anisotropy as a signature of transverse collective flow, Phys. Rev. **D46**, 229 (1992)

[52] Nicolas Borghini, Phuong Mai Dinh, and Jean-Yves Ollitrault, New method for measuring azimuthal distributions in nucleus-nucleus collisions, Phys. Rev. **C63**, 054906 (2001)

[53] Rajeev S. Bhalerao, Jean-Yves Ollitrault, Eccentricity fluctuations and elliptic flow at RHIC, Phys. Lett. **B641**, 260 (2006)

[54] A. Adare, et al., Scaling Properties of Azimuthal Anisotropy in Au + Au and Cu + Cu Collisions at $\sqrt{s_{\rm NN}}$ = 200 GeV, Phys. Rev. Lett. **98**, 162301 (2007)

[55] S. S. Adler, et al., Deuteron and Antideuteron Production in Au + Au Collisions at $\sqrt{s_{\rm NN}}$ = 200 GeV, Phys. Rev. Lett. **94**, 122302 (2005)

[56] Masashi Kaneta and Nu Xu, Centrality Dependence of Chemical Freeze-out in Au + Au Collisions at RHIC, nucl-th/0405068 (2004)

[57] Peter Braun-Munzinger, Krzysztof Redlich, Johanna Stachel, Particle Production In Heavy Ion Coliisions, nucl-th/0304013 (2003)

[58] J. Adams et al., Azimuthally Sensitive Hanbury Brown-Twiss Interferometry in Au + Au Collisions at $\sqrt{s_{\rm NN}}$ = 200 GeV, Phys. Rev. Lett. **93**, 012301 (2004)

[59] F. Cooper, and G. Frye, Single-particle distribution in the hydrodynamic and statistical thermodynamic models of multiparticle production, Phys. Rev. **D10**, 186 (1974)

[60] W-M Yao, et al., Review of Particle Physics, J. Phys. G: Nucl. Part. Phys. 33, 1 (2006)

[61] M. Miller and R. Snellings, Eccentricity fluctuations and its possible effect on elliptic flow measurements, nucl-ex/0312008 (2003)